polymetallic sulfides for bio-inspired electrocatalysis

Kun Yang

To cite this version:

Kun Yang. polymetallic sulfides for bio-inspired electrocatalysis. Inorganic chemistry. Université Grenoble Alpes [2020-..], 2021. English. NNT : 2021GRALV058 . tel-03626525

HAL Id: tel-03626525
https://theses.hal.science/tel-03626525v1

Submitted on 31 Mar 2022

Université
Grenoble Alpes

THÈSE

Pour obtenir le grade de

DOCTEUR DE L'UNIVERSITE GRENOBLE ALPES

Spécialité : **Chimie inorganique et bio-inorganique**

Arrêté ministériel : 25 mai 2016

Présentée par

Kun YANG

Thèse dirigée par **Vincent ARTERO,** directeur de recherche
et co-encadrée par **Matthieu KOEPF, CEA**

préparée au sein du **Laboratoire de Chimie et Biologie des Métaux**
dans **l'École Doctorale de Chimie et Sciences du Vivant**

Sulfures polymétalliques pour l'électrocatalyse bio-inspirée

Thèse soutenue publiquement le **08 décembre 2021**,
devant le jury composé de :

Mme Carole DUBOC
Directrice de recherche, CNRS, Présidente du Jury
Mme Alessandra Elsje QUADRELLI
Directrice de recherche, CNRS, Rapportrice
M. Jean WEISS
Directeur de recherche, CNRS, Rapporteur
M. Vincent ARTERO
Directeur de recherche, CEA, directeur de thèse
Mme Pascale DELANGLE
Ingénieur de recherche, CEA, invitée
M. Matthieu KOEPF
Ingénieur de recherche, CEA, invité

Acknowledgments

Before the rational and objective parts, please give me several minutes to be emotional. For the following part you are going to read, the only name Kun Yang that signed on the cover page could not take all the credits. Taking this opportunity, I would like to thank people whose contribution is notable. Firstly, I would like to thank you, who are now reading these words. Thank you for being interesting in some parts of this work, which means a lot to me. It suggests that during the three years, I am not only enjoyed this beautiful work myself, but have done something could possibly contribute to the coming research.

It seems that most of the Chinese children once had a dream to become a scientist when they grow up, without a single idea of this job but with huge respect and expectation. I was one of them, and I am lucky enough to have realized the dream of that little girl during the marvelous three and a half years. I have to tell her that this is not an easy job at all, but it is more fantastic than she ever imagined. Working as a young researcher is a special experience, during which you could have the pure joy of thinking, of solving problems, of making things happen or fuguring things out; during which time you become more organized, more responsible, more curious, more skeptical, more patient and of course, tougher. Since nobody could succeed in every single experience, or worse, you faced numerous unexpected results, not in a positive way. But when you walk yourself through, you will find it worth every single second.

Approaching the destination of this journey, I look back with gratitude full of my heart. The other person who contributes the most to this project, is my kind supervisor Dr. Matthieu Koepf. Even my background was not fully corresponding to the project, he accepted me and helped me to make progress. He is such an intelligent, creative, patient, kind, responsible guide on my way of the PhD study. He is such a reliable teacher and friend, even when I screwed things up, he had never lost his temper on me but encouraging me and helping me all the time. Moreover, he is such devoted to research and science, always being such a good model. I have met and learnt from

numerous marvelous teachers, but I musy say he is one the best.

That important evening four years ago, there was another person who interviewed me in the reception center of CEA, my director Dr. Vincent Artero. I always impressed of his high-level view which could rapidly and precisely reach the point. He is always supportive and save time for our discussion, which led us to making progress on this route. Leader has a huge impact on the atmosphere and the spirit of a group, and I really want to thank him to make Solhycat such a great family.

Of course, which also credit to other members in the groups: Dr. Adina Morozan, she is so sweet to help me get started on electrochemistry study, to solve many problems that I met, and of course the materials she prepared with Dr. Camille Roiron had huge contribution to this study. Safae Mouftakhir, she did a great job in organic synthesis and helped me to prepared very important products. Louis Dubrulle, we had spent interesting N_2 reduction time together. Mme. Jennifer Fize, she contributes to the well-organized laboratory make our work become easier. Dr. Duc Nguyen Ngoc, he is not only helped me with the experiments but being such a great friend, who left me many great photos. Dr. Yao Fu, she not only provided me materials in work, but made my final year in Grenoble greater around a bravo friend like her. Dr. Murielle Chavarot-Kerlidou, she is so kind to providing precious advises to us and being helpful. Tania, Laura, Jonathan, Nabil, Manos, Ghislain, Nick, Chengbo, even many of them have already left for their next station, but the shared memories in our office will always stay with me. And in the other office, Mariam, Angelica, Bertrand, Matthieu, Luca, Jingxian, Andrew, Afridi, Tim, Christina, Sabastian…And of course the nice people I crossed in LCBM, I am so lucky to spend the great time with you.

This work, could not realize without the contribution of the following people, and I sincerely to express my gratitude to them by this chance. Dr. Martin J. Field assisted our practical work with his great theoretical studies; Dr. Jacques Pecaut analyzed loads of mass samples for us and we had fun to analyze the single crystal structures; Dr. Colette Lebrun and Dr. Laure Fort contributed to our MS study as well; Dr. Jérôme Chauvin, we worked on fluorescence spectroscopy together; Dr. Pierre-Alain Bayle and

Dr. Marina Gromova, we had interesting discussions focusing on the NMR spectra with the advance techniques inspired by their expertise; Dr. Stéphane Torelli and Dr. Marcello Gennari accompanied us with EPR study to exclude the wrong hypothesis…

Grenoble is not a big city, but my short stay here was still enough for me to know a group of fabulous friends, they colored my lonely study time. During all this time, my dear family always stood by me. Even though my father has conquered cancer three times only accompanied by my mother in this five year that I was away from home, they had never been unsupportive for my study aboard not even one second. I love them so much and always fell so lucky to be their daughter. My grandparents, especially my grandfather, he is always a model for me, he never stops learning even in age of 80s. He encourages me to chase all the ambitious dream that I have. Many kind family members and all my friends from all over the world, their love made me stronger to face the challenges. I could not name all of you in the limited space, but my love to you is unlimited.

I have spent long time in school, and I sincerely would like to thank all the other teachers I met on this way that I have not mentioned above: you taught me much more than the knowledges. Especially Dr. Bérangère Toury, she accepted me for the master 1 internship in her group from where I really began my research life.

There is definitely no enough space for all my gratitude that I want to express in this short three pages, but I have to stop here. Briefly, thank for all of you that appeared in my life and made it so marvelous. Holding all the emotions in the bottom of my heart, I will keep positive, kind, active in the following journey.

Hope you all the best. Bisous.

2021.12.06

Grenoble, France

Content

1 Introduction

1.1 Ammonia-economy

Ammonia not only plays crucial roles in various fields such as agriculture, chemical manufacturing, but also shows potential as a sustainable energy carrier.

1.1.1 Nitrogen fertilizer

Over 80 % of the ammonia produced is used for the formulation of fertilizers, resulting in a current worldwide use of nitrogen-based fertilizers of about 100 Tg N (terrogram Nitrogen) per year. Thanks to the increased nitrogen fertilizer productivity, the number of persons supported per hectare of arable land has doubled over the last 100 years.[1] Nitrogen application through mineral fertilizer, indeed, allowed an increase of about 30–50% the yields of crops,[2] which now feed almost half of the world population. Meanwhile, the continuous rise in the food demand keeps challenging our food supply capacity. To meet the needs of the human population, which will reach 9.3 billion individuals by 2050 as projected by the United Nations Population Division (UNPD), the required amount of food calories will increase by about 60 percent from 4×10^{13} kJ needed in 2006, which in turn means a continuous increase in the need of fertilizer supply.

1.1.2 Sustainable energy carrier

Considering the depletion of fossil fuels and their enormous impact on environment and human health, an expanding number of studies are focused on developing sustainable, clean, carbon-free alternative energy carriers, in order to phase out conventional hydrocarbon fuels.

1.1.2.1 Potential fuel and H_2 carrier

In this context, 'the hydrogen-economy'[3] was proposed as an alternative in which hydrogen would be used as a major player, thanks to its high energy capacity (around 3 times greater than hydrocarbon fuels), as well as its advantageous chemistry (only lead to water production).[4] H_2 could be stored in its pure molecular form in high pressure gas cylinders, or physically absorbed on various materials, or even chemically bonded to form hydrides.

However, large-scale hydrogen storage is still challenging and expensive, which highly limited the development of the 'the hydrogen-economy' so far.

The concept of 'ammonia economy' presents ammonia as an alternative choice to fossil fuel.[5] As its clean combustion only exhausting water and nitrogen, furthermore, it is a well-established industrial product with large infrastructures already in place for the production, handling and transporting. NH_3 also possessing several assets with respect to H_2, such as: higher volumetric energy density (11.5×10^3 kJ/L for liquid NH_3 compared to 8.5×10^3 kJ/L for liquid H_2); easier to handle for large scale storage and transportation.[6] Ammonia gas liquefies easily under light pressure and cooling (–33°C, 1 atm).[6] Ammonia and/or ammonia composited fuels (H_2-NH_3; CH_4-NH_3) have already been envisioned to be directly used in Fuel cells.[7] And modified diesel engine has already successfully combusted NH_3.[8]

Nevertheless, ammonia is not flawless candidate fuel. The notable safety issue during storage and distribution should be carefully considered: volatility, low flash point, and invisible flame.[8] Nonetheless, thanks to its smaller density than air, it will float upwards quickly. Luckily, it is non-explosive, and could be easily identified below harmful limit due to the pungent smell.[9] Furthermore, liquid ammonia has higher 'apparent toxicity' than gasoline and methanol,[10] but it can be easily overcome by conversing to the form of metal ammonium salts.[10,11] With this respect, a recent EU-funded report indicated that the implementation of ammonia as a transport fuel do not present more conventional risks than the fuels currently in use, if several requirements are fulfilled regarding vehicle, refueling station.[12]

In addition, ammonia is recognized as a promising decarbonized H_2 carrier, possessing a high storage density: Liquid ammonia at 10 bars has high hydrogen storage density: 17.7% (wt) gravimetrically and 123 kg/m^3 volumetrically. The release of H_2 from NH_3 only requires an easy catalytic decomposition.[10]

1.2 Nitrogen reduction reaction (NRR)

Dinitrogen (N_2), making up about 78% of the atmosphere, is the major source of nitrogen on earth. It could not, however, directly metabolized by most organisms and must be reduced to be assimilated. In nature, the nitrogen reduction reaction (NRR) occurs following two pathways: (a) abiotically by lightning and (b) biotically by bacteria. Before the development of the current prevailing anthropogenic Haber-Bosch process (HBP), microorganisms have been responsible for most of nitrogen reduction (designated as biological nitrogen fixation, BNF).[13]

The direct splitting of N_2 is intrinsically disfavored from a thermodynamic standpoint. Indeed the N≡N triple bond possess a high overall dissociation energy (942 kJ/mol), half of which associated with the extremely stable first bond to break.[14] Additionally, it possess a low electron affinity (−1.8 eV) and high ionization energy (−15.58 eV). On the other hand, N_2 is kinetically stable owing to the lack of permanent dipole, as well as to its poor electro-/nucleophility.[15]

Therefore, industrial HBP (***equation 1***) requires a large energy input (480 kJ/mol for NH_3) and severe high temperature high pressure conditions. Even for the in vivo BNF (***equation 2***, ATP adenosine triphosphate; ADP as adenosine diphosphate; Pi as inorganic phosphate) occurring under mild conditions requires significant biological energy input in form of ATP (380 kJ/ mol for NH_3).[16]

$$N_2 + 3H_2 \xrightarrow[\text{Fe/Ru catalyst}]{\sim 20\text{ MPa} \sim 500\text{ °C}} 2NH_3 \qquad \textbf{(1)}$$

$$N_2 + 8H^+ + 8e^- + 16ATP \xrightarrow[Mo-nitrogenase]{} 2NH_3 + H_2 + 16ADP + 16P_i \qquad \textbf{(2)}$$

1.2.1 The Haber-Bosch Process (HBP)

1.2.1.1 The history and importance

The Haber-Bosch process (HBP) is based on the hydrogenation of metal nitrides obtained by thermal activation of dinitrogen, on iron or ruthenium catalysts, under 400-500 °C and 10-20 MPa.[17] HBP has been applauded as the greatest invention in twentieth century.[18] A patent called “synthesis of ammonia from its elements’ was filed by Fritz Haber in 1908, which granted him the Nobel Prize in chemistry in 1918.[19] His work was then scaled up by Carl Bosch to an industrial process, who was also awarded by the Nobel Price of Chemistry in 1931.[20] Now the HBP has more than 100 year history, and is still fully active since no other comparable NRR industrial process is known to date. HBP, is more than an approach to NRR, but a milestone of the chemical industry.

Progress has been made during the past 100 years, as the daily NH_3 production capacity of a single unit has increased from 5 t to 2200 t, whereas the catalyst remains essentially the same.[21] After Haber implemented high pressure conditions for driving NRR, Bosch and his colleagues Mittasch, and Ertl systematically tested thousands of different catalytic systems before the discovery of magnetite-based fused iron catalyst, which still appears to be the most appropriate catalyst for the HBP. It pertains to the crystalline iron oxides (Fe_3O_4) family and incorporate a small amount of other oxides as promoters, which can be divided into structural and electronic promoters. For instance, Al, Mg, ans Si oxides work as structure modifiers, increasing the overall porosity of the material which is pivotal to expand the active surface of the catalyst. Meanwhile, potassium oxides are used as electronic promoter which favor the dissociative binding of N_2 to the catalyst. It is also proposed that alkali oxides can neutralize the acidic centers of the oxide surface thus preventing the poisoning of the catalyst by the absorption of NHX species.[22] Such a complex industrial catalyst system demonstrated once again the difficulty faced to promote NRR.

1.2.1.2 Defects and situation

The HBP is not, notwithstanding, a flawless process.

First of all, it is a very energy-intensive. About $2.75 \text{ X } 10^7$ kJ is still needed for the production of 1 ton of NH_3 in the most advanced ammonia plant to date. Actually, only 30% of this energy input is directly used for the synthesis, but most of the rest part go for the preparation of H_2.[24] Moreover, the conversion efficiency of a single step of the HBP is only 15%. Even through the recycling of the unreacted gases (N_2, H_2) allows to an overall yield of conversion of nearly 97% it brings obvious increase in the complexity of the industrial process.

Furthermore, the HBP requires pure H_2 as reagent, which is mainly obtained from the natural gas reformation (***Equation 3***). About 22% of the energy input feed to this step is based on coal gasification, while the rest mostly relying on fuel oil.[25] The preparation of H_2 is not only the main energy consumer in HBP, but also the main CO_2 source.

$$CH_4 + 2H_2O \rightarrow 2H_2 + CO_2 \qquad \textbf{\textit{(3)}}$$

As a result from 1) the H_2 production, 2) the purification of the reactant gases and 3) the compression of the reaction mixture,[26] over 100 million metric tons per year of global NH_3 production accounts for more than 1.8% of the world's consumption of fossil fuels, and consequently over 1% of carbon dioxide emissions.[27,28] The excessive dependence of HBP on fossil resources is obviously antagonist to the current needs for developing more eco-friendly industrial process. Besides, HBP need to be run in large scale to be ecologically and economically performant.[29]

In view of all the points mentioned above, HBP has several drawbacks to be addressed, such as the dependence on fossil fuels; the problems brought by the current strategy for H_2 production; the lack of controllable production scales. Attempts to implement water electrolysis to produce H_2 into HBP have been tried. However, it is also facing problems such as high costs and issues related to short-term storage of H_2.

In a word, searching for alternative NRR pathways to the HBP is an environmental imperative.

1.2.2 Biological nitrogen fixation (BNF)

Biological nitrogen fixation (BNF) is formally driven by the coupled transfer of protons and electrons to N_2 in a process fueled by the hydrolysis of ATP. This reaction is catalyzed under physiological conditions by a specialized class of enzymes, the nitrogenases, which are found in diazotrophs. Nitrogenases are the only known biological systems capable of reducing N_2 to NH_3.[30–32] Even for the most efficient nitrogenase the reaction is highly demanding and as described in ***Equation 2***, at least one mole of H_2 is produced for the release of two moles of NH_3 (that is, for each mole of N_2 formally reduced) leading to a net "loss" of 25% of the energy input of the biological process. Besides, nitrogenase could also work as a good catalyst for HER in the absence of N_2, or reduce carbon dioxide (CO_2) to formate ($HCOO^-$) and methane (CH_4) even higher hydrocarbons.[33] Some non-physiological substrates such as diazene, hydrazine, azide, NO_x and even carbon-based substrates like alkene could be reduced by nitrogenase as well.[34]

1.2.2.1 Structures

The crystal structure of nitrogenase is established. Three isozymes are known today, the so-called Mo-, V- and Fe-nitrogenases. They are mainly distinguished by the composition of the co-factor supporting the catalysis, featuring either Mo/Fe-, V/Fe- or all Fe-based sulfides clusters, respectively.

Despite exhibiting some notable differences in their respective sequences, all of the nitrogenases exhibit the same overall structure. Among them, the Mo-containing nitrogenase is the most frequent form found in all diazotrophs, as well as the most efficient for BNF.[30]

Nitrogenases consist of two proteins (***Figure 1.1***):

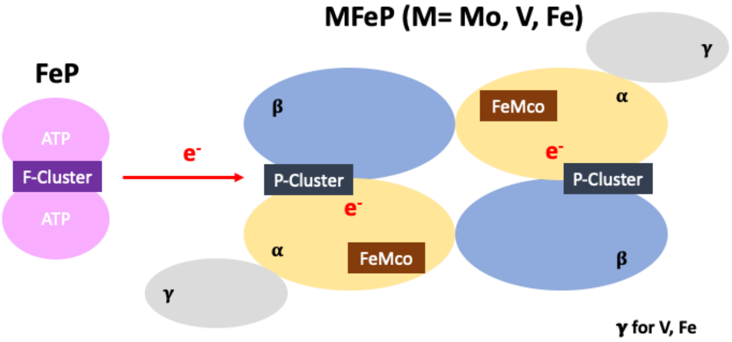

Figure 1.1 *Structure of Fe protein and MFe protein.*

1) One homodimeric Fe protein (FeP, dinitrogenase reductase) weighing around 66 kDa. Each FeP subunit has one nucleotide binding site for one molecule of ATP. The two subunits are bridged by a [4Fe-4S] cluster (F-cluster, ***Figure 1.2***), which is coordinated by two cysteine residues from each monomer. The F-cluster facilitates the hydrolysis of MgATP and initialize the electron flow to MoFe protein.[36]

The F-cluster is highly exposed to the solvent, and exists in the all-ferrous state as [4Fe-4S]^{0} when fully reduced. It successively reaches [4Fe-4S]$^{1+}$ and [4Fe-4S]$^{2+}$ upon the sequential transfer of electrons to the dinitrogenase. In the [4Fe-4S]$^{2+}$ state, all four iron centers were assigned as Fe$^{2.5+}$.[37] The F-cluster appears more reducing when binding to MgATP/ADP, as suggested by calculation, which might result from the proximity of the negative charge of ATP/ADP.[38,39]

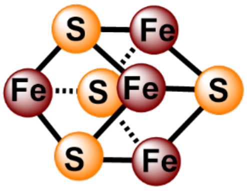

Figure 1.2 *Structure of F-cluster.*

2) One $\alpha_2\beta_2$ heterotetrameric catalytic MoFe protein (MoFeP) weighing about 240–250 kDa or one $\alpha_2\beta_2\gamma_2$ heterohexamer for V-and Fe- nitrogenases (***Figure 1.1***).[40] MoFeP contains an [8Fe-7S] center (P-cluster), and a metal cofactor [$MoFe_7S_9C$] (FeMoCo) (Mo is replaced by Fe, V in the other nitrogenases).

The P-clusters are located at the interface between the α and β subunits in MoFeP, and manage the electron transfer from the F-cluster (FeP) to the FeMoCo. Structurally, the P-cluster can be seen as two Fe-S cubanes sharing a central S (***Figure 1.3***), in which all Fe are in a +2 oxidation state when isolated in the reduced form in presence of dithionite.[41] The P-cluster is coordinated to two bridging and four terminal cysteines, which contribute to reduce the negative charges of cluster, and stabilize it's all ferrous state.[42] It is indicated that P-cluster also contribute to the maturation of MoFeP by helping assembly of FeMoCo.[43]

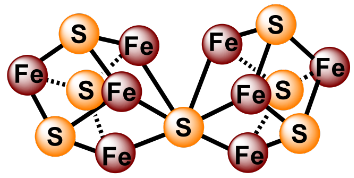

Figure 1.3 *Structure of P-cluster*

In the Mo-nitrogenases, the two FeMoCo are buried 10 Å beneath the protein surface, within the α subunits. Considerable progress has been made on the study of FeMoCo which supports the active site for BNF.[32] FeMoCo $[MoFe_7(\mu_2\text{-}S)_3(\mu_3\text{-}S)_6(\mu_{6}\text{-}C)]$ is also known as one of the most complex cofactors in biology (***Figure 1.4***). It can be described as: three μ_2-S and one μ_6-C bridging one $MoFe_3S_3$ and one Fe_4S_3 unit, with one Mo(III), three Fe(II) and four 'more oxidized' Fe (proposed as $[3Fe^{+2}:4Fe^{+3}:Mo^{+3}]$) but it is also possible to present mixed-valence states due to the delocalization of electrons.[44]

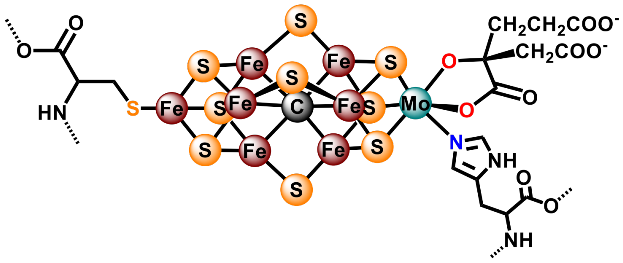

Figure 1.4 *Structure of FeMo cofactors.*

The Mo is coordinated to a histidine while the distal Fe is coordinated to one cysteine of the polypetide backbone.[35] Alongside the inorganic core, the Mo also connect to an organic acid R-homocitrate, whose function still remain elusive.[45]

1.2.2.2 Mechanism

Thanks to the availability of high-resolution structures of the Fe-protein from *Azotobacter vinelandii* and the MoFe-protein from both *A. vinelandii* and *Clostridium pasteurianum*, along with the considerable improvement in theoretical methods, it is possible to uncover the mechanism of nitrogenase.[31,46–48] Moreover with the capture of some frozen intermediates, and the help of advanced spectroscopies, the interpretation has become more profound and convincing.[31,49] However, a complete and detailed description of the mechanism is still under active research.

Electron transfer

Building on the Lowe−Thorneley theory proposed in 1970s, the latest years have witnessed major progress in unveiling the electron transfer (ET) process in nitrogenase, which will be shortly summarized in ***Figure 1.5.***[50]

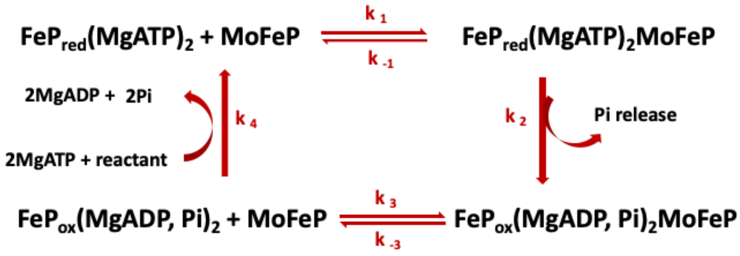

Figure 1.5 *Electron transfer and reaction in Mo-nitrogenase.*

Up to date, there are still some ambiguities on how nitrogenase controls ET and couples it to ATP hydrolysis. Firstly the FeP is reduced by biological electron donors such as flavodoxins and ferredoxins, followed by the subsequent interaction with MoFeP. These two steps involve the same active region of the FeP.[51,52] FeP forms a metastable pre-active complex with MoFeP through electrostatic interactions, where a conformational change occurred which then triggers the ET. The cycle is completed with the dissociation of two proteins and the re-assembly of MoFeP with another reduced FeP.

The successful co-crystallization of FeP with MoFeP, provided insight into the details of the interaction between these two proteins, and led to the following conclusion: 1) The FeP displays a nucleotide dependent conformational change which helps it to adapt to the geometry of the MoFeP; 2) the MoFeP maintains an invariant structure; 3) the modulation of the distance between the P-cluster (MoFeP) and the F-cluster (FeP) is nucleotide dependent.[48] 4) The ET between the two proteins was found to be influenced by parameters other than simple protein diffusion, and suggested the mechanisms of conformation gating.[49]

In the earliest stage of the study of nitrogenase's mechanism, the model proposed inferred that: 1) the hydrolysis of the ATPs bound to the FeP drove the generation of 'super reducing' electrons; 2) these electrons were then transferred to MoFeP and played a crucial role to form partially reduced nitrogen intermediates.[53] However, such 'super-reduced' state has never been observed experimentally. More recently it has been proposed that the electrons generated in FeP are transferred to the MoFe protein through a 'deficit-spending model' termed by Hoffman , Seefeld and Dean.[54] In this scenario, the P-cluster transfers electrons to the FeMoco, before being reduced by the F-cluster. Up to now, no clear MoFeP structure/intermediate observed could elucidate the 'gating' mechanism mentioned above. However, there is no doubt that the P-cluster is involved and work as an electron relay to facilitate the interprotein ET. The coordinated peptide environment change plays essential role, as stabilizing the oxidized P-cluster and facilitating ET to FeMoCo. [48]

Lacking sturdy evidences to discriminate between them, two contradictory views still exists regarding the sequence of ATP hydrolysis and ET. (1) the ATP hydrolysis actually triggers the interprotein ET; or (2) the simple ATP binding initiates the interprotein ET, but ATP hydrolysis occurs afterwards. More experiments are still required to solve this mystery. [48]

Nitrogen reduction

The Lowe−Thorneley kinetic scheme proposed that the catalytic cycle of the nitrogenase involves 10 intermediates for nitrogen reduction (***Figure 1.6***).[50] Each intermediate is characterized by a specific electron, proton and substrate states of FeMoCo, some of which could be confirmed subsequently by intermediate trapping.[55] Eight electrons are involved in total to reduce N_2 molecule, including two leading to the release of H_2,[50] as demonstrated by stoichiometric experiments.[56] One proton is integrated with each electron allowing for electrostatic stabilization of the intermediates.[57] The whole process was elucidated as eight times of one-electron one-proton delivery generating eight catalytic intermediates, denoted as E_n with n as the number of steps, or the number of transferred $[e^-/H^+]$.[34] Each step consumes 2 MgATP, resulting in the need of 16 ATP (ΔG° 488 kJ/mol in total).[33]

This cycle (***Figure 1.6***) starts from the resting E0 state. After the sequential transfer of four electrons and four protons, the E4 state is reached where the N_2 binds. E4 state is called Janus, named after a two-face roman god, signifying beginnings, transitions and endings. The E4 can follow two paths 1) the loss of 2 H_2 and revert to E0, or 2) the binding of N_2 while releasing 1 H_2 which can lead to the production of 2 NH_3 after four additional transfer of proton- electron-equivalents. The four proton- electron- equivalents accumulated in the Janus E4 state led to the formation of two [Fe-H-Fe] hydrides, two –SH bond.[58] From E1 to E4, there are only two formal redox levels of metal-ion core (M^0, M^-), but accumulate 4 reducing equivalents as hydrides (H^-, ***Figure 1.6***). The following mechanism involving the reductive elimination of H_2 is suggested by Hoffman et co-workers (***Equation 4***) (***Figure 1.6)***:[31]

$$E_4(4H) + N_2 \rightleftarrows E_4(2H2N) + H_2 \qquad \Delta_{re}G^0 \sim -8.37 \text{ kJ/mol} \tag{4}$$

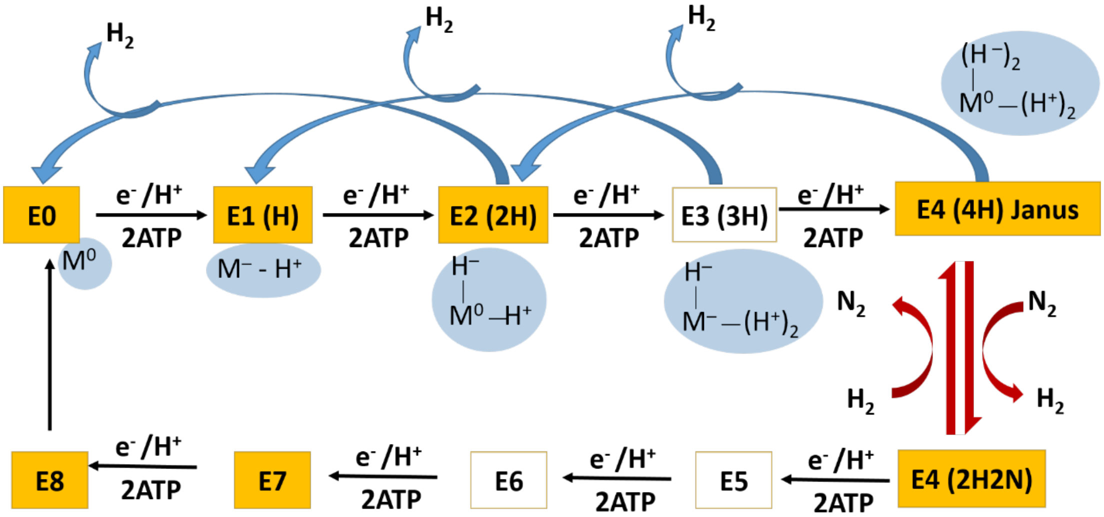

Figure 1.6 *Lowe−Thorneley scheme.*

The equilibrium is essentially thermoneutral comparing to the direct $N_{2(g)}$ hydrogenation which need more than 209 kJ/mol.[59] Two reducing equivalents are stored as hydrides, and their reductive elimination left a doubly reduced iron which could weaken the triple N≡N bond. It is impressive that nitrogenase combines the exothermic H_2 formation with the endothermic N≡N triple bond cleavage.[60] Furthermore, it is truly remarkable that the E4 state is more likely to go forward leading to the reduction of N_2 rather than simply releasing H_2 and go back to the E2 state. Hydrogen is only lost upon binding nitrogen, which is instructive to designing artificial NRR catalyst. This coordination mechanism also highlights the benefits of using multinuclear metal catalysts.

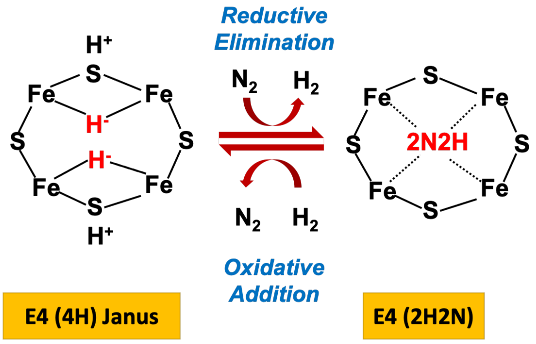

Figure 1.7 *Reductive elimination of H_2 mechanism.*

Starting from the E4 state, two approaches for N_2 fixation were proposed through theoretic calculation as distal pathway (D) and alternating pathway (A) (***Figure 1.8***).[61] Through pathway (D), three first proton are transferred to the same N, releasing one NH_3 and generating a nitrido- intermediate who leads to the second NH_3 after three subsequent steps. [62,63] While in pathway (A), two N take turns for accepting protons and form diazene- and hydrazine-intermediates in sequence.[66] Additionally, Peters et *al*. has proposed a hybrid-A pathway, in which E4 starts with distal way to form hydrazido but the third H is added to another N instead of complete and release the first NH_3.[67] Recently the pathway (A) was substantiated by the observation that hydrazine is both a substrate of nitrogenase and a product of nitrogenase upon acidic and basic hydrolysis.[57,66]

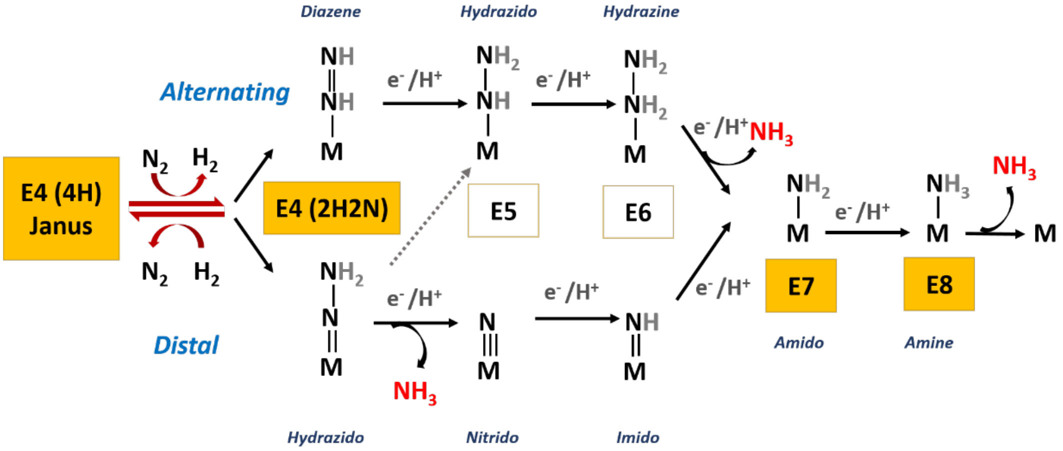

Figure 1.8 *Two pathway of reduction nitrogen to ammonia.*

Interestingly the nitrogenase could be activated chemically, electrochemically and photochemically in absence of ATP supply, this might be convenient for its in vitro application.[48]

1.2.3 Comparison

Here we retrospectively compared two pathways narrated above. Biological nitrogen fixation (BNF) by nitrogenase and Haber-Bosch Process (HBP) currently assume the responsibility, half for each, to cope to the NH_3 demand. The two pathways show differences in several aspects: (1) The overall reaction mechanism and the hydrogen source. HBP uses pure H_2 gas in a thermochemical process, while nitrogenase goes through a proton-electron sequential transfer process.

(2) N_2 activation mechanism. HBP deals it through dissociation mechanism where the first hydrogenation happens on nitride-M, while nitrogenases follows an association mechanism where N-H bonds are formed before the dissociation of dinitrogen, regardless of the path followed (alternating or distal).

(3) Working condition. The HBP requires much higher temperatures and higher pressures then the mild physiological condition of BNF.

(4) Different energy supply. HBP is driven by thermal energy currently obtained from the combustion of fossil fuels while nitrogenases rely on ATP hydrolysis.

Through this comparison, it is obvious that BNF bypasses many issues faced by the HBP, and produces ammonia under milder condition in a carbon free manner. Whereas, direct industrial scale BNF is not yet achievable, due to the delicate protein structure as well as the complicated mechanism coupled to ATP hydrolysis, the sequential proton electron transfer mechanism of the enzyme and the use of abundant metals could be instructive for the development of electrochemical catalyst. Therefore, researchers endeavored to discover system involving biological moieties or synthetic analogues, about which we will discussed in more details in following parts.

1.2.4 Electrochemical nitrogen reduction reaction (ENRR)

The electrochemical nitrogen reduction reaction (ENRR), which is predicted to be 20% more efficient than HBP from a thermodynamic standpoint, appears to be one of the most appealing strategies for developing an alternative process for the production of ammonia.[67]

Different pathways to ENRR can be considered:

1. the direct reduction of N_2 to NH_3 at a cathode, via proton-coupled electron transfers, usually involving a so-called electrocatalyst:

$$N_2 + 6H^+ + 6e^- \xrightarrow[electrocatalyst]{} 2NH_3$$

2. the step-wise formation of a sacrificial intermediate at an electrode followed by its stoichiometric reaction to produce ammonia.

Typical examples of such step wise strategies as mechanism 2 can be seen in the Chatt-type electrochemical process and Li^+-mediated NRR.

Chatt and co works have reported zerovalent molybdenum and tungsten complexes able to coordinate N_2 leading to the release of NH_3 through the following reaction: $[M^{(0)}(N_2)_2P_4] + H^+ \rightarrow N_2 + NH_3 +$ others (M=Mo or W; P=phosphorus ligand). This Chatt-type complex triggered the interest of Pickett and co-workers who discovered that $[W^{(0)}(N_2)_2P_2]$ can react with tosylic acid to form $[W^{(IV)}(NNH_2)TsOP_2]^+$ and sequentially releases NH_3, along with the regeneration of $[W(N_2)_2P_2]$. However, only the second half is realized via electro-reduction, therefore such a cycle is completed in an electrochemical process, however, not an electrocatalytic process.[68,69]

Li^+-mediate forming of Li_3N which subsequently react with H source;[70]

$$6\mathrm{Li}^+ \xrightarrow{6e^-} 6\mathrm{Li} \overset{N_2}{\rightarrow} 2\mathrm{Li_3N} \xrightarrow{6\mathrm{EtOH}} 2NH_3 + 6\mathrm{EtOLi}$$

Nonetheless, the harsh high-pressure condition and extreme cathodic potential is demanded to regenerate Li by Li^+ hinder its application.

In this work, we focus on mechanism 1.

Besides, proper local electronic field or solvation effects erected by electrolyte or promoter are also important for NRR, for instance, they could selectively help to prompt N binding than H binding.[71] ENRR can be done in a large variety of media such as liquid,[72] molten salt,[73] traditional solid mixed with low melting salt and solid electrolytes.

Liquid electrolytes which are typically used in ambient conditions, including organic or aqueous solutions, and attracted most attention for their easiness of use. Acidic,[74] basic,[75] or neutral[76] electrolytes have been reported for aqueous based ENRR. However, these classical media suffer from rather low saturation concentration for N_2, which limit the current density. Besides, it is difficult to control the competing HER in aqueous media for non-selective catalysts. Diminishing available quantity of H^+, or abating its diffusion could be strategies to reduce HER, therefore aprotic electrolyte or aprotic, hydrophobic layer on catalyst were proposed by researchers.[71]

Interestingly a few studies recently demonstrated that specific ionic liquids can develop strong interactions with N_2 thus allowing for an increased solubility. Combined with the improved proton management provided by the use of an all-organic electrolyte, ionic liquid-based systems allowed reaching a remarkable faradaic efficiency (FE) of 60% for ENRR. However, the high viscosity of the media might delayed its activity.[72]

Higher FE could be observed in some studies using molten salts as electrolyte, nevertheless, these systems require complicated set-ups and more severe condition such as high temperature,[73] but the idea of limiting available water amount is still meaningful.

When considering solid-state electrolytes, the direct contact between the N_2 gas and the cathode allows for an optimal interaction with the electrocatalyst and avoids the low N_2 solubility issues faced in liquid media. However the mass transport being even lower, high operating temperatures (often above 100 °C) are required.

So far, liquid based electrolytes remain the most popular media for the development of electrocatalysts for ENRR.

1.2.4.1 Advantages

The electro-chemical nitrogen reduction reaction (ENRR) might provide a viable alternative to HBP, even though the capital costs still need to be minimized.[77,78] ENRR merits can be summarized as follow:

(a) ENRR can help circumvent the massive energy needs and CO_2 emission resulting from the production of H_2 required for HBP, as the process features the direct use of protons in the catalytic cycle. The rise of carbon taxes may even allow ENRR to compete directly with fossil fuel-based ammonia on price alone.

(b) ENRR offers the possibility to valorize the intermittent electricity derived from clean and renewable energy sources, such as solar, wind, hydro energy.

(c) ENRR generally requires lower pressures and lower temperature than HBP.

(d) ENRR offers more flexible processes in terms of load and scale, thus allowing for and easier scaling of the production units to the local needs which opens the possibility to decentralize the ammonia production.

1.2.4.2 Challenges

Reactivity and selectivity

The high activation energy of the N≡N triple bond demands a high energy input, even though the overall nitrogen reduction reaction is exothermic. The associative mechanism (***Figure 1.9***) appears to be more favorable under electrochemical conditions for N_2 reduction.

$$\begin{gathered}
* + N_2 + H^+ + e^- \leftrightarrow * N_2H \\
* N_2H + H^+ + e^- \leftrightarrow * N_2H_2 \\
* N_2H_2 + H^+ + e^- \leftrightarrow * N + NH_{3(g)} \\
* N + H^+ + e^- \leftrightarrow * NH \\
* NH + H^+ + e^- \leftrightarrow * NH_2 \\
* NH_2 + H^+ + e^- \leftrightarrow * + NH_{3(g)}
\end{gathered}$$

Figure 1.9 *Associative mechanism for ENRR.*

The difficulty of driving ENRR not only results from the complexity of NRR itself involving $6e^-$ /$6H^+$ transfer (reactivity), but also the competition with other electrochemical process in presence of proton (selectivity). The current poor efficiency reported for ENRR is mainly caused by competition with the hydrogen evolution reaction (HER). Indeed, the latter implying a simple two electron and two proton process, is often predominant, especially in aqueous environment. Nonetheless, the ENRR has been proved thermodynamically possible with a standard potential $E^0(N_2/NH_3) = 0.092$ V *vs.* NHE ($E^0(H^+/H_2) = 0$ V *vs.* NHE), which open a small window before its competitor.

Indeed, in addition to the facile H_2 evolution form metal hydrides, recent calculations for iron-based catalysts showed that early intermediates of NRR bearing weak N-H bonds (as M(NNH); M(NNH_2)) can release H_2 via bimolecular PCET (proton-coupled electron transfer).[79] Similarly in the Schrock catalyst (see below), the initial Mo-N_2 complex can be regenerated from the Mo-NNH intermediate through competitive β-elimination.[80] Obviously the challenge of cross reactivity of intermediates are valid for both molecular and material based catalysts.

1.2.4.3 Perspectives

Facing the challenges described above, ENRR is not only hampered by a high activation energy barrier but also by the complex nature of the reaction involving multiple electron/proton transfer with often sluggish kinetics for each step. Therefore the development of efficient electrocatalysts is critical to lower the activation energy of the process and drive the reaction at a reasonable overpotential.[81] Over the last few years, a large variety of materials have been proposed as potential catalysts for ENRR, with now hundreds of studies exploring virtually all the chemical landscape including pure organic materials, main elements and transition metal nanoparticles, their (mixed) oxides, nitrides, carbides, phosphides, chalcogenides, synthetic molecular complexes as well as biological systems.[82–86]

The ENRR could become an viable alternative to the HBP only if the ammonia production rate reaches about 2.5 x 10^{-3} mol.cm^{-2}.h^{-1} in a process delivering current densities of 300 mA.cm^{-2} and 90% coulombic efficiency according to the target established in the **REFUEL** (Renewable Electricity to Fuels through Utilization of Energy-dense Liquids) program of the United States Department of Energy (DOE). In comparison, most of the materials reported so far exhibit rates in the range of 10^{-10}-10^{-5} mol.cm^{-2}.h^{-1}. Thus, not even considering the low current densities and often mediocre Faradaic efficiencies achieved, it is apparent that the catalysts currently available are way behind the expected targets, which demonstrates, that the intrinsic difficulties of ENRR mentioned above are still far from being overcome.

In this work, we intend to develop bio-inspired catalysts for ENRR, which will be discussed in details in the following sections.

1.3 Electro catalyst design

Naturally, the rate of an electrochemical reaction is determined by the electrocatalyst activity and the electrolyte (composition and pH). Moreover, the proper selection of the electrochemical cell configuration, the electrode material, the applied potential, and operating conditions (temperature, pressure...) also largely contributes to the performance of the whole electrochemical process. However firstly, we will focus on the most crucial element: the electrocatalyst. In this part, we are about to review some recently reported ENRR catalysts then introduce the system applied for this work.

The reported catalysts could be classified into three types, solid-state catalysts, molecular catalysts, and biocatalysts. Catalysts provide a meeting place for the reactants and promote their union. In some cases, metals such as Pt, Au, or Ru –or their alloy- can directly play the role of both electrode material and electrocatalyst. However, the majority of solid-state electrocatalysts are formulated as inks (suspension of catalytic solids) then deposited on inert conductive supports such as glassy carbon (GC), or immobilized on electrode through chemical bonds, instead of working as electrodes themselves. The picture gets even more complicated for the non-immobilized homogenous catalysts. Herein, we use the generic term "electrocatalysts" to designate reaction places, either active surface of bulk materials or isolated sites surrounded by well-defined matrix.

1.3.1 Review of catalysts

1.3.1.1 Solid-state catalyst

The late decade has witnessed a spurred interest in studying ENRR catalysts, among which solid-state materials focused most of the attention. First of all, they are easily immobilized on electrodes, through a variety of methods such as simple dip/spray/drop-coating, electro-deposition, sputtering or thermally sintering.[88] Besides, they are easier to separated from products and bear overall better stability.

We know that the ENRR reaction is sensitive to the structures of catalysts, and the performance of heterogeneous catalysts could be impacted by factors like particle size, morphology, crystallinity, which have been thoroughly investigated these years.[89] However, their ill-defined structures often result in mediocre selectivity. Furthermore, the heterogeneity of surface on solid state catalyst increase the difficulties to precisely study the reaction mechanisms, which till now rely mostly on modeling and theoretical calculations, by essence leading to much approximation.

Bulk metal surface

Transition metals possessing multi-oxidation states can appear as obvious candidates to catalyze a multi electron process such as NRR. Using theoretical calculations, the binding energy of the intermediate species of putative NRR cycles have been determined on various transition metal surfaces. From this analysis, three probable rate-limiting steps could be proposed as below, (* indicating binding site on metal surface).[36]

Reductive asorption: $N_2 + H^+ + e^- \leftrightarrow {}^*N_2H$ a
Protonation: ${}^*NH + H^+ + e^- \leftrightarrow {}^*NH_2$ b
Reductive desorption: ${}^*NH_2 + H^+ + e^- \leftrightarrow NH_{3(g)}$ c

The comparison between the potentials of the rate limiting steps of NRR and HER calculated for different metal surfaces, show that HER requires systematically less potential (at least 0.4 V lower) than NRR. That is, no metal was found to be instinctually selective for NRR over HER. Even though some metals that are not optimal for *H binding, such as Au,[90] still remains difficult to achieve good selectivity for NRR on simple bulk metal surface.

If we are convinced by the predictions given by the theoretical studies, with a minimum over potential needed of ca –0.5 V in any cases, the energy requirement for driving ENRR on metal surfaces will account for at least 288 kJ/mol of ammonia produced, from which the spare room to compete with HBP process (480 kJ/mol) is not that considerable.

Herein no bulk metal (even traditional noble metal catalysts) present to be ideal NRR catalyst, thus, other classes of materials have been actively explorered.

Nanomaterials

Nanomaterials have at least one dimension pertaining to nanoscale (10^{-9} m). Compared to bulk materials, nanostructured materials expose more atoms on their surface, with 20% of the total atoms for 10 nm particles and 50% for 3 nm.[91] High surface area has significant impact on mass transfer and local concentration, which can promote the catalytic activity of the material considered. Moreover, the physicochemical characteristics of nano-catalysts can be tuned in terms of more precise dispersion of particles, crystalline size, morphology, porosity, etc.[92] Low-coordination sites presenting in amorphous or defects-rich materials showed relatively better performances in ENRR,[76,90] indicating the importance of nanoscale engineering.[92]

Nanostructured metals, metal oxides,[93] nitrides, [94] sulfides,[74] carbides[96] were proposed as ENRR catalysts, in shape of nanosheets, nanorods, nanowires, nanoflowers, nanotubes... Metal oxides occupy a very important position with their unique electrical, chemical properties and their ease of functionalization as well as the high resistance against alkaline corrosion during electrocatalysis.[9697] When incorporated with graphene, especially for non-noble metal derivatives, they exhibit potential for next-generation electrochemical nitrogen reduction reaction.[92] Nitrides have attract quite some attention as these materials exhibit strong N binding sites which might ease the activation of the dinitrogen. However some recent studies pointed out the ambiguity of their use as catalysts for ENRR, since the electro induced decomposition of these materials can lead to the release of ammonia.[97] Inspired by the cofactors of the nitrogenases discussed in section 1.3.2.1, synthetic transition metal sulfides have been one of the first class of materials tested for ENRR. Molybdenum sulfides, specifically, have been reported to exhibit significant reactivity especially for the amorphous and defect-rich materials. Nevertheless, when looking at the overall distribution of activities reported in the literature for the different types of materials tested, as represented in ***Figure 1.10***, the picture become blurry. All the family of catalyst proposed seem to fall within a relatively narrow range of randomly distributed apparent ENRR activities, and not a single material truly stand out from the others. In one word, the current strategy of material nano-engineering has not significantly improved the activity of simple metal-based catalysts.

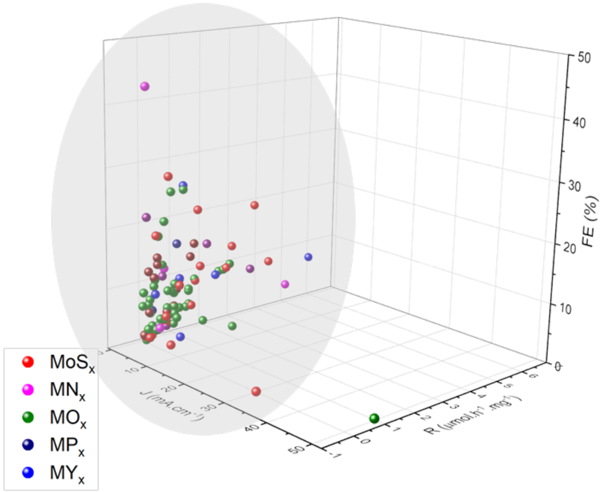

Figure 1.10 *3D graph of different materials reported plotted NH$_3$ production rate (µmol.h^{-1}.mg^{-1}), current density (mA.cm^{-2}), faradaic efficiency (FE %) as x, y, z axis. The red, magenta, green, dark blue, blue spots represent the results of Mo sulfides, nitrites, oxides, phosphates, and the other material families respectively.*

Single atom catalyst (SAC)

Single atoms could be dispersed into supports via organic linkers, weak interactions, encapsulation in microspores, or chemical bonds and form well-defined solid-state catalysts. These supports serve as 'ligand' of the single metal sites, therefore, the variation of the binding elements, metal coordination structures, and redox properties of adjacent metals can affect the activity of SACs.[87]

Obviously, the high density of exposed active sites and the high level of porosity of most graphitic materials used, leads to an optimal atomic utilization. The well-defined coordination environment of the isolated metal centers in these materials provides an outlook to improve the selectivity. In contrast to bulk metals, density functional calculations showed that *H binding is less favorable on SACs contributing to less HER competition. Moreover, it has a weaker absorption of $*NH_2$, favoring the release of NH_3. Moreover, the interaction between SACs and the support can modify the electronic structures of the metal centers, hence substantially influence the N_2 absorption. [98]

Along with the benefits, extremely high surface energy increase the potential of the isolated atoms to aggregate to nanoparticles,[96] when the metal centers are not well anchored on the supports.

Diverse SACs based metals such as Mo,[99] Cu,[100] Ru and Fe[101] have been prepared for ENRR. When Fe was isolated on nitrogen-doped carbon, the FE was drastically increased to ca 57%, and when Ru single atoms was supported on nitrogen-doped carbon, the ammonia producing rate arrived 129 $\mu g.mg^{-1}h^{-1}$ with FE as high as 29.6%.[102] Unfortunately when reported on the ***Figure 1.10***, they do not stand out from the classical random dispersion of reported materials.

To be noticed, SACs could be seen as a bridge between the bulk solid-state and well-defined molecular catalysts.[101]

1.3.1.2 Molecular catalyst

Compared to solid-state catalysts, molecular systems demonstrated unequivoquely ability to drive the catalytic reduction of N_2 via direct electron/proton transfer processes. Up to date, most of the molecular catalysts for NRR have been studied in solution as homogenous catalysts, in the context of chemically driven NRR (CNRR). Nevertheless they do carry potential to be applied for ENRR, possibly with better performances.[14] We will review the two cases in the following part.

Advantages

Unlike solid state catalysts that often display highly heterogeneous surfaces which complicate the description of the system, molecular catalysts offer well-defined species and models to unveil the mechanism of the reaction. Indeed, while mechanistic studies for ENRR on solid state catalysts still mostly relies on computational analysis, actual intermediates of the catalytic cycle can often be prepared and characterized for molecular systems. Additionally, molecular catalysts exhibit improved selectivity thanks to their homogeneity. [103]

The development of molecular catalysts for NRR brought substantial contributions to the understanding of the BNF sustained by the nitrogenases. To be noticed, synthetic catalysts often offers simpler, more robust structures when compared to biological system, to which extent, fully synthetic molecular systems appear as appealing candidates for the development of bio-inspired ENRR catalysts.

Drawbacks

However, molecular catalysts are generally less robust than solid state catalysts due to the lability of ligands which can be largely affected by the redox states of the metal center. Furthermore, the high cost to prepare functional ligand matrices, and their low conductivity can be serious drawbacks in application.[104] Furthermore, chemically driven NRR requires the use of stoichiometric reagents (i.e reducing agents, acids…), leading high E-factor (mass of waste per unit of mass of product) of ca. 23-100, and an estimated energy input of 2073 kJ for conversion of each mol of NH_3 (compared to 480 kJ/mol for HBP). The use of metal complexes for CNRR might, thus, appear to be an unpractical alternative to HBP for the production of ammonia.

Besides, homogenous ENRR catalysts are largely dispersed in the electrolyte, leaving only those present in the diffusion layer possibly to interact (directly or indirectly through the use of electron mediators) with the electrode. Therefore most the complexes remain in the electrolyte reservoir and are not effectively active for the desired reaction most of the time.[133] Notably, homogeneous catalysts suffer from competing bi-molecular reactions leading to the facile deactivation of the reaction intermediates upon diffusion in the bulk electrolyte, when the electron transfer are not fast enough to proceed with the catalytic cycle. In this context, the immobilization of the catalysts on the electrode is a specific challenge that must be tackled for the development of more efficient ENRR strategies based on the use of molecular catalysts.

Perspectives

However, these systems can be used as models to investigate the NRR mechanism, and thus help understand the critical parameters required to drive the reaction, allowing the design better applicable catalysts. Additionally, ENRR avoiding the use of stoichiometric amounts of sacrificial reductants but using simpler proton source as H_2O might be a solution to optimize the impact on environments in a recent work of Nishibayashi.[106]

Review: Chemical nitrogen reduction

Allen and Senoff found that in the first transition metal complex known for coordinating to N_2 ($[Ru(NH_3)_5N_2]X_2$, where X = Br^-, I^-, BF_4^-, and PF_6^-), the vibrational frequency of the bound N_2 is 2000 cm^{-1}, much lower than 2331 cm^{-1} for free dinitrogen, which indicated that the coordination weakened the N≡N bond and favors substantial NRR reactivity.[107]

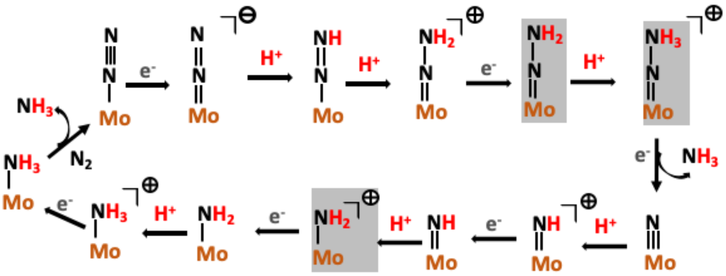

***Figure 1.11**. Chatt cycle intermediates prepared by Schrock team (except those in grey boxes).*

Later on, Chatt together with his team, thoroughly studied [M](N_2) and [M](N_xH_y) complexes as plausible intermediates of a putative NRR process. These studies lead them to propose a hypothetical catalytic cycle, now known as the Chatt cycle, where an end-on N_2 ligand coordinated to [MoP_4] is reduced to NH_3, following sequential proton coupled electron transfers as depicted on ***Figure 1.11,*** which is reminiscent of the so-called “distal pathway” (see section 1.2.2.2). Importantly at the time only few intermediates of this hypothetical cycle had been isolated.[108]. Nevertheless, their pioneering work provide the bedrock of all subsequent studies focusing on molecular catalysts for NRR. The Chatt cycle was validated by Schrock and coworkers who successfully characterized most of the proposed intermediates using a Mo complex coordinated to bulky triamidoamine ligand ($HIPTN_3N$)Mo(N_2) (***Figure 1.12***). This original complex complete the NRR process with decamethylchromocene ($Cp^*{}_2Cr$) as sacrificial reductant and lutidinium tetrakis[3,5-bis(trifluoromethyl)phenyl]borate ($[LutH]BAr^F{}_4$) as proton source, leading to the release of 8 equiv. NH_3/ Mo.[63] Theoretical studies were successfully used to describe the mechanism and lead to the following conclusions: 1) the intermediates from first protonation of N_2 are unlikely to be negatively charged; 2) the protonation of N_2 is the most endergonic step; 3) the rupture of the N-N bond (upon reduction of Mo-NNH_3) is the most exergonic step; 4) the dissociation of the Mo-NH_3 bond, which leads to the regeneration of the initial N_2 complex, is an endergonic step, and remains a big challenge up to date.[109] 5) certain flexibility of Mo-N interaction is perhaps critical for allowing the catalyst to stabilize both π-accepting intermediates and π-donating intermediates and/or low-valent and high-valent states.[109]

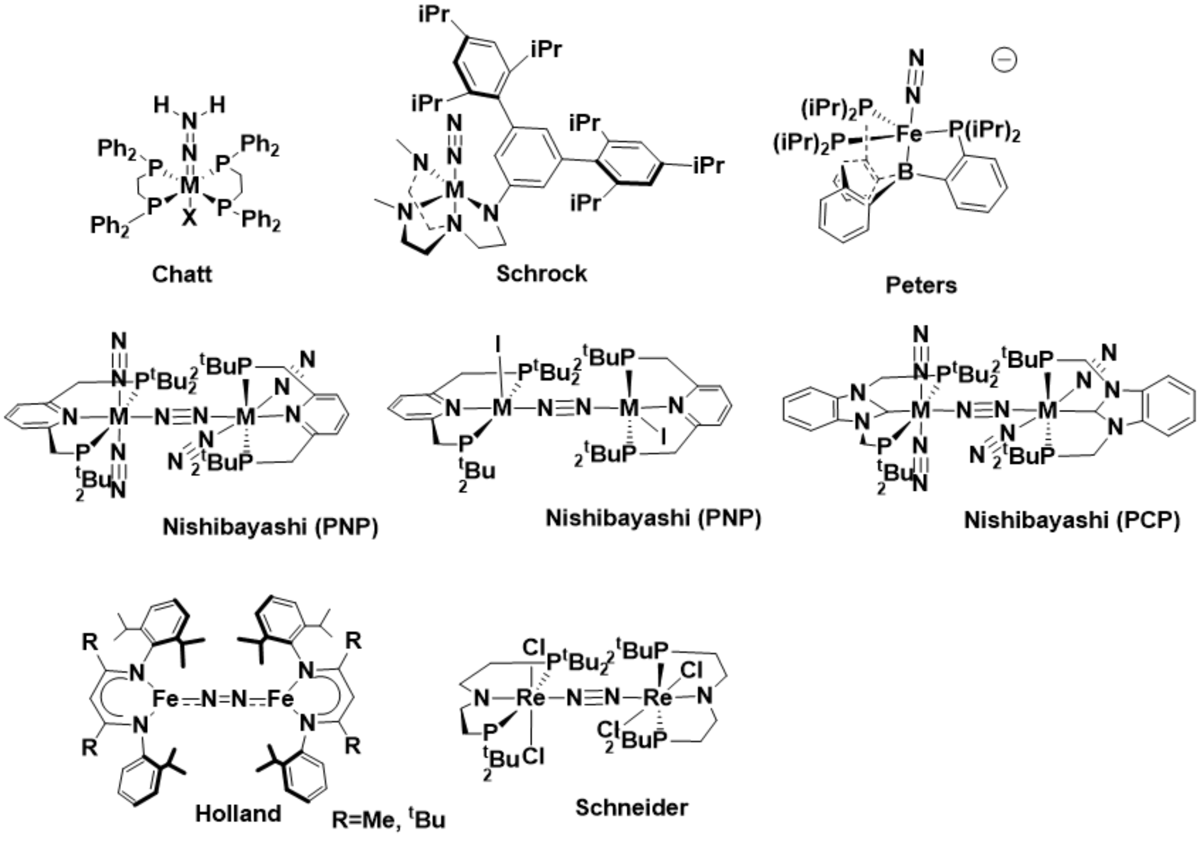

Figure 1.12 *Reported molecular catalysts for CNRR.*

The discovery of V-nitrogenase and Fe-nitrogenase gave significant insights into the nature of the active metal sites supporting the reduction of dinitrogen in biosystems, which was determined to be Fe rather than Mo as initially though.[110] Logically, more researchers become interested in iron-based [Fe](N_2) complex, and it was proved that several Iron complexes were able to support CNRR as well. [109]

Peters group reported a tris- (isopropylphosphino(o-phenylene)borane iron complex, (P_3B)Fe (***Figure 1.12***), which is not only capable to coordinate (N_xH_y) species but is active for NRR in diethyl ether at −78 °C using tetrakis[3,5-bis(trifluoromethyl)phenyl]acid ($HBAr^F_4$) and potassium graphite (KC_8) as the proton and electron sources respectively. This catalyst was also proven to operate through the distal pathway and lead to the release of 7 equiv. NH_3/Fe.[111] Other combination of proton/electron resource showed that the acid strength, the concentration and counter anion of metallocene reductants have huge impact on their catalyst selectivity.[112] The best selectivity was achieved with acid of pKa 2~4, which is akin to MoFe-protein behaviour.[109] Interestingly, an light induced enhancement of the catalytic activity has been shown for Peters triphosphine-Fe species, which is similar to what was observed for the nitrogenase.[113]

By a systematic modulation of the ligand structure (or substituent) it has been shown that for this class of Peters' catalyst, different ligand sets demonstrate impact on catalytic activity. 1) Strong back donating of Fe 3d orbitals to π* orbitals of N_2 could promote the activation of N_2 but impede its reduction, which implies the requirement of flexible electron structure of Fe to manage the overall process. Here the presence of an electron withdrawing B ligand has been shown to be essential to enhance the activity of the system at such critical step, by its ability to act as an electron buffer. The B ligand would have a synergistic effect leading to the the overall transfer of N_2 electron density to the Fe in return and thus facilitate the reduction of the bonded N_2. Moreover, the Fe-B bond can be formed and disrupted during the cycle… [114] 2) The presence of bulky, electro-rich substituents on phosphines helps to reduce the bimolecular H_2 release of early [Fe](N_xH_y) intermediates bearing weak N-H bonds.[115]

So far, we have introduced a few active complexes promoting NRR at single metal centers. However synthetic systems involving multinuclear intermediates are also known.

For example Nishibayashi and co-workers have introduced a family of catalysts based on molybdenum pincer complexes that involves binuclear intermediates during the catalytic cycle. The first system described featured a remarkable dimer, [{(PNP)Mo(N_2)}$_2$-(μN_2)] (PNP = 2,6-bis(di-tert-butyl-phosphinomethyl)pyridine (***Figure 1.12***), prepared by the direct reduction of the [$MoCl_3$(PNP)] precursor on Na/Hg under an N_2 atmosphere. Interestingly this dimer catalyzes CNRR in presence of cobaltocene (Cp_2Co) as electron source and 2,6-lutidinium triflate ([LutH]OTf) as proton source, in toluene at room temperature, releasing up to 12 equiv. NH_3/Mo. Early mechanistic studies demonstrated that the catalytic cycle involves the reduction of an axial N_2 ligand, through a distal-like pathway, on a single center. However, the formation of the dimer, within the ability of the second molybdenum center to share some electron density, is critical to support the reactivity of the system. [115] Later on, the [MoX_3(PNP)] halide precursors (X = Cl, Br, I) were shown to be active as catalysts for CNRR in the presence of decamethyl cobaltocene ($CoCp^*_2$) and colidinium triflate ([ColH]OTf) as electron and proton source respectively, in toluene and at room temperature. These complexes could release of up to 51 equiv. NH_3/Mo in the case of the iodinated species. Remarkably mechanistic studies demonstrated that under these conditions the catalysis proceeds through a completely different pathway than the one followed by the dimer discussed before. In presence of $CoCp^*_{2,}$ the [MoX_3(PNP)] halide complexes lead to the formation of a dinuclear [{MoI (PNP)}$_2$-(μN_2)] intermediates which undergoes direct splitting of the bridging N_2 ligand at room temperature (***Figure 1.12***). It results in the formation of molybdenum nitride species [MoI(N)(PNP)] that undergoes sequential reduction/protonation to release NH_3. Thus this system follows the so-called dissociative mechanism.

The modification of the ligand structure by grafting various substituents on the 4-position of the central pyridine or on the phosphine was systematically investigated and demonstrate the possibility to finely tune the reactivity of the metal centers through chemical engineering of molecular complexes.[106] Specifically the introduction of a carbene binding moiety instead of the pyridine ring led to much more stable complexes that exhibited remarkable activities for molecular based CNRR when SmI_2 and water were used as electron and proton source respectively, leading to the unmatched release of 4350 equiv. NH_3 /Mo.[116] Within this system, water forms a complex with Sm(II) which leads to a dramatic weakening of the O-H bond, enabling the concerted delivery of H^+/e^- to the coordinated nitrido ligand to form the N-H bonds. This demonstrates that besides the ligand effect the choice of the sources of proton and electron sources is particularly critical for promoting the activity of the catalyst in the context of CNRR as well. [117]

Electrochemical nitrogen reduction with molecular complexes

Only few studies have discussed the electrochemically driven nitrogen reduction reaction (ENRR) using molecular complexes, so far resulting in rather modest turnover numbers, often below 2.

Pickett pioneered that approach using the trans-(dmpe)$_2$W(N$_2$)$_2$ (dmpe = 1,2-bis(dimethylphosphino)ethane) complex, which, after protonation with p-toluenesulfonic acid (TsOH) could be reduced at a mercury-pool electrode poised at −2.6 V *vs.* ferrocence, to generate less than 1 equiv. NH$_3$/W along with trace of N$_2$H$_4$.[68] Similar Mo- and W-based bis-diphosphine complexes have been investigated, none of which have reported successful electrocatalytic activity of NRR, but possible stepwise NH$_3$ electrosynthesis.[142]

Similarly Schneider and co-workers recently reported the electrochemically driven N$_2$ splitting using the [ReCl$_2$(PNP)] complex (***Figure 1.12***). Upon reduction of the latter at −1.9 V *vs.* Ferrocene under N$_2$, a bimolecular N$_2$-bridged intermediate is formed, and leads to the dissociation of the bridging N$_2$ ligand to produce nitride species that can react with strong electrophiles.

Peters group highlighted that controlled electrolysis of the [(P$_3$B)Fe]$^+$ complex at −2.6 V *vs.* ferrocence in diethyl ether at low temperature and in the presence of excess HBAr$^F_4$ under N$_2$ can lead to the release of ~2 equiv. NH$_3$/Fe. Interestingly using [Ph$_2$NH$_2$]OTf as acid and introducing [Cp*$_2$Co]BAr$^F_4$ as cocatalyst a true catalytic process was observed at higher potential (−2.1 V *vs.* ferrocene) leading to the release of 4 equiv. NH$_3$/Fe.[104] Ti(IV) complexes bearing cyclopentadienyl ligands (Cp), such as (Cp)$_2$Ti(Cl)$_2$ have also been reported to lead to the production of ammonia under an applied potential in different conditions, including MeOH, THF (with LiCl) ,water, ionic liquids, however with little indications regarding yields or turnover. [109,117]

Finally Nishibayashi recently reported an original approach where the SmI$_2$ mediator was electrogenerated from SmI$_3$ and subsequently used to drive the catalytic reduction of dinitrogen under ambient conditions using [MoCl$_3$(PCP)] and H$_2$O as a proton source.[118] Here, of course, the challenge will be to find a way to regenerate the SmI$_2$ mediator after first cycle in order to develop a true continuous process for electromediated ammonia production.

Conclusions & Perspectives

Over 60-year marvelous work conducted by numerous researchers led to the fruitful results up to date on molecular systems towards NRR, assisting the uncovering of nitrogenase mechanism, discovering synthetic complex active for the nitrogen reduction and so on. Briefly, 1) Most of the catalytic systems are obtained in the form of single metal complexes, but often form at least transient multimetallic assembles during the activation of N_2.

2) The nature of the ligand set have a huge impact on the activity of metal center, providing the opportunity to control the reactivity and selectivity of synthetic catalysts.

3) Several mechanisms of N_2 activation have been described for molecular systems including: a) the dissociative pathway leading to the formation of metal nitrides are followed by some pincer complexes of Mo, Re and other late transition metals and are always involving bimolecular intermediates;[119,120] b) the associative distal mechanism which apply to both bimolecular (Nishibayashi)[121] and exclusive single site catalysts Mo catalysts (Schrock);[122] c) alternative or hybrid distal/alternative pathway as described for single site Fe complexes (Peters).[123]

4) Immobilization of homogeneous catalysts could possibly enhance their stability, allow their use in solvent systems in which the complexes are not soluble, and avoid detrimental intermolecular side-reactions.[105]

1.3.1.3 Enzymatic catalyst

The direct use of nitrogenase for developing hybrid system for the production of ammonia has also attracted attention. As discussed in section 1.1.3 , the delivery of the electrons to the catalytic center of nitrogenase is ATP dependent, and involve several partners, including the nitrogenase reductase. If in vitro protocols for testing the enzymatic activity of the nitrogenases do successfully associate all the required partners of the enzymatic chain, it remains particularly complex. Therefore, several groups investigate ways to bypass the ATP-dependence by using simple redox mediators such as cobaltocene, or methyl viologen.[124]

Others investigated direct electron tunneling from the electrode surface, such as Minteer and her team, who have recently reported a polymer-based electroenzymatic nitrogen fixation system, by using pyrene-functionalized linear polyethyleneimine to immobilize the MoFe protein on carbon electrode surface. The system successfully catalyzed reduction of N_3^-, NO_2^-, and N_2 to produce ammonia under mild conditions.[85,86] Even though immobilized enzymatic catalysts exhibit promising activity towards NRR, the neutral pH and low salinity requirements of these systems may limit the conductivity of the whole device thus limiting achievable current density.

1.3.1.4 Conclusion

Different types of NRR catalyst mentioned above bear different advantages and drawbacks. To be noticed, the successful strategies from the biologic nitrogenase, or well-defined molecular catalysts could inspire the preparation of heterogenous ones.

1.3.2 Bio-inspired metal sulfide catalyst development

The resolution of the structure of nitrogenases, especially of the catalytic co-factor FeMoCo $[MoFe_7(\mu_2\text{-}S)_3(\mu_3\text{-}S)_6(\mu_6\text{-}C)]$, gave a strong momentum to the development of bio-inspired NRR catalysts featuring transition metal sulfides. The FeMoCo itself is relatively robust and can be extracted in organic solvent while maintaining its structure, thanks to its loose coordination inside the active site of the protein involving only two amino acids.[125] But it does not exhibit any NRR activity outside the protein even with the use of highly reducing agents.[126] Nevertheless scientists never stop hunting for analogues that could exhibit the desired reactivity.[32]

The use of non-noble metals to develop catalysts for NRR, like Mo, V and Fe, which are found at the core of the nitrogenase, appears highly appealing. Incidentally, we must notice that the HBP also uses Fe-based catalysts. Furthermore some of the most successful synthetic molecular catalysts are based on Fe and Mo, as described the in previous section 1.2.2. [62,79,80,107,121,122,127] Thus, it is natural that the investigation of Mo-, Fe- and to a lower extant V-based sulfides have attracted much interest in the context of NRR.

Early examples pointed out the potential of heterometallic clusters such as $[MoFe_3S_4]^{3+}$ and $[VFe_3S_4]^{2+}$ to reduce N_2H_4 into to ammonia[128]; $[Mo_2Fe_6S_8(SPh)_9]^{3-}$ and $[Fe_4S_4(SPh)_4]^{4-}$ clusters were even proposed to complete full NRR at low rate under controlled potential electrolysis.[129] More recently this activity was further explored under photocatalytic conditions by entrapping these clusters into a synthetic chalcogenide matrix based on $[Sn_2S_6]^{4-}$ units. These inorganic material indeed lead to a feeble production of ammonia under irradiation, in the presence of ascorbate as sacrificial electron donor.[130] More recently the boom of solid-state electrocatalysts discussed section 1.3.1.1 has witnessed an explosion of studies discussing successful ENRR on Mo- and Fe-based sulfides as well.

Inspired by these precedents and intrigued by some aspects of the reactivity attributed to rather basic synthetic transition metal sulfides clusters and materials, towards N_2, we decided to investigate in a systematic way the reactivity of amorphous molybdenum sulfide (*a*-MoS_x) and its derivatives.

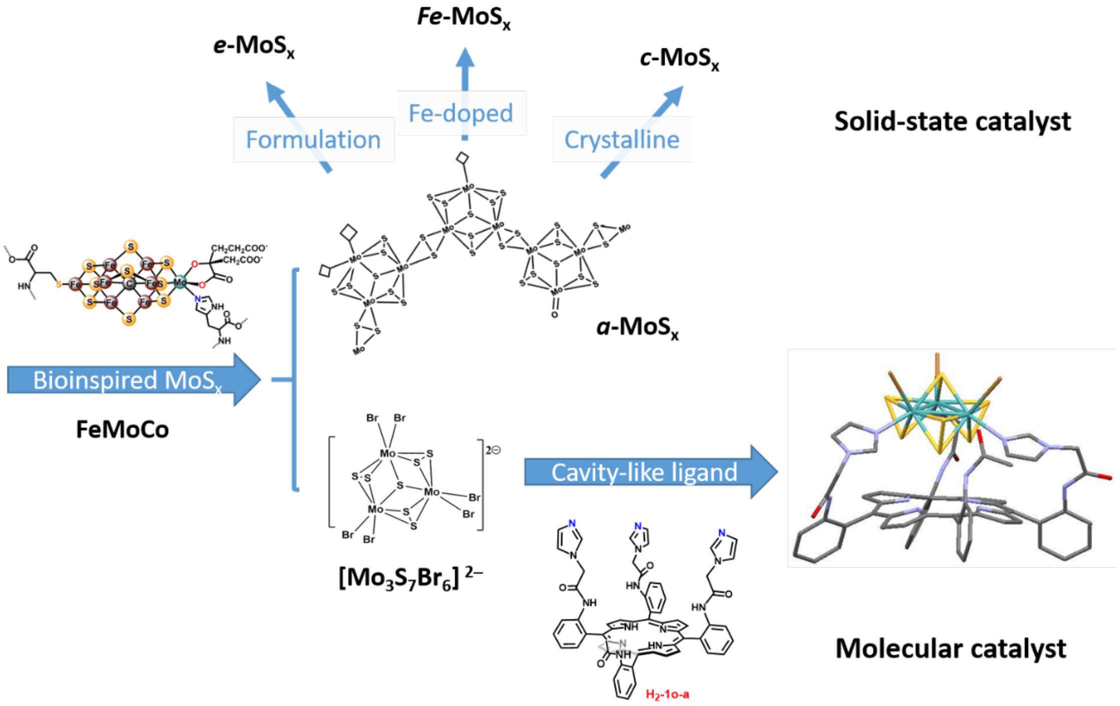

***Figure 11**: Materials used in this work*

References

(1) Erisman, J. W.; Sutton, M. A.; Galloway, J.; Klimont, Z.; Winiwarter, W. How a Century of Ammonia Synthesis Changed the World. *Nat. Geosci.* **2008**, *1*, 636.

(2) Stewart, W. M.; Dibb, D. W.; Johnston, A. E.; Smyth, T. J. The Contribution of Commercial Fertilizer Nutrients to Food Production. *Agron. J.* **2005**, *97* (1), 1–6.

(3) Deign, J. 10 Countries Moving Toward a Green Hydrogen Economy. *gtm*. October 14, 2019.

(4) Lund, P. D.; Lindgren, J.; Mikkola, J.; Salpakari, J. Review of Energy System Flexibility Measures to Enable High Levels of Variable Renewable Electricity. *Renew. Sustain. Energy Rev.* **2015**, *45*, 785–807.

(5) Rostrup-Nielsen, J. R.; Sehested, J.; Nørskov, J. K. Hydrogen and Synthesis Gas by Steam- and C02 Reforming. In *Advances in Catalysis*; Academic Press, 2002; Vol. 47, pp 65–139.

(6) F Service, R. Liquid Sunshine. *Science* **2018**, *361*, 120–123.

(7) Vidal-Iglesias, F. J.; Solla-Gullón, J.; Montiel, V.; Feliu, J. M.; Aldaz, A. Screening of Electrocatalysts for Direct Ammonia Fuel Cell: Ammonia Oxidation on PtMe (Me: Ir, Rh, Pd, Ru) and Preferentially Oriented Pt(100) Nanoparticles. *J. Power Sources* **2007**, *171* (2), 448–456.

(8) Zamfirescu, C.; Dincer, I. Using Ammonia as a Sustainable Fuel. *J. Power Sources* **2008**, *185* (1), 459–465.

(9) Giddey, S.; Badwal, S.; Kulkarni, A. Review of Electrochemical Ammonia Production Technologies and Materials. *Int. J. Hydrog. Energy* **2013**, *38* (34), 14576–14594.

(10) Klerke, A.; Christensen, C. H.; Nørskov, J. K.; Vegge, T. Ammonia for Hydrogen Storage: Challenges and Opportunities. *J. Mater. Chem.* **2008**, *18* (20), 2304–2310.

(11) Christensen, C. H.; Johannessen, T.; Sørensen, R. Z.; Nørskov, J. K. Towards an Ammonia-Mediated Hydrogen Economy? *Front. Catal. Mol. View Ind. Catal.* **2006**, *111* (1), 140–144.

(12) Duijm, N. J., Markert, F., & Paulsen, J. L. *Safety Assessment of Ammonia as a Transport Fuel. Denmark. Forskningscenter Risoe. Risoe-R, No. 1504(EN)*; Forskningscenter Risoe. Risoe-R,; Roskilde: Risø National Laboratory.: Denmark., 2005.

(13) Erisman, J. W.; Sutton, M. A.; Galloway, J.; Klimont, Z.; Winiwarter, W. How a Century of Ammonia Synthesis Changed the World. *Nat. Geosci.* **2008**, *1*, 636.

(14) Ostermann, N.; Siewert, I. Electrochemical N2 Splitting at Well-Defined Metal Complexes. *Curr. Opin. Electrochem.* **2019**.

(15) Smith, J. M.; Sadique, A. R.; Cundari, T. R.; Rodgers, K. R.; Lukat-Rodgers, G.; Lachicotte, R. J.; Flaschenriem, C. J.; Vela, J.; Holland, P. L. Studies of Low-Coordinate Iron Dinitrogen Complexes. *J. Am. Chem. Soc.* **2006**, *128* (3), 756–769.

(16) Appl, M. The Haber-Bosch Heritage: The Ammonia Production Technology; Seville Spain, 1997; Vol. 25.

(17) Milton Ross D.; Cai Rong; Abdellaoui Sofiene; Leech Dónal; De Lacey Antonio L.; Pita Marcos; Minteer Shelley D. Bioelectrochemical Haber–Bosch Process: An Ammonia-Producing H2/N2 Fuel Cell. *Angew. Chem. Int. Ed.* **2017**, *56* (10), 2680–2683.

(18) Smil, V. Detonator of the Population Explosion. *Nature* **1999**, *400* (6743), 415–415.

(19) Haber, F. The Synthesis of Ammonia from Its Elements. *Nobel Lect.* **1920**, 326–340.

(20) Smil, V. *Enriching the Earth: Fritz Haber, Carl Bosch, and the Transformation of World Food Production*; MIT press, 2004.

(21) Pernicone, N.; Ferrero, F.; Rossetti, I.; Forni, L.; Canton, P.; Riello, P.; Fagherazzi, G.; Signoretto, M.; Pinna, F. Wustite as a New Precursor of Industrial Ammonia Synthesis Catalysts. *Appl. Catal. Gen.* **2003**, *251* (1), 121–129.

(22) Bare, S. R.; Strongin, D. R.; Somorjai, G. A. Ammonia Synthesis over Iron Single-Crystal Catalysts: The Effects of Alumina and Potassium. *J. Phys. Chem.* **1986**, *90* (20), 4726–4729.

(23) Reiter, A. J.; Kong, S.-C. Combustion and Emissions Characteristics of Compression-Ignition Engine Using Dual Ammonia-Diesel Fuel. *Fuel* **2011**, *90* (1), 87–97.

(24) Liu, H. Ammonia Synthesis Catalyst 100 Years: Practice, Enlightenment and Challenge. *Chin. J. Catal.* **2014**, *35* (10), 1619–1640.

(25) Hochman, G.; Goldman, A.; Felder, F. A.; Mayer, J.; Miller, A.; Holland, P. L.; Goldman, L.; Manocha, P.; Song, Z.; Aleti, S. The Potential Economic Feasibility of Direct Electrochemical Nitrogen Reduction as a Route to Ammonia. **2019**.

(26) Kyriakou, V.; Garagounis, I.; Vasileiou, E.; Vourros, A.; Stoukides, M. Progress in the Electrochemical Synthesis of Ammonia. *Nitrogen Act.* **2017**, *286*, 2–13.

(27) Michalsky, R.; Pfromm, P. H. Chromium as Reactant for Solar Thermochemical Synthesis of Ammonia from Steam, Nitrogen, and Biomass at Atmospheric Pressure. *Sol. Energy* **2011**, *85* (11), 2642–2654.

(28) Ye, L.; Nayak-Luke, R.; Bañares-Alcántara, R.; Tsang, E. Reaction: “Green” Ammonia Production. *Chem* **2017**, *3* (5), 712–714.

(29) Galloway, J. N.; Dentener, F. J.; Capone, D. G.; Boyer, E. W.; Howarth, R. W.; Seitzinger, S. P.; Asner, G. P.; Cleveland, C. C.; Green, P. A.; Holland, E. A.; Karl, D. M.; Michaels, A. F.; Porter, J. H.; Townsend, A. R.; Vöosmarty, C. J. Nitrogen Cycles: Past, Present, and Future. *Biogeochemistry* **2004**, *70* (2), 153–226.

(30) Cherkasov, N.; Ibhadon, A. O.; Fitzpatrick, P. A Review of the Existing and Alternative Methods for Greener Nitrogen Fixation. *Chem. Eng. Process. Process Intensif.* **2015**, *90*, 24–33.

(31) Hoffman, B. M.; Lukoyanov, D.; Yang, Z.-Y.; Dean, D. R.; Seefeldt, L. C. Mechanism of Nitrogen Fixation by Nitrogenase: The Next Stage. *Chem. Rev.* **2014**, *114* (8), 4041–4062.

(32) Sickerman, N. S.; Tanifuji, K.; Hu, Y.; Ribbe, M. W. Synthetic Analogues of Nitrogenase Metallocofactors: Challenges and Developments. *Chem. – Eur. J.* **2017**, *23* (51), 12425–12432.

(33) Hu, B.; Harris, D. F.; Dean, D. R.; Liu, T. L.; Yang, Z.-Y.; Seefeldt, L. C. Electrocatalytic CO2 Reduction Catalyzed by Nitrogenase MoFe and FeFe Proteins. *Bioelectrochemistry* **2018**, *120*, 104–109.

(34) Seefeldt, L. C.; Yang, Z.-Y.; Lukoyanov, D. A.; Harris, D. F.; Dean, D. R.; Raugei, S.; Hoffman, B. M. Reduction of Substrates by Nitrogenases. *Chem. Rev.* **2020**.

(35) Hu, Y.; Ribbe, M. W. Biosynthesis of the Metalloclusters of Nitrogenases. *Annu. Rev. Biochem.* **2016**, *85* (1), 455–483.

(36) Foster, S. L.; Bakovic, S. I. P.; Duda, R. D.; Maheshwari, S.; Milton, R. D.; Minteer, S. D.; Janik, M. J.; Renner, J. N.; Greenlee, L. F. Catalysts for Nitrogen Reduction to Ammonia. *Nat. Catal.* **2018**, *1* (7), 490–500.

(37) Wenke, B. B.; Spatzal, T.; Rees, D. C. Site-Specific Oxidation State Assignments of the Iron Atoms in the [4Fe:4S]2+/1+/0 States of the Nitrogenase Fe-Protein. *Angew. Chem. Int. Ed.* **2019**, *58* (12), 3894–3897.

(38) Watt, G. D.; Wang, Z. C.; Knotts, R. R. Redox Reactions of and Nucleotide Binding to the Iron Protein of Azotobacter Vinelandii. *Biochemistry (Mosc.)* **1986**, *25* (25), 8156–8162.

(39) Kurnikov, I. V.; Charnley, A. K.; Beratan, D. N. From ATP to Electron Transfer: Electrostatics and Free-Energy Transduction in Nitrogenase. *J. Phys. Chem. B* **2001**, *105* (23), 5359–5367.

(40) VERMA, D. K.; KAUR, B.; PANDEY, A. K.; ASTHIR, B. NITROGENASE: A KEY ENZYME IN MICROBIAL NITROGEN FIXATION FOR SOIL HEALTH.

(41) Smith, B. E.; Lang, G. Mössbauer Spectroscopy of the Nitrogenase Proteins from Klebsiella Pneumoniae. Structural Assignments and Mechanistic Conclusions. *Biochem. J.* **1974**, *137* (2), 169–180.

(42) Peters, J. W.; Stowell, M. H. B.; Soltis, S. M.; Finnegan, M. G.; Johnson, M. K.; Rees, D. C. Redox-Dependent Structural Changes in the Nitrogenase P-Cluster,. *Biochemistry (Mosc.)* **1997**, *36* (6), 1181–1187.

(43) Tanifuji, K.; Lee, C. C.; Sickerman, N. S.; Tatsumi, K.; Ohki, Y.; Hu, Y.; Ribbe, M. W. Tracing the 'Ninth Sulfur' of the Nitrogenase Cofactor via a Semi-Synthetic Approach. *Nat. Chem.* **2018**, *10* (5), 568–572.

(44) Spatzal, T.; Schlesier, J.; Burger, E.-M.; Sippel, D.; Zhang, L.; Andrade, S. L. A.; Rees, D. C.; Einsle, O. Nitrogenase FeMoco Investigated by Spatially Resolved Anomalous Dispersion Refinement. *Nat. Commun.* **2016**, *7* (1), 10902.

(45) Barney, B. M.; Igarashi, R. Y.; Dos Santos, P. C.; Dean, D. R.; Seefeldt, L. C. Substrate Interaction at an Iron-Sulfur Face of the FeMo-Cofactor during Nitrogenase Catalysis. *J. Biol. Chem.* **2004**, *279* (51), 53621–53624.

(46) Kim, J.; Rees, D. Structural Models for the Metal Centers in the Nitrogenase Molybdenum-Iron Protein. *Science* **1992**, *257* (5077), 1677.

(47) Sippel, D.; Rohde, M.; Netzer, J.; Trncik, C.; Gies, J.; Grunau, K.; Djurdjevic, I.; Decamps, L.; Andrade, S. L. A.; Einsle, O. A Bound Reaction Intermediate Sheds Light on the Mechanism of Nitrogenase. *Science* **2018**, *359* (6383), 1484.

(48) Rutledge, H. L.; Tezcan, F. A. Electron Transfer in Nitrogenase. *Chem. Rev.* **2020**.

(49) Danyal, K.; Mayweather, D.; Dean, D. R.; Seefeldt, L. C.; Hoffman, B. M. Conformational Gating of Electron Transfer from the Nitrogenase Fe Protein to MoFe Protein. *J. Am. Chem. Soc.* **2010**, *132* (20), 6894–6895.

(50) Thorneley, R. N.; Lowe, D. J. Kinetics and Mechanism of the Nitrogenase Enzyme System. *Molybdenum Enzym.* **1985**, *7*, 89–116.

(51) Fixen, K. R.; Pal Chowdhury, N.; Martinez-Perez, M.; Poudel, S.; Boyd, E. S.; Harwood, C. S. The Path of Electron Transfer to Nitrogenase in a Phototrophic Alpha-Proteobacterium. *Environ. Microbiol.* **2018**, *20* (7), 2500–2508.

(52) Segal, H. M.; Spatzal, T.; Hill, M. G.; Udit, A. K.; Rees, D. C. Electrochemical and Structural Characterization of Azotobacter Vinelandii Flavodoxin II. *Protein Sci.* **2017**, *26* (10), 1984–1993.

(53) Rees, D. C. Dinitrogen Reduction by Nitrogenase: If N2 Isn't Broken, It Can't Be Fixed: Current Opinion in Structural Biology 1993, 3:921–928. *Curr. Opin. Struct. Biol.* **1993**, *3* (6), 921–928.

(54) Danyal, K.; Dean, D. R.; Hoffman, B. M.; Seefeldt, L. C. Electron Transfer within Nitrogenase: Evidence for a Deficit-Spending Mechanism. *Biochemistry (Mosc.)* **2011**, *50* (43), 9255–9263.

(55) Hoffman, B. M.; Dean, D. R.; Seefeldt, L. C. Climbing Nitrogenase: Toward a Mechanism of Enzymatic Nitrogen Fixation. *Acc. Chem. Res.* **2009**, *42* (5), 609–619.

(56) Simpson, F. B.; Burris, R. H. A Nitrogen Pressure of 50 Atmospheres Does Not Prevent Evolution of Hydrogen by Nitrogenase. *Science* **1984**, *224* (4653), 1095–1097.

(57) Burgess, B. K.; Lowe, D. J. Mechanism of Molybdenum Nitrogenase. *Chem. Rev.* **1996**, *96* (7), 2983–3012.

(58) Doan, P. E.; Telser, J.; Barney, B. M.; Igarashi, R. Y.; Dean, D. R.; Seefeldt, L. C.; Hoffman, B. M. 57Fe ENDOR Spectroscopy and 'Electron Inventory'Analysis of the Nitrogenase E4 Intermediate Suggest the Metal-Ion Core of FeMo-Cofactor Cycles through Only One Redox Couple. *J. Am. Chem. Soc.* **2011**, *133* (43), 17329–17340.

(59) Lukoyanov, D.; Khadka, N.; Yang, Z.-Y.; Dean, D. R.; Seefeldt, L. C.; Hoffman, B. M. Reductive Elimination of H2 Activates Nitrogenase to Reduce the N⍰ N Triple Bond: Characterization of the E4 (4H) Janus Intermediate in Wild-Type Enzyme. *J. Am. Chem. Soc.* **2016**, *138* (33), 10674–10683.

(60) Raugei, S.; Seefeldt, L. C.; Hoffman, B. M. Critical Computational Analysis Illuminates the Reductive-Elimination Mechanism That Activates Nitrogenase for N2 Reduction. *Proc. Natl. Acad. Sci.* **2018**, *115* (45), E10521–E10530.

(61) Neese, F. The Yandulov/Schrock Cycle and the Nitrogenase Reaction: Pathways of Nitrogen Fixation Studied by Density Functional Theory. *Angew. Chem. Int. Ed.* **2006**, *45* (2), 196–199.

(62) Chatt, J.; RL, R. The Reactions of Dinitrogen in Its Metal Complexes. **1982**.

(63) Schrock, R. R. Catalytic Reduction of Dinitrogen under Mild Conditions. *Chem. Commun.* **2003**, No. 19, 2389–2391.

(64) Hinnemann, B.; Nørskov, J. K. Catalysis by Enzymes: The Biological Ammonia Synthesis. *Top. Catal.* **2006**, *37* (1), 55–70.

(65) Rittle, J.; Peters, J. C. An Fe-N2 Complex That Generates Hydrazine and Ammonia via Fe⍰ NNH2: Demonstrating a Hybrid Distal-to-Alternating Pathway for N2 Reduction. *J. Am. Chem. Soc.* **2016**, *138* (12), 4243–4248.

(66) Thorneley, R. N.; Lowe, D. The Mechanism of Klebsiella Pneumoniae Nitrogenase Action. Pre-Steady-State Kinetics of an Enzyme-Bound Intermediate in N2 Reduction and of NH3 Formation. *Biochem. J.* **1984**, *224* (3), 887–894.

(67) Lipman, T.; Shah, N. Ammonia as an Alternative Energy Storage Medium for Hydrogen Fuel Cells: Scientific and Technical Review for Near-Term Stationary Power Demonstration Projects, Final Report. **2007**.

(68) Pickett, C. J.; Talarmin, J. Electrosynthesis of Ammonia. *Nature* **1985**, *317* (6038), 652–653.

(69) Pickett, C. J.; Ryder, K. S.; Talarmin, J. Electron-Transfer Reactions in Nitrogen Fixation. Part 2. The Electrosynthesis of Ammonia: Identification and Estimation of Products. *J. Chem. Soc. Dalton Trans.* **1986**, No. 7, 1453–1457.

(70) Tsuneto, A.; Kudo, A.; Sakata, T. Lithium-Mediated Electrochemical Reduction of High Pressure N2 to NH3. *J. Electroanal. Chem.* **1994**, *367* (1), 183–188.

(71) Liu, K.-H.; Zhong, H.-X.; Li, S.-J.; Duan, Y.-X.; Shi, M.-M.; Zhang, X.-B.; Yan, J.-M.; Jiang, Q. Advanced Catalysts for Sustainable Hydrogen Generation and Storage via Hydrogen Evolution and Carbon Dioxide/Nitrogen Reduction Reactions. *Prog. Mater. Sci.* **2018**, *92*, 64–111.

(72) Zhou, F.; Azofra, L. M.; Ali, M.; Kar, M.; Simonov, A. N.; McDonnell-Worth, C.; Sun, C.; Zhang, X.; MacFarlane, D. R. Electro-Synthesis of Ammonia from Nitrogen at Ambient Temperature and Pressure in Ionic Liquids. *Energy Environ. Sci.* **2017**, *10* (12), 2516–2520.

(73) Licht, S.; Cui, B.; Wang, B.; Li, F.-F.; Lau, J.; Liu, S. Ammonia Synthesis by N2 and Steam Electrolysis in Molten Hydroxide Suspensions of Nanoscale Fe2O3. *Science* **2014**, *345* (6197), 637–640.

(74) Zhao, X.; Lan, X.; Yu, D.; Fu, H.; Liu, Z.; Mu, T. Deep Eutectic-Solvothermal Synthesis of Nanostructured Fe3S4 for Electrochemical N2 Fixation under Ambient Conditions. *Chem. Commun.* **2018**, *54* (92), 13010–13013.

(75) Hughes, M. A.; Homewood, K. P.; Curry, R. J.; Ohno, Y.; Mizutani, T. An Ultra-Low Leakage Current Single Carbon Nanotube Diode with Split-Gate and Asymmetric Contact Geometry. *Appl. Phys. Lett.* **2013**, *103* (13), 133508.

(76) Li, X.; Li, T.; Ma, Y.; Wei, Q.; Qiu, W.; Guo, H.; Shi, X.; Zhang, P.; Asiri, A. M.; Chen, L.; Tang, B.; Sun, X. Boosted Electrocatalytic N2 Reduction to NH3 by Defect-Rich MoS2 Nanoflower. *Adv. Energy Mater.* **2018**, *8* (30), 1801357.

(77) Chen, S.; Perathoner, S.; Ampelli, C.; Centi, G. Chapter 2 - Electrochemical Dinitrogen Activation: To Find a Sustainable Way to Produce Ammonia. In *Studies in Surface Science and Catalysis*; Albonetti, S., Perathoner, S., Quadrelli, E. A., Eds.; Horizons in Sustainable Industrial Chemistry and Catalysis; Elsevier, 2019; Vol. 178, pp 31–46.

(78) Singh, A. R.; Rohr, B. A.; Statt, M. J.; Schwalbe, J. A.; Cargnello, M.; Nørskov, J. K. Strategies toward Selective Electrochemical Ammonia Synthesis. *ACS Catal.* **2019**, 8316–8324.

(79) Matson, B. D.; Peters, J. C. Fe-Mediated HER vs N2RR: Exploring Factors That Contribute to Selectivity in P3EFe(N2) (E = B, Si, C) Catalyst Model Systems. *ACS Catal.* **2018**, *8* (2), 1448–1455.

(80) Weare, W. W.; Schrock, R. R.; Hock, A. S.; Müller, P. Synthesis of Molybdenum Complexes That Contain “Hybrid” Triamidoamine Ligands,[(Hexaisopropylterphenyl-NCH2CH2) 2NCH2CH2N-Aryl] 3-, and Studies Relevant to Catalytic Reduction of Dinitrogen. *Inorg. Chem.* **2006**, *45* (23), 9185–9196.

(81) Artero, V. Bioinspired Catalytic Materials for Energy-Relevant Conversions. *Nat. Energy* **2017**, *2* (9), 17131.

(82) Cao, N.; Zheng, G. Aqueous Electrocatalytic N2 Reduction under Ambient Conditions. *Nano Res.* **2018**, *11* (6), 2992–3008.

(83) Cui, X.; Tang, C.; Zhang, Q. A Review of Electrocatalytic Reduction of Dinitrogen to Ammonia under Ambient Conditions. *Adv. Energy Mater.* **2018**, *8* (22), 1800369.

(84) Xu, H.; Ithisuphalap, K.; Li, Y.; Mukherjee, S.; Lattimer, J.; Soloveichik, G.; Wu, G. Electrochemical Ammonia Synthesis through N2 and H2O under Ambient Conditions: Theory, Practices, and Challenges for Catalysts and Electrolytes. *Nano Energy* **2020**, 104469.

(85) Milton, R. D.; Minteer, S. D. Nitrogenase Bioelectrochemistry for Synthesis Applications. *Acc. Chem. Res.* **2019**, *52* (12), 3351–3360.

(86) Patel, J.; Cai, R.; Milton, R.; Chen, H.; Minteer, S. D. Pyrene-Based Noncovalent Immobilization of Nitrogenase on Carbon Surfaces. *ChemBioChem* **2019**, *n/a* (n/a).

(87) Qin, R.; Liu, P.; Fu, G.; Zheng, N. Strategies for Stabilizing Atomically Dispersed Metal Catalysts. *Small Methods* **2018**, *2* (1), 1700286.

(88) Coutard, N.; Kaeffer, N.; Artero, V. Molecular Engineered Nanomaterials for Catalytic Hydrogen Evolution and Oxidation. *Chem. Commun.* **2016**, *52* (95), 13728–13748.

(89) Chen, G.-F.; Ren, S.; Zhang, L.; Cheng, H.; Luo, Y.; Zhu, K.; Ding, L.-X.; Wang, H. Advances in Electrocatalytic N2 Reduction—Strategies to Tackle the Selectivity Challenge. *Small Methods* **2019**, *3* (6), 1800337.

(90) Shi, M.-M.; Bao, D.; Wulan, B.-R.; Li, Y.-H.; Zhang, Y.-F.; Yan, J.-M.; Jiang, Q. Au Sub-Nanoclusters on TiO2 toward Highly Efficient and Selective Electrocatalyst for N2

(91) Chaturvedi, S.; Dave, P. N.; Shah, N. Applications of Nano-Catalyst in New Era. *J. Saudi Chem. Soc.* **2012**, *16* (3), 307–325.

(92) Zhang, W.; Ge, Q.; Xu, H. Influences of Precipitate Rinsing Solvents on Ni Catalyst for Methane Decomposition to CO X-Free Hydrogen. *J. Phys. Chem. A* **2010**, *114* (11), 3818–3823.

(93) Chang, B.; Liu, Q.; Chen, N.; Yang, Y. A Flower-like Bismuth Oxide as an Efficient, Durable and Selective Electrocatalyst for Artificial N2 Fixation in Ambient Condition. *ChemCatChem* **2019**, *11* (7), 1884–1888.

(94) Ren, X.; Cui, G.; Chen, L.; Xie, F.; Wei, Q.; Tian, Z.; Sun, X. Electrochemical N 2 Fixation to NH 3 under Ambient Conditions: Mo 2 N Nanorod as a Highly Efficient and Selective Catalyst. *Chem. Commun.* **2018**, *54* (61), 8474–8477.

(95) Ren, X.; Zhao, J.; Wei, Q.; Ma, Y.; Guo, H.; Liu, Q.; Wang, Y.; Cui, G.; Asiri, A. M.; Li, B. High-Performance N2-to-NH3 Conversion Electrocatalyzed by Mo2C Nanorod. *ACS Cent. Sci.* **2018**, *5* (1), 116–121.

(96) Farmer, J. A.; Campbell, C. T. Ceria Maintains Smaller Metal Catalyst Particles by Strong Metal-Support Bonding. *Science* **2010**, *329* (5994), 933–936.

(97) Hu, B.; Hu, M.; Seefeldt, L.; Liu, T. L. Electrochemical Dinitrogen Reduction to Ammonia by Mo2N: Catalysis or Decomposition? *ACS Energy Lett.* **2019**, *4* (5), 1053–1054.

(98) Choi, C.; Back, S.; Kim, N.-Y.; Lim, J.; Kim, Y.-H.; Jung, Y. Suppression of Hydrogen Evolution Reaction in Electrochemical N2 Reduction Using Single-Atom Catalysts: A Computational Guideline. *ACS Catal.* **2018**, *8* (8), 7517–7525.

(99) Han, L.; Liu, X.; Chen, J.; Lin, R.; Liu, H.; Lü, F.; Bak, S.; Liang, Z.; Zhao, S.; Stavitski, E.; Luo, J.; Adzic, R. R.; Xin, H. L. Atomically Dispersed Molybdenum Catalysts for Efficient Ambient Nitrogen Fixation. *Angew. Chem. Int. Ed.* **2019**, *58* (8), 2321–2325.

(100) Zang, W.; Yang, T.; Zou, H.; Xi, S.; Zhang, H.; Liu, X.; Kou, Z.; Du, Y.; Feng, Y. P.; Shen, L.; Duan, L.; Wang, J.; Pennycook, S. J. Copper Single Atoms Anchored in Porous Nitrogen-Doped Carbon as Efficient PH-Universal Catalysts for the Nitrogen Reduction Reaction. *ACS Catal.* **2019**, *9* (11), 10166–10173.

(101) Wang, M.; Liu, S.; Qian, T.; Liu, J.; Zhou, J.; Ji, H.; Xiong, J.; Zhong, J.; Yan, C. Over 56.55% Faradaic Efficiency of Ambient Ammonia Synthesis Enabled by Positively Shifting the Reaction Potential. *Nat. Commun.* **2019**, *10* (1), 341.

(102) Geng, Z.; Liu, Y.; Kong, X.; Li, P.; Li, K.; Liu, Z.; Du, J.; Shu, M.; Si, R.; Zeng, J. Achieving a Record-High Yield Rate of 120.9 for N2 Electrochemical Reduction over Ru Single-Atom Catalysts. *Adv. Mater.* **2018**, *30* (40), 1803498.

(103) Lee, K. J.; McCarthy, B. D.; Dempsey, J. L. On Decomposition, Degradation, and Voltammetric Deviation: The Electrochemist's Field Guide to Identifying Precatalyst Transformation. *Chem. Soc. Rev.* **2019**, *48* (11), 2927–2945.

(104) Chalkley, M. J.; Del Castillo, T. J.; Matson, B. D.; Peters, J. C. Fe-Mediated Nitrogen Fixation with a Metallocene Mediator: Exploring PKa Effects and Demonstrating Electrocatalysis. *J. Am. Chem. Soc.* **2018**, *140* (19), 6122–6129.

(105) Bairagya, M. D.; Bujol, R. J.; Elgrishi, N. Fighting Deactivation: Classical and Emerging Strategies for Efficient Stabilization of Molecular Electrocatalysts. *Chem. – Eur. J.* **2020**, *26* (18), 3991–4000.

(106) Ashida, Y.; Nishibayashi, Y. Catalytic Conversion of Nitrogen Molecule into Ammonia Using Molybdenum Complexes under Ambient Reaction Conditions. *Chem. Commun.* **2021**, *57* (10), 1176–1189.

(107) Allen, A.; Senoff, C. Nitrogenopentammineruthenium (II) Complexes. *Chem. Commun. Lond.* **1965**, No. 24, 621–622.

(108) Pickett, C. J. The Chatt Cycle and the Mechanism of Enzymic Reduction of Molecular Nitrogen. *JBIC J. Biol. Inorg. Chem.* **1996**, *1* (6), 601–606.

(109) Chalkley, M. J.; Drover, M. W.; Peters, J. C. Catalytic N2-to-NH3 (or -N2H4) Conversion by Well-Defined Molecular Coordination Complexes. *Chem. Rev.* **2020**.

(110) Hoffman, B. M.; Lukoyanov, D.; Yang, Z.-Y.; Dean, D. R.; Seefeldt, L. C. Mechanism of Nitrogen Fixation by Nitrogenase: The Next Stage. *Chem. Rev.* **2014**, *114* (8), 4041–4062.

(111) Anderson, J. S.; Rittle, J.; Peters, J. C. Catalytic Conversion of Nitrogen to Ammonia by an Iron Model Complex. *Nature* **2013**, *501*, 84.

(112) Chalkley, M. J.; Del Castillo, T. J.; Matson, B. D.; Roddy, J. P.; Peters, J. C. Catalytic N2-to-NH3 Conversion by Fe at Lower Driving Force: A Proposed Role for Metallocene-Mediated PCET. *ACS Cent. Sci.* **2017**, *3* (3), 217–223.

(113) Buscagan, T. M.; Oyala, P. H.; Peters, J. C. N2-to-NH3 Conversion by a Triphos–Iron Catalyst and Enhanced Turnover under Photolysis. *Angew. Chem. Int. Ed.* **2017**, *56* (24), 6921–6926.

(114) Jiang, Y.-F.; Ma, X.-L.; Lu, J.-B.; Wang, J.-Q.; Xiao, H.; Li, J. N2 Reduction on Fe-Based Complexes with Different Supporting Main-Group Elements: Critical Roles of Anchor and Peripheral Ligands. *Small Methods* **2019**, *3* (6), 1800340.

(115) Anderson, J. S.; Cutsail, G. E.; Rittle, J.; Connor, B. A.; Gunderson, W. A.; Zhang, L.; Hoffman, B. M.; Peters, J. C. Characterization of an Fe≡N–NH2 Intermediate Relevant to Catalytic N2 Reduction to NH3. *J. Am. Chem. Soc.* **2015**, *137* (24), 7803–7809.

(116) Ashida, Y.; Arashiba, K.; Nakajima, K.; Nishibayashi, Y. Molybdenum-Catalysed Ammonia Production with Samarium Diiodide and Alcohols or Water. *Nature* **2019**, *568* (7753), 536–540.

(117) Katayama, A.; Inomata, T.; Ozawa, T.; Masuda, H. Electrochemical Evaluation of Titanocenes in Ionic Liquids with Non-coordinating and Coordinating Anions and Application for NH3 Synthesis. *ChemElectroChem* **2017**, *4* (12), 3053–3060.

(118) Arashiba, K.; Kanega, R.; Himeda, Y.; Nishibayashi, Y. Catalytic Ammonia Formation with Electrochemically Reduced Samarium Diiodide from Samarium Triiodide and Water from Dinitrogen. *Chem. Lett.* **2021**, *50* (7), 1356–1358.

(119) Arashiba, K.; Miyake, Y.; Nishibayashi, Y. A Molybdenum Complex Bearing PNP-Type Pincer Ligands Leads to the Catalytic Reduction of Dinitrogen into Ammonia. *Nat. Chem.* **2010**, *3*, 120.

(120) Lindley, B. M.; van Alten, R. S.; Finger, M.; Schendzielorz, F.; Würtele, C.; Miller, A. J. M.; Siewert, I.; Schneider, S. Mechanism of Chemical and Electrochemical N2 Splitting by a Rhenium Pincer Complex. *J. Am. Chem. Soc.* **2018**, *140* (25), 7922–7935.

(121) Nishibayashi, Y.; Iwai, S.; Hidai, M. Bimetallic System for Nitrogen Fixation: Ruthenium-Assisted Protonation of Coordinated N_2 on Tungsten with H_2. *Science* **1998**, *279* (5350), 540.

(122) Schrock, R. R. Catalytic Reduction of Dinitrogen to Ammonia at a Single Molybdenum Center. *Acc. Chem. Res.* **2005**, *38* (12), 955–962. https://doi.org/10.1021/ar0501121.

(123) Kuriyama, S.; Arashiba, K.; Nakajima, K.; Matsuo, Y.; Tanaka, H.; Ishii, K.; Yoshizawa, K.; Nishibayashi, Y. Catalytic Transformation of Dinitrogen into Ammonia and Hydrazine by Iron-Dinitrogen Complexes Bearing Pincer Ligand. *Nat. Commun.* **2016**, *7* (1), 1–9.

(124) Deng, J.; Iñiguez, J. A.; Liu, C. Electrocatalytic Nitrogen Reduction at Low Temperature. *Joule* **2018**, *2* (5), 846–856.

(125) Shah, V. K.; Brill, W. J. Isolation of an Iron-Molybdenum Cofactor from Nitrogenase. *Proc. Natl. Acad. Sci.* **1977**, *74* (8), 3249–3253.

(126) Shilov, A. Catalytic Reduction of Molecular Nitrogen in Solutions. *Russ. Chem. Bull.* **2003**, *52* (12), 2555–2562.

(127) Chatt, J.; Pearman, A. J.; Richards, R. L. Diazenido (Iminonitrosyl) (N2H), Hydrazido(2-) (N2H2, and Hydrazido(1-) (N2H3) Ligands as Intermediates in the Reduction of Ligating Dinitrogen to Ammonia. *J. Organomet. Chem.* **1975**, *101* (3), C45–C47.

(128) Coucouvanis, D.; Newton, W. E.; Stiefel, E. I. *Molybdenum Enzimes, Cofactors, and Model Systems*; American Chemical Society, 1993.

(129) Tanaka, K.; Hozumi, Y.; Tanaka, T. Dinitrogen Fixation Catalyzed by the Reduced Species of [Fe4S4 (SPh) 4] 2− and [Mo2Fe6S8 (SPh) 9] 3−. *Chem. Lett.* **1982**, *11* (8), 1203–1206.

(130) Banerjee, A.; Yuhas, B. D.; Margulies, E. A.; Zhang, Y.; Shim, Y.; Wasielewski, M. R.; Kanatzidis, M. G. Photochemical Nitrogen Conversion to Ammonia in Ambient Conditions with FeMoS-Chalcogels. *J. Am. Chem. Soc.* **2015**, *137* (5), 2030–2034.

2. Electrochemical nitrogen reduction reaction with MoS_x

2.1 State of art

2.1.1 Potential MoS_x catalyst

During the recent upsurge of studies investigating the N_2 reduction reaction (NRR) in aqueous conditions, various electro-catalysts were reported.[1–3] Among them, synthetic transition metal sulfides (MS_x) strongly arouse our curiosity. MS_x can be viewed as analogues of the cofactors of nitrogenases and are appealing candidates for developing bio-inspired catalysts for the electro-driven NRR (ENRR). Iron and molybdenum derivatives have been particularly scrutinized as both metals are involved in the cofactor supporting the most active form of the enzymes.[4] Early examples of synthetic mimics incorporating these transition metals were indeed reported to exhibit some activity towards N_2 reduction.[5–7] Molybdenum sulfides (MoS_x), which are more robust than their iron analogues were investigated in this work.

MoS_2 is a dichalcogenide with a hexagonally packed layered crystal structure, consisting of Mo layer sandwiched between two S layers, as S-Mo-S, with covalent bonds between Mo-S and van der Waals forces between S-S. In between the S-Mo-S layers, other ions or molecules could be incorporated to tune the properties of the material.[8] The derivatives of MoS_2 (MoS_x) have already been largely investigated as electro-catalysts for small molecule activation. Their application showed outstanding performances for the hydrogen evolution reaction (HER)[9] and promising activity for the reduction of CO_2.[10,11] Even though the selectivity for N_2 reduction will be a critical point for the design of any NRR catalyst, we should not ignore that nitrogenase produces H_2 along with NH_3.[4] Moreover, it has been proved that the reductive elimination leading to the release H_2 plays an important role in the coordination of N_2 in the E4 state of nitrogenase.[12] Thus, the modification of HER catalysts to switch their selectivity towards N_2 might be a fruitful strategy to prepare NRR catalysts.

The potential activity of MoS_x for ENRR has firstly been emphasized by theoretical studies,[13–15] and was quickly confirmed experimentally (***Table 2.1***).[16–23] Initial DFT studies indicated that on pristine MoS_2, N_2 activation occurs preferably at the positively charged Mo-edges, where adsorption of dinitrogen on undercoordinated Mo centers allows for the polarization and weakening of the N≡N bond. Interestingly, later reports by X. Sun *et al.*[17] and Lou and *al.*,[24] further highlighted the enhanced NRR performances of crystalline MoS_x derivatives where sulfide vacancies lead to high densities of surface defects.

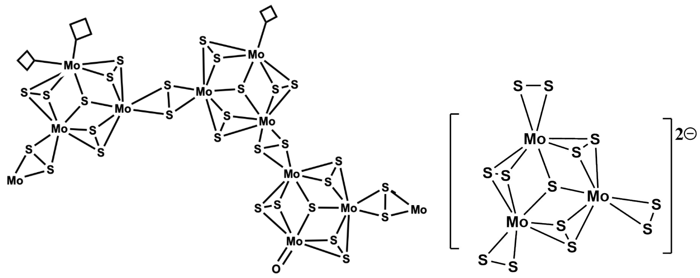

Figure 2.1: *a-MoSx (left); [Mo3S13]2- (right).*

Alternatively, less ordered materials could be interesting. Lacking long-range crystalline order, amorphous molybdenum sulfide (*a*-MoS_x) ***(Figure 2.1)*** is composed of polymeric chains of trigonal molybdenum {Mo_3S_7} and {Mo_3S_6} clusters connected via shared disulfide ligands， and it has similar Raman and X-ray photoelectron spectroscopy (XPS) signatures to the [Mo_3S_{13}](NH_4)$_2$ clusters. [25,26] It is one of the most defective materials in MoS_x family, carrying defect Mo^{V}=O sites in various protonation states.[25] In addition, it has been demonstrated that accessibility of the Mo centers of the individual clusters increases in *a*-MoS_x after partial elimination of the terminal disulfide ligands under reductive conditions.[25] It is attractive to compare the resulting unsaturated Mo sites to the “surface defects” of crystalline MoS_x which showed enhanced ENRR activity in previous studies[17,27] and *a*-MoS_x appeared to us as an ideal candidate for promoting ENRR.

2.1.2 Current catalyst activities

Among the numerous studies discussing ENRR in the literature, we must note that the critical parameters (catalytic rate, loadings …) are often reported in non-normalized units. The main parameters that must be taken into consideration when comparing catalytic materials performances include: the catalyst loading; the nature of electrolyte (the pH); the electrochemical potential applied; the rate and faradaic efficiency (FE). Among these parameters, the rate of ammonia production appears as one of the major figure of merit used to compare the activity of different catalysts. However, researchers report rates in ways that are not directly comparable: sometimes it is based on the geometrical surface of the electrode, or on the mass of the catalytic material (which includes additives such as carbon black, carbon fibers, etc… or not), or sometime on the loading of the expected active center (metal-loading in single atom based catalytic materials). In addition, these rates can be reported according the mass- or the molar-fraction of ammonia produced per second or hour. Herein we converted the original data into a standardized framework, to allow us to compare their activities with more consistency.

In order to compare the reported activities of different catalysts more visually, we considered their NH_3 production rate ($\mu mol.h^{-1}.mg^{-1}$) using the mass of the whole composite deposited

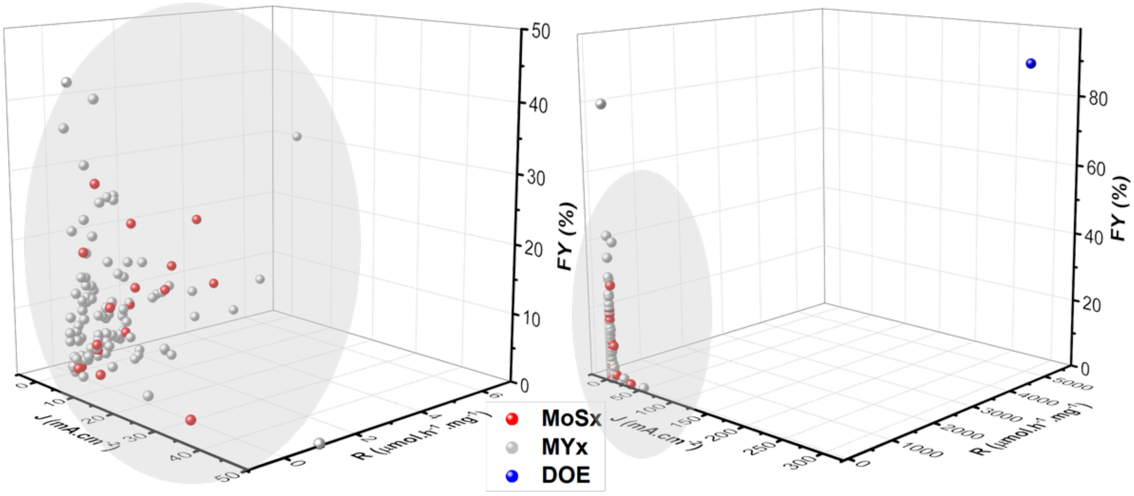

Figure 2.2: *3D graph of different materials reported plotted NH_3 production rate (μmol.h^{-1}.mg^{-1}), current density (mA.cm^{-2}), faradaic efficiency (FE %) as x, y, z axis. The red spot represent the results of Mo sulfides, the gray ones represent the other material families, while the blue one represent target defined by US. DOE Refuel program.*

on the electrode (which includes any solid additive to the original material prepared), the current density (mA.cm^{-2}), and faradaic efficiency (FE %) as coordinates to build a 3D scatter graph ***(Figure 2.2)***. These parameters are important to characterize the reactivity, selectivity and the kinetic of catalysts, and were used by the United States Department of Energy (DOE) within the *Refuel program* to define the target values for an ENRR catalyst to become technologically relevant (2.5 x 10^{-3} mol_{NH3}.cm^{-2}.h^{-1}; 90% FE; 300 mA.cm^{-2}). In the graph, the red spots represent the all reported Mo sulfides derivatives (MoS_x), while the gray ones represent other materials, including oxides, nitrides, phosphides of noble (Au, Ru, Pd…) or non-noble metals (W, V, Fe…).

From ***Figure 2.2***, we observed that in spite of the large variety of materials that has been reported, most of the NH_3 production rates stayed under 3 X 10^{-6} mol_{NH3}.$mg_{cata}{}^{-1}$.h^{-1} Lacking information of the loading details of the catalysts in several cases, the rates per surface unit, which was chosen for defining the DOE target, are not always available from the literature. However, in most cases the catalyst loadings are reported to be between 0.1-1 mg.cm^{-2}. Therefore, if we considered a system reaching the DOE target with a typical loading of 0.5 mg.cm^{-2}, the expected rate would be in the order of 5 x 10^{-3} mol_{NH3}.$mg_{cata}{}^{-1}$.h^{-1}. Briefly, the activity reported for ENRR catalysts is still several orders of magnitude lower than the DOE target, which show that this field is still in its infancy.

Looking closely at the MoS_x family we next listed the main parameters in the ***Table 2.1***.

Table 2.1: *Main catalytic figures and conditions reported for dinitrogen reduction reaction (NRR) promoted by molybdenum sulfide derivatives.*

Material	**Loading WE mater.**	**Electrolyte**	**Bias** (V *vs.* RHE)	**Rate** (µmol. cm^{-2}.h^{-1})	**Rate** (µmol. mg$_{MoSx}$$^{-1}$.h^{-1})	**FE** (%)
MoS_2 nanoflowers (defect-free)[1]	0.4 mg.cm^{-2} CC + Nafion	0.1 M Na_2SO_4	–0.4	0.32	0.79	2.2
MoS_2 nanoflowers (defect-rich)[1]	0.4 mg.cm^{-2} CC + Nafion	0.1 M Na_2SO_4	–0.4	0.68	1.7	8.3
MoS_2 nanosheets[2]	[a,b]	0.1 M Na_2SO_4	–0.5	0.29	[a,b]	1.2
MoS_2 nanosheets[2]	[a,b]	0.1 M HCl	–0.5	0.31	[a,b]	0.1
MoS_2 nanosheets on BC fiberc[c,3]	10 mg.cm^{-2} CC + Nafion	0.1 M Na_2SO_4 pH 3	–0.2	0.2	0.31	0.5
MoS_2 nanosheets on BC fibers[c,3]	10 mg.cm^{-2} CC + Nafion	0.1M Li_2SO_4 pH 3	–0.2	1.6	2.5	9.8
2H-MoS_2[4]	1 mg.cm^{-2} CP + Nafion	0.01 M HCl pH 2	–0.2	0.02[d]	0.02[d]	[e]
1T-MoS_2[4]	1 mg.cm^{-2} CP + Nafion	0.01 M HCl pH 2	–0.2	0.02[d]	0.02[d]	[e]
MoS_2 nanosheets[5]	1 mg.cm^{-2} CP + Nafion	0.1 M Na_2SO_4	–0.3	0.15	0.15	5.2
MoS_2 nanosheets[5]	1 mg.cm^{-2} CP + Nafion	0.1 M HCl pH 1	–0.3	0.1	0.1	0.1
MoS_2 nanosheets[5]	1 mg.cm^{-2} CP + Nafion	0.1 M NaOH pH 13	–0.3	0.88	0.88	2
MoS_2@rGO[6]	0.1 mg.cm^{-2} CP	0.1 M $LiClO_4$	–0.45	0.15	1.46[f]	4.6
N-doped MoS_2 nanoflowers[7]	0.7 mg.cm^{-2} GC	0.1 M Na_2SO_4	–0.3	2.9	4.1	9.1
MoS_2 nanoflowers[7]	0.7 mg.cm^{-2} GC	0.1 M Na_2SO_4	–0.3	0.2[d]	0.3[d]	0.4[d]
Co-doped MoS_{2-x}[8]	[a,b]	0.01 M H_2SO_4	–0.3	[e]	0.6	10
MoS_{2-x}[8]	[a,b]	0.01 M H_2SO_4	–0.3	[e]	0.32	1.7
2H-MoS_2[9]	[a]	0.1 M HCl pH 1	–0.34	0.2	[a]	0.1
Fe doped 2H-MoS_2[9]	[a]	0.1 M HCl pH 1	–0.34	0.82[d]	[a]	0.3[d]
MoS_2 nanodots @rGO[10]	0.8 mg.cm^{-2} CC + Nafion (0.4 mg MoS_2)	0.1 M Na_2SO_4 pH 10	–0.35	0.4[d]	0.5[d,f]	27.9

MoS_2 nanodots @rGO[10]	0.8 mg.cm^{-2} CC + Nafion (0.4 mg MoS_2)	0.1 M Na_2SO_4 pH 10	–0.75	0.8	1[f]	2[d]
15%-wt N-coordinated MoS_2/C_3N_4[11]	[b] CP + Nafion	0.1 M Na_2SO_4	–0.5	[b]	1.2[g]	6.9
MoS_2@C_3N_4[11]	[b] CP + Nafion	0.1 M Na_2SO_4	–0.5	[b]	0.6[g]	3.8
MoS_2[11]	[b] CP + Nafion	0.1 M Na_2SO_4	–0.5	[b]	0.4	2.8
3%-wt 1T-MoS_2/g-C_3N_4[12]	0.7 mg.cm^{-2} GC + Nafion	0.1 M HCl pH 1	–0.3	1.2	1.8[g]	20.5
10%-wt 1T-MoS_2@Ti_3C_2[13]	0.7 mg.cm^{-2} GC + Nafion	0.1 M HCl pH 1	–0.3	1.2	1.8[h]	10.9
1T-MoS_2[13]	0.7 mg.cm^{-2} GC + Nafion	0.1 M HCl pH 1	–0.3	0.5	0.7	5.6
amorphous MoS_3[14]	0.2 mg.cm^{-2} CC	0.5 M Li_2SO_4	–0.3	0.61	3	12.8
MoS_2[14]	[b] CC	0.5 M Li_2SO_4	–0.3	[b]	0.61	3.9
$FeMo_3S_4$ nanorods[15]	0.2 mg.cm^{-2} CC + Nafion	0.5 M $LiClO_4$	–0.3	0.77	3.8	19.2

Article references for ***Table 2.1*** *were listed in S2.1.*

WE mater.: working electrode material; CC: carbon cloth ; BC: bacteriocelulose; CP: carbon paper; [a] *hydrothermally grown MoS_2 nanosheets on working electrode;* [b] *no loading indication;* [c] *calcinated MoS_2 coated bacteriocellulose fibers; loading 64 mg MoS_2.g^{-1};* [d] *estimated on the figures;* [e] *not reported;* [f] *μmol.mg$_{MoS2@rGO}^{-1}$.h^{-1};* [g] *μmol.mg$_{MoS2@C3N4}^{-1}$.h^{-1};* [h] *μmol.mg$_{MoS2@Ti3C2}^{-1}$.h^{-1}.*

From ***Table 2.1***, we can see that 1) different working electrode materials are used, such as carbon cloth (CC); bacteriocelulose (BC); carbon paper (CP); glassy carbon (GC)…with different loadings; 2) the electrolyte composition used is extremely variable including buffered or non-buffered acidic, neutral or basic solutions; 3) some additive such as Nafion was used sometimes, but its influence was not mentioned. All these differences might influence the activity of MoS_x derivatives towards ENRR, but no clear trend pointing out to the beneficial influence of a specific parameter (pH, electrolyte composition, additives loading, etc) is apparent from this global literature analysis.

Nevertheless, two approaches were reported to improve the NRR activity of these catalysts and attracted our attention: 1) the use of defect-rich MoS_x bearing more active sites on Mo than the crystalline materials; 2) doping MoS_x with some other metals such as Co, Fe…

Inspired by these ideas, in the following sections we descibe a rigorous protocol to investigate the NRR activity of different MoS_x prepared *in house*, including nanocrystalline (*c*-MoS_x), defect-rich amorphous (*a,e*-MoS_x) and iron doped (*Fe*-MoS_x) materials.

2.2 Rigorous protocol

While the description of new ENRR catalysts proceeds rapidly in the literature, several studies point out that some results must be taken with caution.[28,29] When considering the relatively low ammonia production rates reported so far, and the various sources of adventitious ammonia susceptible to affect the final quantification of the targeted product, strict requirements are needed in terms of protocol and sensitivity of the method used to evaluate the activity of catalysts.

First the inherent properties of NH_3 lead to its ubiquitous presence of in the laboratory environment. Such a polar, highly soluble (solubility 482 $g.L^{-1}$ in water, at 24 ℃) and basic (pKa 9.25 at 25 ℃) molecule, is not only easy to dissolve in water but also adsorbs to various surfaces with a lifetime of 12 hours to 5 days before decomposition.[30] All these complicate its accurate quantification. For example, 0.05–250 parts per million (ppm) NH_3 exist in ambient air and 0.3–3.0 ppm in human breath.[31,32] In addition, Nafion, generally used as binder to stabilize the catalyst on the cathode or as a proton-conductive membrane in electrochemical cell, is likely to release NH_4^+ too.[28] Thus, a variable concentration of ammonia will be always present in samples, which must be taken into account as background. Given the current low production rate of NH_3 achieved by ENRR, which does not really stand out from the background, it is easy to get false positive results.

Additionally, Nørskov and co-workers pointed out that the influence of some N-containing species other than N_2, which might be more easily reduced to ammonia, need special attention due to their presence in many materials, and even as trace amounts in the N_2 supply gas.[28] From the list of the potential where the N-containing substrates are reduced to NH_3 in ambient condition, it is apparent that NRR occurs theoretically at the lowest potential (***Figure 2.3***).

Among these contaminants, the neutral NO_x from the feeding gas, and the ionic NO_x^- resulting from the hydration of NO_x, or present as traces in the electrolyte, or even released form the catalysts tested, are particularly troublesome.[28,33–35] Each mole of $^{15}N_2$ gas fed through the electrolyte can lead to the accumulation of 34 to 1900 µmoles of ^{15}N-ammonium, 1.8 to 420 µmoles of ^{15}N-nitrate/nitrite, and ⩾21 µmoles of ^{15}N-nitrous oxides. Furthermore, the NO_x have better water solubility than N_2 (N_2O: 2.35×10^{-4}; NO: 3.74×10^{-5}; N_2:1.27×10^{-5} , 293 K, 1 atm, presented in mole fraction).[36]

298,15 K, 1 atm, E^0 *vs.* NHE

$N_2H_5^+$	$N_2H_5^+ + 3H^+ + 3e^- \rightleftharpoons 2NH_4^+$	$E^0 = +1.275$ V
NH_3OH^+	$NH_3OH^+ + 2H^+ + 2e^- \rightleftharpoons NH_4^+ + H_2O$	$E^0 = +1.35$ V
HN_3	$HN_3 + 11H^+ + 8e^- \rightleftharpoons 3NH_4^+$	$E^0 = +0.695$ V
	$HN_3 + 3H^+ + 2e^- \rightleftharpoons NH_4^+ + N_2$	$E^0 = +1.96$ V
N_2	$N_2 + 8H^+ + 6e^- \rightleftharpoons 2NH_4^+$	$E^0 = +0.092$ V
NO	$NO + 6H^+ + 5e^- \rightleftharpoons NH_4^+ + H_2O$	$E^0 = +0.836$ V
HNO_2	$NO_2^- + 8H^+ + 6e^- \rightleftharpoons NH_4^+ + 2H_2O$	$E^0 = +0.897$ V
NO_3^-	$NO_3^- + 10H^+ + 8e^- \rightleftharpoons NH_4^+ + 3H_2O$	$E^0 = +0.875$ V

Figure 2.3: *Potential of different N-containing substrate to be reduced to NH_3.*

Briefly, the establishment of rigorous ENRR study protocol demands both proper control experiments and accurate quantification methods, and the possibility of reduction of NO_x needs special attention.

2.2.1 Electrochemical studies

2.2.1.1 Electrolyte selection

In competition with HER, the ENRR activity could be sensitive towards the pH. We used two electrolyte solutions as: 0.1 M HCl (pH = 1) or 0.1 M potassium phosphate buffer (KPi, K_2HPO_4–KH_2PO_4 8.5–91.5**%**; pH = 5.8). Due to the instability of *a*-MoS_x particles in solutions of pH ≥ 7 for long electrolysis times, this material could not be used in basic environment.

2.2.1.2 Control & electrochemical nitrogen reduction reaction (ENRR) series

The evolution of the background ammonia concentration in the electrolyte was probed over time in 5 control conditions (***Table 2.2***), targeting different contamination sources upon: 1) N_2 feeding gas: (control series HCl-1/KPi-1 for 0.1 M HCl or 0.1 M KPi, respectively, same naming convention for groups below); 2) ENRR on bare GC (control series HCl-2/KPi-2); 3) ENRR on Nafion-coated GC (control series HCl-3/KPi-3); 4) chemical NRR & release of NH_3 from the catalyst film (control series HCl-4/KPi-4); 5) some substrates not coming from N_2 gas reduced to NH_3 (series HCl-5/KPi-5). Two ENRR groups were studied with (series HCl-7/KPi-7) or without (series HCl-6/KPi-6) the Nafion binder.

2.2.1.3 Working electrode (WE) preparation

The working electrodes (WE) were prepared by drop casting a suspension containing the catalyst on glassy carbon (GC), then dried in air to form a homogenous, robust film with a proper thickness. GC was selected thanks to its benefits compared to other electrode materials, such as easier to get pristine surface than carbon paper, as well as easier definition of the geometric surface used than carbon foam. The film should not be too thick in order to optimize the conductivity within the film as well as to ensure an optimal accessibility of the catalytic active sites to the electrolyte interface. Moreover, the incorporation of the Nafion in series HCl-7/KPi-7 groups to favor the stability and homogeneity of the film. Therefore, a thin and homogenous film with a loading of 0.3 mg *a*-MoS_x was prepared on a freshly polished GC electrode (1 cm^2).

2.2.1.4 Electrochemical measurements

To probe the potential catalytic activities of *a*-MoS_x for ENRR in aqueous conditions, we adapted classical conditions from the literatures. Potential-controlled electrolysis were carried out in the three-electrode configuration using a single-compartmented cell (15 mL). A Pt wire isolated by a frit (P4) was used as counter electrode (CE), and an Ag/AgCl/3 M KCl electrode as reference electrode (RE). Bare-, Nafion-, or *a*-MoS_x-coated GC were used as WE for the control and ENRR experiments as summarized in ***Table 2.2***. The potentials reported in this work are referenced *vs.* the Reversible Hydrogen Electrode (RHE) using the following relation: ***E (RHE) = E (applied) + E^0 (Ag/AgCl/3M KCl) + 0.059 x pH*** with pH equals 1 and 5.8 for 0.1 M HCl and 0.1 M KPi buffer, respectively.

The experiments were performed under ambient conditions (room temperature, atmospheric pressure), under a continuous flow of N_2 (Ar) calibrated at 10 $mL.min^{-1}$. During the course of the electrolysis, the WE was poised at –0.3 V *vs.* RHE. 1 mL samples of the electrolyte were taken at fixed times (0h, 2h, 4h…) and kept for the colorimetric quantification of NH_3. The initial volume of electrolyte introduced in the cell was 10 mL for each experiment (controls and NRR).

Table 2.2: *Summary of the control and ENRR groups tested. HCl-1 - HCl-7: experiments run in 0.1 M HCl (pH = 1) electrolyte. KPi-1 - KPi-7: experiments run in 0.1 M KPi buffer (pH = 5.8).*

Series	*a*-MoS_x loading ($mg.cm^{-2}$)	Additive and solvent	Bias (*vs.* RHE)	Feeding gas	Experiment time
HCl-1/KPi-1	n.a[a]	n.a[a]	n.a[a]	N_2	>20 h
HCl-2/KPi-2	0	–	-0.3	N_2	>20 h
HCl-3/KPi-3	0	1 µL Naf + 200 µL IPA [b]	-0.3	N_2	>20 h
HCl-4/KPi-4	0.3	1 µL Naf + 200 µL IPA	O.C.P.[c]	N_2	>20 h
HCl-5/KPi-5	0.3	1 µL Naf + 200 µL IPA	-0.3	Ar	>20 h
HCl-6/KPi-6	0.3	200 µL IPA	-0.3	N_2	>20 h
HCl-7/KPi-7	0.3	1 µL Naf + 200 µL IPA	-0.3	N_2	>20 h

n.a[a]: direct purge, no electrodes/electrochemical set up involved. [b] Naf: commercial 5% Nafion solution. IPA: isopropyl alcohol. O.C.P.[c]: open circuit potential (full setup without connecting the potentistat)

2.2.2 Precise ammonia quantification

2.2.2.1 Colorimetric titration of ammonia (NH_3)

For this assay we used the method proposed by Bower and Holm-Hansen.[37] This approach relies on the spectrophotometric quantification of a quinone-imine derivative, that results from the reaction of chloramine (resulting from the reaction of ammonia and sodium hypochlorite) on salicylic acid in alkaline conditions, and which exhibits a specific absorption band centered around 650 nm. Importantly the reaction time and overall procedure of the assays were optimized for our specific conditions to ensure reliable measurements (see details in S2.3.3). For each sample of electrolyte (1 mL) collected during the course of the ENRR and control experiments, three independent measurements were done. The concentration of ammonia reported for each sample corresponds to the mean value calculated form these measurements (same for all colorimetric measurements).

UV-Vis measurements

The spectra were recorded between 500 nm and 1000 nm using cuvettes of 1 cm of optical pathway. The spectrophotometer was used in dual beam mode using mQ water as reference. When necessary, the baseline was corrected at 1000 nm to adjust the absorbance to ±0.0010 before recording the spectra. For an accurate analysis of the assays, the time required for reaching a stable reading of the absorption at 650 nm (complete conversion) was investigated. As shown on ***Figure 2.4*** the absorbance of samples in HCl evolves greatly up to 40 min before reaching a stable plateau. In the same conditions the assay executed in 0.1 M KPi reaches a stable reading after 30 minutes. In the following assays a reaction time of 90 min was selected for all the samples.

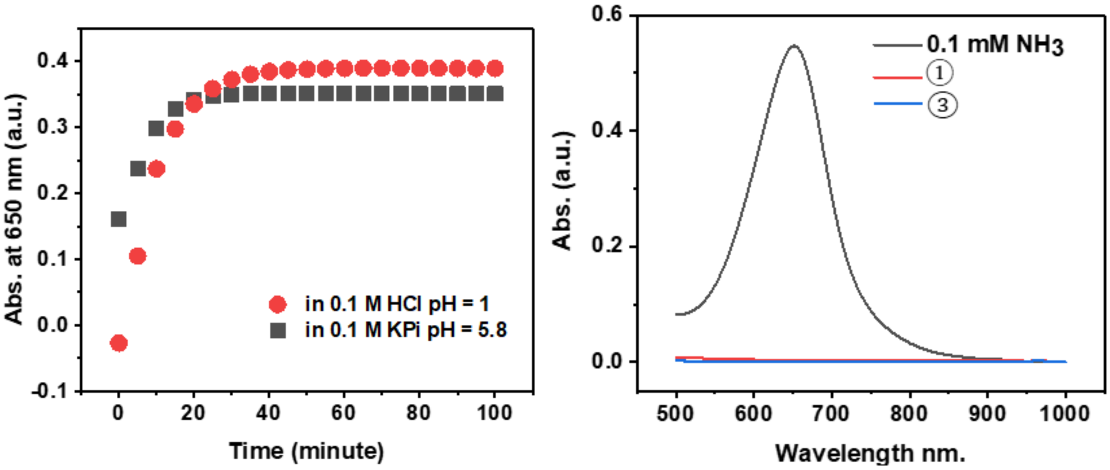

Figure 2.4: *Evolution of the absorbance at 650 nm recorded for a representative sample prepared by treating 0.3 mL of a solution of 0.02 mM* NH_3 *in 0.1 M HCl (red dots) and 0.1 M KPi (black dots) with salicylate reagents (see S2.3.3.1 for details)(left). The absorbance was recorded every 5 min. UV-Vis spectra of: a solution of 0.1 mM ammonia in 0.1 M HCl treated accordingly to the procedure described above after 90 min of reaction time (black curve), the reagent ① (red curve), and reagent ③ (blue curve)(right).*

Calibration curves and quantification of the ammonia concentration

To ensure accurate measurements, the limit of detection and linearity range of the assay in our specific conditions were established from known dilutions of an aqueous ammonia standard solution in 0.1 M HCl and 0.1 M KPi (***Figure 2.5***).

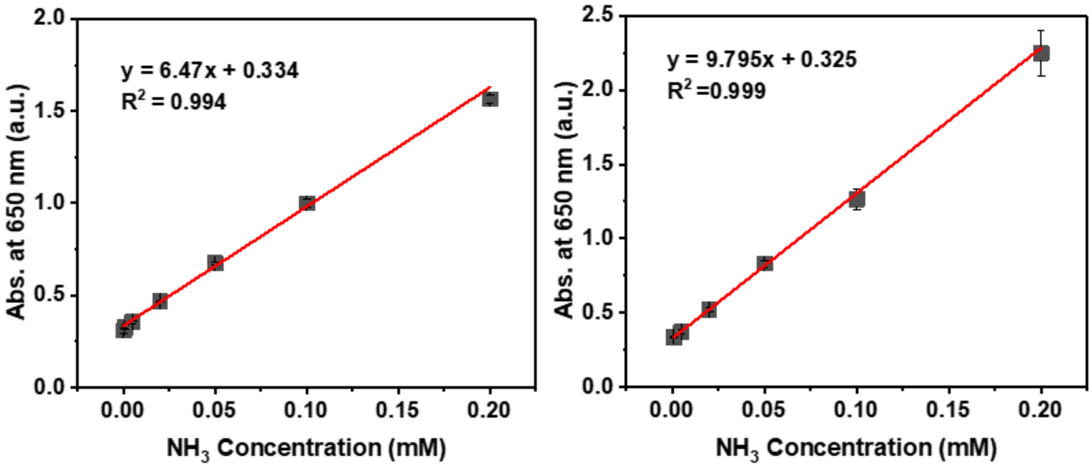

Figure 2.5: *Typical calibration curves obtained for the salicylate assay in 0.1 M HCl (left) and 0.1 M KPi (right) using known dilution of a standard* NH_3 *solution (dilution to: 0.001 mM, 0.005 mM, 0.05 mM, 0.1 mM and 0.2 mM).*

Good linearity (R^2 = 0.994/0.999) was obtained for concentrations of ammonia comprised between 0.001 mM and 0.2 mM in both electrolytes. We note that Bower and Holm-Hansen report a lower limit of detection in pure water (0.0003 mM) of about one order of magnitude lower than in our tests. This apparent discrepancy is likely related to the use, in our case, of relatively concentrated electrolytes (0.1 M HCl/KPi,) which are random and non-negligible source of advantitious ammonia. This is best shown on the ***Figure 2.6*** which depicts the absorbances measured for assays run on freshly prepared electrolytes solutions. From these initial values, we can estimate the presence of 0.03 mM – 0.1 mM (0.02 mM – 0.04 mM) of NH_3 as a trace contaminant in the 0.1 M HCl (0.1 M KPi) electrolyte, thus, limiting the precision of the colorimetric method in our conditions.

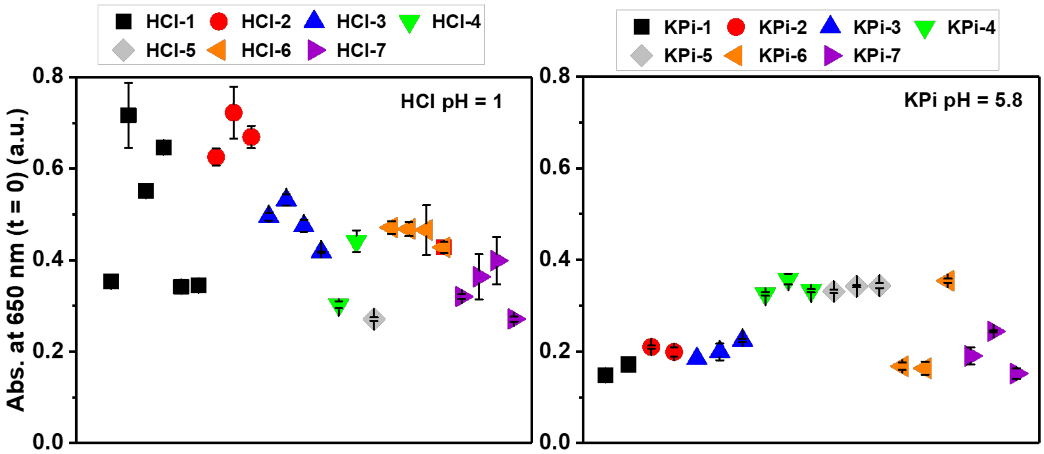

Figure 2.6: *Absorption at 650 nm measured with the salicylate assay for samples from controls and ENRR experimental series at time zero in 0.1 M HCl (left) and 0.1 M KPi (right).*

2.2.2.2 Data correction

All the experiments (control and ENRR) were conducted at least twice to build the datasets discussed in the following. In order to be able to compare the outcome of our experiments in a meaningful way, rigorous data processing was necessary as explained below.

1. Fresh calibration curve

To ensure an accurate determination of the ammonia concentration present in the samples collected during ENRR and control experiments, a fresh calibration curve was established for each individual series of measurements (using the appropriate electrolyte). The calibration curves were built from at least three experimental points, each of which determined from three independent measurements. In the case of NRR and control studies, the individual calibration curves were built for a limited range of concentrations: 0.1 mM, 0.05 mM and "0" mM.

2. Volume of sampling

During the course of the electrolysis, the total volume of electrolyte decreases due to the successive sampling. This induces an overestimation of any variation of the apparent ammonia concentration between successive measurements. To eliminate this bias the data reported for the CA in the discussion are, thus, corrected as follow:

$$[NH_3]_{ic} = \frac{\left([NH_3]_1 \times Vs_1 + \cdots + [NH_3]_{i-1} \times Vs_{i-1} + [NH_3]_i \times (Vs_i + Vel_i)\right)}{(Vs_1 + \cdots + Vs_{i-1} + Vs_i + Vel_i)}$$

where $[NH_3]_{ic}$ is the corrected value of the concentration of the ammonia for sample *i*, $[NH_3]_i$ is the apparent concentration of ammonia measured for the sample *i,* Vs_i the volume of sample *i* and Vel_i the volume of the remaining electrolyte after taking the i^{th} aliquot.

3. Correction with $C_{t=0}$

Due to the overall low concentration of NH_3 typically measured in these experiments, small variations of the concentration of adventitious ammonia can significantly affect the absorbance of the samples in the salicylate assay, even at time zero (t = 0) where virtually no ammonia is expected (***Figure 2.6***).

Because the apparent 'zero' ammonia concentration measured for each experimental series appears random and never null, all the datasets discussed below are corrected for the absorbance at t = 0 for each series. Negative concentrations, thus, indicate a decrease of the apparent ammonia concentration in the electrolyte relative to t = 0.

2.3 Electrochemical nitrogen reduction reaction with *a*-MoS_x

First, let us consider the evolution of the ammonia concentration measured over time for the control series HCl-1/KPi-1 – HCl-5/KPi-5 (***Figure 2.7****, top;* ***Table S2.3***). No strong trends appear in any series. We observe a random distribution of the concentrations with respect to time zero with equal chances of measuring an increase or a decrease of the apparent ammonia concentration over time in both 0.1 M HCl and 0.1 M KPi, as illustrated by the frequency distribution histograms (***Figure 2.7****, bottom*).

Overall, more than 95% of the experimental values remain within ± 10 µM of the initial ammonia concentration for up to 25 hours in all the series (***Table 2.2***). In the following, thus, any variation of the ammonia concentration falling within this range will be considered as mere fluctuation of the experimental background concentration of adventitious NH_3.

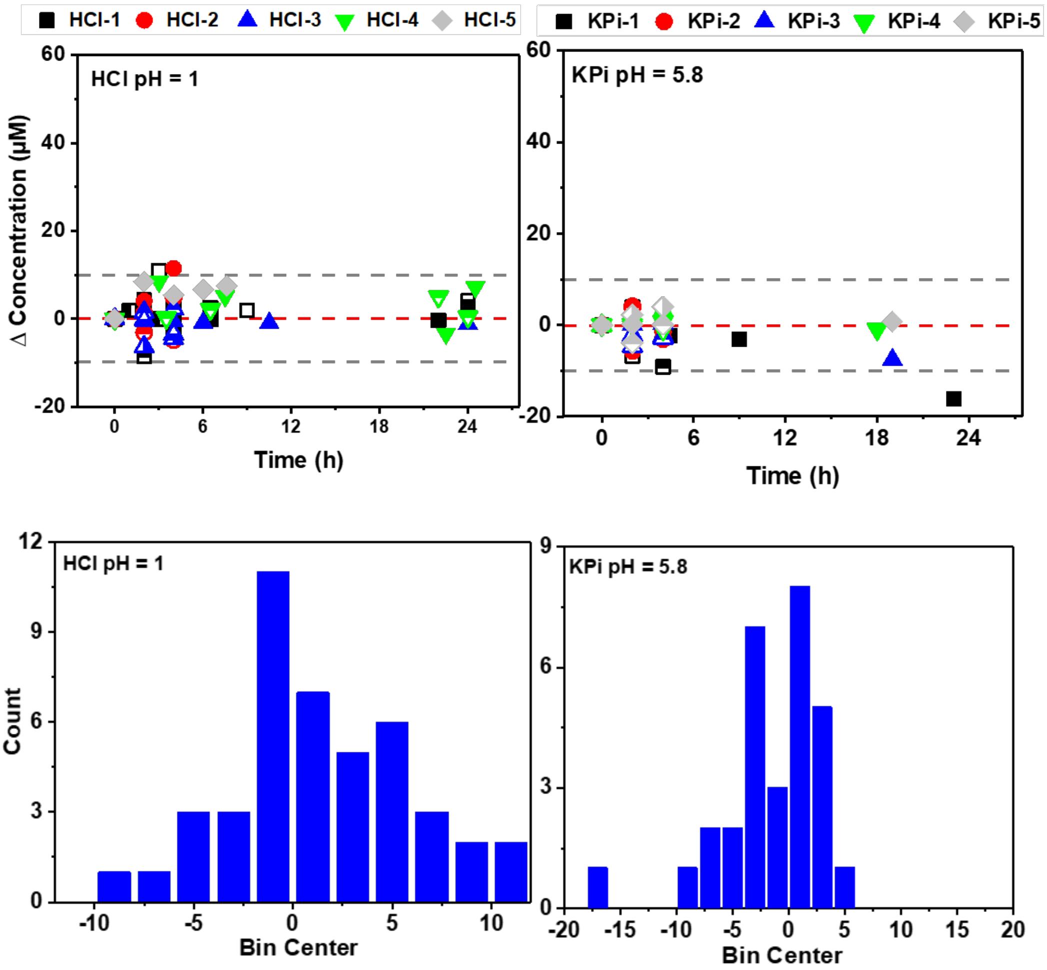

Figure 2.7: *Evolution of the apparent NH_3 concentration over time (top left in HCl; right in KPi) for all control groups. Frequency distribution histograms of the apparent concentration measured with the salicylate assay for samples from controls series (bottom left in HCl; right in KPi).*

We next turned to controlled electrolysis experiments run in N_2-saturated electrolyte over *a*-MoS_x thin-films (series HCl-6/KPi-6 and HCl-7/KPi-7, ***Figure 2.8***). Here again, the concentration of ammonia measured in both 0.1 M HCl and 0.1 M KPi electrolyte remains generally close to the range of the experimental background. Furthermore, hydrazine was considered as a possible side product for NRR, but in these studies no traces could be detected in the electrolyte using the method of Watt and Chrisp (detection limit 5 µM, see S3.3.3.2),[38] in any of the conditions tested. Therefore, *a*-MoS_x does not exhibit the expected activity towards direct electro-driven N_2 reduction.

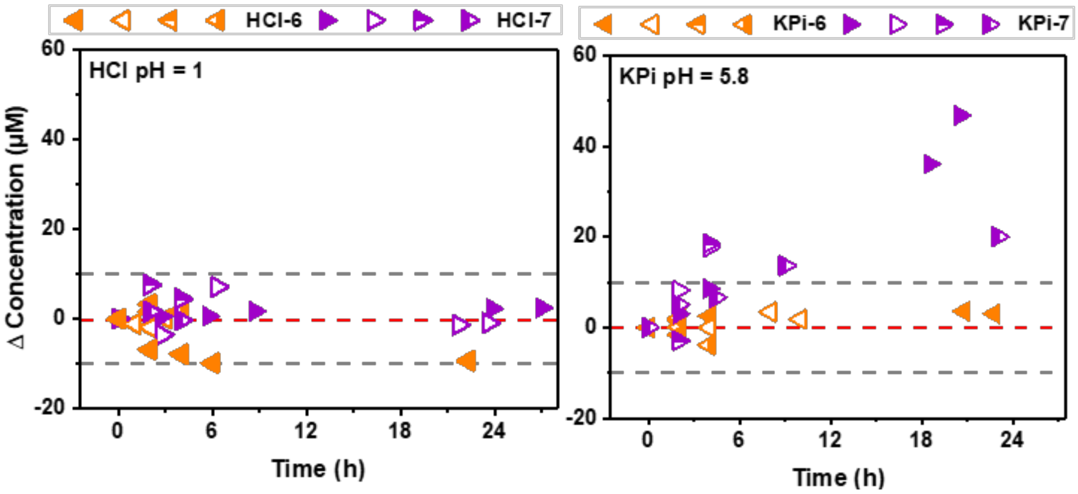

Figure 2.8: *Evolution of the apparent concentration of NH_3 in the electrolyte during potential-controlled electrolysis in N_2-saturated 0.1 M HCl (left) or 0.1 M KPi buffer (pH = 5.8, right) using bare (HCl-6/KPi-6) or Nafion-coated (HCl-7/KPi-7) a-MoS_x films deposited on glassy carbon electrodes. The working electrode was polarized –0.3 V vs. RHE.*

A more detailed analysis of the series is, however, interesting. Controlled electrolysis run on Nafionless films in both electrolytes (series HCl-6, KPi-6) as well as controlled electrolysis conducted over Nafion-containing films in 0.1 M HCl (series HCl-7) lead to an essentially random evolution of the ammonia concentration over time. The dispersion of the individual values remains strictly within the range of the experimental background and *a*-MoS_x is clearly inactive for NRR in these conditions. Surprisingly a small but steady increase in the ammonia

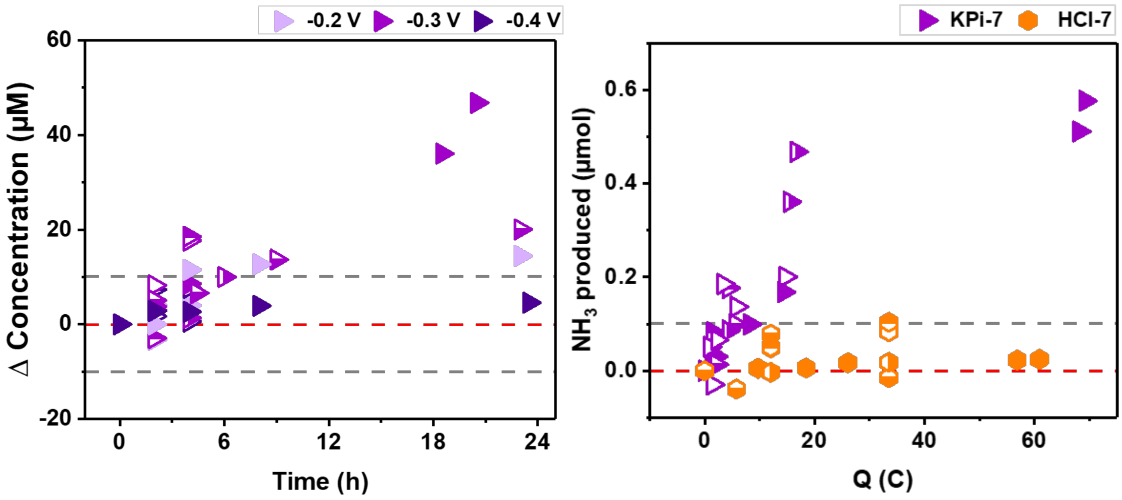

***Figure 2.9**: Evolution of the apparent concentration of NH_3 in the electrolyte during potential-controlled electrolysis at –0.2 V, –0.3 V, or –0.4 V vs. RHE in N_2-saturated 0.1 M KPi buffer (pH = 5.8) (left). Evolution of the quantity of ammonia measured in the electrolyte as a function of the total charge passed during chronoamperometry measurements recorded on thin films of a-MoS_x incorporating Nafion, in 0.1 M HCl (orange hexagen) and 0.1 M KPi (purple right triangle) buffer electrolyte(right). The working electrode was polarized –0.3 V vs. RHE.*

concentration is, however, observed during the controlled electrolysis run in N_2-saturated 0.1 M KPi, on films incorporating Nafion (series KPi-7). The overall quantity of NH_3 released appears slightly dependent on the bias applied, with slightly higher NH_3 concentrations reached after long electrolysis run at –0.3 V *vs*. RHE (***Figure 2.9***, left).

In addition, we note a clear correlation between the quantity of ammonia detected in the electrolyte and the total charge passed during the electrolysis for KPi-7 series, in strong contrast with HCl-7, as shown on ***Figure 2.9*** right.

Electrolyte & Nafion effect

Targeting the improvement of the activity of *a*-MoS_x for ENRR, we next investigated two main parameters. Firstly, knowing that phosphate is a good ligand for multivalent cations, we supposed that the KPi buffer may lead to the poisoning of the active Mo binding sites thus drastically limiting the activity of our material. However, when the electrolyte was replaced by less-coordinating 0.1 M K_2SO_4 solution (pH = 4), we did not observe ammonia accumulation over 24 h of controlled potential electrolysis (−0.3 V vs RHE). To be noticed, in such a long-term CA study with mostly HER happening, the increasing pH the non-buffered electrolyte may induce the degradation of *a*-MoS_x. Thus, we used a solution with an initial pH of 4 to ensure the stability of *a*-MoS_x along the CA course. Therefore, the presence of the phosphate does not appear to drastically limit the ENRR activity of *a*-MoS_x (***Figure 2.10***, left).

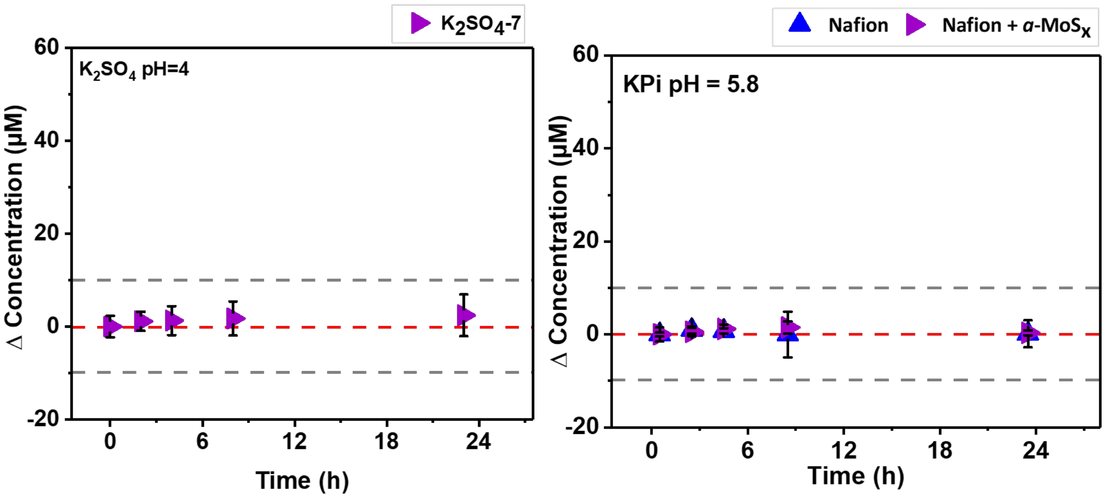

Figure 2.10: *Evolution of the apparent concentration of NH_3 in the electrolyte during potential-controlled electrolysis in N_2-saturated 0.1 M K_2SO_4) (pH = 4, left) using Nafion-coated a-MoS_x films deposited on glassy carbon electrodes. Evolution of the apparent concentration of NH_3 in the electrolyte during potential-controlled electrolysis in N_2-saturated 0.1 M KPi buffer (pH = 5.8) using 0.25% w/v Nafion-coated films with and without a-MoS_x deposited on glassy carbon electrodes (right) The working electrode was polarized at –0.3 V vs. RHE.*

Secondly, the electro-driven NH_3 release observed in KPi-7 (in presence of Nafion) series but not in KPi-6 (in absence of Nafion) strongly aroused our interest. Hence, we tried to further probe the influence of Nafion by increasing 10 times its mass ratio in the catalyst ink. Unfortunately, it led to the suppression of the apparent catalytic activity (***Figure 2.10***, right). We were unable to improve the rate of electro-driven ammonia production in the applied working conditions.

Activity of a-MoS$_x$ compare to the reported MoS$_x$ materials

The observations above suggest that Nafion-coated *a*-MoS_x promotes a sluggish electro-driven release of ammonia in 0.1 M KPi under N_2. Nevertheless, even when assuming direct ENRR for series KPi-7, it should be noted that the mean rate of ammonia production in our experiments (0.070 ± 0.005 $\mu mol_{NH3}.h^{-1}.mg_{a\text{-}MoSx}^{-1}$) are more than one order of magnitude lower than the values typically reported for molybdenum sulfide based materials (0.1 to 4.1 $\mu mol_{NH3}.h^{-1}.mg_{cat}^{-1}$; ***Table 2.1, Figure 2.11***).[16–18,18–22,27] The contrast is really striking with respect to the rates reported for defect-rich MoS_2 (1.7 $\mu mol_{NH3}.h^{-1}mg_{MoS2}^{-1}$; in 0.1 M Na_2SO_4 at –0.4 V *vs*. RHE),[17] and amorphous MoS_3 (3 $\mu mol_{NH3}.h^{-1}.mg_{MoS3}^{-1}$; in 0.5 M $LiClO_4$ at –0.3 V *vs*. RHE) recently described by Liu *et al*.[27] The different nature of the electrolytes may partly explain these observations, however, the magnitude of the difference between the rates of ammonia production determined for *a*-MoS_x and those reported for defect-rich MoS_2 or amorphous MoS_3 is surprisingly large for related forms of molybdenum sulfide. The comparison between *a*-MoS_x with amorphous MoS_3 is particularly relevant. In-depth spectroscopic investigations of MoS_3 films prepared in a similar manner as described by Liu et *al*., strongly suggested that the latter is also composed of chains of interconnected trigonal {Mo_3S_x} clusters.[39] Thus, MoS_3 and *a*-MoS_x are likely closely-related forms of molybdenum sulfides.

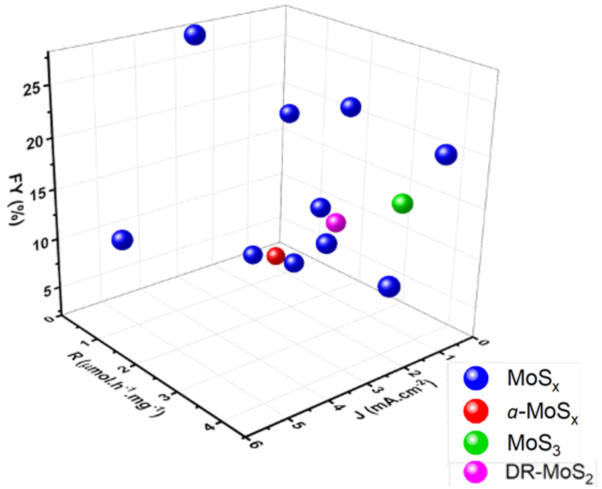

Figure 2.11: *3D graph of different MoSx reported plotted using the NH_3 production rate ($\mu mol.h^{-1}.mg^{-1}$), current intensity ($mA.cm^{-2}$), and faradaic efficiency (FE %) as coordinates. The red dot represents the activity of a-MoS_x measured in 0.1 M KPi with Nafion, the magenta and green dot represent defect-rich MoS_2 and MoS_3, which are very similar to a-MoS_x while the blue ones represent the other reported MoS_x derivatives.*

In fact, noticeable differences between the rates of ammonia production reported for supposedly identical forms of molybdenum sulfide catalysts are found through the literature (***Table 2.1***). Thus, we would like to find out the reason of the low NRR activity of *a*-MoS_x.

The reduction of NO_x

In order to investigate whether direct reduction of NO_x species may contribute to the apparent ENRR activity of our material in KPi-7 group, we firstly probed the possible accumulation of nitrite (NO_2^-) or nitrate (NO_3^-), resulting from the hydration of neutral NO_x residues present in the N_2 feeding gas, in the electrolyte solution using the Griess assay.[40] As shown in ***Figure 2.12***, the variation of the concentration of both anions remained under the detection limit of the assays (~ 1 µM) in 0.1 M KPi buffer under constant N_2 feeding (10 mL.min^{-1}) for at least 24 h. This amount is negligible compared to the quantity of ammonia accumulated in KPi-7 series (***Figure 2.7***). Thus, the electro-driven NH_3 release was not originating from the reduction of ionic NO_x^-.

Next, we tried to remove all traces of neutral NO_x contaminants by flushing the nitrogen gas through a 0.5 M $NaClO_2$ and a 0.5 M H_2SO_4 traps before feeding it into the electrolyte.[41] Upon application of this purification protocol, the variation of the ammonia concentration in the electrolyte during 24 h measurements time keeps strictly within the ± 10 µM contamination range. (***Figure 2.12***, right) Therefore we proved that this electro-driven NH_3 release came from

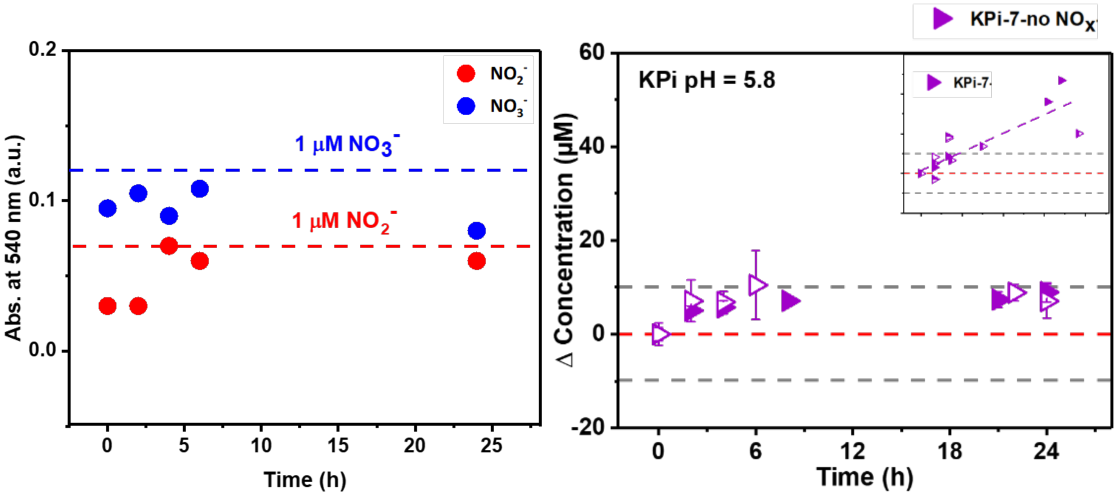

Figure 2.12: *Evolution of the concertation of NO_2^- and NO_3^- species measured by Griess Assay in 0.1 M KPi buffer (pH = 5.8) under a constant flow of N_2 (purity 99.998%, 10 mL.min^{-1}) (left). Evolution of the apparent concentration of NH_3 in the electrolyte during potential-controlled electrolysis in purified N_2-saturated 0.1 M KPi buffer (pH = 5.8) Nafion-coated (KPi-7-no NO_x) a-MoS_x films deposited on glassy carbon electrodes. The working electrode was polarized at –0.3 V vs. RHE. In the small box, shown the KPi-7 (right).*

the reduction of neutral NO_x present in the feeding gas, and that *a*-MoS_x exhibits no activity towards ENRR in our working conditions.

To be noticed, *a*-MoS_x catalyzes the reduction of neutral NO_x only in presence of Nafion binder in KPi-7 group, which demonstrated that specific formulation of the catalyst composite could change the activity of the materials. However, this time, the rich density of defects in *a*-MoS_x did not provide it catalytic activity towards ENRR in our standardized conditions, which must prompted us to reevaluate the general importance of this parameter for the design of efficient ENRR catalysts based on molybdenum sulfide materials.

2.4. Other MoS_x derivatives

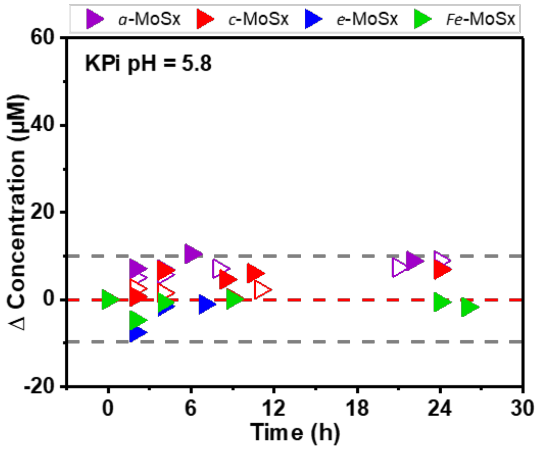

Figure 2.13: *Evolution of the apparent concentration of NH_3 in the electrolyte during potential-controlled electrolysis in purified N_2-saturated 0.1 M KPi buffer (pH = 5.8) Nafion-coated a-MoS_x, c-MoS_x and, Fe-MoS_x films deposited on glassy carbon electrodes. The e-MoS_x was prepared directly from electrodeposition. The working electrode was polarized at –0.3 V vs. RHE.*

Besides the presumably beneficial effect of the presence of abundant surface sulfur vacancies, doping molybdenum sulfides derivatives with transition metals has been highlighted as a second avenue to improve the ENRR activity of these materials.[7] In order to test both factors in a consistent experimental framework, we applied our standardized conditions on different molybdenum sulfides prepared *in house*, including: nanocrystalline molybdenum sulfide (*c*-MoS_x), amorphous molybdenum sulfide doped with Fe (4-9%) (*Fe*-MoS_x), as well as electrodeposited amorphrous MoS_x with a comparable Mo quantity to *a*-MoS_x (*e*-MoS_x) (***Figure 2.13,*** see detailed preparation in S2.2.3). Once again, after elimination of all NO_x contaminants, none of these materials presented any apparent catalytic activity towards N_2 reduction in our working conditions, in strong contrast with several reports presenting in the literature.[17,27]

2.5 Conclusion

In this section, we investigated the ENRR activity of *a*-MoS_x using a rigorous protocol including systematic blanks studies and precise quantification of the evolution of the NH_3 over long experimental time. A feeble electro-driven ammonia release was observed for a 24 h controlled electrolysis at –0.3 V vs. RHE on Nafion-coated *a*-MoS_x films deposited on glassy carbon electrodes in 0.1 M KPi buffer (pH = 5.8, KPi-7). We attempted to enhance the NH_3 production rate by removing the possible phosphate ligand or increasing the mass ratio of Nafion binder, which were unsuccessful. Finally we proved that the apparent activity of *a*-MoS_x for ENRR originated from the reduction of trace amounts of neutral NO_x present in the N_2 feeding gas.[33] Inspired by the variety MoS_x-based materials reported as active catalysts for ENRR we further investigated nanocrystalline MoS_2, electrochemically deposited MoS_x, or Fe doped MoS_x materials prepared in our group. In our standardized condition, none of them showed any catalytic activity towards ENRR, which indicates that we have not yet found the essential parameters required for developing efficient ENRR catalyst materials. Considering the issues recently raised for other families of catalysts,[28] a careful reevaluation of the activity of molybdenum sulfides for NRR appears timely to rationalize the apparent discrepancy found between studies present in the literature.

Appendix

S2.1 References for *Table 2.1*

*1 X. Sun et al., Adv. Energy Mater. 2018, **8**, 1801357*

*2 X. Sun et al., Adv. Mater. 2018, **30**, 18000191*

*3 H. Zhao et al., Adv. Energy Mater 2019, **9**, 1803935*

*4 D.R. MacFarlane et al., ACS Energy Lett. 2019, **4**, 430*

*5 J. Zhang et al., Electrochemica acta 2019, **371**, 34*

*6 D. Wu et al., J. Mater. Chem. A, 2019, **7**, 2524*

*7 A. Cheng et al., Chem. Commun. 2019, **55**, 7386*

*8 J. Lou et al, J. Am. Chem. Soc. 2019, **141**, 19269*

9 X. Quian et al., Chin Chem. Lett. 2020, doi.org/10.1016/j.cclet.2020.02.019

*10 H. Zhang et al., ACS Sustainable Chem. Eng. 2020, **8**, 2320*

*11 J. Ma et al., ACS Sustainable Chem. Eng. 2020, **8**, 8814*

*12 M. Shao et al., Appl. Cat. B: Environmental 2020, **272**, 118984*

*13 J. Tian et al., ACS Appl. Mater. Interfaces 2020, **12**, 26060*

*14 W. Liu, et al., J. Energy Chem. 2021, **53**, 132*

*15 J. K. Chu, et al., ACS Sustainable Chem. Eng. 2020, **8,** 12733*

S2.2 Materials & Equipments

S2.2.1 Materials

Potassium persulfate, ammonium tetrathiomolybdate, ethanol, carbon disulfide, diethyl ether, concentrated aqueous hydrochloric acid (37%), dibasic potassium phosphate, potassium dihydrogen phosphate, hydroxylamine, salicylic acid, sodium nitroprusside dihydrate, sodium hydroxide, citric acid, diluted aqueous sodium hypochlorite solution (~10-15%), 4-(dimethylamino)benzaldehyde, hydrazine monohydrate, sodium nitrite, sulfanilamide (SULF) acidic nitrite, n-(1-naphthyl)ethylenediamine (NED) were purchased from Aldrich. All reagents were ACS reagent grade and used as received. 0.1 M aqueous ammonia standard solution (NH_3, H4001-01) and alkaline ionic strength adjuster buffer (ISA, H4014-00) were obtained from Hanna Instruments. Milli-Q water (H_2O) was purified through a Millipore system. N_2 (99.998%) or Ar (99.9999%) were purchased from Air Products and used without additional purification, unless otherwise stated.

S2.2.2 Equipment

The electrochemical studies were conducted on a Biologic SP-300 workstation. The electrochemical cell (BMM-EC 15 mL), glassy carbon working electrodes (GC 25/25/ CUSTOM, 1 mm or 3 mm) and Ag/AgCl/3M reference electrode (Ag/AgCl 70mm) were obtained from Redox-me. The flow of the feeding gas was controlled using Bronkhorst EL-FLOW mass-flow meters. The GC working electrodes were polished using a Struers LaboPol-1 polishing machine. The catalytic ink suspensions were homogenized in a Bandelin Sonorex sonication bath. The Ammonia selective electrode (HI4101/Hanna Instruments,) was connected to a Mettler Toledo (FiveEasy-FE20) pH meter. UV-Visible spectra were recorded on a Shimadzu UV-1800 UV spectrophotometer using the dual beam mode. Hydrogen was quantified using a Micro Gas Chromatograph S3000 (SRA Instruments) with a diamond LV Ms5A 14m module which was operated via the Soprane chrome interface

S2.2.3 Catalyst material preparation

Amorphous molybdenum sulfide preparation[25]

Amorphous molybdenum sulfide can be obtained using several methods. In this work we applied two of them:

1) Chemical oxidation of thiomolybdate using strong oxidizing agent (e.g. sodium persulfate, $Na_2S_2O_8$) The material obtained by this method is referred to as *a*-MoS_x in this work.

2) Electrochemical deposition from thiomolybdate solution by applying a constant cathodic potential or by repeating potential cycle. The later is referred to as *e*-MoS_x.

Chemical synthesis of amorphous molybdenum sulfide (a-MoS_x)

1.3 g of ammonium tetrathiomolybdate $[MoS_4](NH_4)_2$ was firstly dissolved in 250 mL Milli-Q water to form a deep-red solution and then 2.7 g $K_2S_2O_8$ was added, the mixture was stirred in a closed round-bottomed flask in Ar for 3 hours resulting in the formation of a dark brown suspension. The product was collected and then washed by centrifugation with 3 x 15 mL Milli-Q water; 3 x 15 mL ethanol; 3 x 15 mL carbon disulfide; 3 x 15 mL diethyl ether. The obtained black solid was then dried by natural evaporation under dried under an Ar stream and kept under an Ar atmosphere. The powder was stored under Ar and used for subsequent reactions without further purification.[25]

Electrochemical synthesis of amorphous molybdenum sulfide (e-MoS_x)

e-MoS_x thin films were directly grown on 1 cm^{-2} glassy carbon disk electrodes at anodic potentials of 0.5 V versus RHE in a deposition bath consisting of 1.0 mM $[MoS_4](NH_4)_2$ in degassed pH 7 phosphate buffer. During deposition, the solution was constantly purged with Ar. The total density of charges of 193 mC cm^{-2} was passed through the working electrode, resulting in the deposition of 1×10^{-6} $mol_{\text{Mo catalyst}}$ to obtain the equivalent Mo loading to the deposition of 0.3 mg *a*-MoS_x.cm^{-2}. When the resulting film was formed, it was thoroughly washed with water and ethanol, then dried in air.[25]

Crystalline molybdenum sulfide (c-MoS_x)

130 mg *c*-MoS_x were prepared as monocrystalline solid in our group via a thermally assisted synthesis.[43] 1.8 mmol 492 mg of $MoCl_5$ and 5.4 mmol 412 mg of thiourea precursors were dispersed in 20 mL ethanol under magnetic stirring. After solvent evaporation, the resulting powder was transferred to an alumina boat, inserted into a

quartz tube, and heated at 5 °C·min^{-1} up to 550 °C in a flowing atmosphere (Ar or Ar + H_2), held at this temperature for 2 h, and then allowed to cool down to room temperature.

Fe doped amorphous molybdenum sulfide (Fe-MoS$_x$)

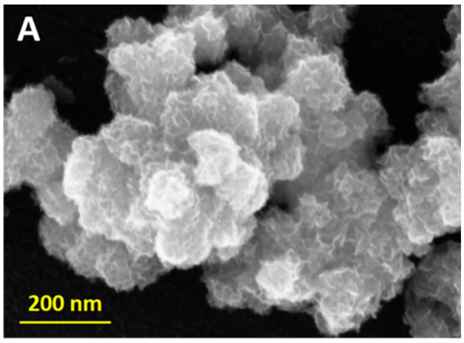

Figure S2.1: *Scanning electron microscopy (SEM) images were recorded with a scanning electron microscope Zeiss Ultra 55 (acceleration tension 5 kV) of Fe-*MoS$_x$.

Fe-MoS$_x$ were synthesized through one-step reaction between metal salts precursors and thiourea in ethylene glycol (EG) under microwave irradiation. The molar ratio of the reagents were $MoCl_3$: $FeCl_x$: thiourea = 1:1:3. Precursors were added in 10 mL of EG in a vial of 30 mL and stirred for 5 min. Then the vial was placed in the microwave oven and the reaction was conducted under the following conditions: irradiation varying from 0 to 300 W in order to maintain the temperature at 255 °C leading to the pressure of 8 bars for 20 min. The black precipitate obtained is put in ethanol for centrifugation (10000 rpm, 1 h). The supernatant is removed and the precipitate is washed again repeatedly with ethanol and distilled water until the supernatant remains clear. The obtained solid is dried under vacuum overnight. [43]

S2.3 Experimental methods

S2.3.1 Working electrode preparation

The catalytic ink was typically prepared by sonicating 2 mg of catalyst materials (except *e*-MoS$_x$ prepared by electrodeposition) in 200 µL of isopropanol for 30 minutes to obtain a homogenous suspension. When needed, the Nafion ionomer was incorporated, 1 µL of a commercial Nafion solution at 5% (wt/v) was added to the mixture prior sonication. The working electrodes were prepared by drop-casting 3 x 10 µL of the ink on a freshly polished GC electrode (1 cm^2) and dried in air to obtain a loading of 0.3 mg catalyst materials (*e*-MoS$_x$ was prepared to have comparable quantity of Mo in *a*-MoS$_x$) per square centimeter. For WE coated only with Nafion, a similar protocol was followed without incorporating the *a*-MoS$_x$ in the Nafion/isopropyl alcohol solution.

S2.3.2 Control groups

HCl-1/KPi-1: continuously purging 10 mL of the selected electrolyte with N_2 (10 mL.min^{-1}) for 20 minutes (“t = 0”) to 25 hours

HCl-2/KPi-2: running a CA under the standard conditions on bare GC for up to 25 h

HCl-3/KPi-3: running a CA under the standard conditions on Nafion-coated GC for up to 25 h

HCl-4/KPi-4: continuously purging 10 mL of the electrolyte with N_2 (10 mL.min^{-1}) in the complete three-electrode configuration using 0.3 mg of Nafion coated *a*-MoS$_x$ on GC, for 20 minutes (“t = 0”) to 25 hours

HCl-5/KPi-5: running a CA under the standard conditions on 0.3 mg of Nafion coated *a*-MoS$_x$ on GC for up to 25 h under Ar

S2.3.3 Quantification method (Colorimetric titration)

S2.3.3.1 Salicylate Method (NH_3)

Reagent preparation and storage

The assay requires the preparation of three reagents.

Reagent ①: 9.5 g (68.8 mmol) of salicylic acid, 2.75 g (68.8 mmol) of sodium hydroxide and 7 mg (0.023 mmol) of sodium nitroprusside dihydrate are dissolved in 25 mL of water. This solution is stable at 5 °C, in the dark, for up to 3 months.

Reagent ②: 6.53 g (34.0 mmol) of citric acid and 5.85 g (146.3 mmol) of sodium hydroxide are dissolved in 100 mL of water. This solution is stable and can be stored several months without degradation.

Reagent ③: 0.5 mL of sodium hypochlorite solution (Commercial bleach~10-15% NaOCl) is added to 9.5 mL of ②. This solution must be prepared freshly, just before use.

Assays conditions

a) 0.1 M HCl electrolyte

The samples (1 mL) collected during the course of the control or NRR studies were split into 3 fractions of 0.3 mL, which were treated separately. Each fraction was first neutralized with the addition of 0.3 mL of aqueous 0.1 M NaOH. Next 80 µL of reagent ① was added and the mixture was homogenized, before the addition of 135 µL of reagent ③. The resulting samples were reacted in dark for 90 minutes before measuring the absorbance at 650 nm using UV-Visible spectroscopy.

b) 0.1 M KPi buffer

The samples (1 mL) collected during the course of the control or N_2RR studies were diluted by the addition 0.5 mL mQ water, then the solutions were split into 3 fractions of 0.5 mL, which were treated separately. Each fraction was directly mixed with 100 µL of reagent ① followed by the addition of 200 µL of reagent ③. The resulting samples were reacted in dark for 90 minutes before measuring the absorbance at 650 nm using UV-Visible spectroscopy.

S2.3.3.2 Hydrazine (N_2H_4)

The determination of the concentration of hydrazine was done following the approach introduced by Watt and Chrisp.[3] This procedure is based on the quantification of a yellow dye resulting from acid catalyzed condensation of hydrazine with 4-(Dimethylamino)benzaldehyde and exhibiting a specific absorption band centered at 455 nm. The yellow color develops immediately and the absorbance measured at 455 nm stabilizes after 10 min. It remains stable for up to 12 h.[38]

Calibration curves and quantification of the ammonia concentration

To ensure accurate measurements, the limit of detection and linearity range of the assay in our specific conditions were established from known dilutions of hydrazine hydrate standard solution in 0.1 M KPi (***Figure S2.2***). A good linearity ($R^2 = 0.997$) was obtained for concentrations of ammonia comprised between 0.005 mM and 0.5 mM.

For this assay, each sample (0.5 mL) collected during the electrolysis was diluted by the addition of 1 mL of a 1 M HCl solution, and divided in three samples of 0.5 mL which are then treated independently. The concentration of hydrazine reported for each sample corresponds to the mean value calculated form these measurements.

Reagent preparation and storage

The color reagent was prepared by adding 0.2 g 4-(Dimethylamino)benzaldehyde (1.34 mmol) and 1 mL concentrated hydrochloric acid (37%) into 10 mL Ethanol.

Assay conditions

0.1 M HCl electrolyte/ 0.1 M KPi buffer

The sample (0.5 mL) collected during the electrolysis are diluted by the addition of 1 mL 1 M HCl solution, then divided into three parts. Each 0.5 mL sample is mixed with 0.5 mL of the color reagent then reacted for 20 min before measuring the absorbance at 455 nm using UV-Visible spectroscopy.

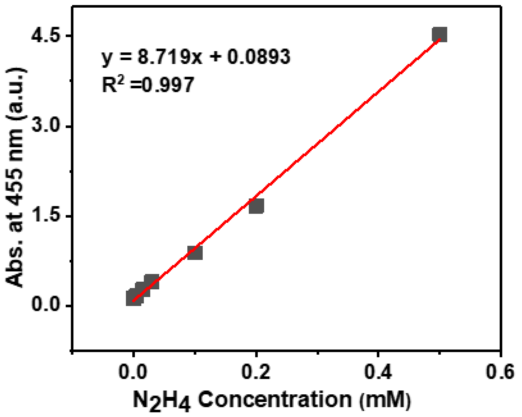

Figure S2.2: *Calibration curve for the determination the concentration of hydrazine using Watt and Chrisp method in 0.1 M KPi, using 0.005 mM, 0.015 mM, 0.03 mM, 0.1 mM, 0.2*

S2.3.3.3 Nitrite and nitrate (NO_2^-, NO_3^-)

The determination of the concentration of adventitious NO_x contaminants possibly present in the electrolyte, and susceptible to lead to the accumulation of ammonia under reductive conditions, was investigated via the method proposed by Griess *and coll.*(Griess 1879a) The procedure is based on the spectrophotometric quantification of an azo dye formed upon reaction of the *in situ* generated diazonium salt of the sulfanilamide (SULF) on n-(1-naphthyl)ethylenediamine (NED), which exhibits a specific absorption band centered at 540 nm. The nitrate (NO_3^-) is firstly reduced to nitrite (NO_2^-) by vanadium (III). Importantly we optimized the reaction time protocol to increase the sensitivity of the method for our specific conditions and ensure reliable measurements.

Calibration curves and quantification of the NO_x^-concentration

To ensure accurate measurements, the limit of detection and linearity range of the assay in our specific conditions were established from known dilutions of $NaNO_2$ / KNO_3 standard solutions in 0.1 M KPi (***Figure S2.3***).

Good linearity (R^2 = 0.997) is observed for nitrite concentrations between 0.001 mM and 0.1 mM (***Figure S2.3***, left). In the case of nitrate (***Figure S2.3***, right*)* a linear region (R^2 = 0.997) is obtained for concentrations between 0.001 mM and 0.1 mM.

Reagent preparation and storage

SULF (2% w/v in 5% HCl): 10 mL of concentrated HCl solution (37%) are firstly diluted in 64 mL of H_2O to obtain a 5% HCl solution. 1.48 g (8.6 mmol) of sulfanilamide are dissolved in the previous HCl solution. This solution is stable at 5 °C, in the dark, for up to several months.

NED (0.1% w/v in H_2O): 30 mg of n-(1-naphthyl)ethylenediamine (0.1 mmol) are dissolved in 30 mL H_2O. This solution is stable at 5 °C, in the dark, for up to several months.

Vanadium solution: 40 mg (0.2 mmol) of vanadium (III) chloride are dissolved in 5 mL 1M HCl solution. This solution is stable at 5 °C, in the dark, for less than 2 weeks.

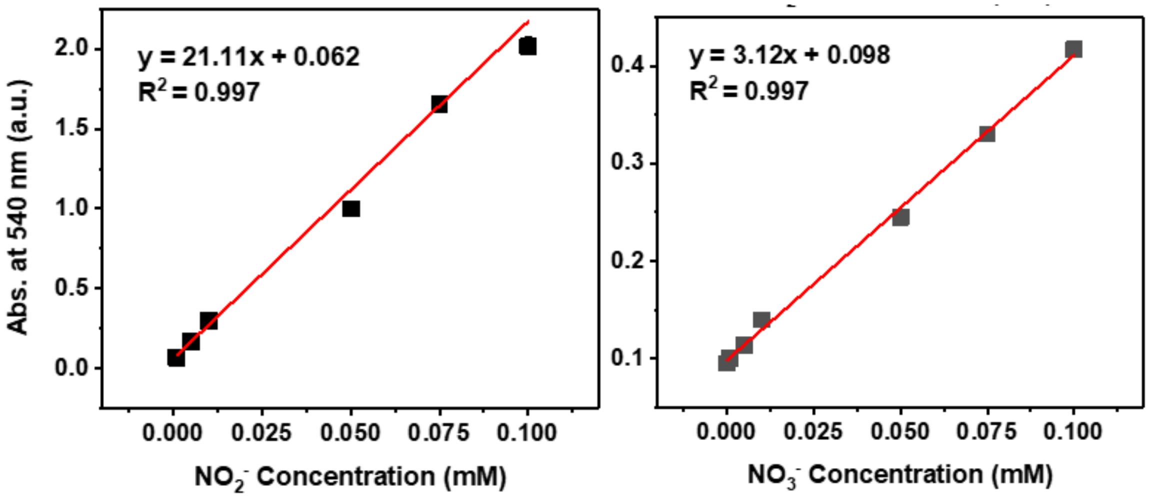

Figure S2.3: *Typical calibration curves used for the determination of the concentration of nitrite (a) and nitrate (b) ions using the Griess assay.*

Assay conditions

0.1 M HCl electrolyte/ 0.1 M KPi buffer

200 µL of the electrolyte is mixed with 200 µL of 1M HCl solution (or 200 µL of the Vanadium solution for NO_3^- titration, in which case the mixture is reacted 20 minutes before the next step). 100 µL SULF is then added followed by the addition of 100 µL of NED. The resulting samples are reacted in dark for 60 minutes before measuring the absorbance at 540 nm using UV-Visible spectroscopy.

The concentration of KPi buffer has a limited influence on the absorbance at 540 nm for the Griess assay between 0 M and 0.2 M as showed in ***Table S2.2***.

Table S2.2: *Influence of KPi concentration on Griess Assay. 0.001mM NO_3^- samples were prepared in different KPi buffer with concentration 0, 0.1, 0.2 M.*

Concentration of KPi (M)	Abs. at 540 nm (a.u.)	S
0	0.10701	0.01167
0.1	0.12039	0.01936
0.2	0.12254	0.01129

s standard deviation (*vide infra*)

Table S2.3: *Dispersion of the variation of the background ammonia concentrations measured for control series HCl-1/KPi-1 – HCl-5/KPi-5 with respect to t = 0. Bin size: 2 µM, the values indicated in red correspond to punctual variation higher than 10 µM with respect to time zero.*

HCl-1 – HCl-5			KPi-1 – KPi-5		
Bin Center	Count	Cumulative Count	Bin Center	Count	Cumulative Count
-9	1	1	-17	1	1
-7	1	2	-15	0	1
-5	3	5	-13	0	1
-3	3	8	-11	0	1
-1	11	19	-9	1	2
1	7	26	-7	2	4
3	5	31	-5	2	6
5	6	37	-3	7	13
7	3	40	-1	3	16
9	2	42	1	8	24
11	2	44	3	5	29
			5	1	30

References

(1) Wang, D.; Azofra, L. M.; Harb, M.; Cavallo, L.; Zhang, X.; Suryanto, B. H. R.; MacFarlane, D. R. Energy-Efficient Nitrogen Reduction to Ammonia at Low Overpotential in Aqueous Electrolyte under Ambient Conditions. *ChemSusChem* **2018**, *11* (19), 3416–3422.

(2) Li, R.; Wei, Z.; Gou, X. Nitrogen and Phosphorus Dual-Doped Graphene/Carbon Nanosheets as Bifunctional Electrocatalysts for Oxygen Reduction and Evolution. *ACS Catal.* **2015**, *5* (7), 4133–4142.

(3) Wang, T.; Xia, L.; Yang, J.-J.; Wang, H.; Fang, W.-H.; Chen, H.; Tang, D.; Asiri, A. M.; Luo, Y.; Cui, G.; Sun, X. Electrocatalytic N2-to-NH3 Conversion Using Oxygen-Doped Graphene: Experimental and Theoretical Studies. *Chem. Commun.* **2019**, *55* (52), 7502–7505.

(4) Seefeldt, L. C.; Yang, Z.-Y.; Lukoyanov, D. A.; Harris, D. F.; Dean, D. R.; Raugei, S.; Hoffman, B. M. Reduction of Substrates by Nitrogenases. *Chem. Rev.* **2020**.

(5) Tanaka Koji; Hozumi Yoshiyuki; Tanaka Toshio. DINITROGEN FIXATION CATALYZED BY THE REDUCED SPECIES OF [Fe4S4(SPh)4]2− AND [Mo2Fe6S8(SPh)9]3−. *Chem. Lett.* **1982**, *11* (8), 1203–1206.

(6) Banerjee, A.; Yuhas, B. D.; Margulies, E. A.; Zhang, Y.; Shim, Y.; Wasielewski, M. R.; Kanatzidis, M. G. Photochemical Nitrogen Conversion to Ammonia in Ambient Conditions with FeMoS-Chalcogels. *J. Am. Chem. Soc.* **2015**, *137* (5), 2030–2034.

(7) Liu, J.; Kelley, M. S.; Wu, W.; Banerjee, A.; Douvalis, A. P.; Wu, J.; Zhang, Y.; Schatz, G. C.; Kanatzidis, M. G. Nitrogenase-Mimic Iron-Containing Chalcogels for Photochemical Reduction of Dinitrogen to Ammonia. *Proc. Natl. Acad. Sci.* **2016**, *113* (20), 5530–5535.

(8) Theerthagiri, J.; Senthil, R. A.; Senthilkumar, B.; Reddy Polu, A.; Madhavan, J.; Ashokkumar, M. Recent Advances in MoS2 Nanostructured Materials for Energy and Environmental Applications – A Review. *J. Solid State Chem.* **2017**, *252*, 43–71.

(9) Benck, J. D.; Hellstern, T. R.; Kibsgaard, J.; Chakthranont, P.; Jaramillo, T. F. Catalyzing the Hydrogen Evolution Reaction (HER) with Molybdenum Sulfide Nanomaterials. *ACS Catal.* **2014**, *4* (11), 3957–3971.

(10) Dave, M.; Rajagopal, A.; Damm-Ruttensperger, M.; Schwarz, B.; Nägele, F.; Daccache, L.; Fantauzzi, D.; Jacob, T.; Streb, C. Understanding Homogeneous Hydrogen Evolution Reactivity and Deactivation Pathways of Molecular Molybdenum Sulfide Catalysts. *Sustain. Energy Fuels* **2018**, *2* (5), 1020–1026.

(11) Amiinu, I. S.; Pu, Z.; Liu, X.; Owusu, K. A.; Monestel, H. G. R.; Boakye, F. O.; Zhang, H.; Mu, S. Multifunctional Mo–N/C@ MoS2 Electrocatalysts for HER, OER, ORR, and Zn–air Batteries. *Adv. Funct. Mater.* **2017**, *27* (44), 1702300.

(12) Doan, P. E.; Telser, J.; Barney, B. M.; Igarashi, R. Y.; Dean, D. R.; Seefeldt, L. C.; Hoffman, B. M. 57Fe ENDOR Spectroscopy and ‘Electron Inventory’Analysis of the Nitrogenase E4 Intermediate Suggest the Metal-Ion Core of FeMo-Cofactor Cycles through Only One Redox Couple. *J. Am. Chem. Soc.* **2011**, *133* (43), 17329–17340.

(13) Azofra, L. M.; Sun, C.; Cavallo, L.; MacFarlane, D. R. Feasibility of N2 Binding and Reduction to Ammonia on Fe-Deposited MoS2 2D Sheets: A DFT Study. *Chem. – Eur. J.* **2017**, *23* (34), 8275–8279.

(14) Guo, H.; Li, L.; Wang, X.; Yao, G.; Yu, H.; Tian, Z.; Li, B.; Chen, L. Theoretical Investigation on The Single Transition Metal Atom Decorated Defective MoS2 for Electrocatalytic Ammonia Synthesis. *ACS Appl. Mater. Interfaces* **2019**.

(15) Zhao, J.; Zhao, J.; Cai, Q. Single Transition Metal Atom Embedded into a MoS2 Nanosheet as a Promising Catalyst for Electrochemical Ammonia Synthesis. *Phys. Chem. Chem. Phys.* **2018**, *20* (14), 9248–9255.

(16) Zhang, L.; Ji, X.; Ren, X.; Ma, Y.; Shi, X.; Tian, Z.; Asiri, A. M.; Chen, L.; Tang, B.; Sun, X. Electrochemical Ammonia Synthesis via Nitrogen Reduction Reaction on a MoS2 Catalyst: Theoretical and Experimental Studies. *Adv. Mater.* **2018**, *30* (28), 1800191.

(17) Li, X.; Li, T.; Ma, Y.; Wei, Q.; Qiu, W.; Guo, H.; Shi, X.; Zhang, P.; Asiri, A. M.; Chen, L.; Tang, B.; Sun, X. Boosted Electrocatalytic N2 Reduction to NH3 by Defect-Rich MoS2 Nanoflower. *Adv. Energy Mater.* **2018**, *8* (30), 1801357.

(18) Li, X.; Ren, X.; Liu, X.; Zhao, J.; Sun, X.; Zhang, Y.; Kuang, X.; Yan, T.; Wei, Q.; Wu, D. A MoS2 Nanosheet–reduced Graphene Oxide Hybrid: An Efficient Electrocatalyst for Electrocatalytic N2 Reduction to NH3 under Ambient Conditions. *J. Mater. Chem. A* **2019**, *7* (6), 2524–2528.

(19) Liu, Y.; Han, M.; Xiong, Q.; Zhang, S.; Zhao, C.; Gong, W.; Wang, G.; Zhang, H.; Zhao, H. Dramatically Enhanced Ambient Ammonia Electrosynthesis Performance by In-Operando Created Li–S Interactions on MoS2 Electrocatalyst. *Adv. Energy Mater.* **2019**, *9* (14), 1803935.

(20) Zeng, L.; Chen, S.; van der Zalm, J.; Li, X.; Chen, A. Sulfur Vacancy-Rich N-Doped MoS2 Nanoflowers for Highly Boosting Electrocatalytic N2 Fixation to NH3 under Ambient Conditions. *Chem. Commun.* **2019**, *55* (51), 7386–7389.

(21) Zhang, J.; Tian, X.; Liu, M.; Guo, H.; Zhou, J.; Fang, Q.; Liu, Z.; Wu, Q.; Lou, J. Cobalt-Modulated Molybdenum–Dinitrogen Interaction in MoS2 for Catalyzing Ammonia Synthesis. *J. Am. Chem. Soc.* **2019**, *141* (49), 19269–19275.

(22) Guo, J.; Tadesse Tsega, T.; Ul Islam, I.; Iqbal, A.; Zai, J.; Qian, X. Fe Doping Promoted Electrocatalytic N2 Reduction Reaction of 2H MoS2. *Chin. Chem. Lett.* **2020**.

(23) Liu, Y.; Wang, W.; Zhang, S.; Li, W.; Wang, G.; Zhang, Y.; Han, M.; Zhang, H. MoS2 Nanodots Anchored on Reduced Graphene Oxide for Efficient N2 Fixation to NH3. *ACS Sustain. Chem. Eng.* **2020**, *8* (5), 2320–2326.

(24) Ting, L. R. L.; Deng, Y.; Ma, L.; Zhang, Y.-J.; Peterson, A. A.; Yeo, B. S. Catalytic Activities of Sulfur Atoms in Amorphous Molybdenum Sulfide for the Electrochemical Hydrogen Evolution Reaction. *ACS Catal.* **2016**, *6* (2), 861–867.

(25) Tran, P. D.; Tran, T. V.; Orio, M.; Torelli, S.; Truong, Q. D.; Nayuki, K.; Sasaki, Y.; Chiam, S. Y.; Yi, R.; Honma, I.; Barber, J.; Artero, V. Coordination Polymer Structure and Revisited Hydrogen Evolution Catalytic Mechanism for Amorphous Molybdenum Sulfide. *Nat. Mater.* **2016**, *15* (6), 640–646.

(26) Xi, F.; Bogdanoff, P.; Harbauer, K.; Plate, P.; Höhn, C.; Rappich, J.; Wang, B.; Han, X.; van de Krol, R.; Fiechter, S. Structural Transformation Identification of Sputtered Amorphous MoSx as an Efficient Hydrogen-Evolving Catalyst during Electrochemical Activation. *ACS Catal.* **2019**, *9* (3), 2368–2380.

(27) Chu, K.; Nan, H.; Li, Q.; Guo, Y.; Tian, Y.; Liu, W. Amorphous MoS3 Enriched with Sulfur Vacancies for Efficient Electrocatalytic Nitrogen Reduction. *J. Energy Chem.* **2021**, *53*, 132–138.

(28) Andersen, S. Z.; Čolić, V.; Yang, S.; Schwalbe, J. A.; Nielander, A. C.; McEnaney, J. M.; Enemark-Rasmussen, K.; Baker, J. G.; Singh, A. R.; Rohr, B. A.; Statt, M. J.; Blair, S. J.; Mezzavilla, S.; Kibsgaard, J.; Vesborg, P. C. K.; Cargnello, M.; Bent, S. F.; Jaramillo, T. F.; Stephens, I. E. L.; Nørskov, J. K.; Chorkendorff, I. A Rigorous Electrochemical Ammonia Synthesis Protocol with Quantitative Isotope Measurements. *Nature* **2019**, *570* (7762), 504–508.

(29) Zhao, Y.; Wu, F.; Miao, Y.; Zhou, C.; Xu, N.; Shi, R.; Wu, L.-Z.; Tang, J.; Zhang, T. Revealing Ammonia Quantification Minefield in Photo/Electrocatalysis. *Angew. Chem. Int. Ed.* **2021**, *60* (40), 21728–21731.

(30) Walker, J.; Nelson, D.; Aneja, V. P. Trends in Ammonium Concentration in Precipitation and Atmospheric Ammonia Emissions at a Coastal Plain Site in North Carolina, U.S.A. *Environ. Sci. Technol.* **2000**, *34* (17), 3527–3534.

(31) Schlesinger, W. H.; Hartley, A. E. A Global Budget for Atmospheric NH3. *Biogeochemistry* **1992**, *15* (3), 191–211.

(32) Turner, C.; Španěl, P.; Smith, D. A Longitudinal Study of Ammonia, Acetone and Propanol in the Exhaled Breath of 30 Subjects Using Selected Ion Flow Tube Mass Spectrometry, SIFT-MS. *Physiol. Meas.* **2006**, *27* (4), 321–337.

(33) Dabundo, R.; Lehmann, M. F.; Treibergs, L.; Tobias, C. R.; Altabet, M. A.; Moisander, P. H.; Granger, J. The Contamination of Commercial 15N2 Gas Stocks with 15N–Labeled Nitrate and Ammonium and Consequences for Nitrogen Fixation Measurements. *PLOS ONE* **2014**, *9* (10), e110335.

(34) Choi, J.; Du, H.-L.; Nguyen, C. K.; Suryanto, B. H. R.; Simonov, A. N.; MacFarlane, D. R. Electroreduction of Nitrates, Nitrites, and Gaseous Nitrogen Oxides: A Potential Source of Ammonia in Dinitrogen Reduction Studies. *ACS Energy Lett.* **2020**, *5* (6), 2095–2097.

(35) Suryanto, B. H. R.; Du, H.-L.; Wang, D.; Chen, J.; Simonov, A. N.; MacFarlane, D. R. Challenges and Prospects in the Catalysis of Electroreduction of Nitrogen to Ammonia. *Nat. Catal.* **2019**, *2* (4), 290–296..

(36) Kertes, A. *Solubility Data Series*; Pergamon Press Oxford, 1979; Vol. 37.

(37) Bower, C. E.; Holm-Hansen, T. A Salicylate–Hypochlorite Method for Determining Ammonia in Seawater. *Can. J. Fish. Aquat. Sci.* **1980**, *37* (5), 794–798.

(38) Watt, G. W.; Chrisp, J. D. Spectrophotometric Method for Determination of Hydrazine. *Anal. Chem.* **1952**, *24* (12), 2006–2008.

(39) Weber, T.; Muijsers, J.; Niemantsverdriet, J. Structure of Amorphous MoS3. *J. Phys. Chem.* **1995**, *99* (22), 9194–9200.

(40) Griess, P. Bemerkungen Zu Der Abhandlung Der HH. Weselsky Und Benedikt „Ueber Einige Azoverbindungen". *Berichte Dtsch. Chem. Ges.* **1879**, *12* (1), 426–428.

(41) Liu, H.; Zhang, Y.; Luo, J. The Removal of Inevitable NOx Species in Catalysts and the Selection of Appropriate Membrane for Measuring Electrocatalytic Ammonia Synthesis Accurately. *J. Energy Chem.* **2020**, *49*, 51–58.

(42) Guo, J.; Tadesse Tsega, T.; Ul Islam, I.; Iqbal, A.; Zai, J.; Qian, X. Fe Doping Promoted Electrocatalytic N2 Reduction Reaction of 2H MoS2. *Chin. Chem. Lett.* **2020**.

(43) Morozan, A.; Johnson, H.; Roiron, C.; Genay, G.; Aldakov, D.; Ghedjatti, A.; Nguyen, C. T.; Tran, P. D.; Kinge, S.; Artero, V. Nonprecious Bimetallic Iron–Molybdenum Sulfide Electrocatalysts for the Hydrogen Evolution Reaction in Proton Exchange Membrane Electrolyzers. *ACS Catal.* **2020**, *10* (24), 14336–14348.

3. Electrochemical azide reduction reaction (EN_3RR)

In section 2, we demonstrated that the MoS_x derivatives tested do not present significant reactivity towards N_2 in aqueous electrolytes under reductive conditions. However, probing and understanding their reactivity towards other N-containing substrates, may provide valuable insights for the long end goal of rational designing systems able to promote the direct activation of N_2.

Under non-physiological turnover conditions, nitrogenases exhibit catalytic activity towards the reduction of some nitrogenous substrates other than N_2, leading to the release of NH_3, [1,2] such as hydrazine (N_2H_4), hydroxylamine (NH_2OH), nitrate (NO_3^-), nitrite (NO_2^-), and azide (N_3^-). The reduction of these substrates to NH_3 occurs at more anodic potentials than N_2, that is, these reactions are easier than NRR from a thermodynamic standpoint. [4–6] The latter substrates, thus, appear as interesting references for probing alternative electro-driven processes potentially leading to the release of NH_3 by molybdenum sulfide derivatives, and characterizing plausible intermediates of a putative ENRR scheme.

Two types of MoS_x were studied in this section. Besides the heterogeneous crystalline or amorphous derivatives used in section 2, we also considered molecular $\{Mo_3S_x\}$ clusters (i.e. $[Mo_3S_7Br_6](NBu_4)_2$ and $[Mo_3S_{13}](NH_4)_2$). The investigation of $\{Mo_3S_x\}$ clusters could provide useful molecular models to understand the mechanism of small molecules activation on molybdenum sulfides, especially NRR in our case.

3.1 Inorganic azide reduction on heterogeneous MoS_x

3.1.1 Reactivity screening of other N-containing substrates

The investigation of the electro driven reduction of hydrazine (N_2H_4), hydroxylamine (NH_2OH), nitrate (NO_3^-), nitrite (NO_2^-), and azide (N_3^-) substrates was first tested under potential-controlled electrolysis on pristine *a*-MoS_x films (loading 0.5 mg.cm^{-2} on 0.02 cm^2 GC electrode), in argon-saturated 0.1 M KPi electrolyte (pH = 5.8) with an applied potential of –0.2 V *vs*. RHE (***Figure 3.1***).

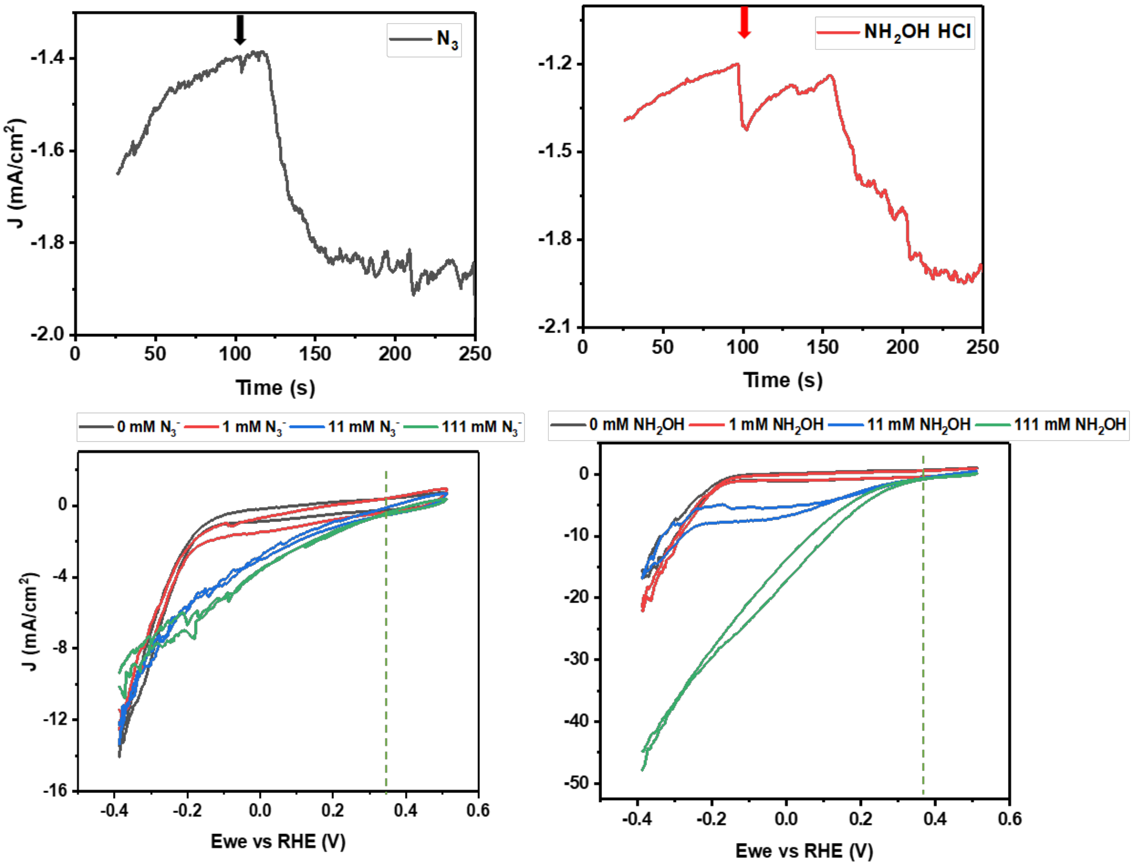

Figure 3.1: *Evolution of the current density recorded during the potential-controlled electrolysis of 2 mL 0.1 M KPi (pH = 5.8) on a thin film of a-MoSx poised at –0.2 V vs. RHE. The arrow indicates the addition of 20 µL of a 1 M sodium azide solution (top left, t = 100 s) or 1 M hydroxylamine hydrochloride solution (top right, t = 100 s). Cyclic voltammograms recorded from –0.4 V to 0.6 V vs. RHE, with an increasing concentration of sodium azide (bottom left, on-set potential 0.36V vs. NHE) or hydroxylamine hydrochloride (bottom right, on-set potential 0.38V vs. NHE) in 0.1 M KPi (pH = 5.8). Scan rate 2 mV/s.*

During the initial screening, only the addition of hydroxylamine hydrochloride and sodium azide (NaN_3) aliquots resulted in a significant increase of current density and a clear accumulation of ammonia in the electrolyte. From cyclic voltammetry (CV) measurements, the onset potentials of the catalytic processes can be estimated at 0.38 V and 0.36 V *vs*. RHE for the reduction of NH_2OH and N_3^- respectively (***Figure 3.1***). Unfortunately, NH_2OH interfered with the salicylate assay, impeding the accurate quantification of NH_3 produced during the electrolysis. Such issues were not faced with azide, which allowed us to investigate the activity of *a*-MoS_x for its reduction in more details.

Despite the rich reactivity known for azido ligands in transition metal complexes,[7]only a limited number of studies have been focusing on the direct electrochemical reduction of inorganic azides. Among the notable studies, Bayachou *et al*. have investigated the catalytic activity of self-assembled films of myoglobin (Mb) and dimethyldidodecylammonium bromide (ddab) formed on graphite electrodes.[8] They demonstrated that these Heme proteins are indeed able to drive the reduction of azide to ammonia at –1.1 V *vs*. SCE, through a three-proton two-electron process, reminiscent of the reduction of inorganic azide by the Nitrogenase:

$$N_2 + 3H^+ + 2e^- \xrightarrow[Mb/ddab]{} NH_3 + N_2$$

Exploring the reactivity of sodium azide on bulk metal electrodes in aqueous conditions (Na_2SO_4, pH 7), Dalmia *et al*. demonstrated that NaN_3 is reduced to N_2, hydrazine and possibly NH_3 on Pt electrodes at −1.2 V *vs.* RHE, when no reduction could be observed on gold electrodes.[9] This led the authors to postulate that that the adsorbed hydrogen atom on platinum surface (Pt-H) are the active species for the reduction of azide, which is in agreement with the known reactivity of several transition metal hydride complexes towards inorganic azide.[7]The lack of reactivity on gold electrodes, under cathodic conditions, was proposed to be related to the very low propensity of gold to lead to adsorbed hydrogen atoms. This hypothesis is interesting in the context of the reactivity observed for *a*-MoS_x, as that the highly favorable formation of surface molybdenum hydrides (Mo-H) on this material could also play a critical role in the reduction of inorganic azides as well.

3.1.2 Inorganic azide reduction on *a*-MoS_x

3.1.2.1 Electrochemical studies

Electrolyte selection & Working electrode (WE) preparation

To avoid a too strong competition with HER while ensuring the stability of *a*-MoS_x during the electrolysis (see section 2.2.1.1), we used 0.1 M potassium phosphate buffer (KPi, K_2HPO_4–KH_2PO_4 8.5–91.5; pH = 5.8) as the electrolyte for studying the EN_3RR. The working electrode preparation is the same as in chapter 2 for the ENRR study: a thin and homogenous film of *a*-MoS_x was prepared on a freshly polished GC electrode (1 cm^2) with a loading of 0.3 $mg.cm^{-2}$. No Nafion was added to the films for EN_3RR experiments.

Electrochemical measurements

Potential-controlled electrolysis were carried out in the three-electrode configuration using a single-compartmented cell (15 mL). A Pt wire isolated by a frit (P4) was used as counter electrode (CE), and an Ag/AgCl/3 M KCl electrode as reference electrode (RE). The potentials reported in this work are referenced *vs*. the Reversible Hydrogen Electrode (RHE) using the following relation: ***E (RHE) = E (applied) + E^0 (Ag/AgCl/3M KCl) + 0.059 x pH*** with pH equals 5.8 for 0.1 M KPi buffer.

The experiments were performed under ambient conditions (room temperature, atmospheric pressure), under a continuous flow of N_2 or Ar calibrated at 10 mL/min. During the course of the electrolysis, the WE was poised at –0.2 V *vs*. RHE (this potential was selected to avoid overloading of the potentiostat while allowing for a fairer comparison with the ENRR experiments that were typically run at –0.3 V *vs*. RHE). 1 mL samples of the electrolyte were taken at fixed times (0h, 2h, 4h…) and kept for the colorimetric quantification of NH_3. The initial volume of electrolyte introduced in the cell was 10 mL for each experiment.

Control series

During the course of the initial EN_3RR tests on *a*-MoS_x, the NH_3 concentration in the electrolyte increased rapidly well above the contamination range of ±10 µM defined as the background ammonia concentration in our experimental conditions (*cf.* chapter 2). Therefore, here, we only considered two control conditions (***Table 3.1***), to investigate the possibility of accumulating NH_3 due to: 1) direct EN_3RR on bare GC (control series N_3RR-1); 2) chemical N_3RR and/or release of NH_3 from the catalyst (control series N_3RR-2).

Table 3.1: Summary of the EN_3RR experiments groups tested in 0.1 M KPi buffer (pH = 5.8).

Series	***a*-MoS$_x$ loading** (mg/cm^2)	**solvent**	**Potential** (*vs.* RHE)	**Feeding gas**	**Time**
N_3RR-1	0	–	–0.2	Ar	4 h
N_3RR-2	0.3	200 µL IPA^a	O.C.P.^{b}	Ar	>6 h
N_3RR-3	0.3	200 µL IPA^a	–0.2	Ar	>6 h

IPA^a: isopropyl alcohol. O.C.P.^{b}: open circuit potential (full setup without connecting the potentiostat)

3.1.2.2 Results and discussion

A significant and steady increase of the concentration of ammonia was observed during the electrolysis of a 10 mM solution of sodium azide in 0.1 M KPi, at –0.2 V *vs.* RHE (***Figure 3.2***, series N_3RR-3). The ammonia concentration reached values (> 200 µM) well above the experimental background (± 10 µM) after 4h of electrolysis in each run, and we observed a quasi-linear relationship between the total charge passed through the films and the quantity of ammonia produced as shown on ***Figure 3.3*** (left).

During control experiments, we only observed a limited increase in NH_3 concentration (ca. 40 µM) in solution after a 4h-long electrolysis run under similar conditions on a bare glassy carbon electrode (***Figure 3.2***, series N_3RR-1). Furthermore, *a*-MoS$_x$ did not demonstrate any intrinsic chemical reactivity towards azide leading to the release of ammonia in the electrolyte at room temperature in the absence of an applied potential (***Figure 3.2***, series N_3RR-2). *a*-

MoS$_x$ thus, exhibits a clear activity for the electro-driven reduction of azide to ammonia. Nitrogenases catalyze the reduction of azide to ammonia via a two electron three proton process. The rate is around three times that of the reduction of N$_2$, while consuming electrons in similar rate,[7] which means that nitrogenases are also efficient catalysts for electro-N$_3$RR. [7]

Considering EN$_3$RR as an ideal two-electron reduction process in the case of *a*-MoS$_x$ as well, we can calculate an average Faradaic efficiency (FE) of ca 50 ± 10% for azide reduction with a production rate of 3.5 ± 1.8 mmol$_{NH3}$.h^{-1}mg$_{a\text{-MoSx}}$$^{-1}$.

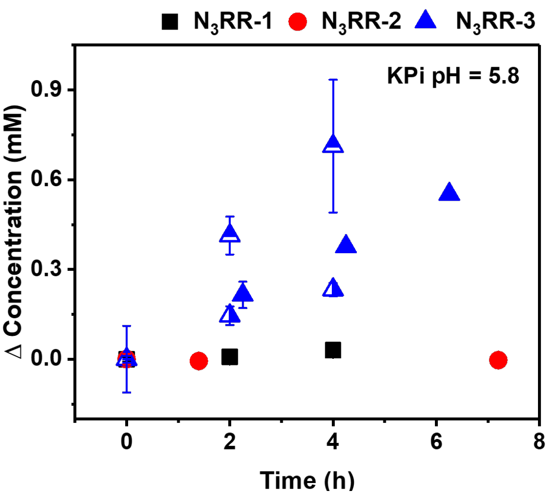

Figure 3.2: *Evolution of the concentration of NH$_3$ measured during potential-controlled electrolysis (–0.2 V vs. RHE) of a 10 mM solution of sodium azide in argon saturated 0.1 M KPi, over bare glassy carbon (N$_3$RR-1) or a-MoS$_x$ coated electrodes (N$_3$RR-3). Series N$_3$RR-2 (red dots) shows the evolution of the ammonia concentration measured in a 10 mM solution of sodium azide in 0.1 M KPi over time, in presence of an a-MoS$_x$ coated electrode in the absence of an applied potential.*

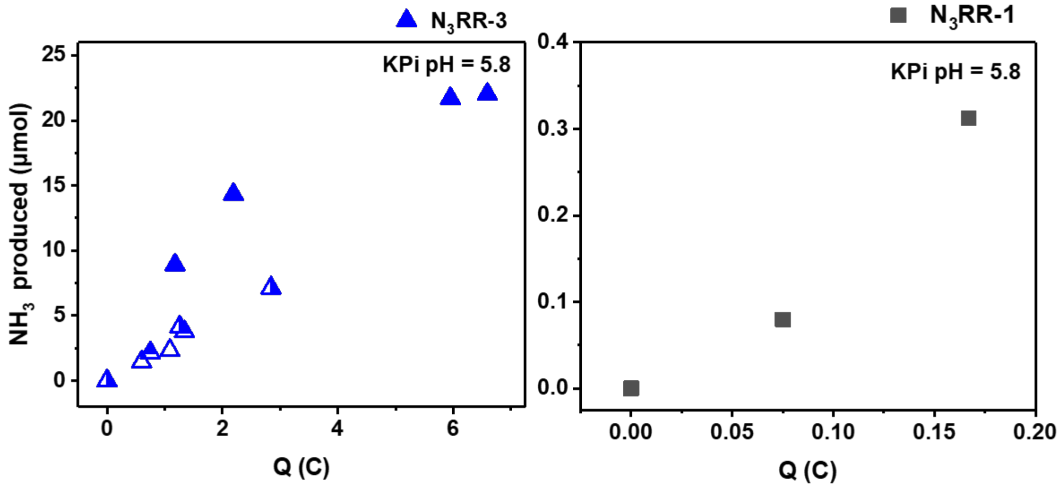

Figure 3.3: *Evolution of the quantity of ammonia produced as a function of the charge passed during the CA of pristine a-MoS$_x$ films (N$_3$RR-3, left) or bare GC (N$_3$RR-1, right) in the presence of 10 mM of NaN$_3$, in 0.1 M KPi electrolyte (pH = 5.8), potential applied –0.2V vs. RHE. The distinct filling patterns within series indicates measurements executed on samples collected from independent runs.*

Since *a*-MoS$_x$ is an excellent catalyst for HER, the competition between EN$_3$RR and HER could be an explanation for the limited FE observed here. The competitive production of hydrogen in these conditions was confirmed using gas chromatography analysis. For this, a pristine film of *a*-MoS_x was polarized at –0.2 V *vs.* RHE for 6h, in 0.1 M KPi while continuously monitoring the quantity of hydrogen produced. After 2h of electrolysis, 1 M sodium azide solution was added to reach a concentration of 10 mM at the cathode. It led to a sharp increase in the current density and a large drop in the production rate of hydrogen as shown on ***Figure 3.4***. Before addition of NaN_3 in the electrolyte, the FE calculated for HER reaches about 70 ± 20% (t = 0 to 2h), whereas after the addition of NaN_3 the FE for HER sharply decreases to ca 2 ± 20% (t = 2h to 6h). Concomitantly a large quantity of ammonia is formed and a concentration of 2.2 mM of NH_3 is measured at the end of the electrolysis (6h).

It is worth noting that the average FE of ammonia production calculated in the latter experiment (71%) is significantly higher than the average FE (50 ± 10%) determined for electrolysis run in in the presence of 10 mM of azide from the beginning. This observation suggests a partial poisoning of the *a*-MoS_x catalytic sites by long-term exposure to N_3^- ligand under non-catalytic conditions (no applied potential).

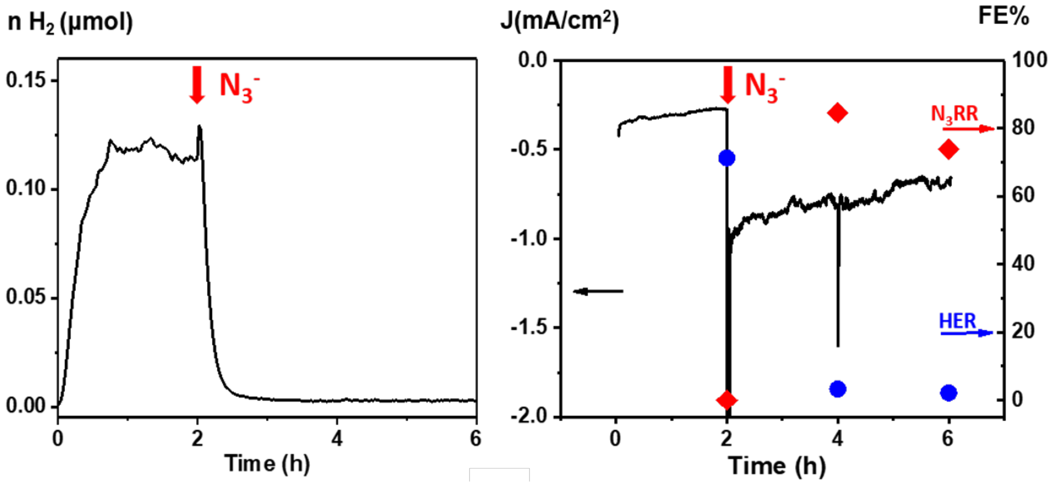

Figure 3.4: *Real-time quantification of the hydrogen produced during a potential-controlled electrolysis in argon saturated 0.1 M potassium phosphate (pH = 5.8), using bare a-MoS_x film deposited on a GC electrode poised at −0.2 V vs. RHE (left). Evolution of the current density recorded during the electrolysis and (right) faradic efficiencies determined for N_3^- reduction (N_3RR, red diamonds) and proton reduction (HER, blue dots) at selected times. The red vertical arrows indicate the time of addition of a solution of 1 M NaN_3 in the cathode compartment (t = 2h, concentration reached at the cathode: 10 mM NaN_3).*

3.1.3 Inorganic azide reduction on other heterogeneous MoS_x

As we mentioned in chapter 2, many strategies have been proposed to tune the ENRR activity of MoS_x in the literature, such as providing more Mo binding sites by using defect-rich materials, or doping MoS_x with other transition metals.[11] Even though we have failed to characterize any conclusive NRR activity with our homemade MoS_x materials, it is interesting to probe whether such parameters (defects, dopants) could actually modulate their N_3RR activity. Therefore, *c*-MoS_2, *Fe*-doped MoS_x, and *e*-MoS_x were also considered here, as well as two type of trinuclear Mo(IV) clusters ($[Mo_3S_7Br_6](NBu_4)_2$ and $[Mo_3S_{13}](NH_4)_2$) which model the basic structural units present in *a*- MoS_x.[12]

The electro-catalytic activity of these derivatives for N_3RR have been systematically investigated under the same conditions as *a*-MoS_x (–0.2 V *vs*. RHE, KPi pH=5.8), under potential-controlled electrolysis using Ar saturated 10 mM NaN_3 solutions in 0.1 M KPi buffer, with an applied potential of –0.2 V *vs*. RHE. Quantification of the ammonia produced was done according to the protocol described in section S2.3.3.1 to determine the rate and FE of the process for each material (***Figure 3.5**, **Table 3.2***) assuming as above a 2 electrons reduction process. The electrodes were prepared by drop casting 10 mg/mL dispersion of crystalline molybdenum sulfide (*c*-MoS_x), Fe-doped amorphous molybdenum sulfide (*Fe*-MoS_x, 4%-8.8%

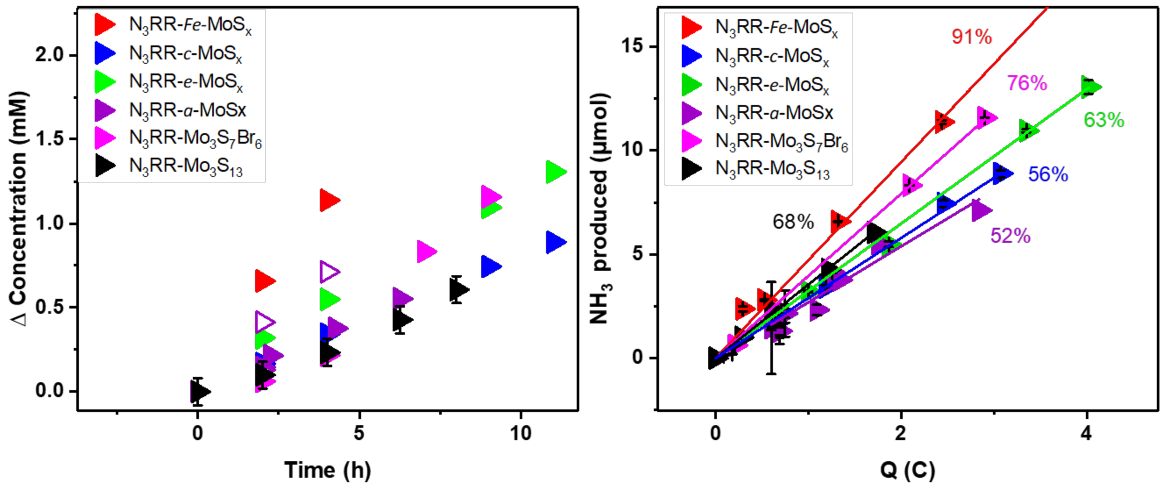

***Figure 3.5**: Evolution of the concentration of NH_3 measured during potential-controlled electrolysis (–0.2 V vs. RHE) (left) and evolution of the quantity of ammonia produced as a function of the charge passed (right) of a 10 mM solution of sodium azide in argon saturated 0.1 M KPi, the faradaic efficiency indicated by different color are calculated from the slopes of the fitting lines.*

Fe), $[Mo_3S_{13}](NH_4)_2$ clusters in isopropanol onto 1 cm^2 glassy carbon electrodes (loading: 0.3 $mg.cm^{-2}$). Alternatively, *e*-MoS_x was electrodeposited as described in section S2.2.3 to obtain the same loading of Mo than for *a*-MoS_x thin films (1×10^{-12} $mol_{Mo}.cm^{-2}$). Finally, $[Mo_3S_7Br_6](NBu_4)_2$ was deposited by drop casting 30 µL of a 10 mM acetonitrile solution (0.3 mg) on GC (1 cm^2).

From the significant increase of the ammonia concentration over time, and the quasi-linear relationship between the quantity of ammonia produced and the charge passed during the CA (***Figure 3.5***), we confirmed that all the MoS_x derivatives possess a convincing and stable activity towards EN_3RR. However, we observe large variations in the production rates of NH_3 and apparent FE of the materials (***Table 3.2***). To be noticed, the possible contribution of NH_4^+ from $[Mo_3S_{13}](NH_4)_2$ was ignored in the above calculations. If we consider that all the ammonium cations contained in the material deposited (0.3 mg) were released during the course of the CA, it would contribute to a maximum of 0.8 µmol of the total 6 µmol of ammonia obtained after 8h of electrolysis. This would account for an overestimation of 13% of our measurement and is neglected, here, as a first gross approximation.

Table 3.2: Summary of the average EN_3RR activity on different MoS_x.

Materials	Rate ($mmol_{NH3}/h/mg_{MoSx}$)	FE %^{a}	FE %^{b} (fitting)	R^2 (fitting)
***Fe*-MoS_x**	8.3 ± 3.3	82 ± 20	91	0.987
***c*-MoS_x**	2.8	55± 3.5	56	0.998
***a*-MoS_x**	3.5 ± 1.8	50 ± 10	52	0.980
***e*-MoS_x**	4.5	61 ± 3	63	>0.999
$[Mo_3S_7Br_6]^{2-}$	2.8 ± 1.6	68 ± 10	76	0.999
$[Mo_3S_{13}]^{2-}$	2.1	70 ± 3	68	>0.999

^{a} average FE obtained from individual measurement. ^{b} calculated from the slope of the linear fit of each series reported on ***Figure 3.5*** right.

The rates and FE determined for each material tested are listed in ***Table 3.2***. Despite the relatively large errors on the values obtained we can observe that:

1) *Fe*- MoS_x stands out with the highest overall EN_3RR activity both in terms of rate of NH_3 production and FE (rate: 8.3 ± 3 $mmol_{NH3}.h^{-1}.mg_{a\text{-}MoSx}^{-1}$; FE: 82 ± 20%); 2) Crystalline MoS_x (*c*- MoS_x) and amorphous species (*a/e*- MoS_x) exhibit comparable FE, ranging between 50% to 61%, but we note that *c*- MoS_x leads to a slightly lower rate of ammonia production (2.8 $mmol_{NH3}.h^{-1}.mg_{a\text{-}MoSx}^{-1}$) than its amorphous counterparts; 3) $\{Mo_3S_7\}$ based cluster clusters possess a slightly better selectivity than the amorphous materials (*a/e*- MoS_x) with FE of 68 ± 10% and 70 ± 3% for $[Mo_3S_7Br_6]^{2-}$ and $[Mo_3S_{13}]^{2-}$, respectively . However, their rates remain in the lower range of ammonia production (≤ 2.8 $mmol_{NH3}.h^{-1}.mg_{a\text{-}MoSx}^{-1}$).

The above observations indicate that, overall the amorphous MoS_x materials do exhibit better EN_3RR activity than their crystalline counterpart especially in terms of ammonia production rate; additionally the incorporation of Fe sites boosts both the rate and selectivity of MoS_x, which would be worth investigating further. Interestingly we can also notice that, within experimental errors the $\{Mo_3S_7\}$ based clusters show relatively comparable EN_3RR activities to *a/e*- MoS_x materials albeit with a slight bias towards better selectivity towards N_3RR and lower ammonia production rates. Acknowledging that the cluster and *a/e*- MoS_x share similar $\{Mo_3S_7\}$ units but with a significant amount of defects among the material,[13],it is tempting to propose that the higher rates observed for *a/e*- MoS_x results from a higher conductivity within the extended structure of the material (interconnected $\{Mo_3S_7\}$ through bridging S_2^{2-}), and that the higher selectivity of $[Mo_3S_7Br_6]^{2-}$ and $[Mo_3S_{13}]^{2-}$ may be linked to their overall higher homogeneity (well defined molecular systems).

3.2 Inorganic azide reduction with $\{Mo_3S_7\}$ clusters in homogenous environment

As shown in the previous section, $[Mo_3S_{13}]^{2-}$ and $[Mo_3S_7Br_6]^{2-}$ offer a unique opportunity to gain insights into the EN_3RR activity of molybdenum sulfides. Here, we selected $[Mo_3S_7Br_6]^{2-}$ (presented as ***Mo-1*** below, ***Figure 3.6***) as an archetypal model for *a*-MoS_x that is well soluble in organic solvents and probe its

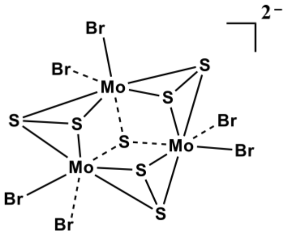

Figure 3.6. *Structure of* ***Mo-1***.

reactivity under reductive homogeneous conditions, with the use of electrochemical and spectroscopic methods.

3.2.1 Methods

Electrochemistry

Cyclic voltammetry (CV) studies were carried out at a scan rate of 100 $mV.s^{-1}$, in the three-electrode configuration using a single-compartmented cell (3 mL). 1 mL solution of the desired compound was purged with Ar for 20 minutes beforehand, then the experiments were performed under ambient conditions (room temperature, atmospheric pressure), under an atmosphere of Ar. A GC electrode was used as working electrode (WE) and was well polished between each series of measurement. A platinum (Pt) wire was used as the counter electrode (CE). A silver (Ag) wire or a commercial non-aqueous Ag/Ag^+ electrode (Redoxme AB, Norrköping, Sweden) was used as (pseudo)reference electrode (RE) depending on the requirement of the electrochemical cell. Ferrocene (Fc) was used as an internal standard in our measurements and the potentials reported below are given *vs.* NHE using $E°(Fc^+/Fc)$ = 0.65V *vs.* NHE in N,N-dimethylformamide (DMF).[14]

The electrochemical studies have been conducted using 1 mM $[Mo_3S_7Br_6](NBu_4)_2$ in anhydrous DMF solutions containing 50 mM KPF_6 as electrolyte. We also tried anhydrous acetonitrile (ACN) as the solvent, but the mediocre solubility of the cluster limited its' use in our studies. When required, H_2O was added to the system as the proton source (20% v/v in DMF), to have a better comparaison of studies in aqueous environment in section 3.1. The characterization of the initial molecular species and post-reaction species was completed with the help of mass spectrometry (MS), Infrared (IR) and UV-Visible spectroscopy.

Infrared spectroscopy

The FT-IR spectra were recorded on a spectrum-100 (Perkin Elmer) spectrometer. Two techniques were applied according to the range of vibrationnal bands targeted and the state of samples (solid or liquid).

1) Solid state IR spectra were recorded from potassium bromide (KBr) pellets (spectral window

400-4000 cm^{-1}). The desired compound was mixed with KBr in a 1/100 mass ratio, and grinded to obtain a fine homogeneous powder. The resulting mixture was transferred into a a pellet die set and subjected to a pressure of 8 tons for 1 or 2 minutes to obtain a transparent pellet. The spectra were recorded against pure KBr as background.

2) Solution state IR spectra were recorded using a single reflection-ATR module (MIRacle ATR, Pike) equipped with a Germanium crystal. The spectra were recorded against 50 mM KPF_6 in DMF (or 50 mM KPF_6 in DMF-H_2O 80-20) in range of 600-4000 cm^{-1}. To be noticed the Ge-ATR spectral window does not allow for the observation of the signature of the μ_3-(Mo-S) and μ_2-(S-S) bonds of the cluster.

The coupled IR spectroelectrochemical measurements were done in a dedicated spectroelectrochemical cell (Spectroelectrochemistry Partners, SP-02 cell) that was fitted on the Ge-ATR plate. The measurements were conducted in the three electrode configuration using a glassy carbon working electrode (GC, 1.6 mm) a Pt wire as counter electrode and an Ag wire as pseudo reference. A micrometric screw allowed to position the working electrode in close vicinity to the Ge crystal of the ATR to form a thin film of electrolyte. In brief, using a multimeter (20 MΩ), the resistance between the WE and the ATR plate was monitored while gradually lowering the WE. The position of the WE was fixed as soon as the resistance begun to drop.

UV-visible spectroscopy

The UV-visible spectra were recorded on a Cary 60 UV-Vis (Agilent Technologies) spectrometer. The coupled UV-visible spectroelectrochemical measurements were done in a dedicated spectroelectrochemical cell kit (Pt, 012904 SEC-C Thin Layer Quartz Glass, ALS). The measurements were conducted in the three-electrode configuration using a platinum mesh working electrode a Pt wire as counter electrode and an Ag wire as pseudo reference.

3.2.2 Electrochemical study on {Mo$_3$S$_x$} cluster

The CV of pristine [Mo$_3$S$_7$Br$_6$]$^{2-}$ (***Mo-1***) (***Figure 3.7,*** *left*) presents three ill-defined irreversible waves centered at red1: –0.6 V; red2: –1 V, and red3: –1.55 V, respectively, followed by a sharp increase in current below –1.75 V *vs*. NHE. The latter is observed concomitantly to the deposition of a film on the working electrode and is likely due to the decomposition of the clusters. The non-reversibility of the CV recorded for ***Mo-1***, implies that the composition of the clusters likely evolves as well, even at low potential, which is supported by the evolution of the UV-Vis spectrum upon reduction. As shown on ***Figure 3.7*** (right) the absorption at 300 nm is significantly reduced upon reduction at –1V *vs*. NHE, meanwhile, we start seeing a shoulder rising between 350-450 nm which bear similarities with the spectra of {Mo$_3$S$_4$} species.[15] Further reduction at −1.5 V *vs*. NHE lead to the further desapearance of the initial band at 300 nm and rise of bands centered at 320 nm, 400 nm and 475 nm. These initial observations thus, highlight the complexity of the electrochemical response of ***Mo-1*** which appears rather unstable in the conditions tested.

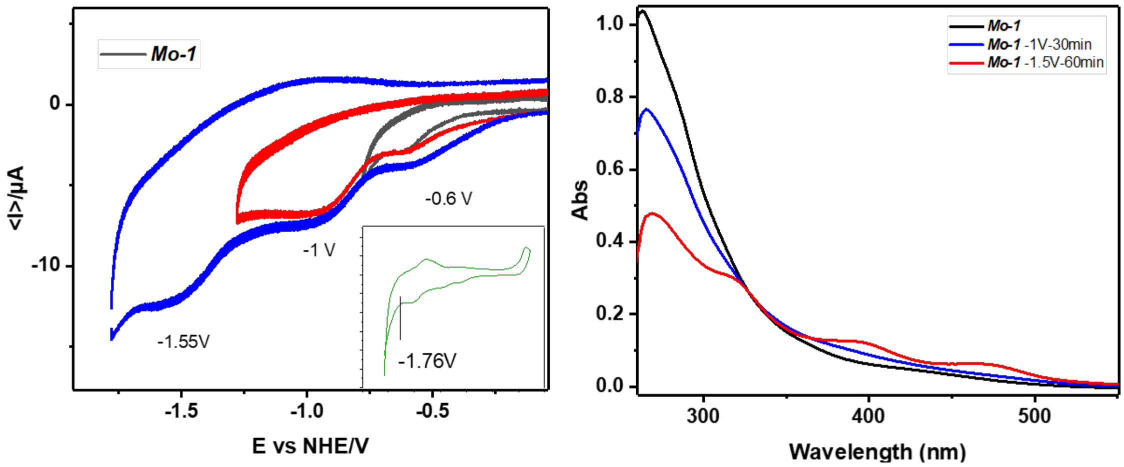

Figure 3.7*: Cyclic voltammograms of 1mM [Mo$_3$S$_7$Br$_6$]$^{2-}$ (****Mo-1****) recorded with different potential ranges in anhydrous DMF in presence of 50 mM KPF$_6$. Scan rate 100 mV/s.(left) UV-vis spectroscopy of* ***Mo-1*** *under reduction* and ***Mo-2*** recorded *in anhydrous DMF in presence of 50 mM KPF$_6$.*

Using DFT calculations and mass spectrometry analysis, it has been previously proposed that in similar clusters, the μ$_2$-S$_2$$^{2-}$ ligands can be reduced to μ$_2$-S^{2-} at applied potentials close to –0.6 V leading to the conversion of the initial {Mo$_3$S$_7$} core to {Mo$_3$S$_4$} derivatives (***Figure 3.8***, left). [13] To confirm this hypothesis, we conducted a controlled potential electrolysis of 1 mL of 1 mM solution of ***Mo-1*** followed by the characterization of the resulting species using IR

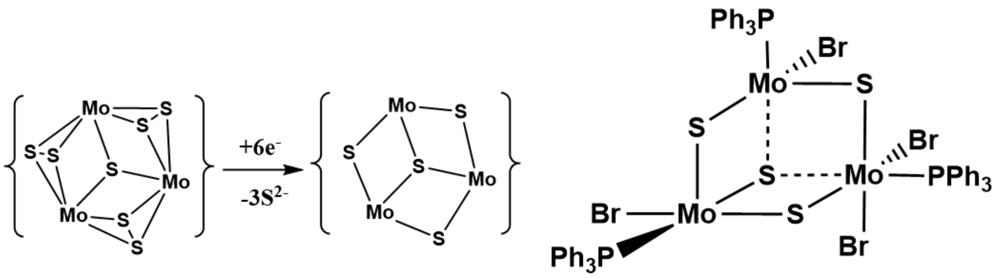

***Figure 3.8**. Reduction of {Mo_3S_7} to {Mo_3S_4} (left). One possible structure of **Mo-2** (right).*

spectroscopy. Because the redox processes are relatively ill-defined for ***Mo-1***, we run the electrolysis near the onset potential (–0.4 V) of the peak centered at –0.6 V *vs*. NHE, and we followed the reduction via chronoamperometry (CA). After 3 hours the orange solution turned to green. The reduced ***Mo-1*** was dried in vacuum and further characterized using IR spectroscopy. As a reference we prepared the well-defined $Mo_3S_4Br_4(PPh_3)_3$ cluster (***Mo-2***, **Figure 3.8**, right) from the reaction between ***Mo-1*** and PPh_3 following an established procedure.[17] The comparison of their IR (KBr) spectra together with the starting ***Mo-1*** is shown in ***Figure 3.9***.

In the IR spectra of the reduced ***Mo-1***(***red-Mo-1, Figure 3.9***), the characteristic signature of the bridging disulfide ligands ($\nu(\mu_2\text{-S-S}) = 540$ cm^{-1}) of the pristine ***Mo-1*** is absent, which confirms that the disulfide ligands have been reduced at –0.4 V *vs.* NHE. The signature of the μ_3-sulfide ligand ($\nu(\mu_3\text{-Mo-S}) = 460$ cm^{-1}) present in both pristine ***Mo-1*** and ***Mo-2*** samples is hardly seen on the spectra of the reduced ***Mo-1***. A weak band can, however, be distinguished at 470 cm^{-1} and may be reminiscent of the expected signal.

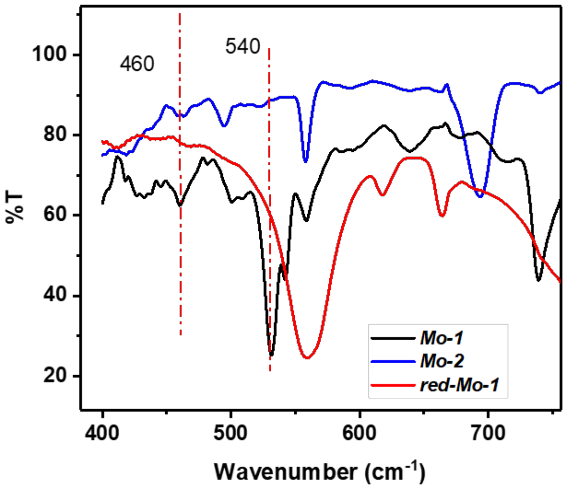

***Figure 3.9**: FT-IR spectra recorded on KBr pellets of **Mo-1** (blue), **Mo-2** (black) and reduced **Mo-1** after a CA at –0.4 V for 3h (red).*

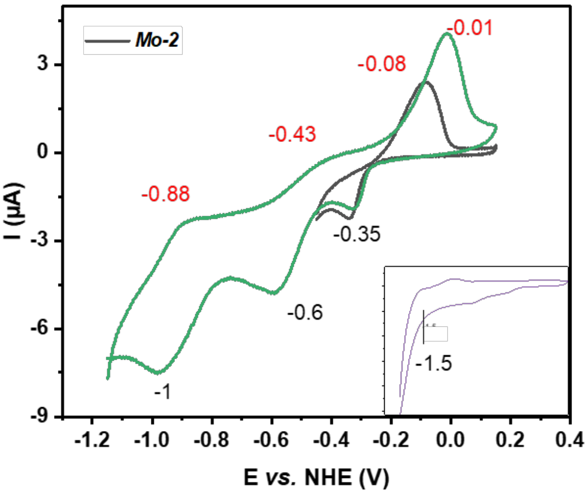

Figure 3.10: *Cyclic voltammograms of 1mM* ***Mo-2*** *recorded from different potential ranges in anhydrous DMF. Scan rate 100 mV/s.*

In order to get more insights in the likelihood of an electro-induced conversion of the initial {Mo_3S_7} core to {Mo_3S_4} we next turn back to cyclic voltammetry. First, let us focus on ***Mo-2***. The CV of the latter features three well-defined redox processes before a sharp irreversible wave past –1.5 V *vs*. NHE (***Figure 3.10***). The first process exhibits a cathodic peak centered at red1 = –0.35 V which is coupled to an anodic peak centered at ox1 = –0.08 V *vs*. NHE. The second process features a cathodic peak centered at red2 = –0.6 V *vs*. NHE and seems to be coupled to an anodic peak overlapping with the anodic peak of the first redox couple, leading to an apparent anodic peak centered at ox1' = 0.01 V *vs*. NHE. Finally the third redox process feature a more classical couple of peaks centered at red3 = –1 V *vs*. NHE and ox3 = –0.88 V *vs*. NHE respectively. These three redox couples are likely related to the sequential reduction of the three Mo (IV) centers to Mo (III) in ***Mo-2***. The unusual splitting of the first two redox couples (red1/ox1 and red2/ox1') is likely due to the irreversible loss of the Br^- anion upon subsequent reduction of the Mo centers or the modification of the ligands. Therefore, we tried to recover the reversibility by using tetra(N-butyl)ammonium bromide (TBABr) as an alternative electrolyte, unfortunately we did not obtain better defined redox pairs.

The CV of the ***red-Mo-1*** exhibits interesting similarities with the CV of pristine ***Mo-2*** (***Figure 3.11***). Due to the presence of PPh_3 ligands in ***Mo-2***, it is difficult to directly compare the peak potentials of the redox process featured in the both CVs. However, it is apparent that the first reduction wave of ***red-Mo-1*** occurs near –0.3 V (shoulder) and is followed by a second one centered at –0.5 V and a third centered at –0.8 V *vs*. NHE. Additionally we can note the apparition of an anodic process centered at 0.03 V *vs*. NHE. The similarity between the CVs of ***red-Mo-1*** and ***Mo-2*** consolidate our previous conclusion that the first reduction process observed in the CV of ***Mo-1*** centered at –0.6 V *vs*. NHE is due to the reduction of the μ_2-S_2^{2-}, and initiates the conversion of ***Mo-1*** to new species likely featuring the {Mo_3S_4} core. In turn this electro-driven structural rearrangement greatly complicates the analysis of the reactivity, especially in the context of reductive electro-catalytic processes.

Considering the above observations it appeared important to investigate the reactivity of both ***Mo-1*** and ***Mo-2*** towards azide to gain a more complete picture of the system and try to describe the interplay between {Mo_3S_7} and {Mo_3S_4} species during EN_3RR.

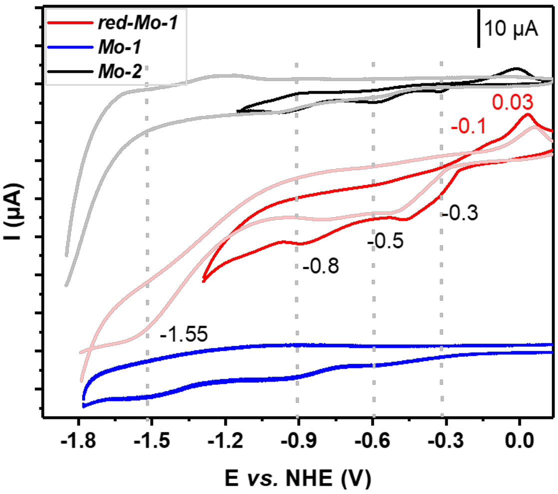

Figure 3.11*: Cyclic voltammograms of 1mM solutions of* ***Mo-1*** *(blue),* ***Mo-2*** *(black) and of reduced* ***Mo-1*** *(red) in anhydrous DMF with 50mM KPF_6. Scan rate 100 mV/s. The reduced Mo-1 was obtained recorded after 3h of a controlled potential electrolysis of a 1 mM of* ***Mo-1*** *at –0.4 V vs. NHE.*

3.2.3 Electrochemical azide reduction with {Mo_3S_x}

3.2.3.1 Coordination of azide with {Mo_3S_x}

To investigate the coordination of N_3^- to {Mo_3S_x} clusters, we turn to Infrared (IR) spectroscopy.

We started with the analysis of the evolution of the solid-state FTIR spectra of ***Mo-1*** (and ***Mo-2***) recorded after the addition of 0, 2, 6, and 20 (0, 3, 9, and 20) equivalents (equiv.) of NaN_3. Here, the clusters were reacted with the desired amount of NaN_3 in anhydrous DMF overnight, at room temperature, then the samples were dried in vacuum and KBr pellets were prepared and analyzed immediately.

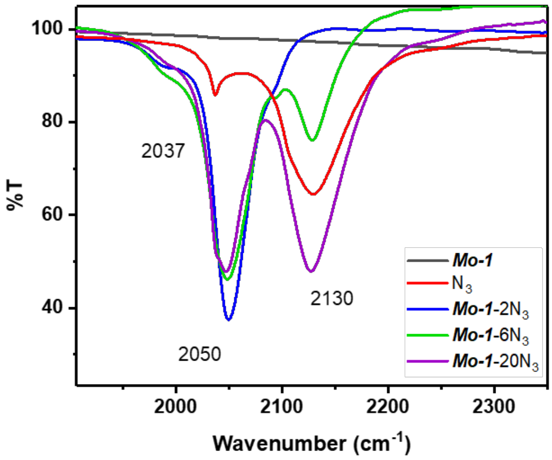

Figure 3.12*: evolution of the antisymmetric stretching band $\nu(N_3^-)_{as}$ of N_3^- for different [N_3^-:**Mo-1**] ratio.*

First let us consider the pure NaN_3 in KBr.

In this sample (red curve ***Figure 3.12***) we note that the antisymmetric stretching band of NaN_3 has a broad main component centered at $\nu(N_3^-)_{free}$ = 2130 cm^{-1} and a second weaker component centered at 2037 cm^{-1}. Upon addition of 2 equiv. of NaN_3 to ***Mo-1*** the antisymmetric stretching band of the azide appears as a single band centered at $\nu(N_3^-)_{co}$ = 2050 cm^{-1} suggesting the full complexation of the azide to the cluster.[18] Addition of more equivalents of NaN_3 (3 and more) to ***Mo-1*** resulted in the gradual increase of the main band related to free azide ($\nu(N_3^-)_{free}$ = 2130 cm^{-1}).

In order to study in more details the nature of the species resulting from the treatment of ***Mo-1*** with 2 and 20 equiv. NaN_3 we turned to ESI-MS (***Figure 3.13***). In both samples, we observe a mixture of clusters where 0 to 6 bromine ligands were substituted by azide ligands. We can note an apparent increase of the relative intensity of the signal of the cluster bearing 6 azido ligands upon treatment of ***Mo-1*** with 20 equiv. NaN_3, but the substitution appears statistical in all cases.

Thus, even in the absence of any applied potential, ***Mo-1*** readily reacts with azide, at room temperature, leading to the statistical substitution of bromide ligands and forms stable species.

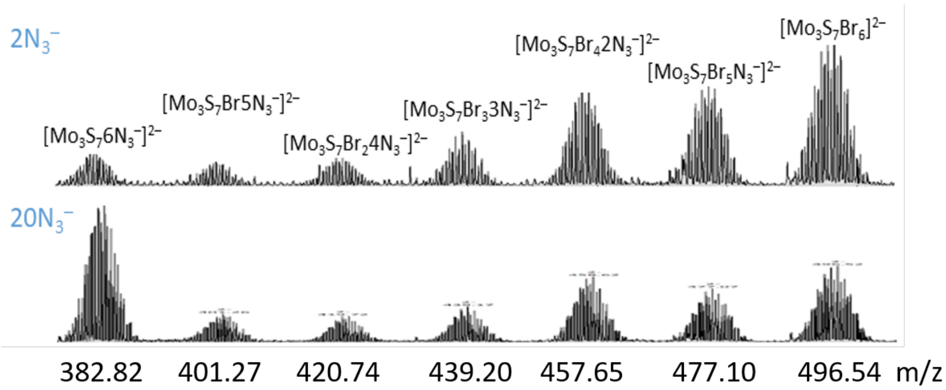

Figure 3.13*: ESI-MS spectroscopy of reaction mixture of $2N_3^-$-$[Mo_3S_7Br_6]^{2-}$(top), $20N_3^-$-$[Mo_3S_7Br_6]^{2-}$(bottom) in acetone.*

Considering the C_3 symmetry of the original ***Mo-1***, the bromides ligands occupy two inequivalent coordination sites on the Mo centers (***Figure 3.8,*** right), namely equatorial and horizontal sites, which are not distinguishable in the IR spectra of the coordinated azido ligands.

Next let us consider the addition of azide to ***Mo-2*** (***Figure 3.14***). Upon addition of 3 equiv. of NaN$_3$ the IR spectrum of the resulting mixture does not feature the signature of the free azide ($\nu(N_3^-)_{free}$ = 2037, 2130 cm^{-1}) but coordinated azido ligands leading to two distinct bands centered respectively at $\nu_2(N_3^-)_{co}$ = 2095 cm^{-1} and $\nu_1(N_3^-)_{co}$= 2055 cm^{-1}. This suggests the presence of two differentiated coordination modes of the azides in ***Mo-2*** with variations of the N−N distances within the azido ligands.[18] Addition of more than 3 equiv. NaN$_3$ results in the gradual increase of the signature of the free azide in addition to a broadening of the bands corresponding to the coordinated azido ligands. Unfortunately, in the case of ***Mo-2*** ESI-MS was of no use for investigating the nature of the compounds obtained upon direct treatment with NaN$_3$, as no signature of clusters nor cluster fragments could be observed in any conditions/ionization mode tested. No information regarding the selectivity of the ligand exchange is, thus, accessible for ***Mo-2*** at this stage. Nevertheless, the observation of the coordinated azido ligand on ***Mo-2*** indicates that, just as for ***Mo-1***, stable species are formed upon simple exposure of ***Mo-2*** to NaN$_3$ at room temperature and in the absence of any applied potential.

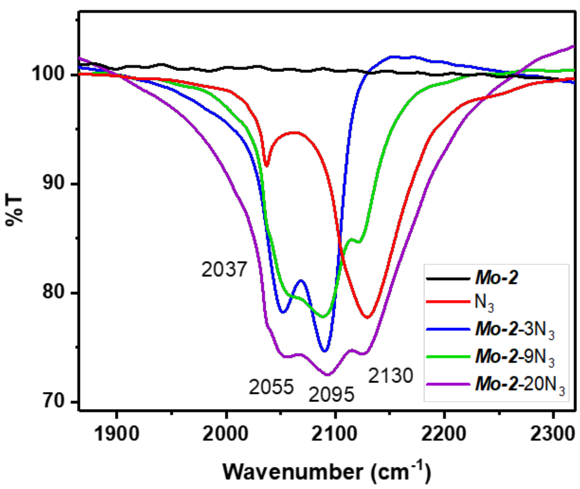

Figure 3.14*: evolution of the antisymmetric stretching band $\nu(N_3^-)_{as}$ of N_3^- for different [N_3^-:**Mo-2**] ratio.*

it is interesting to note that despite possessing largely different structures ***Mo-1*** and ***Mo-2*** appears to offer at least one similar coordination mode for the azide ligands resulting in the bands centered between 2050 cm^{-1} and 2055 cm^{-1} while ***Mo-2*** offer an additional coordination mode leading to the characteristic band centered at 2095 cm^{-1}.

In order to get more insights regarding the preservation of the clusters' cores upon azide coordination we next focused on the characteristic bands related to the vibrations of the Mo-S and S-S bonds. On the left of ***Figure 3.15*** we can see that in the case of ***Mo-1***, both the $\nu(\mu_3$-Mo-S) centered around 460 cm^{-1} and the $\nu(\mu_2$-S-S) = 540 cm^{-1} are kept while

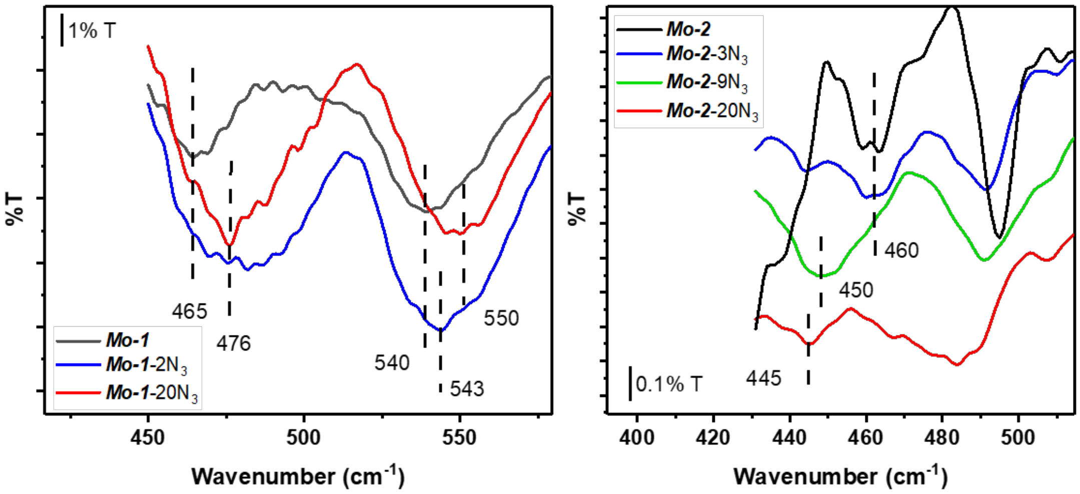

Figure 3.15: *Evolution of the asymmetric stretching band ν(N$_3^-$)$_{as}$ of N$_3^-$ for different [N$_3^-$:**Mo-1/2**] ratio.*

shifting/broadening according to the amount of NaN$_3$ added. This suggests that the substitution of Br$^-$ by N$_3^-$ does not affect the integrity of the core of the cluster in agreement with the MS studies. In the case of ***Mo-2***, the band related to ν(μ$_3$-Mo-S) and centered around 460 cm^{-1} shifts towards lower wavenumbers upon addition of NaN$_3$. It remains well visible up to the addition of 9 equiv. of NaN$_3$ at which point it has shifted to 450 cm^{-1} and suggests that at least a significant fraction of the clusters are preserved upon coordination of azide. This band appears much more affected by the addition of larger excess of azide (20 equiv.) losing its resolution and further shifting to 445 cm^{-1}. Here, we cannot exclude that the cluster is partially rearranged upon the addition of a large excess of azido ligands. Importantly, the structural evolution of an increasing fraction of ***Mo-2*** clusters in the samples, upon addition of increasing amounts of NaN$_3$, may explain the gradual broadening of the antisymmetric stretching bands of the azido ligands (ν$_2$(N$_3^-$)$_{co}$ = 2095 cm^{-1} and ν$_1$(N$_3^-$)$_{co}$= 2055 cm^{-1}) discussed above.

3.2.3.2. Electrochemical study on reduction of azide with Mo-2

Effect of the coordination of azide with Mo-2

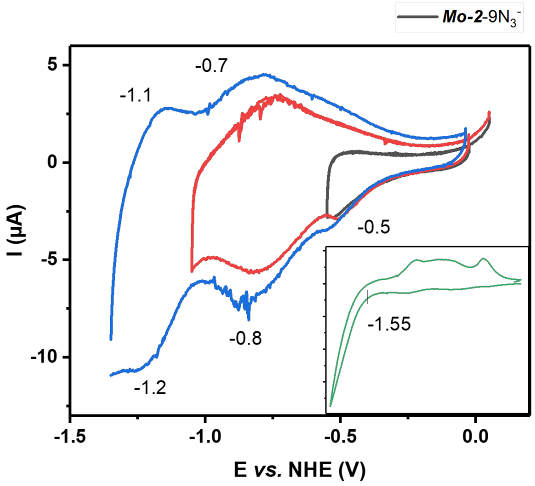

Figure 3.16*: Cyclic voltammograms of* ***Mo-2*** *with 9 equiv. N_3^- added one day before in anhydrous DMF with 50 mM KPF_6. Scan rate 100 mV/s.*

Assuming that the core of ***Mo-2*** is mostly preserved after reaction with a moderate excess of NaN_3, we next investigate the electrochemical response of the system after treatment with 9 equiv. of NaN_3, overnight, as described above. The resulting system will hereafter be referred to as ***Mo-2****-9N$_3$*. The CV ***Mo-2****-9N$_3$* recorded in anhydrous DMF appears rather ill defined, and share some similarities with the CV of pristine ***Mo-2***. Three reduction processes are distinguished (red1: –0.5 V, red2: –0.8 V; red3: –1.2V) before the development of a sharp irreversible wave after –1.55 V *vs*. NHE. Overall the first three processes occur at more cathodic potentials than for ***Mo-2*** and the second and third reduction peaks appear quite reversible, *i.e.* coupled to anodic peaks centered at ox2: –0.7V and ox3: –1.1V *vs*. NHE, respectively. Considering the similarities between the CVs of both ***Mo-2*** and ***Mo-2***-9N$_3$ it is, tempting to assign the three processes observed for ***Mo-2****-9N$_3$* to the sequential reduction of the three Mo(IV) centers to Mo(III) as proposed for ***Mo-2***.

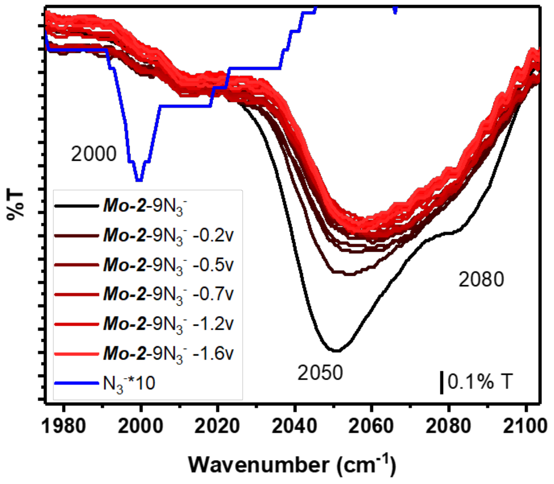

Figure 3.17*: FT-IR spectra on Ge-ATR of asymmetric stretching of N_3^- in* ***Mo-2****-9N$_3^-$ DMF solution reduced at different potentials.*

Next, we turn to liquid phase IR spectroscopy to follow the evolution of the IR spectra of ***Mo-2***-9N$_3$ during the reduction (***Figure 3.17***) in anhydrous DMF, in presence of 50 mM KPF_6. Limited by the use of a Ge-ATR (spectral windows 600 cm^{-1} – 4000 cm^{-1}) we mostly focused on the antisymmetric stretching bands of the azide. As shown in ***Figure 3.17*** the two differentiated coordination modes of the azido ligand noticed in the solid-state IR spectrum of ***Mo-2***-9N_3 are preserved in solution, leading to two antisymmetric stretching bands centered at $\nu_2(N_3)_{co}$ = 2080 cm^{-1} and $\nu_1(N_3)_{co}$= 2050 cm^{-1}. As observed in the solid-state IR spectrum these band appears rather broad. In addition, the mixture still features a very weak signal resulting from free azide in solution ($\nu(N_3)$ = 2000 cm^{-1}) as indicated on ***Figure 3.17***.

Upon application of potentials between –0.2 V and –0.5 V *vs*. NHE a rapid evolution of the IR spectrum occurs, leading to the overall decrease of the intensity of the antisymmetric stretching bands of the coordinated azido ligands. Noteworthy, the band centered at $\nu_1(N_3)_{co}$ = 2050 cm^{-1} appears to be much more affected than $\nu_2(N_3)_{co}$= 2080 cm^{-1}. This suggests that the reduction of ***Mo(IV)$_3$-2***-9N_3 to ***Mo(IV)$_2$Mo(III)-2***-9N_3 does affect the azido ligands, possibly leading to the specific release or reaction of a fraction of the ligands associated with stretching band centered at $\nu_1(N_3)_{co}$. Due to the weak signature of the free azide in these conditions, we cannot discriminate between the two possibilities here, but both could explain the irreversibility of the first reduction process observed on the CV of ***Mo-2***-9N_3. Upon application of more cathodic potentials (down to –1.6 V *vs*. NHE), the IR spectrum did not evolve further (***Figure 3.17***) which is compatible with the observation of the two reversible redox processes in the CV of ***Mo-2***-9N_3 as described above.

Effect of water

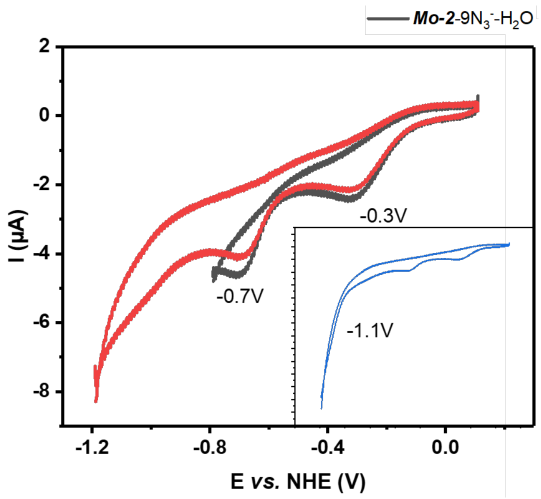

Figure 3.18: *Cyclic voltammograms of* ***Mo-2*** *with 9 equiv. N_3^- added one day before in anhydrous DMF (20% H_2O) with KPF_6. Scan rate 100 mV/s.*

When 20% H_2O was present in the media, the CV of the ***Mo-2***-9N$_3$ was drastically affected, and lost all reversibility (***Figure 3.18***). Only two reduction processes are easily distinguished (red1: –0.3 V, red2: –0.7 V, *vs*. NHE) before the development of a sharp irreversible wave below –1.1 V *vs*. NHE. Overall, all the reduction process occurs at less cathodic potentials than in absence of water suggesting the non-innocent role of water/protons in this case. To gain more insights into the evolution of ***Mo-2***-9N$_3$ in these conditions, we turned to liquid phase IR spectroscopy.

In the presence of water, the antisymmetric stretching bands of the azido ligands appeared less resolved than in anhydrous DMF, and the two components $\nu_1(N_3)_{co}$ and $\nu_2(N_3)_{co}$ are hardly distinguished before the application of any potential (***Figure 3.19***). Additionally the weak signature of the free azide appears at $\nu(N_3)$ = 2030 cm^{-1}, slightly shifted compared to the value observed in anhydrous conditions.

Upon application of potentials between –0.2 V and –0.4 V *vs*. NHE (first irreversible reduction wave of ***Mo-2***-9N$_3$) a rapid evolution of the IR spectrum occurs. It led the to overall decrease

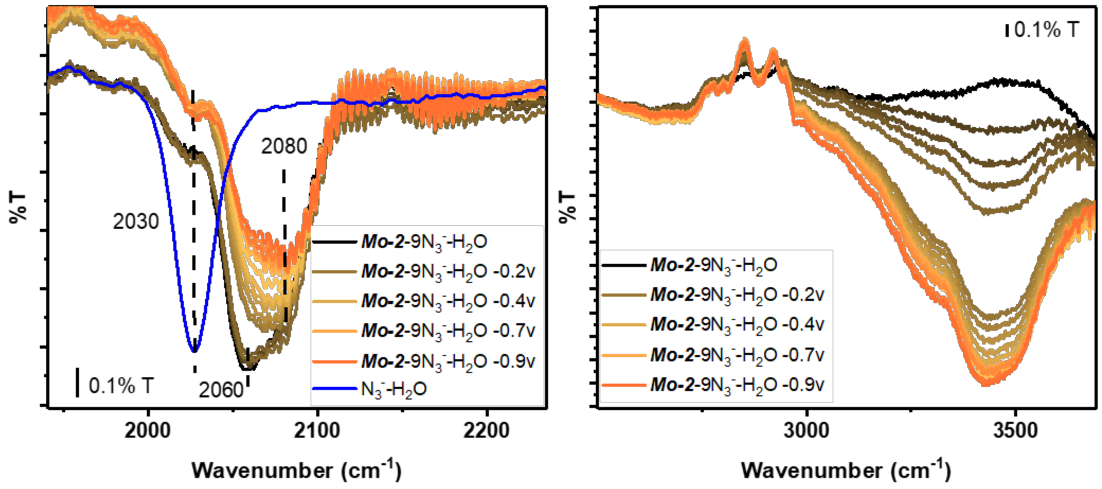

Figure 3.19: *FT-IR spectra on Ge-ATR of asymmetric stretching of N_3^- in* ***Mo-2***-*9N_3^- DMF (20% H_2O) reduced at different potential.*

of the intensity of the antisymmetric stretching bands of the coordinated azido together with an apparent shift of the maxima of the band from 2059 cm^{-1} to 2072 cm^{-1}. A broad massif with a maximum centered at 3420 cm^{-1} appears concomitantly, which can be attributed to the signature of the antisymmetric/symmetric stretching bands of newly formed N−H bonds [19]. Interestingly the application of more cathodic potentials between –0.7 V and –0.9 V *vs*. NHE (second irreversible reduction wave of ***Mo-2***-9N$_3$) resulted in a marked decrease of the component of lower frequency ($\nu_1(N_3)_{co}$) of the antisymmetric stretching band of the azido ligands. This is clearly seen on ***Figure 3.19*** with the further shifting of the maximum of the band to 2080 cm^{-1}, much closer to the frequency of the second component $\nu_2(N_3)_{co}$ observed in anhydrous conditions. Noteworthy, only a very limited increase in the intensity of the stretching band of the N−H bounds is observed concomitantly, implying that during this process only a very limited fraction of the azido ligands leads to the formation of new N-H bonds.

Overall, we can conclude that in presence of water the first reduction of ***Mo-2***-9N$_3$ triggers the reaction of an azido ligand with proton(s) to generate N−H bonds. In the absence of any other specific IR signatures pointing towards specific intermediates, and considering the likelihood of a clean 2 electron-3 protons reduction of azide by MoS$_x$ derivatives, it is tempting to propose that this first step correspond to the following sequential conversion:

$$\mathbf{Mo(IV)_3\text{-}2}\text{-}9N_3 + e^- \rightarrow \mathbf{Mo(IV)_2Mo(III)\text{-}2}\text{-}9N_3$$

$$\mathbf{Mo(IV)_2Mo(III)\text{-}2}\text{-}9N_3 + 3H^+ \rightarrow \mathbf{Mo(IV)_2Mo(V)\text{-}2}\text{-}8N_3\text{-}(NH_3) + N_2$$

The picture then gets blurry, as the second reduction still induces a significant evolution of the antisymmetric stretching band of the azido ligands, and specifically the $\nu_1(N_3)_{co}$ component, but without a marked increase in the intensity of the stretching band of the N−H bond. In the absence of additional data/evidences it is difficult to rationalize this observation at this point. Nevertheless, an obvious conclusion is that potentials more cathodic than −0.9 V *vs*. NHE are required to trigger the full reduction of the free and coordinated azide to ammonia present in the system, as in the present experiment ammonia likely remains coordinated to the Mo centers.

3.2.3.3. Electro-driven catalytic reduction of azide with Mo-2

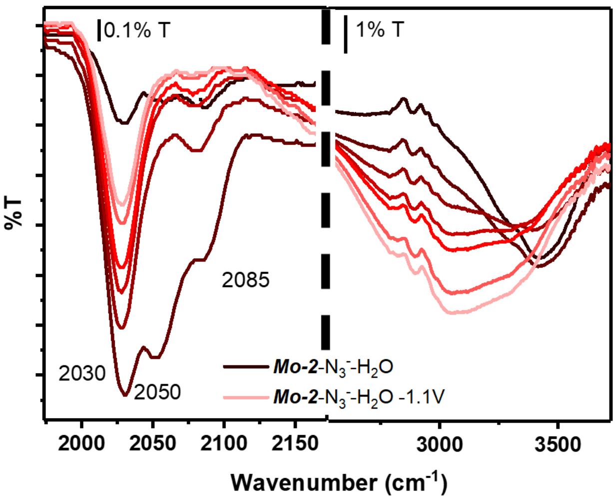

Figure 3.20: *FT-IR spectra on Ge-ATR of asymmetric stretching of N_3^- in **Mo-2** with freshly added 20 equiv. N_3^- in DMF (20% H_2O) reduced at −1.1 V* vs. *NHE.*

With the limited quantity of azide present in ***Mo-2***-9N_3, and the range of potential applied (up to −0.9 V *vs*. NHE) we could not initiate a true catalytic process leading to EN$_3$RR. Hence, we next considered the case where 20 equiv. of NaN$_3$ DMF was added to a 1 mM solution of ***Mo-2*** in DMF-20% H_2O containing 50 mM KPF$_6$, and under stronger reductive conditions (−1.1 V *vs*. NHE). Having demonstrated that the long term exposure of ***Mo-2*** to such a large excess of NaN$_3$ in solution may be leading to a significant structural reorganization of the cluster under static conditions (no potential applied, see section 3.2.3.1), in the following experiment we introduced 100 mM NaN$_3$ DMF solution to an oxygen free solution of ***Mo-2*** in a short time before applying the desired potential. Using liquid-phase IR spectroscopy we then followd the evolution of the antisymmetric stretching band of azide in the reaction mixture as shown on ***Figure 3.20***.

After addution of NaN$_3$ we observe the apparition of both antisymmetric stretching bands of the azido ligands ($\nu_2(N_3^-)_{co}$ = 2085 cm^{-1} and $\nu_1(N_3^-)_{co}$= 2050 cm^{-1}) suggesting the coordination of azide on ***Mo-2*** according to the two modes discussed before. In addition, the expected band of the free azide clearly stands out at $\nu(N_3)$ = 2030 cm^{-1}. Interestingly, upon application of –1.1 V *vs*. NHE we observe a fast disappearance of the antisymmetric stretching band of lower frequency $\nu_1(N_3^-)_{co}$= 2050 cm^{-1}, together with the decrease of intensity of the stretching band of the free azide and the apparition of a broad band between 2500 cm^{-1} and 3250 cm^{-1}. We attributed this to the release of NH$_3$ in solution (N−H stretching bond). Keeping the system under an applied potential of –1.1 V *vs*. NHE, for 180 minute we observe the gradual decrease in intensity of both $\nu_2(N_3^-)_{co}$ = 2085 cm^{-1} and $\nu(N_3^-)_{free}$ = 2030 cm^{-1} together with the increase of ν (NH_3) = ~3000 cm^{-1}. To confirm the nature of the products formed we proceeded with the colorimetric detection and quantification of ammonia and hydrazine, after a running a 1 hour long potential controlled electrolysis at –1.2 V vs. NHE on a 1 mM solution of ***Mo-2*** in 20% v/v H_2O/DMF containing 20 mM NaN_3 and 50 mM KPF_6 as electrolyte. The quantification of NH_3 via salicylate method confirmed the production of NH_3 with 85% FE, while no trace of N_2H_4 could be detected using the Watt and Chrisp assay, confirming the assignment of the large band around 3000-3500 cm^{-1} to ν(NH_3).

Thus, ***Mo-2*** is able to catalyze the selective reduction of N_3^- to NH_3 at –1.1 V *vs*. NHE, in DMF–H_2O solution. Moreover we observe that the azido ligand coordinated in the mode associated with the antisymmetric stretching band $\nu_1(N_3^-)_{co}$ appears systematically more reactive than the azido ligand associated with the $\nu_2(N_3^-)_{co}$. In the absence of additional experimental or theoretical data available, the assignment of these different coordination modes and a deeper understanding of the system remains currently out of reach.

3.2.3.4. Electro-driven reduction of azide with Mo-1

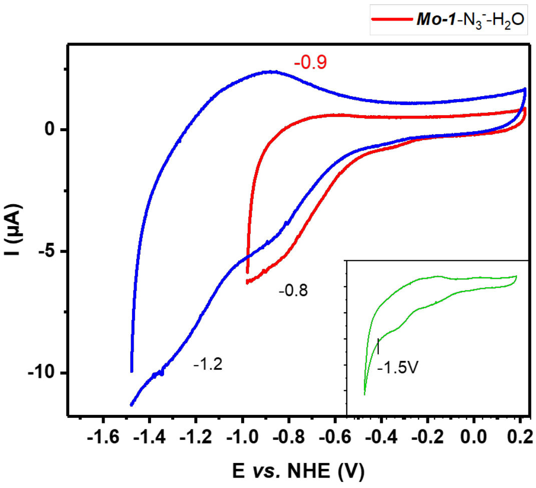

Figure 3.21: *Cyclic voltammograms of **Mo-1** with freshly added N_3^- from different potential ranges in DMF (20% H_2O) with KPF_6. Scan rate 100 mV/s.*

Having lain down some basis for the understanding of the reactivity of model species we came back to the study of the reactivity of **Mo-1** towards azide. Here we analyzed the response of a system in which NaN_3 was added before the CV and/or IR experiments. First we recorded the CV of ***Mo-1*** in the presence of an excess of NaN_3 (hereafter named ***Mo-1***-N_3) in 20% v/v H_2O/DMF containing 50 mM KPF_6 (***Figure 3.21***). Two reduction processes are distinguished (red1: –0.8 V; red2: –1.2V *vs.* NHE) before the development of a sharp irreversible wave after –1.5 V *vs.* NHE. Due to the electro-driven rearrangement of ***Mo-1*** discussed in section 3.2.2, the poor reversibility of the system was expected. Interestingly red2: –1.2V seems to have an ill-defined anodic pair centered at ox2: –0.9 V *vs.* NHE. As discussed in section 3.2.2 the first reduction process (red1) is likely due to reduction of disulfides, and the following processes associated to the reduction of the Mo(IV) centers to Mo(III). However, a more detailed discussion is out of reach with the current data, knowing that the system likely evolves under the range of potential applied.

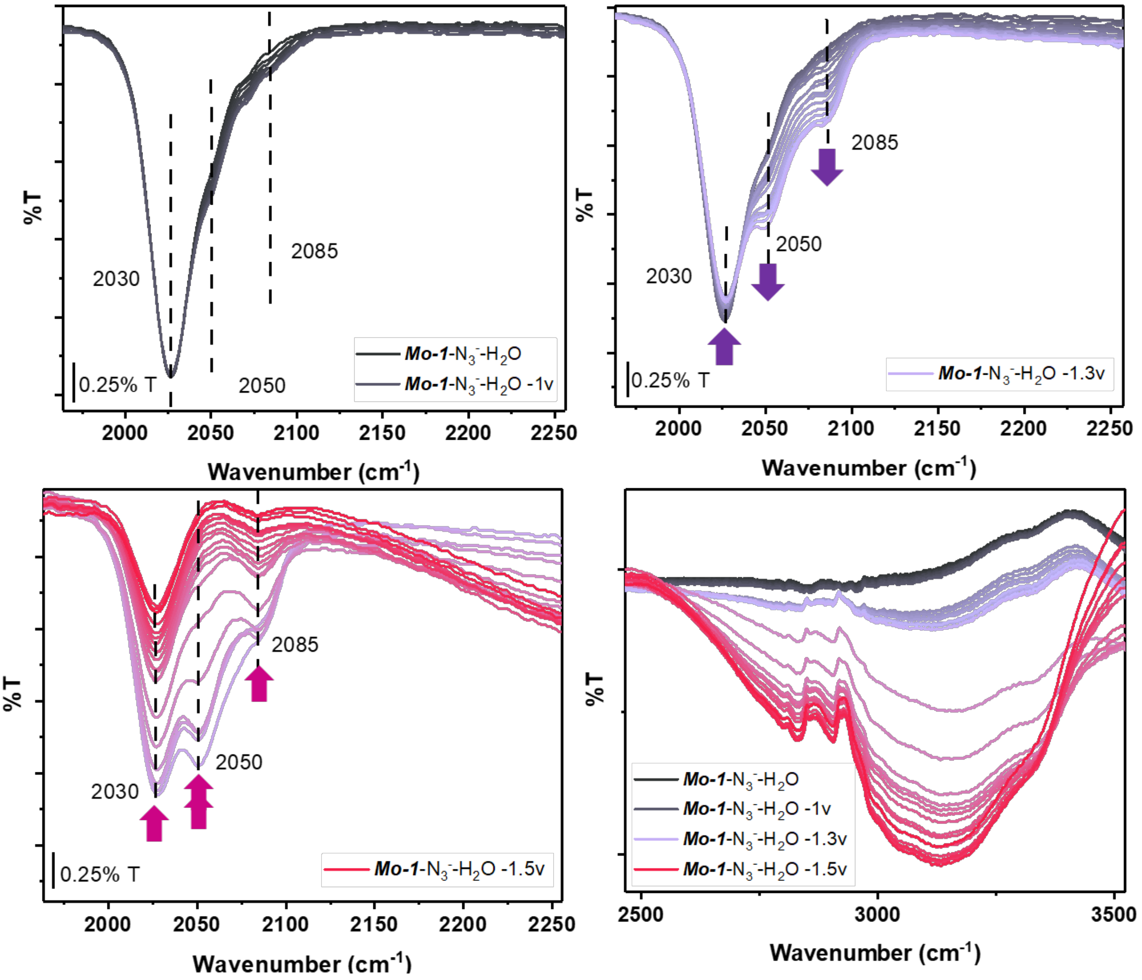

Figure 3.22: *FT-IR spectra on Ge-ATR of asymmetric stretching of N_3^- (left) and in* ***Mo-1*** *with freshly added 20 equiv. N_3^- in DMF (20% H_2O) reduced at different potential.*

Nevertheless, the analysis of the evolution of the IR spectra of ***Mo-1***-N_3 in presence of H_2O and under reductive conditions permits us to gain some insights into the reactivity of the system, as shown in ***Figure 3.22***. Upon application of a potential of –1 V *vs.* NHE (first reduction process; ***Figure 3.22*** top left, gray curves) we can observe the gradual increase of small shoulders centered at $\nu_1(N_3^-)_{co}$ = 2050 cm^{-1} and $\nu_2(N_3^-)_{co}$ = 2085 cm^{-1} on the asymmetric stretching band of the free azide $\nu(N_3^-)_{free}$=2030 cm^{-1} that dominates the initial spectra of ***Mo-1***-N_3. Importantly no significant evolution of the IR spectra is observed between 2500 cm^{-1} and 3500 cm^{-1} indicating that no ammonia (or a negligible quantity) is produced during this first process. This observation, thus, suggests that at potentials down to –1 V *vs.* NHE ***Mo-1***-N_3 principally undergoes the electro-driven rearrangement of ***Mo-1*** {Mo_3S_7} core to new species featuring a {Mo_3S_4} core as supported by the raise of $\nu_2(N_3^-)_{co}$ = 2085 cm^{-1}.

Application of a more cathodic potential (–1.3 V *vs.* NHE, second reduction process) leads to the further raise of both the $\nu_1(N_3^-)_{co}$ and $\nu_2(N_3^-)_{co}$ shoulders together with the marked decrease in the $\nu(N_3^-)_{free}$ antisymmetric stretching band (***Figure 3.22*** top right, purple curves). In addition we do observe the concomitant increase in the signature of $\nu(NH_3)$ stretching bands between 2500 cm^{-1} and 3500 cm^{-1} indicating that the system starts evolving NH_3 with moderate rates (***Figure 3.22*** bottom right, gray curves).

Further lowering the potential to –1.5 V *vs.* NHE, leads to a rapid decline of both $\nu_1(N_3^-)_{co}$ and $\nu_2(N_3^-)_{co}$ components as well as the antisymmetric stretching band $\nu(N_3^-)_{free}$ associated with the free azide. Concomitantly the intensity of the $\nu(NH_3)$ stretching bands of ammonia largely increases (***Figure 3.22*** bottom red curves) indicating catalytic EN_3RR. Interestingly in this case as well, under catalytic conditions, we observe that the component centered at $\nu_1(N_3^-)_{co}$ = 2050 cm^{-1} is more affected and disappears before the component centered at $\nu_1(N_3^-)_{co}$ = 2085 cm^{-1}, again supporting a differentiated reactivity of the azido ligands of the catalytically competent {Mo_3S_4} species.

Briefly, ***Mo-1*** appears to be firstly converted to a ***Mo-2***-like species which is catalytically competent for EN_3RR. The similar IR spectra evolution discussed thorough this section strongly suggests that the EN_3RR is indeed supported by similar intermediates in both cases. The study of ***Mo-1*** is, thus, relevant but particularly challenging due to its structure evolution under reductive conditions.

3.2.3.5. Electro-driven catalytic reduction of azide with a-MoS_x

Having sketched a first draft showing the intricate relation between {Mo_3S_7} and {Mo_3S_4} species in the context of E_3NRR in homogeneous conditions, we wanted to know whether *a*-MoS_x could follow a similar evolution when used as a heterogeneous catalyst. To approach this question, we investigated the solid state FTIR of the material before and after running a potential controlled electrolysis in the conditions introduced in section 3.1.2 for investigating

EN$_3$RR on the various MoS$_x$ derivatives. The spectra were recorded on the Ge-ATR module which did not allowed the observation of the Mo-S core but was suitable for probing the signature of the azide.

As described in section 3.1, we prepared the WE by drop-casting an homogeneous suspension of *a*-MoS$_x$ in isopropanol (10 mg/L) on glassy carbon surface. After drying, the electrode was either simply immersed into a 10 mM solution of sodium azide 0.1 M KPi (pH = 5.8) for 1 hour (hereafter named ***a*-MoS$_x$**-N$_3^-$), or it was polarized at –0.2 V *vs.* RHE in 10 minutes in the 10 mM azide solution in KPi then left equilibrating without potential applied for one hour in the electrolyte (hereafter named ***a*-MoS$_x$**-N$_3^-$-red). The electrodes were then rinsed with mQ water, dried, and the catalyst was scraped off before recording a FTIR spectrum on the Ge-ATR module.

In ***Figure 3.23***, we can observe that the coordination of N$_3^-$ on *a*-MoS$_x$ is very similar to that of ***Mo-1***, which shares a similar {Mo$_3$S$_7$} core, only presenting $\nu_1(N_3)_{co}$ = 2050 cm^{-1}. After reduction, however, we clearly see the raise of a shoulder that can be attributed to $\nu_2(N_3)_{co}$ = 2080 cm^{-1} suggesting as well that part of the material now exhibit coordination modes reminiscent of the one observed in {Mo$_3$S$_4$} cores. The crude analysis of the evolution of IR spectra of coordinated N$_3^-$ on *a*-MoS$_x$ before and after polarization, strongly suggests that *a*-MoS$_x$ follow a similar process as ***Mo-1*** during EN$_3$RR, where some {Mo$_3$S$_7$} motifs will firstly be reduced to {Mo$_3$S$_4$}, then initiate the reduction of azides to ammonia.

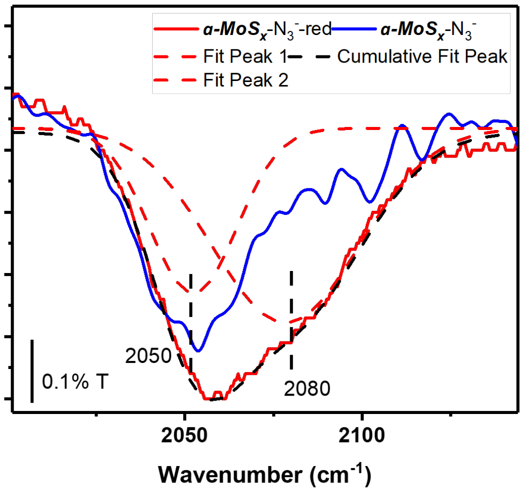

***Figure 3.23**: FT-IR spectra on Ge-ATR of asymmetric stretching of N$_3^-$ in solid sample of a-MoS$_x$ coordinated to N$_3^-$ or after using potential-controlled electrolysis (–0.2 V vs. RHE) of a 10 mM solution of sodium azide 0.1 M KPi solution.*

3.2.3.6. Conclusions

Through the study of EN$_3$RR on pristine {Mo$_3$S$_x$} clusters using electrochemistry and infrared spectroscopy, we can draw the following conclusions:

1. During the reduction of ***Mo-1***, the disulfide ligands S_2^{2-} of the $\{Mo_3S_7\}$ core undergo a reductive cleavage leading to μ_2-S ligands at –0.4 V vs NHE in DMF, thus forming $\{Mo_3S_4\}$-like species

2. $\{Mo_3S_4\}$-like species can complete the reduction of N_3^- after the reduction of Mo(IV) to Mo(III). After $\{Mo_3S_7\}$ is reduced to $\{Mo_3S_4\}$-like species, it goes through a similar eletrochemical driven N_3RR process.

3. There are two modes of coordination for N_3^- in $Mo_3S_4\}$-like species, leading to the observation of two distinct asymmetric stretching bands $\nu(N_3^-)_{co}$ in the IR spectra, as ν_1= 2050-2055 cm^{-1} and ν_2= 2080-2090 cm^{-1}.

4. In $\{Mo_3S_4\}$ species the azido ligand associated with ν_1 appears systematically more reactive than the ligand associated with ν_2 .

5. *a*-MoS_x which has a coordination polymer structure based on $\{Mo_3S_7\}$ units, catalyzes the EN_3RR process through a similar pathway to $[Mo_3S_7Br_6]^{2-}$, i.*e.* possibly undergoes a (partial) conversion of the $\{Mo_3S_7\}$ units to $\{Mo_3S_4\}$ units during the catalytic process.

3.3 Conclusions

In this chapter, we have investigated the electro-driven azide reduction (EN_3RR), which could efficiently occur on molybdenum sulfides catalysts (MoS_x).

The initial studies with different heterogenous MoS_x catalysts in aqueous environment, suggest that various forms of MoS_x do bear different type of catalytic sites, which in turn have noticeable impact on their EN_3RR rate and selectivity, especially upon doping with heterometals (Fe). Moreover, the well-defined $\{Mo_3S_7\}$ cluster derivatives exhibit comparable rates and better selectivity towards EN_3RR than amorphous *a/e*- MoS_x.

These molecular systems carrying $\{Mo_3S_7\}$ moieties offered the chance to study the EN_3RR in homogeneous environment and to monitor the process using classical analytical methods. Through these studies, we confirmed that the $\{Mo_3S_7\}$ units would firstly be reduced to $\{Mo_3S_4\}$ via the reduction of the μ_2-S-S ligands into μ_2-S ligands. The investigation of another cluster bearing $\{Mo_3S_4\}$ core, allowed to identify two coordination modes of the azido ligands using IR spectroscopy (ν_1= ~2055 cm^{-1} and ν_2= ~2085 cm^{-1}), and to reveal that the azido ligands associated to the ν_1 mode are more easily reduced to ammonia through a two electrons three protons processes. Interestingly the $\{Mo_3S_7\}$ core only display the ν_1 coordination mode and, after reduction to $\{Mo_3S_4\}$-like species, follows the same N3RR route as the original $\{Mo_3S_4\}$ cluster. Finally we could confirm that a-MoS_x, with a structure based on $\{Mo_3S_7\}$ clusters share the reactivity with isolated $\{Mo_3S_7\}$ species.

The relative (in)stability of these systems and the complexity of the catalytic process do not allow to give a definitive information on the exact nature of the two coordination modes of the N_3^- ligand; the evolution of the oxidation states of the $\{Mo_3S_x\}$ cores in the course of the reduction; the nature of the active sites; the nature of the intermediates such as the possible formation of Mo≡N species…. However this study did open some interesting questions which put a 'to be continued' to the end of this chapter.

Appendix 3: Mo_3S_x Cluster preparation and characterization

S3.1. Preparation

$[Mo_3S_{13}]^{2-}$ and $[Mo_3S_7X_6]^{2-}$ incorporating $[Mo_3S_7]^{4+}$ core were prepared according to established procedures ***(Scheme S3.1)***. [17](Müller et al. 1978)

turned into incomplete cubane-type $\{Mo_3S_4\}$ via reaction with PPh_3. The three equatorial sulfurs are removed by forming $S{=}PPh_3$, simultaneously PPh_3 coordinate to Mo instead. $\{Mo_3S_4\}$ reacts with a range of metals (M= Pd, Pt Ru, Ni, Fe..)(ref j.phyd.chem.c2008, 112, 17492-17498) and forms heterometallic complete cubane type of clusters, bringing versalities. $[Mo_3S_7Br_6]^{2-}$ was easily prepared from the reaction between $[Mo_3S_{13}]^{2-}$ and HBr (see

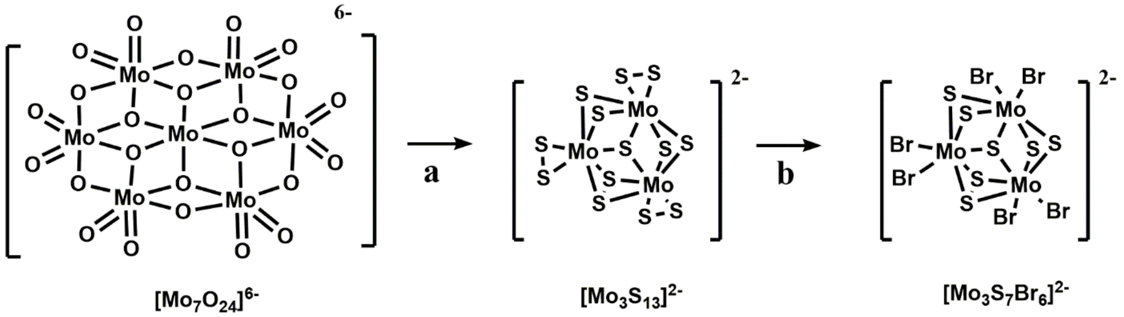

Scheme S3.1 *a. $NH_2OH.HCl$, S(s), $(NH_4)_2Sx$, 46°C 2h then filtrate 90°C overnight; b. HBr, reflux 127 °C, 20 mins, Ar, $(nBu)_4NBr$.*

details in section 2).

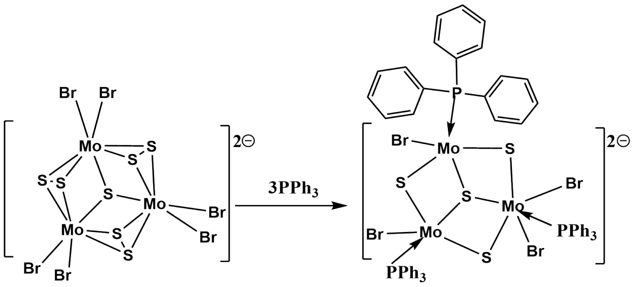

Scheme S3.2. *PPh$_3$, MeOH, 50°C, 2h*

The [$Mo_3S_4Br_4$]3PPh_3 was prepared from the [$Mo_3S_7Br_6$]$^{2-}$ by using 6 equivalents PPh_3 to eliminate the equatorial sulfur in μ_2-S_2^{2-} ligand with a high selectivity.(ref v.p.fe [14]) ***(Scheme S3.2)*** During the reaction, the orange solution turned green. As described in publication,[17] the three molybdenum (Mo) form a surface and the linked to one μ_3-S.

S3.2 Characterization

Infrared spectra

Different technics of IR have been applied targeting in different bands. For the region 4000 -400 cm^{-1} where we could see the bands of cluster core (400-600 cm^{-1}), the spectra was obtained with KBr pellets.In IR KBr spectra, we could easily observed that μ_3-Mo-S^{2-} presented in all the clusters as a wake band around 460 cm^{-1}; μ_2-S-S^{2-} showed in {Mo_3S_7} and {Mo_3S_{13}} ; and ter-S-S^{2-} only in {Mo_3S_{13}}.

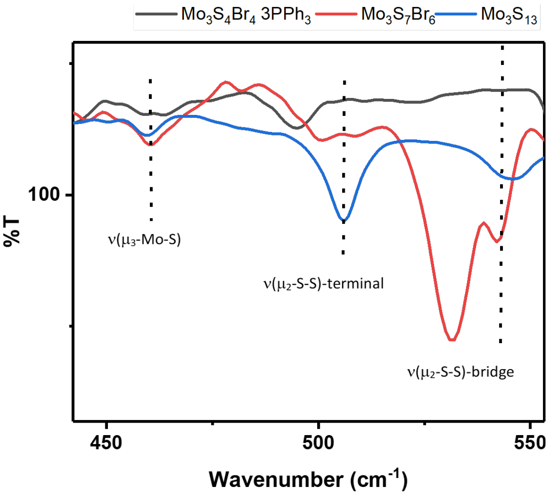

Table S2.1 *Infrared spectra (in KBr) important band data.*

Bond type	Wavenumber cm^{-1}		
	[Mo_3S_{13}]$^{2-}$	[$Mo_3S_7Br_6$]$^{2-}$	[$Mo_3S_4Br_4$]3PPh_3
μ_3-Mo-S^{2-}	459	462	467
μ_2-S-S^{2-}	547	540	-
ter-S-S^{2-}	506	-	-

References

(1) Seefeldt, L. C.; Yang, Z.-Y.; Lukoyanov, D. A.; Harris, D. F.; Dean, D. R.; Raugei, S.; Hoffman, B. M. Reduction of Substrates by Nitrogenases. *Chem. Rev.* **2020**.

(2) Milton, R. D.; Abdellaoui, S.; Khadka, N.; Dean, D. R.; Leech, D.; Seefeldt, L. C.; Minteer, S. D. Nitrogenase Bioelectrocatalysis: Heterogeneous Ammonia and Hydrogen Production by MoFe Protein. *Energy Environ. Sci.* **2016**, *9* (8), 2550–2554.

(3) Guevara, I.; Iwanejko, J.; Dembińska-Kieć, A.; Pankiewicz, J.; Wanat, A.; Anna, P.; Gołąbek, I.; Bartuś, S.; Malczewska-Malec, M.; Szczudlik, A. Determination of Nitrite/Nitrate in Human Biological Material by the Simple Griess Reaction. *Clin. Chim. Acta* **1998**, *274* (2), 177–188.

(4) Kertes, A. *Solubility Data Series*; Pergamon Press Oxford, 1979; Vol. 37.

(5) Vanysek, P. Electrochemical Series. *CRC Handb. Chem. Phys.* **2000**, *8*.

(6) Rosca, V.; Duca, M.; de Groot, M. T.; Koper, M. T. M. Nitrogen Cycle Electrocatalysis. *Chem. Rev.* **2009**, *109* (6), 2209–2244.

(7) Fehlhammer, W. P.; Beck, W. Azide Chemistry – An Inorganic Perspective, Part I Metal -Azides: Overview, General Trends and Recent Developments. *Z. Für Anorg. Allg. Chem.* **2013**, *639* (7), 1053–1082.

(8) Bayachou, M.; Elkbir, L.; Farmer, P. J. Catalytic Two-Electron Reductions of N2O and N3- by Myoglobin in Surfactant Films. *Inorg. Chem.* **2000**, *39* (2), 289–293.

(9) Dalmia, A.; Wasmus, S.; Savinell, R. F.; Liu, C. C. Electrochemical Behavior of Sodium Azide at Pt and Au Electrodes in Sodium Sulfate Electrolyte: A DEMS Study. *J. Electrochem. Soc.* **1995**, *142* (11), 3735–3740.

(10) Mitchell, P. C. H.; Scarle, R. D. Reaction of Azide Ion with Compounds of Molybdenum (III) and (V) and the Observation of Proton Hyperfine Splitting of Molybdenum E.S.R. Signals in a Model System. *J. Common Met.* **1974**, *36* (1), 501–511.

(11) Guo, J.; Tadesse Tsega, T.; Ul Islam, I.; Iqbal, A.; Zai, J.; Qian, X. Fe Doping Promoted Electrocatalytic N2 Reduction Reaction of 2H MoS2. *Chin. Chem. Lett.* **2020**.

(12) Tran, P. D.; Tran, T. V.; Orio, M.; Torelli, S.; Truong, Q. D.; Nayuki, K.; Sasaki, Y.; Chiam, S. Y.; Yi, R.; Honma, I.; Barber, J.; Artero, V. Coordination Polymer Structure and Revisited Hydrogen Evolution Catalytic Mechanism for Amorphous Molybdenum Sulfide. *Nat. Mater.* **2016**, *15*, 640.

(13) Artero, V. Bioinspired Catalytic Materials for Energy-Relevant Conversions. *Nat. Energy* **2017**, *2* (9), 17131.

(14) Barrière, F.; Geiger, W. E. Use of Weakly Coordinating Anions to Develop an Integrated Approach to the Tuning of ΔE1/2 Values by Medium Effects. *J. Am. Chem. Soc.* **2006**, *128* (12), 3980–3989.

(15) Cotton, F. A.; Diebold, M. P.; Dori, Z.; Llusar, R.; Schwotzer, W. The Cuboidal Mo4S46+ Aquo Ion and Its Derivatives. *J. Am. Chem. Soc.* **1985**, *107* (23), 6735–6736. https://doi.org/10.1021/ja00309a066.

(16) Llusar, R.; Polo, V.; Velez, E.; Vicent, C. Sulfur-Based Redox Reactions in Mo3S74+ and Mo3S44+ Clusters Bearing Halide and 1,2-Dithiolene Ligands: A Mass Spectrometric and Density Functional Theory Study. *Inorg. Chem.* **2010**, *49* (17), 8045–8055.

(17) Fedin, V. P.; Sokolov, M. N.; Mironov, Yu. V.; Kolesov, B. A.; Tkachev, S. V.; Fedorov, V. Ye. Triangular Thiocomplexes of Molybdenum: Reactions with Halogens, Hydrohalogen Acids and Phosphines. *Inorganica Chim. Acta* **1990**, *167* (1), 39–45.

(18) Dori, Z.; Ziolo, R. F. Chemistry of Coordinated Azides. *Chem. Rev.* **1973**, *73* (3), 247–254.

(19) Nakamoto, K. *Infrared and Raman Spectra of Inorganic and Coordination Compounds, Part B: Applications in Coordination, Organometallic, and Bioinorganic Chemistry*; John Wiley & Sons, 2009.

(20) Müller, A.; Sarkar, S.; Bhattacharyya, R. G.; Pohl, S.; Dartmann, M. Directed Synthesis of [Mo3S13]2−, an Isolated Cluster Containing Sulfur Atoms in Three Different States of Bonding. *Angew. Chem. Int. Ed. Engl.* **1978**, *17* (7), 535–535. https://doi.org/10.1002/anie.197805351.

4. Towards well-defined polymetallic sulfides

4.1 Porphyrin Ligands

As we described in chapter 3, {Mo_3S_7} clusters exhibit EN_3RR activity under reductive conditions when used as both homogeneous and heterogeneous catalysts. However, under homogeneous conditions the detailed study of these systems is complicated by their relative instability especially when decorated with labile monodentate ligands such as bromine. Herein, we intend to describe our efforts to develop new cavity-like ligand scaffolds for isolating and stabilizing the {Mo_3S_7} clusters, or from a more ambitious point of view, tuning the clusters activity.

In enzymes, the inorganic cofactors supporting the catalytic activity are usually protected by a complex protein scaffold. The protein environment is critical to control the reactivity and selectivity of the catalytic center, which is particularly important for complex reactions such as NRR. As mentioned before, protons are required reagents for NRR but are obviously the source of a major competitive reaction namely the HER. For the design of synthetic catalysts for NRR, a fine control of the interactions between the protons, the catalytic center and nitrogen is important. Encaging polymetallic sulfide clusters within controlled environments by the use of synthetic macromolecular ligands could allow *in fine* for such an exquisite control. If the *ad hoc* design of such functional ligand is out of reach at first, following a systematic approach while gradually increasing the ligand complexity appears to be the best way to understand the factors that influence the reactivity of the clusters, and ultimately rationally optimize their catalytic activity.

With the idea of designing such ligand system as a far-end goal, we first focused on the design of basic cavity-like tridentate macromolecular ligands[1], which may be able to accommodate the {Mo_3S_7} core within a binding pocked of suitable size and geometry. Targeting the stabilization of a trinuclear molybdenum clusters, we considered ligand possessing a C_3 symmetry.

Cavity-like ligand sets have been proposed and successfully applied to stabilize different biomimetic metal complexes and clusters.[1,2] Usually polydentate ligands offers more robust coordination sphere for metal centers, and thus, permits a better stabilization of the intermediates during catalytic reactions. To be noticed, the binding between ligands and clusters should be strong enough, while leaving open coordinating sites for substrates as well. Within more functionalized ligand sets, more subtle interplay between the metal centers and ligands could be implemented. For instance, the second and the third coordination spheres could potentially tune the activity through key steps such as substrate binding and preorganization, stabilization of transition states, activation of intermediates, as well as ease the release of the products. Furthermore, for their use as electrocatalysts, active hybrid cluster-ligand assemblies should ideally offer simple strategies for their immobilization onto electrochemically active surfaces.[3]

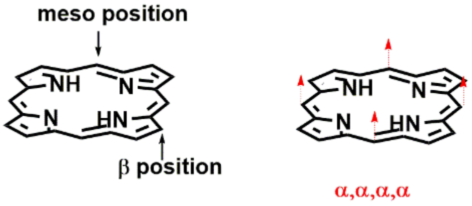

Figure 4.1 Different positions in porphyrins (a); different conformation of porphyrins (b).

With the above considerations in mind, porphyrin derivatives were chosen as a platform for designing a new class of cavitands adapted to the complexation of trinuclear molybdenum sulfides clusters.[4] These planar macrocycles are composed of four pyrrole units and offer a stable aromatic system with a well-known chemistry. Porphyrin derivatives possess advantages such as: 1) The possibility of introducing various peripheral substituents on their so-called *meso*-positions ***(Figure 4.1)*** to form well-defined cavities. In the following, the cluster-coordination side of the porphyrin plane is referred to as ‘α’ and the opposite side as ‘β’.

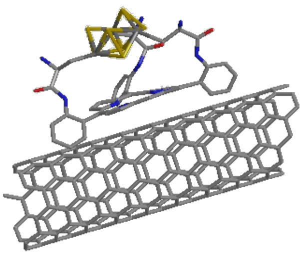

Figure 4.2 *Proposed synthetic molecular catalyst on CNT.*

2) Their planar aromatic macrocycles provide a base (‘β’ side), which can strongly adsorb on graphitic materials and be immobilized on electrochemically active surface by π-π interaction. [5-7]***(Figure 4.2)***

4.1.1 Ligand selection

4.1.1.1 First ligand model H_2-1o-a

Inspired from the "picket fence porphyrins" proposed by Collman et al. in 1974,[6] we firstly considered the meso-tetrakis(amino-phenyl)porphyrins. 2-Aminophenyl substituted porphyrins derivatives appeared as obvious building blocks, thanks to the possibility to introduce a variety of substituents via simple reactions with the amino groups such as amide coupling, nucleophilic substitutions etc….[7] Upon substitution of the 2-aminophenyl positions, bulky side chains can block the rotation around the porphyrin-phenyl bond leading to the formation of stable conformers. In our case the orientation of all side chains on the same plane of the porphyrin is be needed to form an appropriate binding pocket, in other words the α,α,α,(α)-conformation is required for the cluster assembly ***(Figure 4.2)***.

Short amide-linked chains appears as ideal substituents for building a competent binding pocket for $\{Mo_3S_7\}$:[7] 1) a variety coupling agents and synthetic strategies are available ; 2) their mild preparation condition will not change the established α,α,α,(α)-conformation of the 2-aminophenyl substituents. An interesting observation is that in nitrogenases, the protein scaffold coordinates to the cofactor via cysteine and histidine residues, which guided us for the initial choices binding motifs for our synthetic scaffold. Imidazole substituents, which can be considered as proxy of histidine, were thus chosen to be the end groups to bind the $\{Mo_3S_7\}$ clusters.

To wrap up the above ideas, we proposed a first ligand model, **H_2-1o-a,** as a meso-tetrakis(amino-phenyl)porphyrin whose four phenyl groups on meso positions are substituted by amide-linked side chains derived from the ortho positions, three of which carrying an imidazole coordinating sites, while leaving the last one deactivated for future post functionalization (***Figure 4.3***).

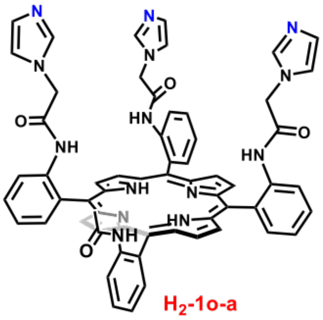

Figure 4.3: H_2-1o-a.

4.1.1.2 Other ligands models

In addition to **H_2-1o-a**, we considered several additional ligand scaffolds in which the position and nature of the side chains were altered to probe the effects of different parameters on the binding efficiency of the latter with {Mo_3S_7} (***Figure 4.4***):

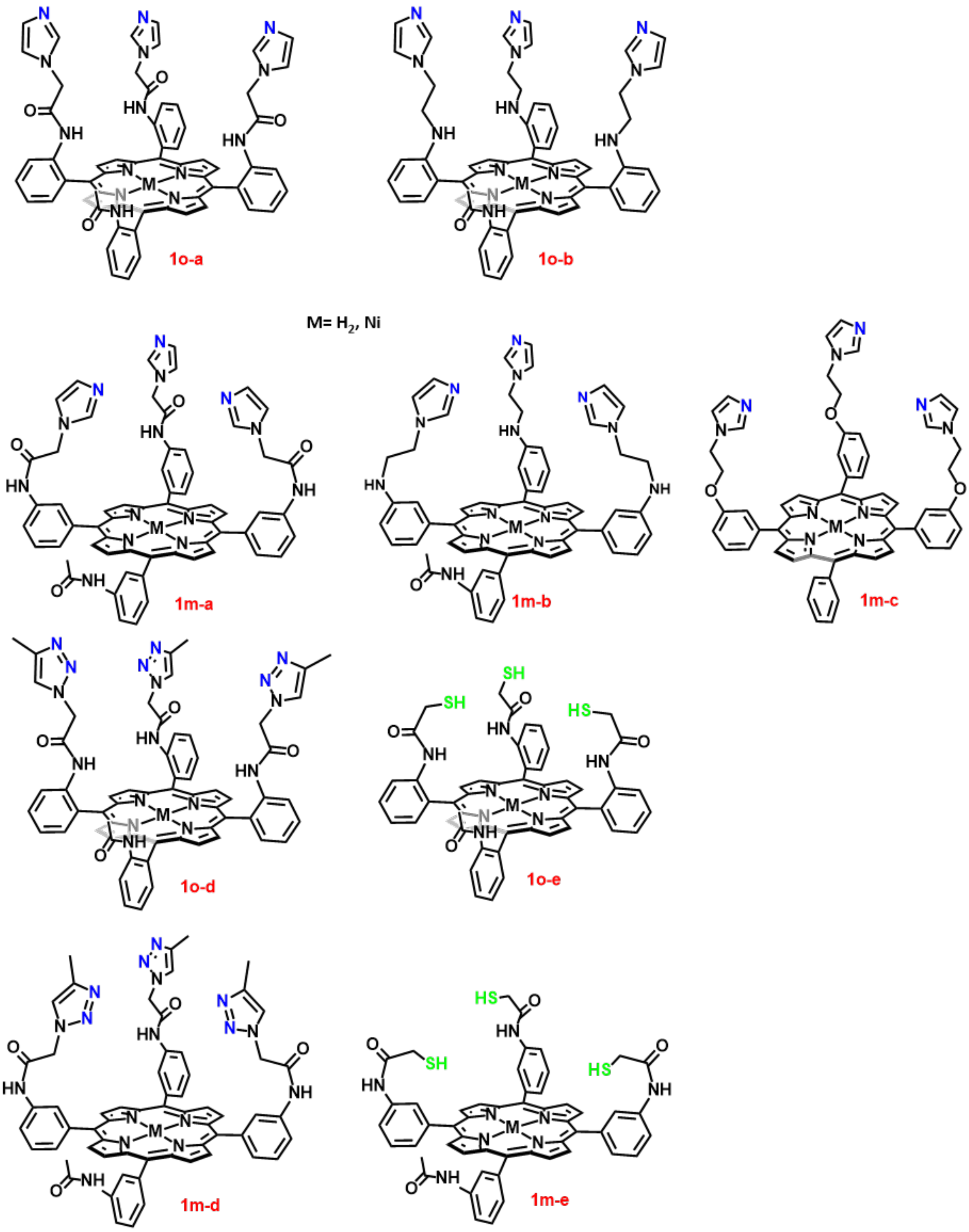

Figure 4.4: *Different porphyrin-based ligands screened.*

1. Geometric constraints. Firstly, porphyrin scaffolds featuring meta-substituted instead of ortho-substituted phenyls were considered, as in **H_2-1m-a,** in which the rotation of the phenyl substituents are not be restricted anymore. Secondly, the introduction of flexible aminoethyl linkers between the phenyl substituents and the imidazole moieties, instead of the acetamide linker was considered as in **H_2-1o-b** and **H_2-1m-b**. Further increasing the flexibility of the ligands by introducting an ether- instead of the amino-linker was also considered as **H_2-1m-c**.

2. Coordination versatility. Next the substitution of the imidazoles by triazoles, bearing two potential nitrogen binding sites each, was evaluated as **H_2-1o-d** and **H_2-1m-d**.

3. Effect of the charge. We also considered the introduction of ionizable side-groups (SH) to ease the substitution of Br^- in $[Mo_3S_7Br_6]^{2-}$, as **H_2-1o-e** and **H_2-1m-e**.

4. Metallation of the porphyrin macrocycle. Additionally for all the ligands proposed we considered the effect of the metalation the porphyrin center on the binding efficiency with with $\{Mo_3S_7\}$ core.

The actual preparation of all these ligands being unrealistic within the timeframe of this work, we turned to theoretical calculations to guide our choices *via* an *in-silico* screening aimed to designate the most promising structures for binding trinuclear molybdenum sulfide clusters and specifically ***Mo-1***.

4.1.2 *In-sillico* guided ligand selection

In collaboration with Martin Fields (CBM) we systematically evaluated the relative binding energy of ***Mo-1*** with the different porphyrin-based ligands proposed following the approach succinctly described below:

1. Molecular Mechanics (MM) was first used to explore the accessible and most plausible structures of one-to-one triligated clusters; the association between the cluster and the ligands involved the direct substitution of 3 bromide ligands of the $[Mo_3S_7Br_6]^{2-}$with the binding motifs of the ligand considered. Two modes of coordination were explored in each

case, where the cluster is oriented with its μ_3-S ligand facing towards or opposite to the porphyrin macrocycle and which are named down- or up-orientations, respectively.

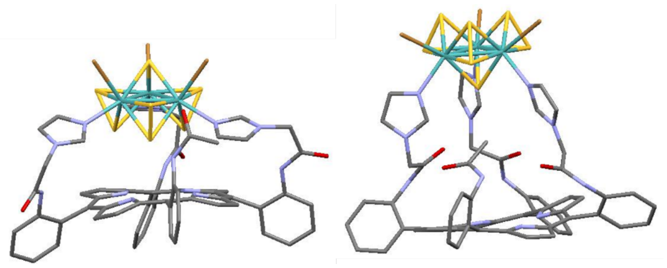

Figure 4.5: *up-(left)/down-(right) orientated {$Mo_3S_7Br_3$} assembled to* ***H_2-1o-a****.*

2. Density Functional Theory (DFT) was then applied to optimize the selected geometries (using acetonitrile as an implicit solvent); importantly in these calculations triligated species were considered, thus, three bromides are lost by the cluster. In the case of neutral binding sites, the overall ligand-cluster assembly are mono-cationic, and in the case of ionizable thiol binding sites the species remained bi-anionic.

The relative binding energy of each complex was then calculated through the difference between the energy of the 1:1 assembly (obtained as described above) and the energy calculated for the ligand and clusters taken separately using:

for neutral ligands

$$\Delta E = (E_{[\text{Ligand: } Mo_3S_7Br_3]^{+}\text{DFT}} + 3*E_{Br^-}) - (E_{\text{Ligand DFT}} + E_{[Mo3S7Br6]^{2-}\text{ DFT}})$$

or in the case of anionic thiolated ligands

$$\Delta E = (E_{[\text{Ligand: } Mo_3S_7Br_3]^{2-}\text{ DFT}} + 3*E_{HBr}) - (E_{\text{Ligand DFT}} + E_{[Mo3S7Br6]^{2-}\text{ DFT}})$$

We summarized the obtained ΔE for different complexes in **Table 4.1**.

1) Firstly, we found that generally the up-oriented conformation appears to be more stable

Table 4.1 *Relative binding energies of* ***Mo-1*** *to* **MP** *ligands using theoretical calculations.* ***Mo-1_u*** *refers to the up orientation of the cluster* ***Mo-1_d*** *to the down orientation within the complexes.*

M	H_2-1o-a kJ.mol^{-1}		H_2-1m-a kJ.mol^{-1}	H_2-1o-b kJ.mol^{-1}	H_2-1m-b kJ.mol^{-1}	H_2-1m-c kJ.mol^{-1}	H_2-1o-d kJ.mol^{-1}	H_2-1m-d kJ.mol^{-1}	H_2-1o-e kJ.mol^{-1}	H_2-1m-e kJ.mol^{-1}
	Mo-1_u	*Mo-1_d*	*Mo-1_u*	*Mo-1_u*	*Mo-1_u*	*Mo-1_u*	*Mo-1_u*	*Mo-1_u*	*Mo-1_u*	*Mo-1_u*
H_2	**94**	**178**	**-9**	**136**	**-60**	**-72,8**	**123**	**37**	**206**	**149**
Zn	**93**	**143**	**-25**	**140**	**-78**	**-86,9**	**169**	**22**	**188**	**140**
Ni	**88**	**155**	**-34**	**66**	**-96**	**-91,7**	**--**	**--**	**--**	**--**

than the down analogues (with the noticeable exception of **H_2-1o-b**, which we did not consider it in this work). Here in this table, we focused on the ΔE of ***Mo-1*** assembled in up-orientation, but only left the **H_2-1o-a-*Mo-1*_d** as an example to show the difference of ΔE between up- and down- orientations.

2) Overall the decrease of the geometric constraints of the side chains as observed in the series of **H_2-1o-a** > **H_2-1m-a** > **H_2-1m-b** > **H_2-1m-c**, leads the a gradual lowering of the free energy of the complexes (increasingly negative ΔE), which indicates that the increase of flexibility of side chain in H_2P ligands led to an easier coordination to ***Mo-1.***
3) However, the increased coordination versatility of triazole (**H_2-1o-d** > **H_2-1o-a**); or the introduction of charged binding sites (**H_2-1m-e** > **H_2-1m-a**) do not favor the coordination.

4) Additionally, the metalation of the porphyrin often led to an unexpected lowering of the binding energy with the cluster as well, even though no coordination between the metal center (Zn/Ni) and the sulfide ligands in cluster was observed. It is difficult to this stage to fully explain this effect which will require a more in-depth analysis.

From the above analysis, we selected a series of ligands derived from **H_2-1o-a** featuring decreasing geometry constraints (**H_2-1m-a, H_2-1o-b, H_2-1m-b,** and **H_2-1m-c**), as our first synthetic targets (***Figure 4.6***).

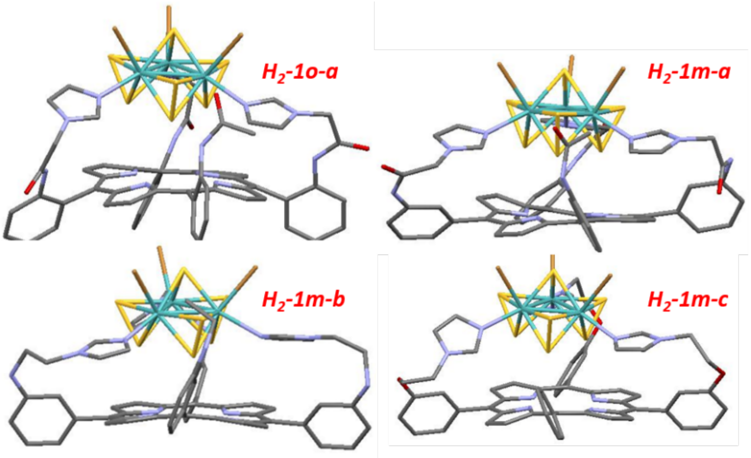

Figure 4.6: *Up-orientated {$Mo_3S_7Br_3$} assembled to **H_2-1o-a, H_2-1m-a, H_2-1m-b, H_2-1m-c**.*

4.2 Preparation of porphyrin ligands

4.2.1 First ligand prototype (H_2-1o-a)

4.2.1.1 2-Aminophenyl substituted porphyrin preparation

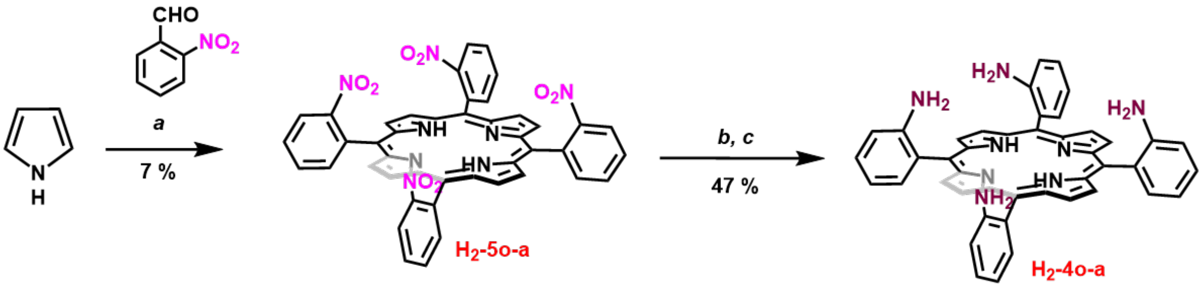

Scheme 1: *a) AcOH, 120-130 °C, 20 min; b) $SnCl_2·2H_2O$, HCl, 65-70 °C, 1 h, NH_4OH_{aq}; c) SiO_2, toluene, 100°C, 4-5h Ar.*

The synthesis of a tetra substituted porphyrin was conducted with a 'one pot' strategy inspired by the work of Collman et al[6] and depicted on ***Scheme 1***. Starting with the condensation of pyrrole and 2-nitrobenaldehyde in acetic acid, the tetrakis-(2-nitrophenyl) porphyrins (**H_2-5o-a**) was obtained as a mixture of the four possible atropisomers (α,α,α,α; α,α,α,β; α,α,β,β and α,β,α,β). Without separation, all **H_2-5o-a** were reduced to obtain the (2-aminophenyl) porphyrins. The mixture of amino-porphyrins was then annealed in presence of silica, to increase the fraction of desired α,α,α,α-tetrakis-(2-aminophenyl) porphyrin (**H_2-4o-a**) in the mixture which was easily separated from the other atropisomers using column chromatography.[8]

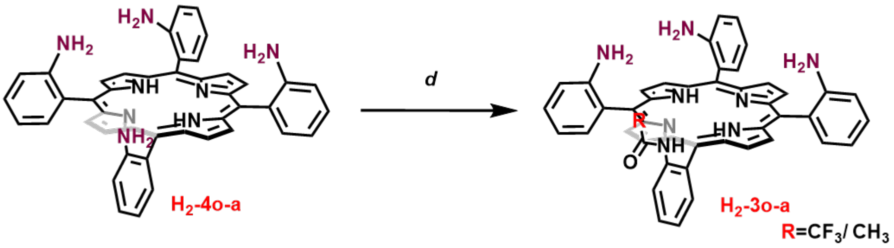

Scheme 2 *d-1) CF_3COOH, DCM, rt, overnight.(28%); d-2) $ClCOCH_3$, K_2CO_3, DCM, 0 °C(30-36%).*

Next **H_2-4o-a** was mono-acetylated to protect one of the four available amino groups. Firstly we considered the possibility to introduce a trifluoroactate substituent, due to the ease its hydrolysis under mild conditions for a potential postfunctionalisation of the final ligands. For that, **H_2-4o-a** was treated with trifluoroacetic acid anhydride (TFAA) in the presence of a base.[9] However, the reaction mixture was rather complicated. It is possible that the isomerization occurred due to the impact on amino groups from the strong acidic TFA. Overall, the desired product was obtained with a maximum yielded of 28%.

Next, we turned to simple acetyl group instead. The reaction with acetyl chloride produced less byproducts and allowed the preparation of the desired product in 30-36% yield with 0.75-0.8 equivalent of acetyl chloride added. Impotently in this case nearly half of the starting materail was recovered for each reaction which could be recycled later on.

4.2.1.2 Imidazole substituted porphyrins

Two strategies were then evaluated to introduce the imidazole groups on the periphery of the porphyrin: 1) via nucleophilic substitution of 1H-imidazole on halogenated derivatives; 2) via amide bond formation between the 2-aminophenyl substituents of the porphyrin and 1H-imidazole-1-acidic acid (IAA).

Via nucleophilic substitution [10]

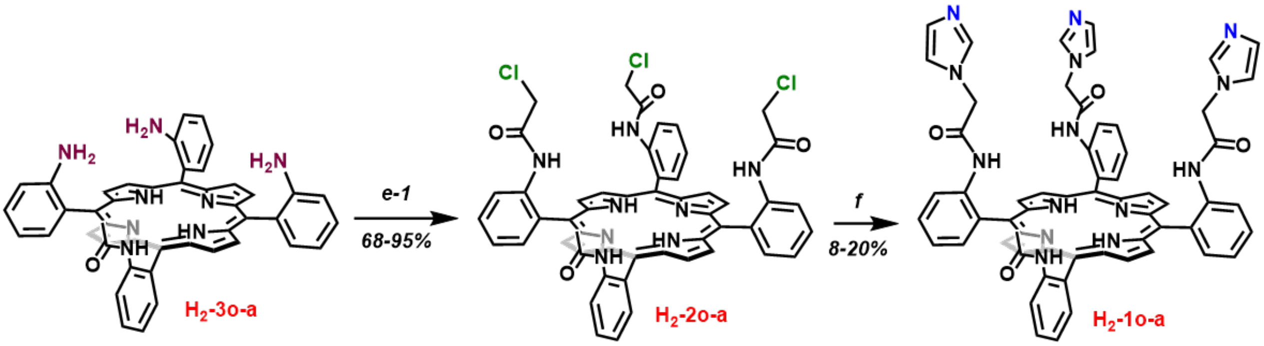

Scheme 3 *e) $ClCOCH_2Cl$, K_2CO_3, DCM, 0 °C; f) imidazole, K_2CO_3, DMSO, 55 °C, overnight.*

The three free amines were firstly reacted with chloroacetyl chloride in the presence of a base to obtain the trichloro derivative **H_2-2o-a**. Then the nucleophile attack of imidazole towards **H_2-2o-a** was attempted. In our initial test we followed a two-step approach. Imidazole was treated with NaH in THF to generate the highly nucleophile sodium imidazolate which was then reacted with the trichloro porphyrin derivative. The latter had been metalated with zinc acetate beforehand to avoid the possible deprotonation of the porphyrin core when exposed to imidazolate. This strategy led to unsatisfactory yields in all cases. Next, we tried to react imidazole directly with the trichloro-porphyrin derivative in presence of potassium carbonate, which led to a moderate yield of imidazole substitution (8-20%). In an attempt to improve this step, an iodinated derivative **H_2-2o-a_1** was prepared by simple treatment of **H_2-2o-a** with KI in acetone. ***(Scheme 3)*** Unfortunately, further reaction of the triiodinated derivative with imidazole in presence of a base led to a complex mixture of products mostly resulting from the degradation of **H_2-2o-a_1** into unidentified products. Therefore, this strategy was dropped.

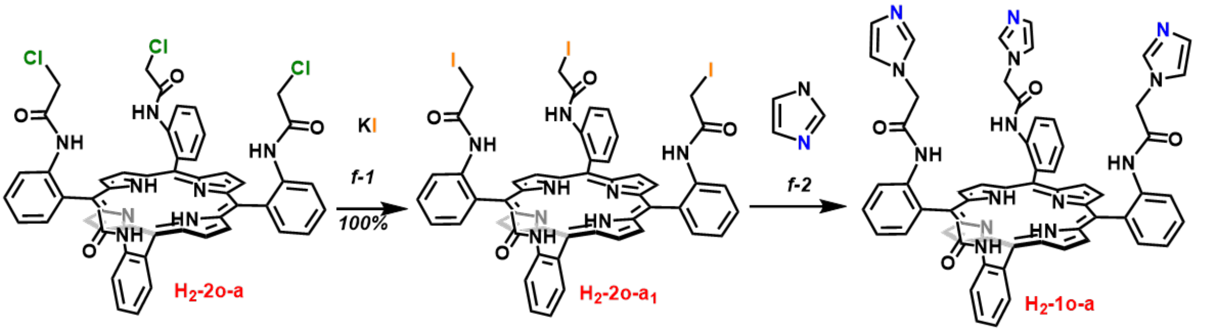

Scheme 4 *Optimization study with an iodinated derivative H_2-2o-a_1 Acetone, overnight, under dark; e' Acetone, rt, 3h 0% yield.*

Via amide coupling

The 1H-imidazole-1-acidic acid (IAA) was reacted as an electrophilic reagent on **H_2-3o-a** with the assistance of different coupling reagents, in presence of a base (N,N-diisopropylethylamine DIPEA in this case). We tested different classical coupling agents

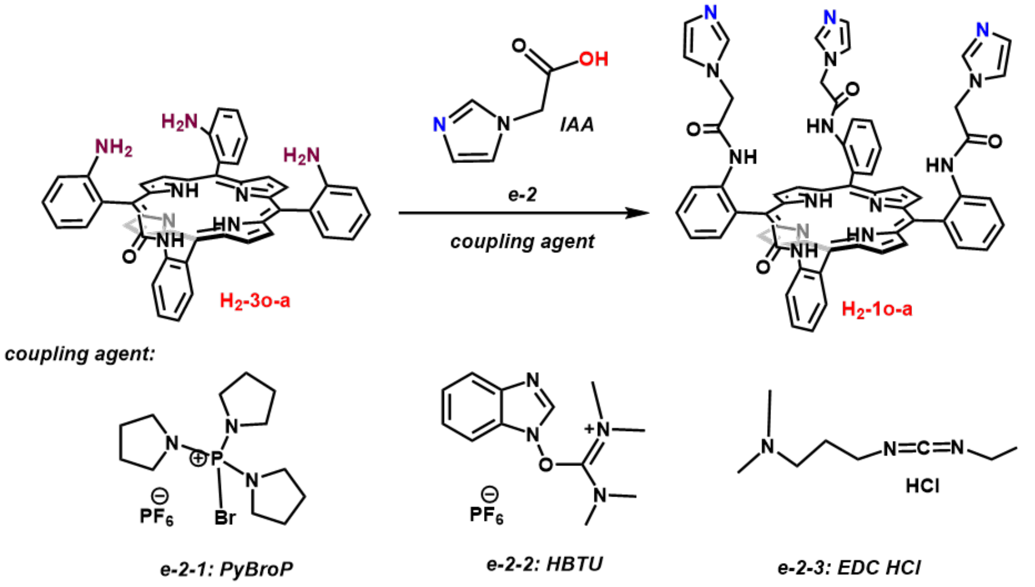

Scheme 5 e-2-1) *DIPEA, DMF, 35°C, Ar, 24 h**;** **e-2-2)** DIPEA, DMF, 35°C, Ar, 24 h; **e-2-3)** DIPEA, DMF, 0- 35°C, Ar, 24 h.*

(PyBrop, HBTU, EDC·HCl*[1]) mentioned above, however only leading to complex mixture of compounds with unsatisfying rates.

Instead, the preparation of the 1H-imidazole-1-acyl chloride from the treatment of IAA with oxalyl chloride, in presence of a catalytic amount of DMF, was successfully achieved within 1 hour. The later derivative was then reacted smoothly on **H_2-3o-a** to give the desired product **H_2-1o-a** in 66% yields. (***Scheme 6***) This approach was selected for the final step since it is rapid and clean.

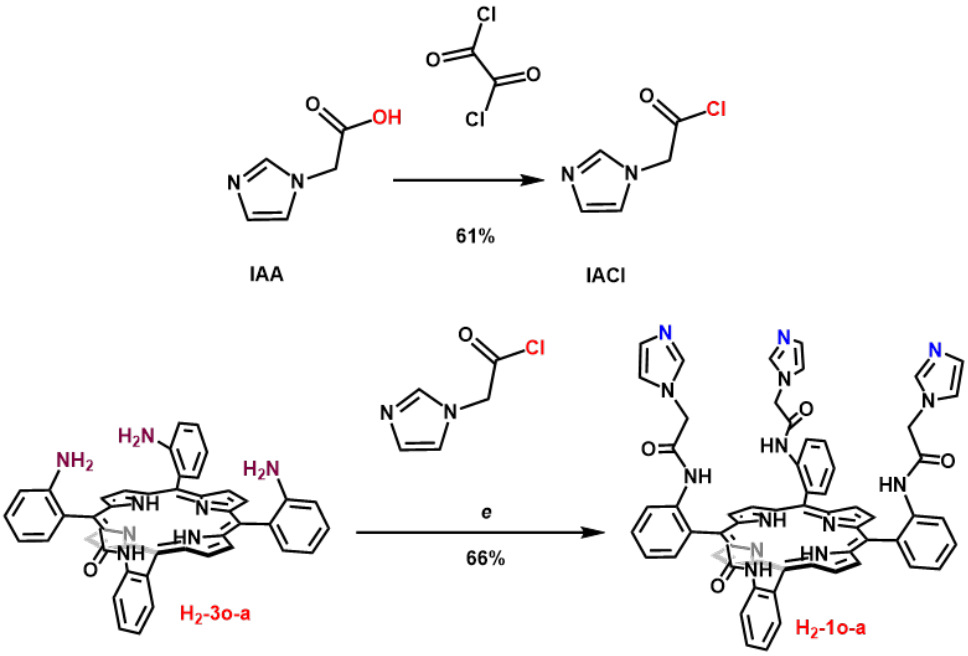

Scheme 6 *e) DCM, 40°C, 1h, Ar; DIPEA, DMF, rt, 2h, Ar.*

Our optimized protocol for preparation of **H_2-1o-a** is depicted in ***Scheme 7***, and allows to prepare ~100 mg of the desired ligand in five-steps with an overall yield of 0.8%.

---

[1] *Bromo-tris-pyrrolidino-phosphonium hexafluorophosphate **(PyBroP)**, N-(3-Dimethylaminopropyl)-N'-ethylcarbodiimide hydrochloride **(EDC HCl);** N,N,N',N'-Tetramethyl-O-(1H-benzotriazol-1-yl)uronium hexafluorophosphate **(HBTU).**

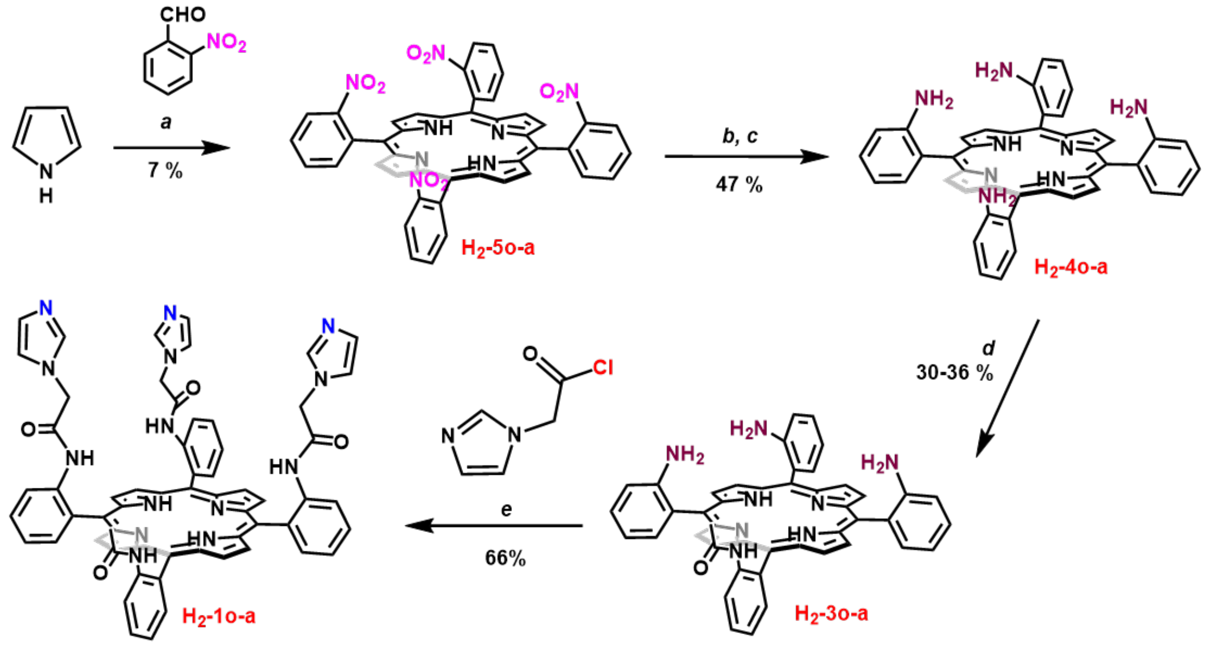

Schema 7: *a) AcOH, 120-130 °C, 20 min, O_2; b) $SnCl_2 \cdot 2H_2O$, HCl, 65-70 °C, 1 h, NH_4OH_{aq}; c) SiO_2, toluene, 100°C, 4-5h Ar; d) $ClCOCH_3$, K_2CO_3, DCM, 0 °C, 30 min; e) DIPEA, DMF anhydrous, rt, 2h Ar.*

4.2.2 Other ligand preparations

4.2.2.1 meta substituted H_2-1m-a

The meta substituted **H_2-1m-a** was prepared following the main steps of the procedure described for the ortho homologue **H_2-1o-a**, using 3-nitrobenzaldehyde instead of 2-nitrobenzaldehyde for the porphyrin condensation. In the absence of steric constraints limiting the rotational freedom of the phenyl substituents, no atropismers were stable at

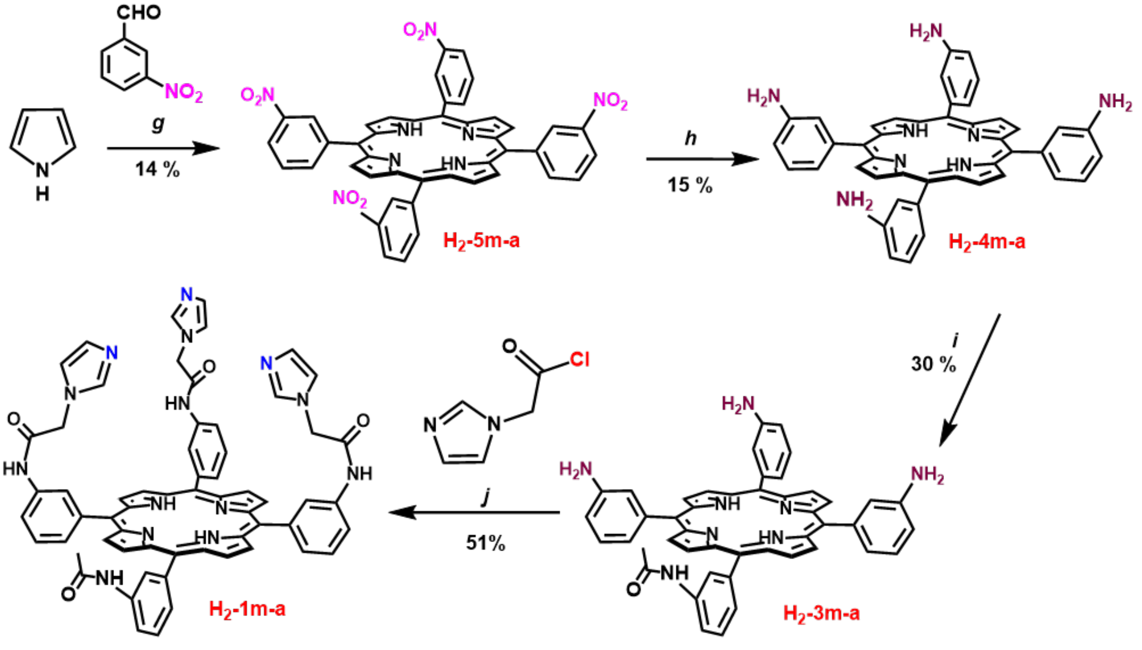

Schema 8: synthesis of H_2-4m-a: *g) AcOH, 120-130 °C, 20 min, O_2; h) $SnCl_2 \cdot 2H_2O$, HCl, 65-70 °C, 1 h, NH_4OH_{aq}; i) $ClCOCH_3$, K_2CO_3, DCM, 0 °C, 30 min; j) DIPEA, DMF anhydrous, rt, 2h Ar.*

room temperature and above. Therefore, the step c could be bypassed. However, the reduction of **H_2-5m-a** produced more side products and led to a rather low **15%** yield of the tetramino porphyrin. Moreover, **H_2-4m-a** was found to yield larger quantity of multi-substituted acetyl derivatives during the mono acetylation step d which led us to lower down the quantity of acetyl chloride used to ~0.7 equivalent to keep a reasonable yield of the desired product (***Schema 8***). We are able to prepare ~50 mg of the desired ligand in four-step with an overall yield of 0.3%.

4.2.2.2 meta-substituted amino linked H_2-1m-b

To obtain more flexible ligands, we intend to prepare meta-substituted amino linked **H_2-1m-b**, for which two approaches were considered: 1) Reduction of the secondary amide in **H_2-1m-a**; 2) Alkylation of amino groups in **H_2-3m-a**.

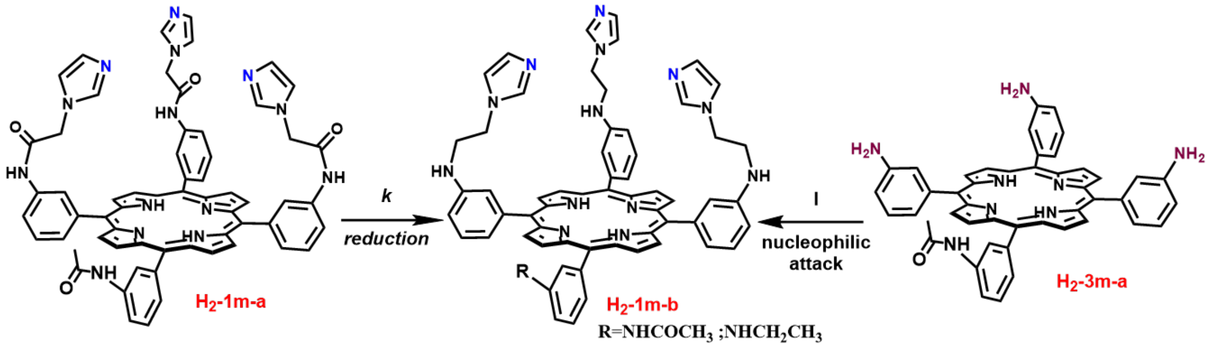

***Schema 9** k, l) see below.*

Reduction of secondary amide

Having successfully prepared the **H_2-1m-a** ligands provided us a chance to prepare the amine linked **H_2-1m-b** through one step reduction. Here we tested different approaches including (conditions in ***Schema 10***): 1) The reduction of the amide via an hydrosilylation catalyzed by lewis acids such as $IrCl_3$, $ZnCl_2$, $Zn(OTf)_2$ and ruthenium polycarbonyl complexes such as $Ru_3(CO)_{12}$.[11,12] However, none of the conditions tested led to the desired products

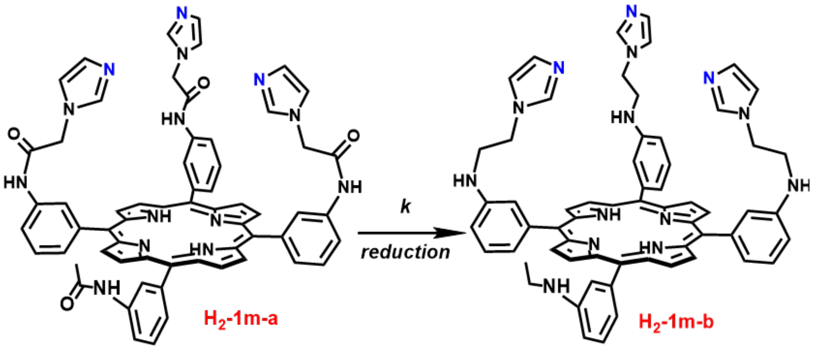

***Scheme 10** k-1) silane, catalyst, 1,4-dioxane, 40°C, 24h, Ar; k-2) hydrides, 1,4-dioxane, 40°C, 24h, Ar.*

(***Table 4.2***). 2) Besides, hydrides have been proposed as a possible reductants as well to convert amides to amines.[13] However, in our case the use of Lithium aluminum hydride ($LiAlH_4$) only resulted in the cleavage of the amide bonds. So far, we have not found proper conditions to prepare the desired amine-linked ligand from the parent **H_2-1m-a** derivatives.

Table 4.2 *Reduction of amide to amine. Silane tested:Tetramethylsilane (TMS); Tetramethyldisiloxane (TMDS).*

Reaction type	Reductant	Catalyst	Results
Hydrosilylation (*g-1*)	TMS	$IrCl_3$	×
	TMS	$ZnCl_2$	×
	TMDS	$Zn(OTf)_2$	×
	TMDS	$Ru_3(CO)_{12}$	×
Hydrides (*g-2*)	$LiAlH_4$	-	×

Electrophilic attack on amino group H_2-3-a

1-(2-bromoethyl)-1H-imidazole (IBr)

Firstly, we considered the reaction between 1-(2-bromoethyl)-1H-imidazole (IBr) and the aminophenyl substituents of **H_2-3m-a** as a straightforward strategy to obtain the desired amino linked **H_2-1-b** ligands. Following an established procedure, we prepared the 1-(2-bromoethyl)-1H-imidazole (IBr) from the reaction between imidazole and 1,2-dibromoethane[14]**,** albeit with a very low yield (8%). Next ImiBr was reacted, in presence of $CsCO_3$ with the **H_2-3-a** derivatives. However, the aminophenyl subsitutents were not alkylated, even under reflux conditions in acetonitrile. Alternatively, NaH, was used to deprotonate the aminophenyl groups for promoting a subsequent nucleophilc attack towards ImiBr. Unfortunately, it only resulted in the hydrolysis of the acetyl groups and no traces of even

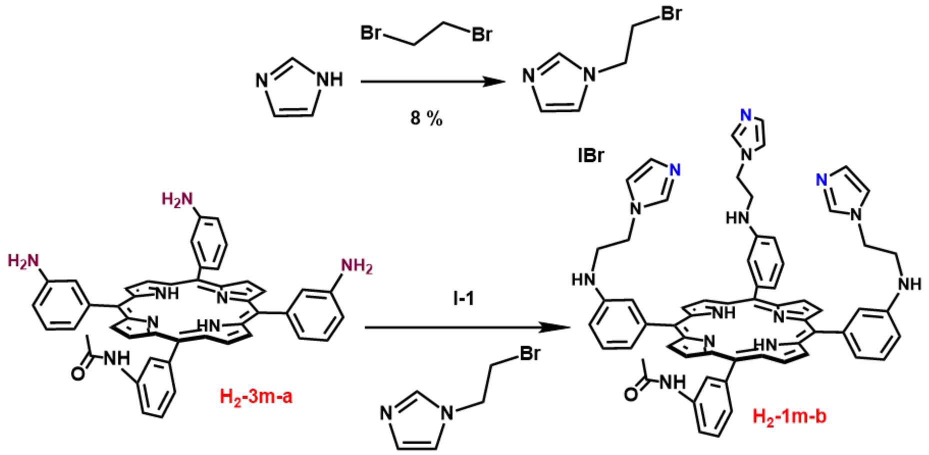

Scheme 11 *l-1) ACN, 80 °C, 5h, Ar; $CsCO_3$/NaH, DMF, from 0 °C to rt, 24h, Ar.*

partially alkylated aminophenyl porphyrin could be observed. Thus, this path did not appear to be valid for the preparation of the desired **H_2-1m-b**.

Via sulfonates

Sulfonyl ester groups leaving groups were next considered. Herein, we reacted 2-(1H-imidazole-1-yl)ethanol with methyl-/tosyl- sulfonate chloride, in presence of a base ($CsCO_3$, NaH) to prepare the corresponding sulfonic esters low to medium yield (yield~20% for methylate-; 50% for tosylate-). Unfortunately, initial tests with an aniline analogue (4-methylaniline) showed that both sulfonyl ester derivatives led to complex mixtures of products in all conditions tested. Thus, this path was also dropped.

So far, we have not found a proper pathway to prepared **H_2-1m-b**.

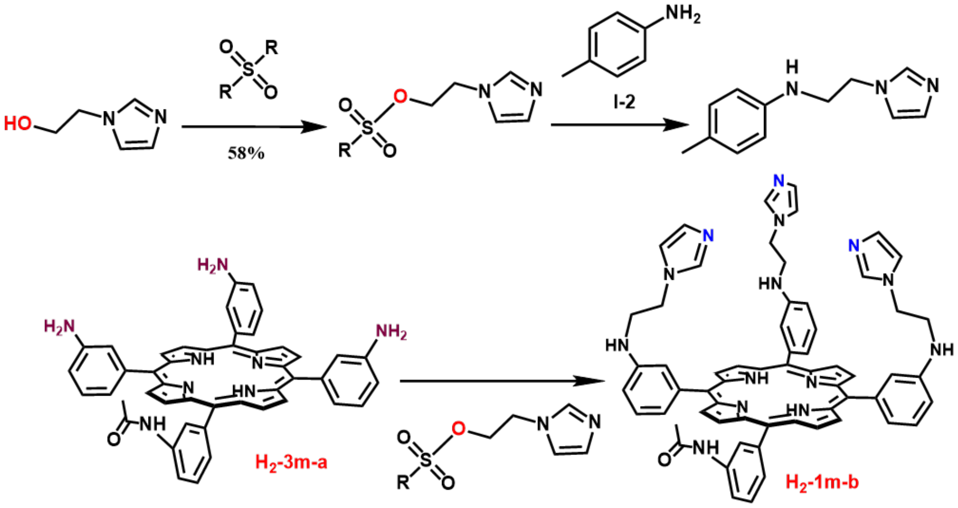

Scheme 12 *I-2) ACN, 80 °C, 5h, Ar; $CsCO_3$/NaH, DMF, from 0 °C to rt, 24h, Ar.*

4.2.2.3 meta-substituted ether-linked H_2-1m-c

Considering the difficulties faced for the preparation of amino linked porphyrins **H_2-1-b**, we turned to the synthetically less challenging ether linkages for building the most flexible ligand scaffold **H_2-1m-c** (***Schema 13***).

The preparation of the desired ligand started with the statistical condensation between pyrrole, benzaldehyde, and 3-methoxybenzaldehyde in refluxing propionic acid.[15] After recovering the desired trimethoxy derivative **H_2-4m-c** by column chromatography, it was treated with boron tribromide in anhydrous DCM to cleave the methoxy ethers and recover the trihydroxy derivative **H_2-3m-c** in excellent yield. The latter was then treated with an excess of 1,2-dibromoethane in presence of Cs_2CO_3 to yield the tri(2-bromoethyl) derivative **H_2-2m-c** which was obtained in good yield after column chromatography. Finally, the desired **H_2-1m-b** ligand was obtained by reaction between **H_2-2m-c** and a large excess of imidazole in the presence of Cs_2CO_3 at room temperature. We are able to prepare ~130 mg of the desired **H_2-1m-c** ligand in four-step with an overall yield of 2.1%.

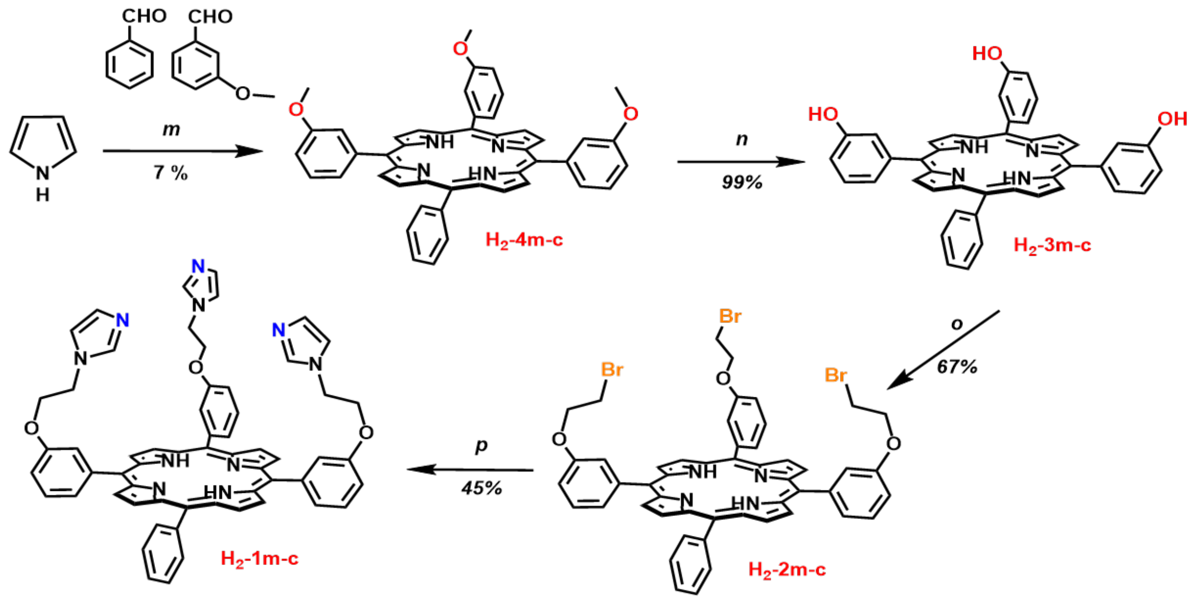

Schema 13: *a) Pyrrole, benzaldehyde, metaanisaldehyde, propionic acid, 140°C for 1 h; b) BBr_3, anhydrous DCM, –20°C for 3 h then rt overnight c) 1,2-dibromoethane, Cs_2CO_3, anhydrous DMF at 35 °C under Ar overnight; d) imidazole, Cs_2CO_3, anhydrous DMF, rt overnight*

4.3 Complexation studies

4.3.1 Complexation followed by NMR

To study the complexation of ***Mo-1*** with the porphyrin ligands prepared, we first turned to ^1H NMR spectroscopy. In brief, **H_2-1o-a**, **H_2-1m-a** and **H_2-1m-c** were dissolved in DMSO-d_6 in the presence of 1 equivalent of $[Mo_3S_7Br_6](nBu_4N)_2$ to obtain solutions where the final concentration of each species was set to 2mM. The solutions were introduced in NMR tubes which were flushed with argon before being sealed. The tubes were kept in the dark between the measurements. Unless otherwise stated the ^1H NMR spectra were recorded at 25 °C.

When the solutions were left at room temperature the spectra remained identical to the spectra of the ligands in absence of the cluster even after several hours (> 20 h), when heated at 65 °C in the dark, however, a quick evolution of the spectra was observed.

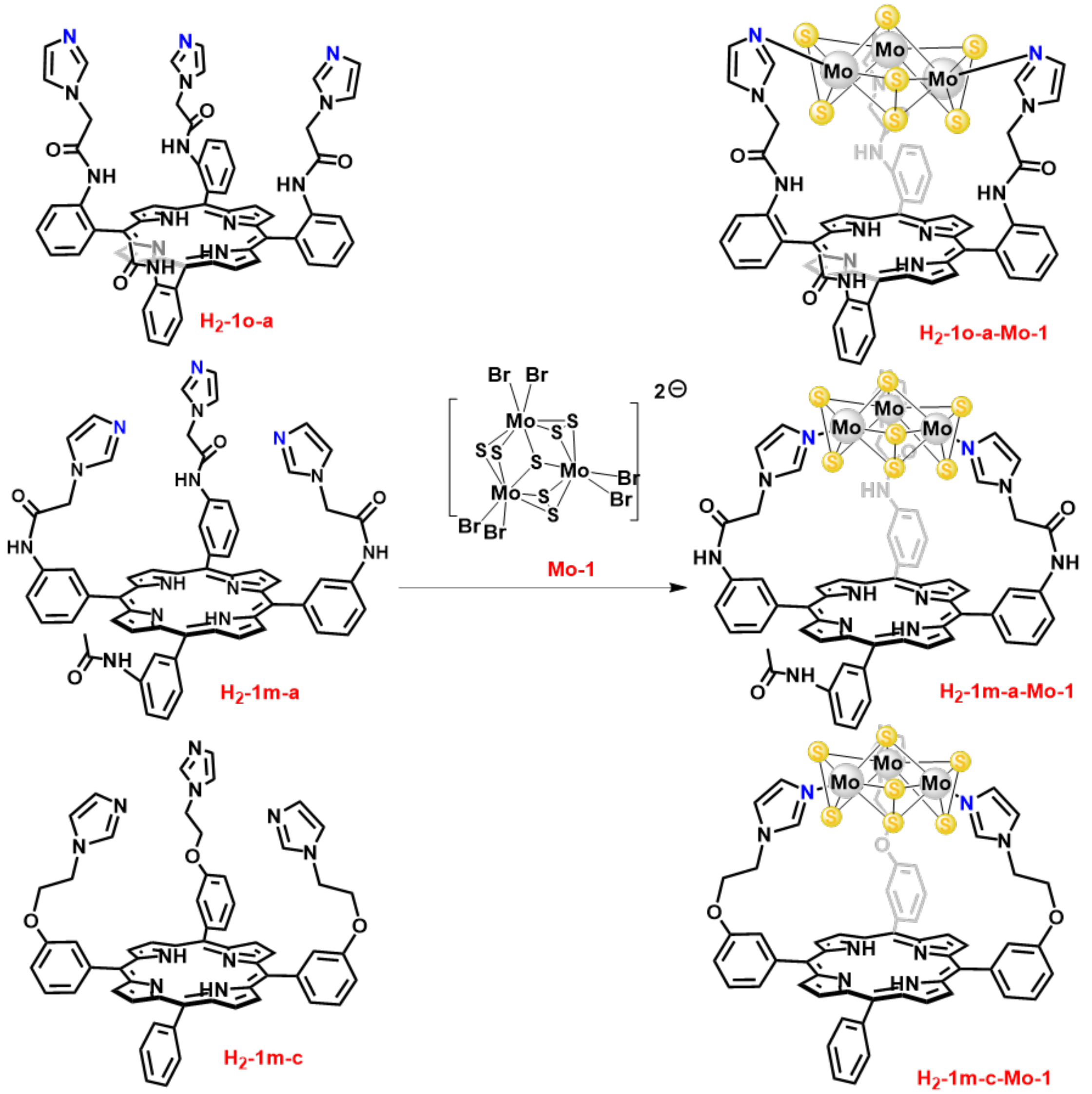

Scheme 14 *Assembly of* ***H$_2$-1o-a*** *(top),* ***H$_2$-1m-a*** *(middle) and* ***H$_2$-1m-b*** *(bottom) +* ***Mo-1****.*

H$_2$-1o-a

As shown on ***Figure 4.5*** the spectrum of **H$_2$-1o-a-*Mo-1*** significantly broadens over the course of 270 hours, then only little evolution is observed even after further annealing for 90 hours. Enlarging the spectral window to 200 ppm (-100ppm to 100ppm) did not permitted to identify signals shifted due a possible paramagnetic contribution of (partially) oxidized {Mo_3S_7} core. EPR spectroscopy further confirmed that the starting [$Mo_3S_7Br_6$](nBu_4N)$_2$ was silent. As the reaction was conducted under inert atmosphere, a partial oxidation of the {Mo_3S_7} core during the annealing at moderate temperature appears unlikely. Variable temperature ^{1}H NMR experiments (from −80 °C to 50 °C) did not permitted to significantly increase the resolution of the spectra either (***Figure 4.4***), ruling out a possible broadening effect due to a fast dynamic equilibrium between species in solution at room temperature.

Generally, all the signals broadened, which suggest that the system evolved into a heterogeneous mixture of species. Importantly the spectrum of the **H_2-1o-a** annealed 96 hours at 65 °C in the absence of ***Mo-1***, in the dark, perfectly matches the initial spectrum of the ligand**.** This exclude the possibility of a broadening due to the thermal equilibration of the system into a mixture of atropisomers under the conditions used, and strongly supports that the evolution of the spectra is due to the direct interaction between **H_2-1o-a** and ***Mo-1***.

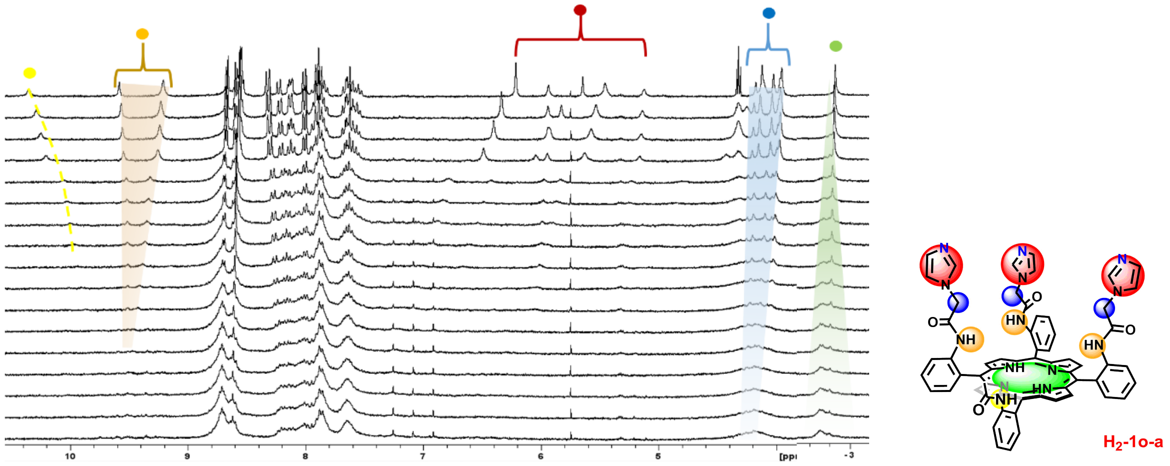

Figure 4.5: *Selected region of the ^{1}H NMR spectra of **H_2-1o-a** + **Mo-1** upon annealing at 65°C in DMSO-d6 for 270 hours.*

Looking at the evolution of the spectra more precisely we observe that: 1) the N−H signal of the free-base porphyrin (−2.8 ppm, green dot on ***Figure 4.5***) is preserved but splits into an ill-defined massif between (−2.5 ppm and −2.8 ppm) indicating that no metalation of the porphyrin core occurred during the process but that several species are present in the final mixture; 2) the signal of the CH_2 bridges (4 ppm – 4.3 ppm, blue dot on ***Figure 4.5***) are strongly affected and collapsed into a broad featureless massif centered at 4.2 ppm; 3) the signals associated with the C−H bond of the imidazole moieties (5.1 ppm – 6.2 ppm, red dot on ***Figure 4.5***) follow and interesting evolution, globally shifting downfield while broadening. Strong differences between the individual signals can be noticed with some shifting downfield 0.6 ppm while other being seemingly much less affected and shifting only 0.3 ppm during the initial evolution of the spectra. Unfortunately a detailed analysis is not possible due to the rapid loss of resolution of the spectra and the apparent disappearance of the signals of the imidazole due to excessive broadening; 4) the signals associated with the protons of the phenyl and porphyrin C−H bonds (7.5 ppm – 9 ppm) do not experience significant shift upon annealing in presence of the cluster, but gradually lose their resolution leading to a broad massif roughly covering their initial positions; 5) finally the signal of the N−H of the amide bonds are also affected and became almost invisible in after 90 h of heating. However, in the initial phase of the annealing, when all the resolution is not yet lost, we can observed the upfield shifting of the N-H of the acetamide protection group (10.3 ppm, yellow dot on ***Figure 4.5***) and the downfield shifting of the N-H of the amide linker chain (9.2 ppm and 9.6 ppm, orange dot on ***Figure 4.5***).

As we have seen all the ^{1}H NMR signals of **H_2-1o-a** are affected suggesting a strong interaction between the ligand and the cluster. Interestingly a downfield shifting (Δppm = 0.3-0.5) of the signals associated to the the C−H of the imidazole was observed in an independent experiment were ***Mo-1*** and N-methyl imidazole were mixed and annealed in similar conditions to the one used here, leading to the coordination of the N-methyl imidazole to the cluster. While coordination of ***Mo-1*** and **H_2-1o-a** led to downfield shifting with a Δppm between 0.3-0.6 ppm, which is comparable to the N-methyl imidazole reference system. Thus, in the case of **H_2-1o-a,** we can safely postulate that the evolution of the imidazole signals (and more generally to all ^{1}H NMR signals of **H_2-1o-a**) is due to the coordination of the later to ***Mo-1*** effectively leading to the desired complex. However the lack of resolution of the spectra also indicate that the system does not lead to a single, well defined species in solution, but rather a mixture of porphyrin-cluster complexes exhibiting a strong structural heterogeneity. At this stage it is not possible to discriminate between the different species and we could not isolate those using classical chromatographic techniques (silica, or sephadex). Nevertheless **H_2-1o-a** appears competent for binding ***Mo-1*** but certainly in a non-optimal way possibly due to the rather constraint geometry of the ligand and its limited flexibility.

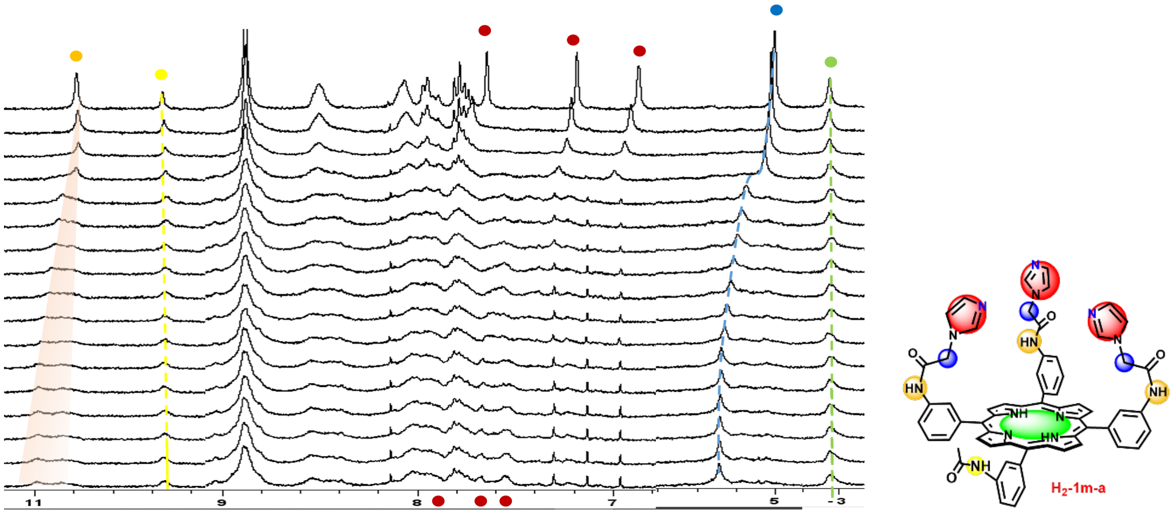

***Figure 4.6**: Selected region of the ^{1}H NMR spectra of **H_2-1m-a** + **Mo-1** upon annealing at 65°C in DMSO-d6 for 270 hours.*

H$_2$-1m-a

Upon heating in presence of ***Mo-1*** the ^{1}H NMR spectrum of **H$_2$-1m-a** globally followed a similar evolution to the spectrum of **H$_2$-1o-a**. We observe a general broadening of the signals associated with the N−H of the porphyrin core (– 2.8 ppm, green dot on ***Figure 4.6***), as well as the signals associated with the C−H of the porphyrin and phenyl substituents (7.5 ppm – 9 ppm); a clear downfield shift of the C−H signals of the imidazole (6.8 ppm, 7.2 ppm and 7.6 ppm, red dots on ***Figure 4.6***) indicate again that the coordination of the ***Mo-1*** occurs through the imidazole moieties; the signals of the bridging CH_2 (5 ppm, blue dot on ***Figure 4.6***) broaden slightly and shift downfield to 5.3 ppm; finally we note that the signal of the N−H bond from the acetamide protecting group (10.3 ppm, yellow dot on ***Figure 4.6***) is only slightly affected; while the N−H from the bridges (10.8 ppm, orange dot on ***Figure 4.6***) appears much more affected, splitting into two broad massifs centered at 10.9 ppm and 11 ppm. Unfortunately the low resolution of the signal again impeded a more precise analysis.

Here despite a significant broadening of the spectrum upon coordination to ***Mo-1***, the spectrum of the **H$_2$-1m-a** remains overall better resolved than in the case of **H$_2$-1o-a-*Mo-1*.** This suggests that **H$_2$-1m-a-*Mo-1***, while still exhibiting some heterogeneity may be more biased towards the formation of one family of species (or conformation) that dominates the mixture, leading to the observation of more defined signals.

H$_2$-1m-c

In the case of the most flexible ether-linked **H_2-1m-c** ligand, the coordination with ***Mo-1*** led to a rather simple spectrum where almost all signals keep a decent resolution (***Figure 4.7***). More precisely we can observe that the signals associated with the N−H of the porphyrin core (– 2.8 ppm, green dot on ***Figure 4.7***) are only very slightly affected, as well as the signals associated with the C−H of the porphyrin and phenyl substituents (7.4 ppm – 8.8 ppm). Very significant downfield shifts of the C−H signals of the imidazole are observed from 6.9 ppm, 7.3 ppm and 7.9 ppm, to 7.6 ppm, 7.8 ppm and 9.2 ppm respectively (red dots on ***Figure 4.7***). This indicates again that the coordination of the ***Mo-1*** occurs through the imidazole moieties. Finally, the signals of the bridging CH_2 (4.5 ppm, blue dot on ***Figure 4.7***) broaden, slightly shift downfield and splits into two signals at 4.6 ppm and 4.7 ppm. This differentiation suggests that the imidazole arms locks into a more defined conformation upon coordination to ***Mo-1***.

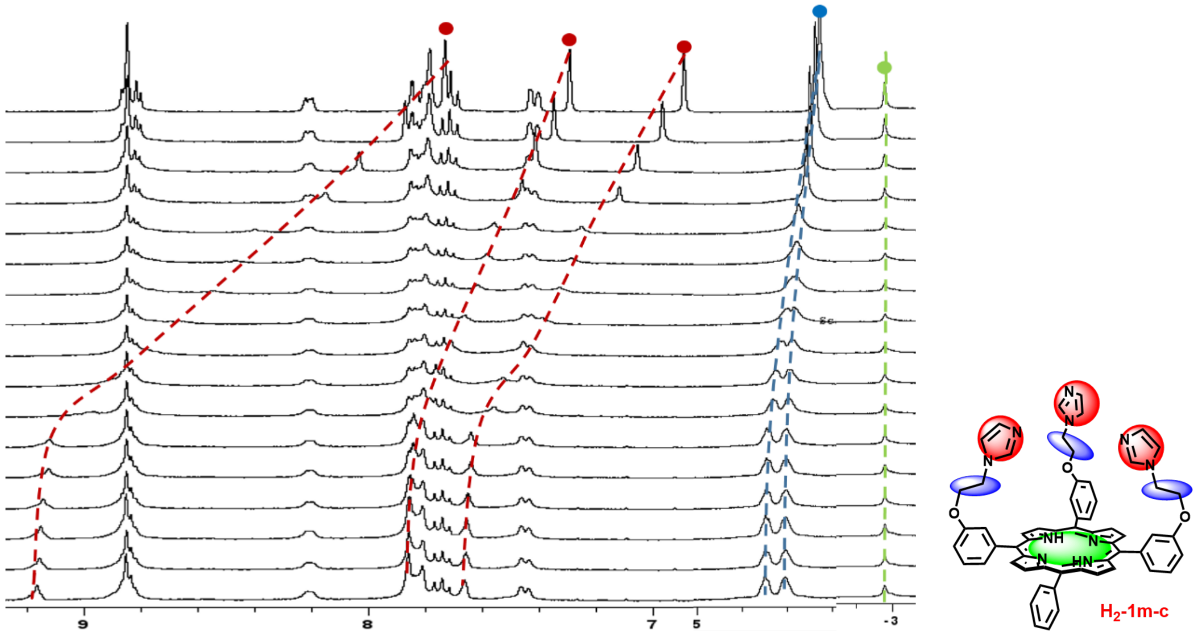

Figure 4.7: *Selected region of the ^1H NMR spectra of* ***H_2-1m-c*** *+* ***Mo-1*** *upon annealing at 65°C in DMSO-d6 for 270 hours.*

To be noticed, the signals associated with the C−H of the imidazole rings follow a very interesting evolution during the process. Along with the global shift discussed above we can observe that during the initial 100 h of aneling, during which the downfield shifting of the imidazole signals is the most pronounced, we observe a significant broadening of the latter some of them collapsing almost completely down to the baseline. Further annealing at 65 °C leads to the (partial) recovery of the resolution of the imidazole signals with only minor further downfield shifting observed (***Figure 4.7*** red dotted lines). This evolution suggests that during the complexation the system transitory goes through ill-defined species (or conformations) before gradually reaching a more stable and defined state.

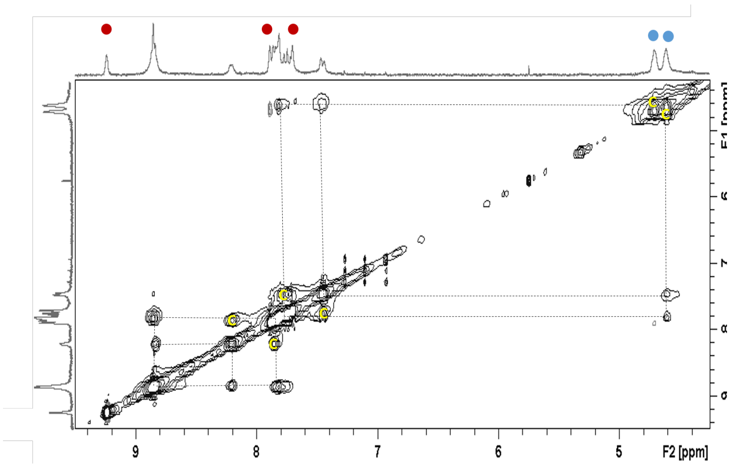

Figure 4.8: *Selected region of the 2D NOESY NMR spectra of* ***H$_2$-1m-c*** *+* ***Mo-1*** *after annealing at 65°C in DMSO-d6 for 270 hours. The red dots represent C-H signals of imidazole, and the blue dots represent the signals of CH$_2$ bridging. The yellow 'C' represent COSY couplings.*

Importantly after complexation with ***Mo-1***, strong NOE interactions develop between specific protons of the ligand (***Figure 4.8***), in contrast with the free ligand where none of these interactions were present. We observe an interaction between one CH$_2$ of the linkers (δ 4.6 ppm) and aromatic C–H form the phenyl substituents (δ 7.5, 7.8 ppm), as well as between the C–H from the porphyrin (δ 8.9 ppm) and C–H form the phenyl substituents (δ 7.8, 8.2 ppm). Due to the overlay of the aromatic signals in the ^{1}H NMR spectra of **H$_2$-1m-c-*Mo-1*** we cannot properly attribute the specific protons of the phenyl that are involved. Nevertheless, the observations of NOE contacts support the idea that upon coordination with ***Mo-1*** the conformation of the ligand is constraint within a more defined (rigid) geometry.

From this basic analysis it is tempting to conclude that just as the computational screening suggested, increasing the flexibility of the side chain appears beneficial to the formation more stable complexes, and leading to well defined species in solution, that dominates the NMR spectrum. It is likely that in the case of **H$_2$-1o-a** the intrinsic rigidity of the pre-formed cavity does not allow for an optimal interaction with ***Mo-1*** thus leading to complex mixtures of imperfectly coordinated clusters, or even oligomers, which lead to the observation of broad NMR spectra. The case of **H$_2$-1m-a** is intermediate. Since the meta substitution of the phenyl allows the free rotation of the latter around the porphyrin-phenyl bond initially the imidazole substituents can adopt various orientation in solution in the absence of ***Mo-1***, and no stable cavity can be formed. However the complexation with ***Mo-1*** occurs forcing the ligand to adapt its conformation, but having kept a rigid amide anchoring group to link the imidazole binding motifs to the porphyrin, the system cannot relax in an optimal geometry.

4.3.2 Conclusions

In this chapter we demonstrated the successful use of a computational guided approach to propose competent ligands for binding {Mo3S7} based clusters.

Initially interested in the design of cavity-like ligands, we first considered a rigid ligand **H_2-1o-a** featuring three imidazole binding sites grafted to a porphyrin, via the ortho position of the phenyl substituents of the porphyrin. In such preformed cavity we expected an efficient coordination of the cluster. In parallel we considered other structures featuring more flexible ligand architectures as well as other binding motifs than imidazole.

A rapid computational screening of these ligands against the selected **Mo-1** cluster suggested that imidazole was the most interesting binding motif to obtain the desired assemblies, as well as, that ligands with increasingly flexible side chains could lead to more stable complexes than our initial proposition. Thus we considered four main synthetic target of increasing flexibility, **H_2-1o-a**, **H_2-1m-a, H_2-1m-b** and **H_2-1m-c** where the porphyrin macrocycles was decorated with three imidazoles through 1) acetamide linkers on the ortho (**H_2-1o-a**) or meta (**H_2-1m-a**) positions of the phenyl substituents of the porphyrin; 2) aminoethyl linkers on the meta (**H_2-1m-b**) position of the phenyl substituents of the porphyrin; 3) ethoxyethyl linkers on the meta (**H_2-1m-c**) position of the phenyl substituents of the porphyrin.

We successfully prepared **H_2-1o-a**, **H_2-1m-a** and **H_2-1m-c** through multiple step synthesis, and investigated their coordination to ***Mo-1***. The coordination only happens when the solutions were heated to 65 ^{o}C and reached equilibrium after around 90 hours. Following the evolution of the complexation with NMR ^{1}H spectra, we could in all case observe a more broadening of the spectra and significant shift of the signal associated with the imidazole moieties, which proved a successful ligand-cluster interaction in all cases. Interestingly clear differences are observed in the behavior of the ligands, **H_2-1o-a** only yields and extremely broad spectrum after equilibration suggesting the formation of a heterogeneous mixtures of species in presence of ***Mo-1***. **H₂-1m-a** and **H₂-1m-c** lead to much better resolved spectra after equilibrating in presence of ***Mo-1*** suggesting the formation of more defined species in solution. If the resolution of the spectra of **H₂-1m-a-*Mo-1*** remains mediocre, **H₂-1m-c-*Mo-1*** offer a very well defined spectra suggesting the presence of a major species in solution. Furthermore 2D NOESY experiments indicated that the ligand adopts a new, more rigid conformation upon coordination with ***Mo-1*** which strongly suggest of formation of the desired ligand-cluster assembly.

Further effort will be necessary to fully characterize the species obtained in these initial studies. Nevertheless, as suggested by pour computational screening the more flexible ligand of this series appears the most promising to isolate the {Mo_3S_7} units, and further study their electrochemical (re)activity.

4.4 Synthesis

a-1. 5,10,15,20-Tetra-(2-nitrophenyl)porphyrin **H_2-5o-a**

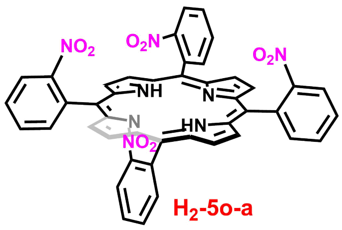

H_2-5o-a

2-Nitrobenzaldehyde (10 g, 0.066 mol) was dissolved in refluxing glacial acetic acid (200 mL) and pyrrole (4.5 g, 0.067 mol) was slowly added. The resulting dark solution was heated under reflux (125-130 °C) for 20 min. The resulting mixture was cooled to room temperature and the purple crystalline product was isolated by filtration and washed with $CHCl_3$ (25 mL) until the washings were essentially colorless. The crude product **H_2-5o-a** was used directly in the subsequent step without further purification. ($C_{44}H_{26}N_8O_8$, 2 g, 2.52 mmol, 7.2%)

b,c. 5,10,15,20-Tetra-(2-aminophenyl)porphyrin **H_2-4o-a**

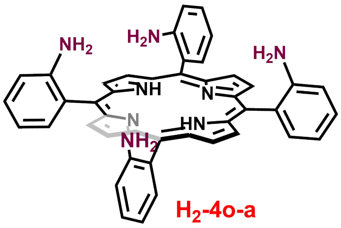

H_2-4o-a

H_2-5o-a (2 g, 0.003 mol) was dissolved in concentrated hydrochloric acid (100 mL) at room temperature then $SnCl_2{\cdot}2H_2O$ (8.3 g, 0.037 mol) was added. The resulting green mixture was heated at 65-70 °C for 1 h. After cooling down, the reaction mixture was treated with concentrated aqueous ammonia in ice bath to adjust the pH to ~7. The mixture was extracted with DCM/Ethyl acetate until the organic layers appears lightly colored. The combined organic phases were filtered, concentrated, washed with dilute aqueous ammonia (x 10) and water. After the solution was dried over Na_2SO_4 and filtered, then dried to solid.

Toluene (250 mL) and silica (50 g) were added in a round bottom flask equipped with a Dean-stark apparatus. The slurry was stirred under reflux at 125 °C for 1 h. The water was taken out from the Dean-stark trap. After cooling several minutes, the crude product was added, then heated to 100 °C for 5 h. After cooling down to room temperature, the slurry was added directly onto a silica chromatography column, the product was eluted with a gradient of acetone in DCM (1-30% acetone-DCM, **H_2-5o-a** was obtained with 25% acetone-DCM) (tetra-α-conformation, $C_{44}H_{34}N_8$, 800 mg, 1.18 mmol, 47%).

^{1}H-NMR (DMSO-d_6)**:** δ (ppm) 8.80 (s, 8H, pyrrole), 7.68 (d, 4H, phenyl), 7.52 (t, 4H, phenyl), 7.15 (d, 4H, phenyl), 7.00 (t, 4H, phenyl); –2.7 (2H, NH pyrrole).

d. 5,10,15 tris-(2-aminophenyl)-20-(2-acetylamidophenyl)-porphyrin **H_2-3o-a**

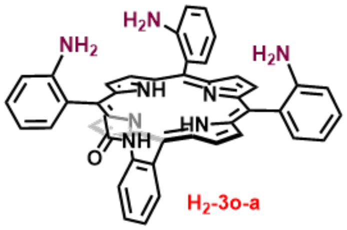

H2-3o-a

H_2-4o-a (100 mg, 0.15 mmol) was dissolved in 100 mL of freshly distilled DCM under argon, and potassium carbonate (205 mg, 1.50 mmol) was added before cooling the mixture to 0 °C. Acetyl chloride (8 µL, 0.11 mmol) was then added and the solution was stirred at 0 °C for 1 h. The solvent was evaporated and the crude material was purified on silica column chromatography using a gradient of acetone in DCM (10-30% acetone–DCM). **H_2-3o-a** was obtained with 25% acetone, 3rd band. ($C_{46}H_{36}N_8O$, 37.2 mg, 0.04 mmol, 35.9%)

^{1}H-NMR (DMSO-d_6)**:** δ (ppm) 8.69(1H, NH); 8.69(4H, pyrrole); 8.81 (2H, pyrrole); 8.76 (2H, pyrrole); 8.07 (1H, phenyl); 8.02 (1H, phenyl); 7.80 (1H, phenyl); 7.69 (3H, phenyl); 7.57 (1H, phenyl); 7.53 (3H, phenyl); 7.16(3H, phenyl); 7.02 (3H, phenyl); 4.55(2H, NH); 4.52(4H, NH); 1.18(3H, CH_3); –2.9 (2H, NH pyrrole).

HRAM-ESI: calculation for $C_{46}H_{36}N_8O + H^+$: 717.3 m/z, found: 717.31 m/z.

e. 5,10,15 tris-(2-imidazolylamidophenyl)-20-(2-acetylamidophenyl)-porphyrin **H_2-1o-a**

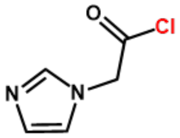

IACl

500 mg (4.0 mmol) 1H-imidazole-1-acidic acid (**IAA**) was dispersed in 15 mL of anhydrous DCM. 30 µL of anhydrous DMF was added and the white suspension was stirred under Ar for 5 minutes, then 450 µL (5.23 mmol) oxalyl chloride was added dropwise. The mixture was stirred at 40 °C for 30 minutes leading to the precipitation of a slightly yellow solid. The solvent was evaporated to dryness, the light yellow solid was recovered and used directly, without further purification, for the next step. The product is stable for up to one week at -26 °C. ($C_5H_5N_2OCl$, 610 mg, 4.2 mmol, 100%)

^{1}H-NMR (DMSO-d_6): δ (ppm) 9.1 (s, 1H, imidazole); 7.7 (d, 2H, imidazole); 5.1 (s, 2H, CH_3).

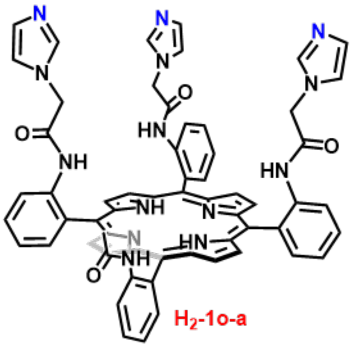

H2-1o-a

50 mg (0.07 mmol) **H_2-3o-a**, 150 mg **ImiACl** (1.04 mmol), 150 µL DIPEA (202 mg, 1.57 mmol) were dissolved in anhydrous DMF (20 mL) and the mixture was stirred for 2 hours at room temperature. The solution was diluted with DCM (20 mL) then washed with 5% LiCl aqueous solution (x 3), saturated $NaHCO_3$ aqueous solution (x 3), and water (x 3). The organic layer was dried over Na_2SO_4, filtered, and the solvent was evaporated. The crude solid was purified using silica column chromatography with a gradient of MeOH in DCM (0-3%). **H_2-1o-a** was obtained with 1% MeOH. ($C_{61}H_{48}N_{14}O_4$, 47 mg, 0.045 mmol, 66%)

^{1}H-NMR (DMSO-d_6)**:** δ (ppm) 10.32 (1H, NH); 9.57(1H, NH); 9.21 (2H, NH); 8.66 (2H, pyrrole); 8.58 (2H, pyrrole); 8.56 (2H, pyrrole); 8.53 (2H, pyrrole);8.32 (2H, phenyl); 8.23 (2H, phenyl); 8.1(2H, phenyl); 7.9 (2H, phenyl); 7.84 (2H, phenyl); 7.55 (2H, phenyl); 8.1 (1H, phenyl); 8.01 (1H, phenyl) 7.9 (1H, phenyl) 7.9 (2H, phenyl); 7.6 (1H, phenyl); 6.22(3H, imidazole); 5.94 (3H, imidazole) 5.66 (3H, imidazole); 5.12 (3H, imidazole); 4.1 (4H, CH_2); 3.97 (2H, CH_2); 1.23 (3H, CH_3); –2.9 (2H, NH pyrrole)

MS-ESI: calculation for $C_{61}H_{48}N_{14}O_4 + H^+$: 1041.4 m/z, found: 1041.42 m/z

g. 5,10,15,20-Tetra-(3-nitrophenyl)porphyrin **H_2-5m-a**

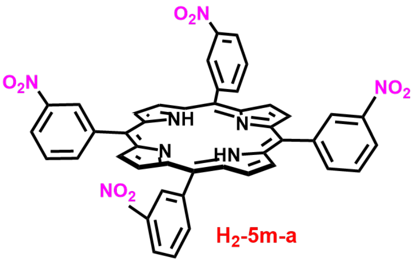

H$_2$-5m-a

3-Nitrobenzaldehyde (20 g, 0.13 mol) was dissolved in refluxing in propionic acid (400 mL) and pyrrole (8.32 mL, 0.119 mol) was slowly added. The resulting dark solution was heated under reflux (140 °C) for 2 hours. The resulting mixture was cooled to room temperature for overnight for the precipitation. The purple crystalline product was isolated by filtration and washed with cyclohexane (25 mL) until the washings were essentially colorless. The crude product **H$_2$-5m-a** was used directly in the subsequent step without further purification. ($C_{44}H_{26}N_8O_8$, 3.57 g, 4.5 mmol, 14%)

h. 5,10,15,20-Tetra-(3-aminophenyl)porphyrin **H$_2$-4m-a**

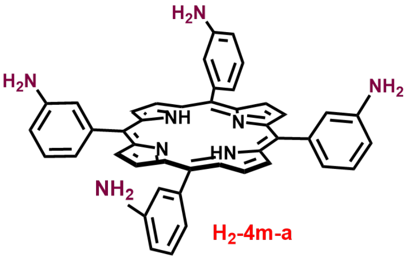

H$_2$-4m-a

H$_2$-5m-a (500 mg, 0.63 mmol) was dissolved in concentrated hydrochloric acid (25 mL) and purged with Ar for 1 hour. Then a solution of 2.25g $SnCl_2 \cdot 2H_2O$ (2.25 g, 10 mmol) in concentrated hydrochloric acid (37.5 mL) was slowly added. The resulting green mixture was heated at 75-80 °C in water bath for 30 minutes. After cooling down, the reaction mixture was treated with concentrated aqueous ammonia in ice bath to adjust the pH to ~7 under Ar. The resulted mixture was filtrated and the obtained greenish precipitates are dried under vacuum for overnight. The purification was done with chromatography (**H$_2$-5m-a** was obtained with 4/6 acetone/DCM) ($C_{44}H_{34}N_8$, 64.8 mg, 1.18 mmol, 15%).

ESI-MS: calculation for $C_{46}H_{36}N_8O + H^+$: 675 m/z, found: 675.4 m/z.

i. 5,10,15 tris-(3-aminophenyl)-20-(3-acetylamidophenyl)-porphyrin **H$_2$-3m-a**

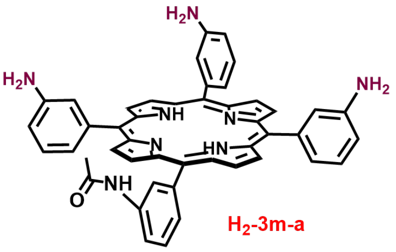

H$_2$-3m-a

H$_2$-4m-a (100 mg, 0.15 mmol) was dissolved in 100 mL of freshly distilled THF under argon, and potassium carbonate (240 mg, 1.8 mmol) was added before cooling the mixture to 0 °C. Acetyl chloride (8 µL, 0.12 mmol, 0.75 equiv.) was then added and the solution was stirred at 0 °C for 1 h30min. The solvent was evaporated and the crude material was purified on silica column chromatography using a gradient of (10-70% THF/DCM). **H$_2$-3m-a** was obtained ($C_{46}H_{36}N_8O$, 33 mg, 0.04 mmol, 30%)

^{1}H-NMR (DMSO-d$_6$): δ (ppm) 8.8(4H, pyrrole); 8.75(2H, pyrrole); 8.0(2H, pyrrole); 7.8 (2H, phenyl); 7.7 (3H, phenyl); 7.6-7.5 (4H, phenyl); 7.15 (3H, phenyl); 7.0 (3H, phenyl); 4.55 (6H, NH); 1.18 (3H, CH_3); −2.9(2H, NH pyrrole)

ESI-MS: calculation for $C_{46}H_{36}N_8O + H^+$: 717.3 m/z, found: 717.31 m/z.

j. 5,10,15 tris-(3-imidazolylamidophenyl)-20-(3-acetylamidophenyl)-porphyrin **H$_2$-1m-a**

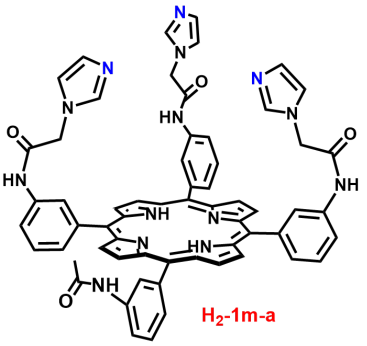

H$_2$-1m-a

IACl was prepared as in step e.

60 mg (0.08 mmol) **H$_2$-3m-a**, 180 mg **IACl** (1.25 mmol), 180 µL DIPEA (133 mg, 1 mmol) were dissolved in anhydrous DMF (20 mL) and the mixture was stirred for 1 hours at room temperature. The solution was diluted with DCM (20 mL) then washed with 5% LiCl aqueous solution (x 3), saturated $NaHCO_3$ aqueous solution (x 3), and water (x 3). The organic layer was dried over Na_2SO_4, filtered, and the solvent was evaporated. The crude solid was

purified using silica column chromatography with a gradient of MeOH in DCM (0-10%). **H_2-1m-a** was obtained ($C_{61}H_{48}N_{14}O_4$, 43 mg, 0.052 mmol, 51%)

^{1}H-NMR (DMSO-d_6): δ (ppm) 10.7 (2H, NH); 10.3 (2H, NH); 8.8 (8H, pyrrole); 8.5 (4H, phenyl); 8.0 (4H, phenyl); 7.9 (4H, phenyl); 7.6 (s, 3H, imidazole); 7.2 (s, 3H, imidazole); 6.8 (s, 3H, imidazole); 4.99 (6H, CH_2); 1.18 (3H, CH_3); –2.9 (2H, NH pyrrole).

MS-ESI: calculation for $C_{61}H_{48}N_{14}O_4 + H^+$: 1041.4 m/z, found: 1041.42 m/z

m. 5,10,15- Tris-(*3*-methoxyphenyl)-20-phenyl- porphyrin **H_2-4m-c**

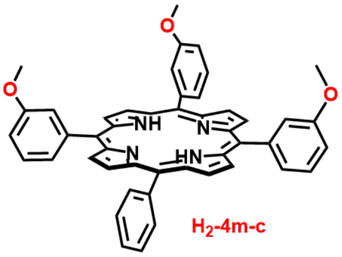

H_2-4m-c

Freshly distilled pyrrole (5.5 mL, 0.08 mol), benzaldehyde (2.02 mL, 0.02 mol) and metaanisaldehyde (6.7 mL, 0.06 mol) are dissolved in propionic acid (250 mL). The solution was refluxed for 1 h. After cooling down and concentrated under vacuum of the crude black solution, 100 mL methanol was added. The blue precipitate was filtered and washed with cold methanol. The mixture was separated by chromatography column eluted with DCM/cyclohexane (7/3, v/v). The fourth band was collected.($C_{47}H_{36}N_4O_3$: 986 mg, yield 7%).pyrrole

^{1}H-NMR (CD_2Cl_2): δ (ppm) 8.8(s, 6H, pyrrole); 8.76(d,2H, pyrrole); 8.1 (d, 2H, phenyl); 7.68-7.72 (8H, phenyl); 7.55 (t, 3H, phenyl) 3.9 (s, 9H, OCH3) –2.79 (s, 2H, NH pyrrole).

MS-ESI: calculation for $C_{47}H_{36}N_4O_3 + H^+$: 705.3 m/z, found: 705.5 m/z

n.5,10,15- Tris-(*3*-hydroxyphenyl)-20-phenyl- porphyrin **H_2-3m-c**

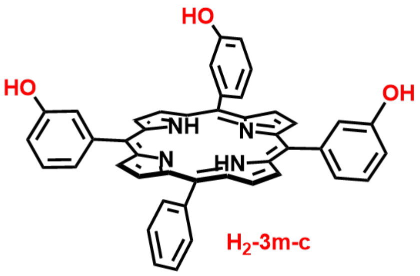

H_2-3m-c

H_2-4m-c (303 mg, 0.42 mmol) was dissolved in anhydrous DCM (75 mL) at –20°C (temperature cooled by mixture of ice+NaCl) under Ar. BBr_3 (5g, 46 equiv., 19.32 mmol) was slowly added. The green solution was stirred at –20°C for 3 h then at rt overnight. The green mixture was diluted in cold water and neutralized by a saturated $NaHCO_3$ aqueous solution. Then it was extracted by ethyl acetate, and the organic phase was washed with H_2O *2, dried with Na_2SO_4, filtered and evaporated. The pure porphyrin was obtained after crystallization from ethyl acetate/heptane ($C_{44}H_{30}N_4O_3$, 285 mg, yield 99%).

^{1}H-NMR (DMSO-d_6): δ (ppm) 9.9 (s, 9H, OH); 8.9 (s, 6H, pyrrole); 8.81 (d,2H, pyrrole); 8.2 (d, 2H, phenyl); 7.84-7.83 (3H, phenyl); 7.6 (9H, phenyl); 7.23 (3H, phenyl); –2.9 (s, 2H, NH).

MS-ESI: calculation for $C_{44}H_{30}N_4O_3$, $+ H^+$: 663 m/z, found: 662.6 m/z

o.5,10,15- Tris-(*3*-(2-bromoethoxy)phenyl)-20-phenyl- porphyrin **H_2-2m-c**

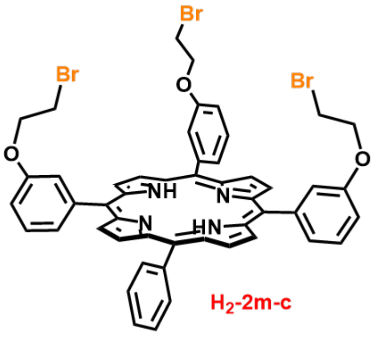

H_2-2m-c

9 mL anhydrous DMF was bubbled by Ar in a flask, then **H_2-3m-c** (303 mg, 0.42 mmol), cesium carbonate (3.38 g, 54 equiv., 24.5 mmol) and 1,2-dibromoethane (7.06 mL, 180 equiv., 81 mmol) were added. The mixture was stirred overnight at 35 °C under Ar. The solution was extracted with DCM*2 and H_2O *3, and the crude product was purified by chromatography with DCM/cyclohexane= 55/45 as eluent to obtain a purple solid. ($C_{50}H_{39}Br_3N_4O_3$, 300mg, yield 67%)

^{1}**H-NMR** ($CDCl_3$): δ (ppm) 8.86 (s, 6H, pyrrole); 8.84 (d,2H, pyrrole); 8.2 (d, 2H, phenyl); 7.86-7.83 (3H, phenyl); 7.7 (6H, phenyl); 7.65 (3H, phenyl); 7.35 (3H, phenyl); 4.5 (t, H, CH_2); 3.7 (t, H, CH_2); –2.8 (s, 2H, NH).

MS-ESI: calculation for $C_{50}H_{39}Br_3N_4O_3$, + H^+: 981 m/z, found: 981.3m/z

p.5,10,15- Tris-(*3*-(2-imidpzol)ethoxy)phenyl)-20-phenyl- porphyrin **H_2-1m-c**

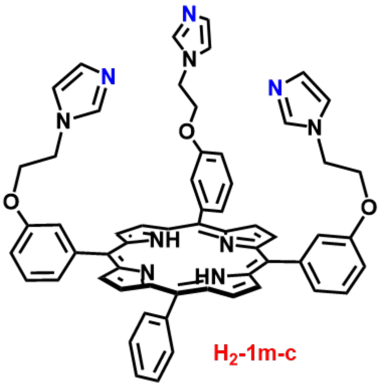

H_2-1m-c

30 mL anhydrous DMF was bubbled by Ar in a flask, then **H_2-2m-c** (300 mg, 0.3 mmol), cesium carbonate (3.5 g, 33 equiv., 10 mmol) and imidazole (6.22 g, 180 equiv., 91.5 mmol) were added. The mixture was stirred overnight at room temperature. The crude products was dissolved in minimum methanol than precipitated with NaCl salt. The solid was purified by chromatography with 6% MeOH/DCM as eluent and precipitated to yield a purple solid. ($C_{59}H_{48}N_{10}O_3$, 200 mg, yield 67%)

^{1}**H-NMR** ($CDCl_3$): δ (ppm) 8.84 (6H, pyrrole); 8.81 (2H, pyrrole); 8.22-8.19 (2H, phenyl); 7.85-7.84 (3H, phenyl); 7.79 (6H, phenyl); 7.73 (s, 3H, imidazole); 7.71-7.68 (3H, phenyl); 7.40-7.33 (3H, phenyl); 7.3 (s, 3H, imidazole); 6.9 (s, 3H, imidazole); 4.45 (s, 12H, CH_2); –2.9 (s, 2H, NH).

MS-ESI: calculation for $C_{59}H_{48}N_{10}O_3$, + H^+: 945.3 m/z, found: 945.9m/z

References

(1) Stack, T. D. P.; Weigel, J. A.; Holm, R. H. The Cavitand Concept in the Synthesis of Subsite-Differentiated Analogs of Biological [4Fe-4S/Se]2+ Clusters: Cluster Capture Reactions, Ligand Conformational Analysis, and the Structure of a Trigonal [4Fe-4Se]2+ Analog. *Inorg. Chem.* **1990**, *29* (19), 3745–3760.

(2) Rebilly, J.-N.; Colasson, B.; Bistri, O.; Over, D.; Reinaud, O. Biomimetic Cavity-Based Metal Complexes. *Chem. Soc. Rev.* **2015**, *44* (2), 467–489.

(3) Abdinejad, M.; Dao, C.; Deng, B.; Sweeney, M. E.; Dielmann, F.; Zhang, X.; Kraatz, H. B. Enhanced Electrochemical Reduction of CO2 to CO upon Immobilization onto Carbon Nanotubes Using an Iron-Porphyrin Dimer. *ChemistrySelect* **2020**, *5* (3), 979–984.

(4) Kadish, Karl M and Smith, Kevin M and Guilard, Roger. *The Porphyrin Handbook: Inorganic, Organometallic and Coordination Chemistry*; Vol. 3.

(5) Collman, J. P.; Marrocco, M.; Denisevich, P.; Koval, C.; Anson, F. C. Potent Catalysis of the Electroreduction of Oxygen to Water by Dicobalt Porphyrin Dimers Adsorbed on Graphite Electrodes. *J. Electroanal. Chem. Interfacial Electrochem.* **1979**, *101* (1), 117–122.

(6) Collman, J. P.; Gagne, R. R.; Reed, C.; Halbert, T. R.; Lang, G.; Robinson, W. T. Picket Fence Porphyrins. Synthetic Models for Oxygen Binding Hemoproteins. *J. Am. Chem. Soc.* **1975**, *97* (6), 1427–1439.

(7) Collman, J. P.; Decréau, R. A. 5,10,15-Tris(o-Aminophenyl) Corrole (TAPC) as a Versatile Synthon for the Preparation of Corrole-Based Hemoprotein Analogs. *Org. Lett.* **2005**, *7* (6), 975–978.

(8) Lindsey, J. Increased Yield of a Desired Isomer by Equilibriums Displacement on Binding to Silica Gel, Applied to Meso-Tetrakis(o-Aminophenyl)Porphyrin. *J. Org. Chem.* **1980**, *45* (25), 5215–5215.

(9) Protection for the Amino Group. In *Greene’s Protective Groups in Organic Synthesis*; Wiley-Blackwell, 2014; pp 895–1193.

(10) He, X.-C.; Feng, S.; Wang, Z.-F.; Shi, Y.; Zheng, S.; Xia, Y.; Jiang, H.; Tang, X.; Bai, D. Study on Dual-Site Inhibitors of Acetylcholinesterase: Highly Potent Derivatives of Bis- and Bifunctional Huperzine B. *Bioorg. Med. Chem.* **2007**, *15* (3), 1394–1408.

(11) Das, S.; Addis, D.; Junge, K.; Beller, M. Zinc-Catalyzed Chemoselective Reduction of Tertiary and Secondary Amides to Amines. *Chem. – Eur. J.* **2011**, *17* (43), 12186–12192.

(12) Reeves, J. T.; Tan, Z.; Marsini, M. A.; Han, Z. S.; Xu, Y.; Reeves, D. C.; Lee, H.; Lu, B. Z.; Senanayake, C. H. A Practical Procedure for Reduction of Primary, Secondary and Tertiary Amides to Amines. *Adv. Synth. Catal.* **2013**, *355* (1), 47–52.

(13) Burchat, A. F.; Chong, J. M.; Nielsen, N. Preparation of (Aminomethyl) Stannanes by Reduction of α-Amidoorgano Stannanes. *J. Org. Chem.* **1996**, *61* (21), 7627–7630.

(14) Li, M.; Dong, Y.; Yu, X.; Li, Y.; Zou, Y.; Zheng, Y.; He, Z.; Liu, Z.; Quan, J.; Bu, X.; Wu, H. Synthesis and Evaluation of Diphenyl Conjugated Imidazole Derivatives as Potential Glutaminyl Cyclase Inhibitors for Treatment of Alzheimer’s Disease. *J. Med. Chem.* **2017**, *60* (15), 6664–6677.

(15) Adler, A. D.; Longo, F. R.; Finarelli, J. D.; Goldmacher, J.; Assour, J.; Korsakoff, L. A Simplified Synthesis for Meso-Tetraphenylporphine. *J. Org. Chem.* **1967**, *32* (2), 476–476.

5. Conclusion

Ammonia (NH_3), the most reduced form of dinitrogen (N_2), has and will play a pivotal role in our industrialized societies. Historically as a major bioavailable nutriment, it has been the basis of the fertilizers that allowed to sustain the growth of the human population over the past century. It is now proposed as a next generation energy carrier, which could help or even compete with hydrogen, for the development of a carbon free economy. Driven by the imperative task of proposing alternatives to the current prevailing industrial ammonia production process, *i.e* the Haber Bosch Process (HBP) which is still mainly relying on the use of fossil fuels, the scientific community is actively seeking to develop innovative catalysts for the electrochemical nitrogen reduction reaction (ENRR). In nature, the nitrogenase, a unique enzyme found in diazotrophs, is able reduce N_2 to NH_3 through a sequential transfer of protons and electrons to dinitrogen in physiological, thus very mild conditions. This reaction is catalyzed at a highly preserved inorganic co-factors featuring transition metal sulfides clusters with general composition of MFe_7S_9C with M = Mo, V, and Fe. Among the three known cofactors for supporting dinitrogen reduction the so-called FeMoCo –Iron Molybdenum based cofactor, $MoFe_7S_9C$ is the most efficient for driving the reaction and provides a very appealing model for designing bio-inspired ENRR catalysts. Molybdenum sulfides (MoS_x), can be considered as simple synthetic analogues of the catalytic center of nitrogenase. It this class of materials, known for over a decade to be among the best proton reduction catalysts has, thus, been largely investigated as solid-state ENRR catalysts over the last few years with variable success.

In general the field of heterogeneous catalysts for ENRR still suffer from low efficiencies in the apparent yields and kinetics of ammonia production, and appear still far off the target proposed by the United States Department of Energy for an economical viable process comparing to HBP. This can be seen in the ***Figure 1*** where the main experimental parameters (ammonia production rate, current density and Faradaic efficiency) are reported within a standardized framework for a representative selection of materials described in the literature. As shown in ***Figure 1*** MoS_x do not part from the other systems, and as most materials, showed similar but random low activity. Considering the issues recently raised for other families of catalysts,[1] a careful re-evaluation of the activity of molybdenum sulfides for ENRR appeared timely to rationalize the apparent discrepancy found between studies present in the literature.

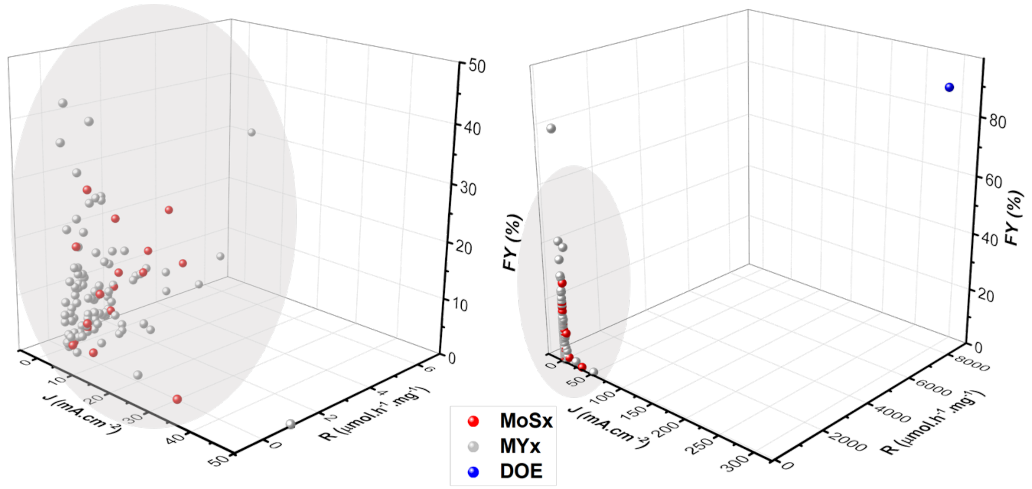

Figure 1: *3D graph of different materials reported plotted NH_3 production rate (µmol.h-1.mg-1), current density (mA.cm^{-2}), faradaic efficiency (FE %) as x, y, z axis. The red spot represents the results of Mo sulfides, the gray ones represent the other material families, while the blue one represent target defined by US. DOE Refuel program.*

Therefore, we established a rigorous protocol to study the ENRR potential of a variety of molybdenum sulfides derivatives in two different electrolyte solutions: 0.1 M HCl, and the 0.1 M KPi buffer (pH = 5.8). Our systematic protocol included: 1) the definition of proper control series targeting different contamination sources possibly leading to the release of ammonia in the medium; 2) the precise quantification of ammonia present in the electrolyte using systematic data correction.

First, we investigated the specific activity of amorphous molybdenum sulfide (*a*-MoS_x). From the analysis of our control series (***Figure 2***, left) we observed the inevitable presence of a random background of ± 10 µM NH_3 in our electrolytes. Therefore, only when the ammonia produced stands out from this range, we could rule out the possibility of false positive resulting from adventitious sources of ammonia. In our experiments, only a feeble electro-driven ammonia release was observed for a 24 h controlled electrolysis at –0.3 V vs. RHE on Nafion-coated *a*-MoS_x films deposited on glassy carbon electrodes in 0.1 M KPi buffer (pH = 5.8, KPi-7), suggesting a possible activity of this material for ENRR. Finally we proved that this apparent activity originated from the reduction of trace amounts of neutral NO_x present in the N_2 feeding gas.[2]

Inspired by the variety MoS_x-based materials reported as active catalysts for ENRR in the literature, we also investigated the potential of nanocrystalline MoS_2 (*c*-MoS_x), electrochemically deposited MoS_x (*e*-MoS_x), or Fe doped MoS_x (*Fe*-MoS_x) materials prepared in our group. In our standardized condition, none of them showed any catalytic activity

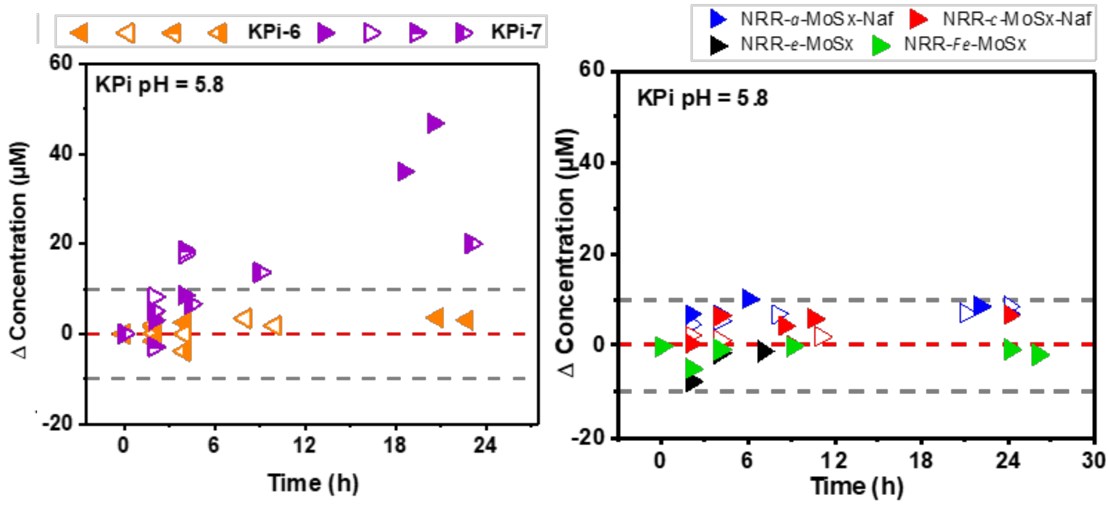

Figure 2: *Evolution of the apparent concentration of NH_3 in the electrolyte during potential-controlled electrolysis in non-purified N_2-saturated 0.1 M HCl or 0.1 M KPi buffer (pH = 5.8) on Nafion-coated a-MoS_x (left); in purified N_2-saturated 0.1 M KPi buffer (pH = 5.8) (right) on Nafion-coated a-MoS_x, c-MoS_x and, Fe-MoS_x films deposited on glassy carbon electrodes. The e-MoS_x was prepared directly from electrodeposition. The working electrode was polarized at –0.3 V vs. RHE.*

towards ENRR (***Figure 2***, right) in great contrast with the materials of this family previously discussed in the literature.

The reason leading to the huge difference of apparent ENRR activity between our materials and the others bearing close structure still remain elusive but highlight that the field of ENRR is still young and still lacks sturdy foundations.

As the MoS_x family did not show any direct activity towards ENRR in our hands, we next investigated their potential activity towards the other N-containing substrates of nitrogenase. Through a short chronoamperometry screening study on *a*-MoS_x of various substrates including: hydrazine (N_2H_4), hydroxylamine (NH_2OH), nitrate (NO_3^-), nitrite (NO_2^-), and azide (N_3^-), we found that *a*-MoS_x possesses a clear activity for the electrocatalytic reduction of inorganic azide (N_3^-) to ammonia (EN_3RR). This process might lead to similar intermediates of ENRR, and help us to understand and develop the MoS_x family as potential ENRR catalyst. As before we extended the investigation to the other molybdenum sulfide materials available in our group, including $\{Mo_3S_7\}$ clusters, which share the structure of the units forming *a*-MoS_x.

The initial tests with these different heterogenous MoS_x-based catalysts in aqueous environment, suggest that various forms of MoS_x do bear different type of catalytic sites, which in turn have noticeable impact on their EN_3RR rate and selectivity, especially upon doping with heterometals (*Fe*-MoS_x). Moreover, the well-defined $\{Mo_3S_7\}$ cluster derivatives exhibit comparable but lower rates of ammonia production possibly resulting from the worse intermolecular connection of the $\{Mo_3S_7\}$ units than in *a/e*-MoS_x. In the same time, the cluster exhibited higher selectivity thanks to their more homogenous characters (***Figure 3***).

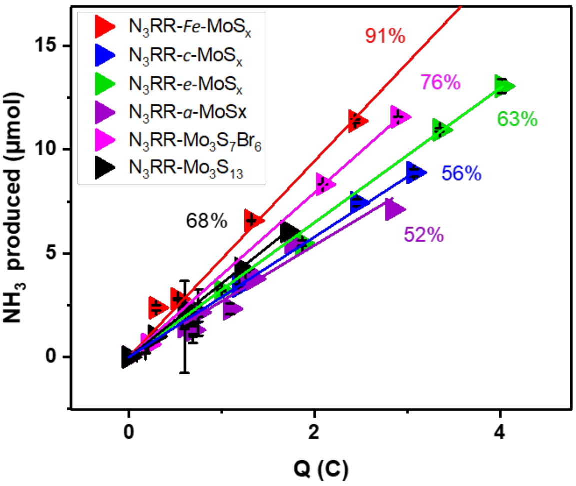

***Figure 3**: Evolution of the quantity of ammonia produced as a function of the charge passed (right) of a 10 mM solution of sodium azide in argon saturated 0.1 M KPi, the faradaic efficacy indicated by different color are calculated from the slopes of the fitting lines.*

These molecular systems, thus, offers a unique model to study the EN_3RR catalyzed by materials carrying $\{Mo_3S_7\}$ moieties under homogeneous conditions, with the help classical analytical methods. Using a combination of electrochemical and IR spectroscopic methods, we were able to probe the evolution of the $\{Mo_3S_7\}$ core of an archetypal cluster, $[Mo_3S_7Br_6](NBu_4)_2$ **Mo-1**, in presence of the N_3^- substrate under reductive conditions.

Through these studies, we demonstrated that the $\{Mo_3S_7\}$ core firstly undergoes an electro-driven reorganization to $\{Mo_3S_4\}$ via the reductive cleavage of μ_2-S-S bonds and loss of S^{2-} fragments, as confirmed by CV (***Figure 4***), IR and UV-Visible spectroscopies. This structural evolution increases the complexity of the analysis of the reactivity of $\{Mo_3S_7\}$-based clusters, therefore, we prepared the **Mo-2** bearing $\{Mo_3S_4\}$ core and used it as a reference system.

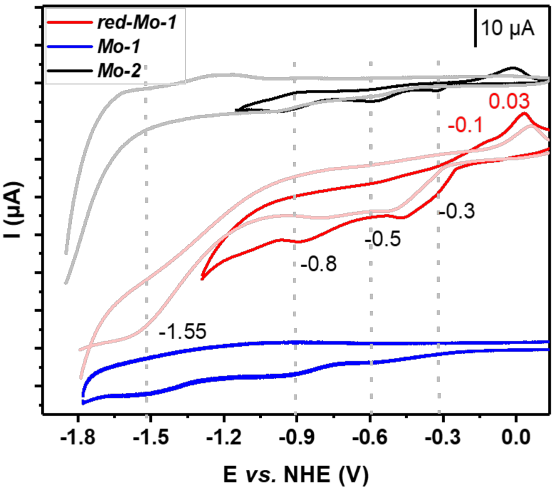

***Figure 4**: Cyclic voltammograms of 1mM solutions of **Mo-1** (blue), **Mo-2** (black) and of reduced **Mo-1** (red) in anhydrous DMF with 50mM KPF_6. Scan rate 100 mV/s. The reduced Mo-1 was obtained recorded after 3h of a controlled potential electrolysis of a 1 mM of **Mo-1** at –0.4 V vs. NHE.*

Using this model we could refine our understanding of the reactivity of this family of clusters towards azide. Interestingly in **Mo-2** two coordination modes of the azido ligand were characterized by IR spectroscopy. These two modes are distinguished by the frequencies of the antisymmetric stretching band of the azido that appears at ν_1= ~2050 cm^{-1} and ν_2= ~2085 cm^{-1} respectively. Under reductive condition the ν_1 mode appears more reactive and quickly leads to the evolution of ammonia in presence of proton (***Figure 5***). The nature of these two coordination modes still remains unknown, which might be addressed by theoretical work in future.

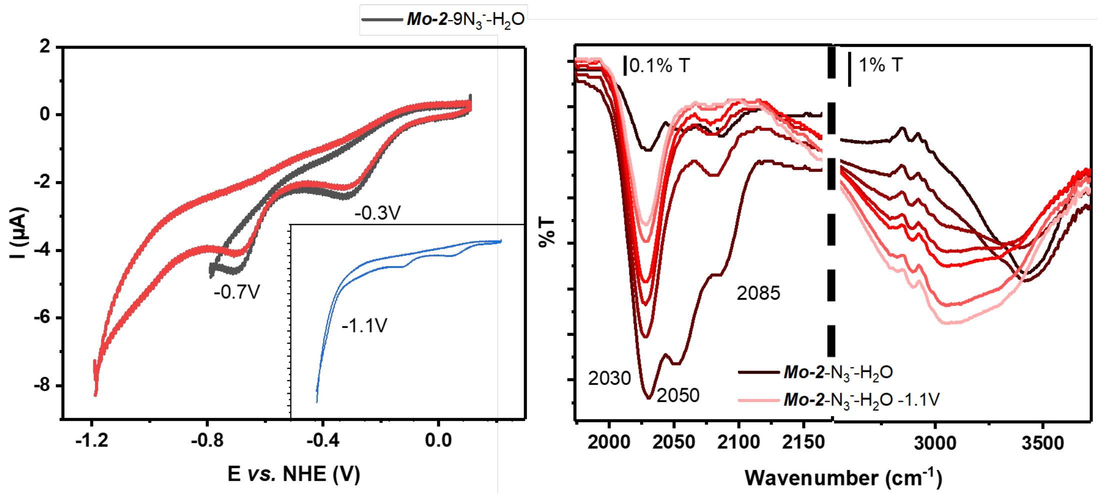

***Figure 5**: Cyclic voltammograms of **Mo-2** with 9 equiv. N_3^- added one day before in anhydrous DMF (20% H_2O) with KPF_6. Scan rate 100 mV/s (left). FT-IR spectra on Ge-ATR of antisymmetric stretching of N_3^- in **Mo-2** with freshly added 20 equiv. N_3^- in DMF (20% H_2O) reduced at −1.1 V vs. NHE (right).*

The observation of a significant decrease in the intensity of ν_1 upon the first reduction of **Mo-2** (at –0.4 V vs. NHE), and the clear apparition of N−H stretching bands in presence of protons allowed us to propose that the initiation of the catalytic cycle may involve the following sequence:

$$\boldsymbol{Mo(IV)_3\text{-}2}\text{-}9N_3 + e^- \rightarrow \boldsymbol{Mo(IV)_2}\color{blue}{\boldsymbol{Mo(III)}}\boldsymbol{\text{-}2}\text{-}9N_3 + 3H^+ \rightarrow \boldsymbol{Mo(IV)_2}\color{red}{\boldsymbol{Mo(V)}}\boldsymbol{\text{-}2}\text{-}8N_3\text{-}(NH_3)$$

However additional experiments are necessary to understand the following steps and describe a full catalytic cycle for EN$_3$RR.

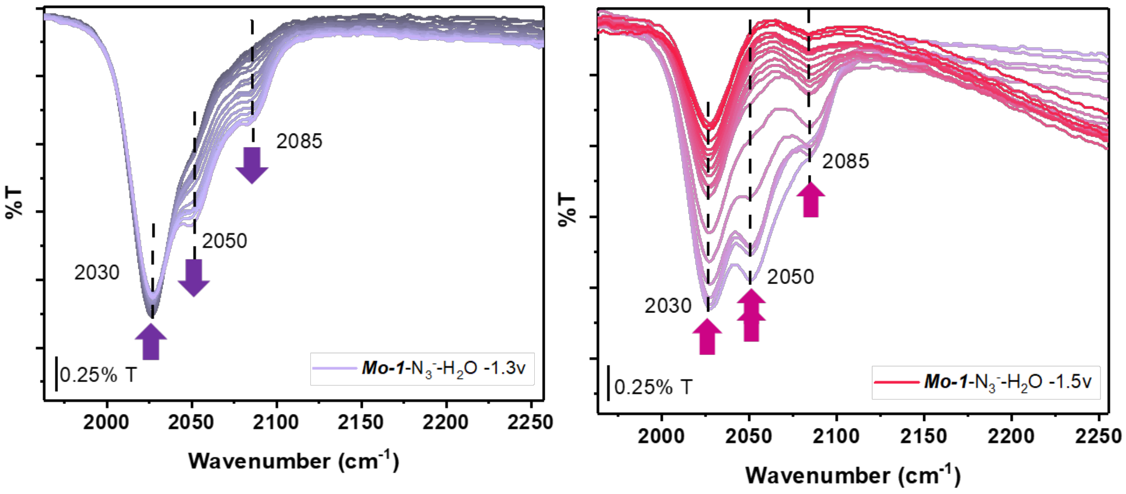

***Figure 6**: FT-IR spectra on Ge-ATR of asymmetric stretching of N_3^- and in **Mo-1** with freshly added 20 equiv. N_3^- in DMF (20% H_2O) reduced at different potential (left).*

Importantly, monitoring the evolution of the IR signature of azide in presence of **Mo-1** under reductive conditions, we could clearly identify the formation of related intermediates as both ν_1 (2050 cm^{-1}) and ν_2 (2085 cm^{-1}) component arouse upon reduction of **Mo-1**. This indicates that both clusters follow a similar EN$_3$RR pathway after the initial conversion of the $\{Mo_3S_7\}$ core into $\{Mo_3S_4\}$ (***Figure 6***). We note that coordination of azide to pure $\{Mo_3S_7\}$ core only leads to the identification of a single coordination mode of the azide, which is reminiscent of ν_1 (2050 cm^{-1}).

Moreover, following the evolution of the IR signature of N_3^- coordinated to *a*-MoS$_x$ we observed a similar evolution, where on pristine *a*-MoS$_x$ a single coordination mode is apparent, with ν_1 = 2055 cm^{-1} whereas after application of a short potential-controlled electrolysis (–0.2 V vs. RHE) in presence of azide, two coordination modes can be distinguished with ν_1 = 2050 cm^{-1} and ν_2 = 2080 cm^{-1} (***Figure 7***). Limited by time and analytical support, so far there are still some un-resolved questions, such as the exact nature of the two coordination modes of N_3^-; the evolution of Mo-S bonds in course of reduction; the nature of active sites on Mo and the variation of the oxidation states of each center thorough the catalytic cycle…

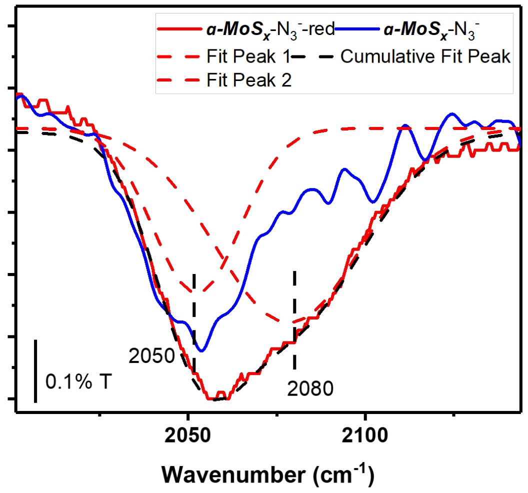

***Figure 7**: FT-IR spectra on Ge-ATR of asymmetric stretching of N_3^- in solid sample of a-MoS$_x$ coordinated to N_3^- or after using potential-controlled electrolysis (–0.2 V vs. RHE) of a 10 mM solution of NaN$_3$ 0.1 M KPi solution.*

$\{Mo_3S_7\}$ cluster, thus, appears as an interesting model to investigate in details the reactivity of *a*-MoS$_x$. Unfortunately, the “naked” **Mo-1** cluster suffers from its instability under reductive conditions, especially after its conversion to the $\{Mo_3S_4\}$ core in the conditions tested, which complicated the analysis of the system. Knowing that the FeMoCo preserved its structure by the use of an advanced ligand scaffold, we intended to prepare cavity-like ligands to stabilize the $\{Mo_3S_7\}$ cluster. The choice of the porphyrin macrocycle as a platform of suitable size and rigidity, with a well-developed chemistry, appeared as particularly well suited for building such a ligand system.

Inspired by the concept of picket-fence porphyrins proposed by Collman *et al.*,[3] we firstly considered the preparation of **H$_2$-1o-a** where the porphyrin macrocycle are functionalized with imidazoles through short acetamide chains grafted on the ortho positions of the phenyls. We also considered a variety of other related imidazole-based ligands of increasing flexibility or ligands featuring other binding motifs. In total 5 possible ligands were proposed and were engaged in a computational screening to find the best synthetic targets.

Through the theoretical calculation of the binding energy of these ligand models to ***Mo-1***, we found that 1) the imidazole groups appears to be the best suited binding motifs tested; 2) an increasing degree of flexibility of the linker between the imidazole binding motifs and the porphyrin macrocycle appears beneficial to allow for the optimal orientation of the imidazole binding motifs, thus favor the complexation (***Figure 8***); 3) the conformation where the μ_3-S ligand of the cluster is facing opposite to the porphyrin macrocycle (up-orientation) is generally more favorable for the complexation. This led us to select ligands **H_2-1o-a**, **H_2-1m-a**, **H_2-1m-b**, and **H_2-1m-c** as main synthetic targets for the design of ligands for **Mo-1** (***Figure 9***). The predicted total energies of the complexes between Mo-1 and these ligands decreases as: **H_2-1o-a** > **H_2-1m-a** > **H_2-1m-b** > **H_2-1m-c** indicating that the most flexible ligand (**H_2-1m-c**) should lead to the most stable complex.

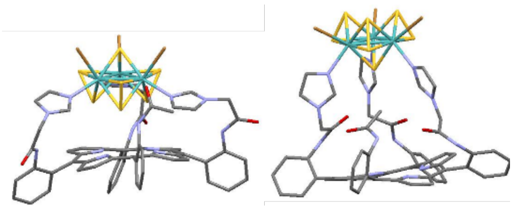

Figure 8: *Up-(left)/down-(right) orientated {$Mo_3S_7Br_3$} assembled to* ***H_2-1o-a****.*

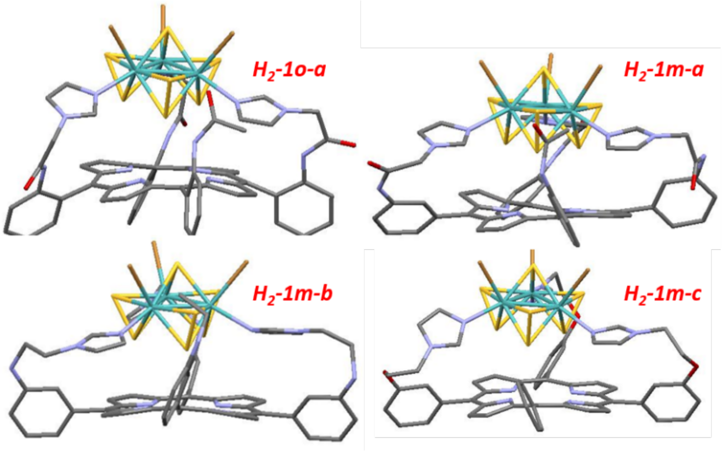

Figure 9: *Up-orientated {$Mo_3S_7Br_3$} assembled to* ***H_2-1o-a, H_2-1m-a, H_2-1m-b, H_2-1m-c****.*

We successfully prepared **H_2-1o-a**, **H_2-1m-a**, and **H_2-1m-c** through multi-step synthesis, and investigated their coordination to ***Mo-1*** (***Figure 10***). The successful coordination between the cluster and each ligand was confirmed with Maldi-TOF MS, as well as by the quenching of the fluorescence of the porphyrin core in solution. Interestingly the strong perturbation of the ^{1}H NMR spectra of each ligand, in presence of the cluster, further supports the formation of the expected assemblies. Importantly we observe that the overall broadening of the ^{1}H NMR spectra of the assemblies decreases in the order **[Mo-1@H_2-1o-a]** > **[Mo-1@H_2-1m-a]** > **[Mo-1@H_2-1m-c]**, suggesting the formation more defined species in solution as the flexibility of the ligand increases. This observation appears in good agreement with the expected formation of more stable species as proposed by the computational screaming.

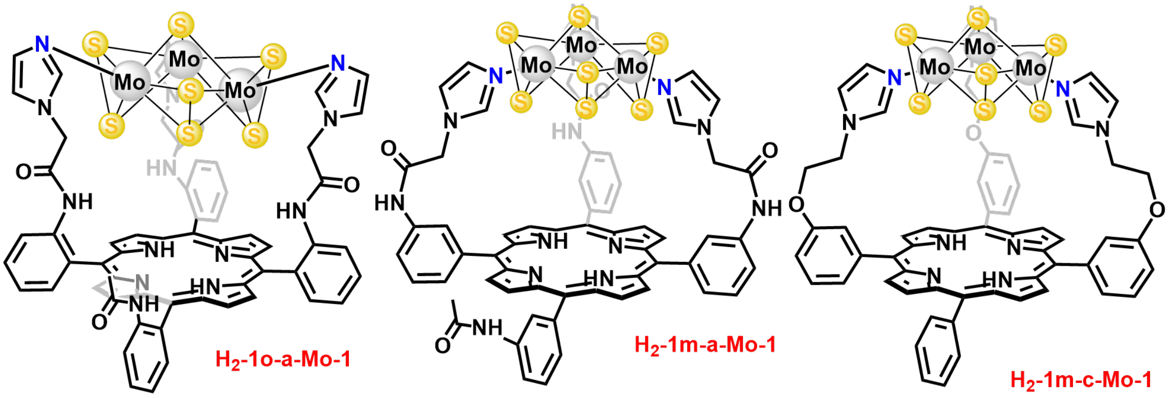

Figure 10: *Assembly of* ***H_2-1o-a*** *(left),* ***H_2-1m-a*** *(middle) and* ***H_2-1m-b*** *(right) +* ***Mo-1****.*

Searching for the electrocatalyst for nitrogen reduction reaction is a demanding task, with the problems to be addressed including the coordination of inert N_2, the multielectron transfer to the substrate, the stabilization of different intermediates… Up to date, no promising solid-state catalyst exhibited satisfying ENRR activity. Meanwhile, more and more successful NRR molecular catalysts were reported recently. Even though most of them act as chemical catalyst with mediocre turnover numbers, with the successful activity of these molecules we could understand better the mechanism. Both challenging and meaningful, study ENRR as a potential alternative process of HBP could make a huge impact on agriculture, energy and environment issues facing by human beings. To develop such an intelligent model as in nitrogenase, which was created by nature in thousands of years of evolution, we need to be a little more patient but always ambitious.

References

(1) Andersen, S. Z.; Čolić, V.; Yang, S.; Schwalbe, J. A.; Nielander, A. C.; McEnaney, J. M.; Enemark-Rasmussen, K.; Baker, J. G.; Singh, A. R.; Rohr, B. A.; Statt, M. J.; Blair, S. J.; Mezzavilla, S.; Kibsgaard, J.; Vesborg, P. C. K.; Cargnello, M.; Bent, S. F.; Jaramillo, T. F.; Stephens, I. E. L.; Nørskov, J. K.; Chorkendorff, I. A Rigorous Electrochemical Ammonia Synthesis Protocol with Quantitative Isotope Measurements. *Nature* **2019**, *570* (7762), 504–508.

(2) Dabundo, R.; Lehmann, M. F.; Treibergs, L.; Tobias, C. R.; Altabet, M. A.; Moisander, P. H.; Granger, J. The Contamination of Commercial 15N2 Gas Stocks with 15N–Labeled Nitrate and Ammonium and Consequences for Nitrogen Fixation Measurements. *PLOS ONE* **2014**, *9* (10), e110335..

(3) Collman, J. P.; Gagne, R. R.; Reed, C.; Halbert, T. R.; Lang, G.; Robinson, W. T. Picket Fence Porphyrins. Synthetic Models for Oxygen Binding Hemoproteins. *J. Am. Chem. Soc.* **1975**, *97* (6), 1427–1439.

L'ammoniac (NH_3), la forme la plus réduite du diazote (N_2), a un rôle central dans nos sociétés. Historiquement, en tant que nutriment bio assimilable essentiel, il a été la base des engrais qui ont permis de soutenir la croissance de la population humaine au cours du siècle dernier. Il est aujourd'hui proposé comme vecteur énergétique de nouvelle génération, qui pourrait aider ou même concurrencer l'hydrogène, pour le développement d'une économie décarbonée. Poussée par le besoin impérieux de trouver une alternative au procédé actuel de production industrielle d'ammoniac, à savoir le procédé Haber-Bosch (HBP), qui repose principalement sur l'utilisation de combustibles fossiles, la communauté scientifique cherche activement à développer des catalyseurs innovants pour la réduction électrochimique du diazote (ENRR). Dans la nature, la nitrogénase, une enzyme unique présente chez les diazotrophes, est capable de réduire le diazote en NH_3 par transfert de protons et d'électrons dans des conditions physiologiques. Cette réaction est catalysée grâce à un cofacteur inorganique unique à base de sulfures et carbure métalliques, dont la composition générale est MFe_7S_9C avec M = Mo, V et Fe. Parmi les trois cofacteurs connus pour permettre la réduction du diazote, le cofacteur FeMoCo - Fer-Molybdène, $MoFe_7S_9C$ est le plus efficace et fournit un modèle très intéressant pour concevoir des catalyseurs d’ENRR bio-inspirés.

Les sulfures de molybdène (MoS_x) peuvent, en particulier, être considérés comme des analogues synthétiques simplifiés du centre catalytique de la nitrogénase. Cette classe de matériaux, connue depuis plus d'une décennie pour être parmi les meilleurs catalyseurs de réduction des protons, a donc été largement étudiée comme catalyseurs hétérogène d’ENRR au cours des dernières années avec un succès variable.

En général, le domaine des catalyseurs hétérogènes pour l'ENRR souffre encore de faibles efficacités dans les rendements apparents et la cinétique de production d'ammoniac, et semble encore loin d’atteindre de l'objectif fixé par le *Department Of Energy* (DOE) des États-Unis pour un procédé économiquement viable par rapport au procedé HBP. Cela est clairement visible sur la ***Figure 1*** où les principaux paramètres expérimentaux (vitesse de production d'ammoniac, densité de courant et efficacité faradique) sont rapportés dans un cadre standardisé pour une sélection représentative de matériaux de la littérature. Comme le montre la ***Figure 1***, les sulfures de molybdène ne se distinguent pas des autres systèmes, et comme la plupart des autres matériaux, ils présentent des activités faibles et dispersés de façon aléatoire dans un espace de valeurs assez restreint. Compte tenu des questions récemment soulevées pour d'autres familles de catalyseurs,[1] une réévaluation minutieuse de

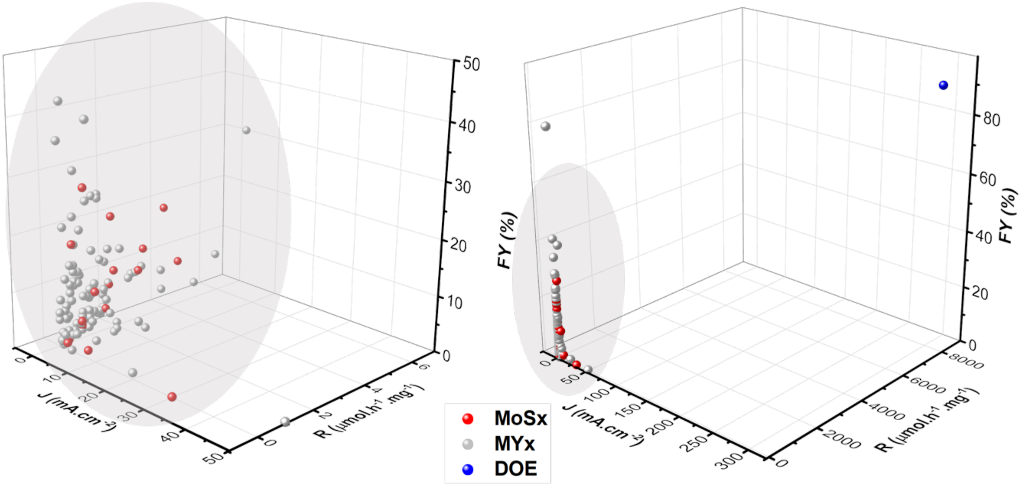

Figure 1: *Distribution des performances différents matériaux de la littérature en utilisant la vitesse de production de* NH_3 *(µmol.h*$^{-1}$*.mg*$^{-1}$*), la densité de courant (mA.cm*$^{-2}$*), et l'efficacité faradique (FE %) de chaque catalyseur comme axes x, y, z. Les points rouges représentent les performances rapportées de sulfures de Molybdène, les points gris représentent celles des autres familles de matériaux, tandis que le point bleu représente la cible définie par le programme le DOE dans le cadre de son programme de rechechre « Refuel ».*

l'activité des sulfures de molybdène pour l'ENRR apparait opportune afin de rationaliser les divergence apparentes entre les études présentes dans la littérature.

Avec cet objectif en vue, nous avons établi un protocole rigoureux pour étudier le potentiel d'une variété de dérivés de sulfures de molybdène pour catalyser la réduction du diazote par voie électrochimique, dans deux milieux différentes : une solution de HCl à 0,1 M, et une solution de tampon phosphate (KPi) à 0,1 M (pH = 5,8). Notre protocole comprenait 1) l'établissement d'une série de blancs appropriés, ciblant différentes sources de contamination pouvant conduire à la libération d'ammoniac dans le milieu; 2) la quantification précise de l'ammoniac présent dans l'électrolyte en utilisant une correction systématique des données.

Nous avons d'abord étudié l'activité spécifique du sulfure de molybdène amorphe (*a*-MoS_x). A partir de l'analyse de nos blancs (***Figure 2***, gauche), nous avons pu déterminer la présence inévitable d'ammoniac dans le milieux (contamination aléatoire) dans une gamme de concentration de l'ordre de ±10 µM dans nos électrolytes. Par conséquent, ce n'est que lorsque la quantité d'ammoniac produite s'écarte de manière significative de cette gamme de concentration, que nous pouvons considérer que le matériau possède bien une activité catalytique conduisant à la production d'ammoniac. Dans nos expériences, une faible production d'ammoniac a été observée lors les électrolyses de 24 heures réalistées à –0.3 V *vs*. RHE sur des films *a*-MoS_x incorporant du Nafion, déposés sur des électrodes en carbone vitreux, en tampon KPi 0.1 M (pH = 5.8, KPi-7), suggérant une activité possible de ce matériau pour l'ENRR. Cependant, par des expériences complémentaires nous avons pu prouver que cette activité provenait en fait de la réduction de traces de d'oxydes d'azote présents dans le gaz (N_2) utiilse, et non pas du fait de la réduction directe du diazote par le matériau.[2]

Inspirés par la variété de matériaux dérivés de MoS_x rapportés comme potentiel catalyseurs d'ENRR dans la littérature, nous avons également étudié le potentiel des du MoS_2 nanocristallin (*c*-MoS_x), du MoS_x amorphe déposés électrochimiquement (*e*-MoS_x), ou de MoS_x amorphes dopés au Fe (*Fe*-MoS_x) préparés dans notre groupe. Dans nos conditions standardisées, aucun d'entre eux n'a montré d'activité catalytique envers l'ENRR (***Figure 2***, droite), ce qui contraste fortement avec les matériaux de cette famille précédemment discutés dans la littérature.

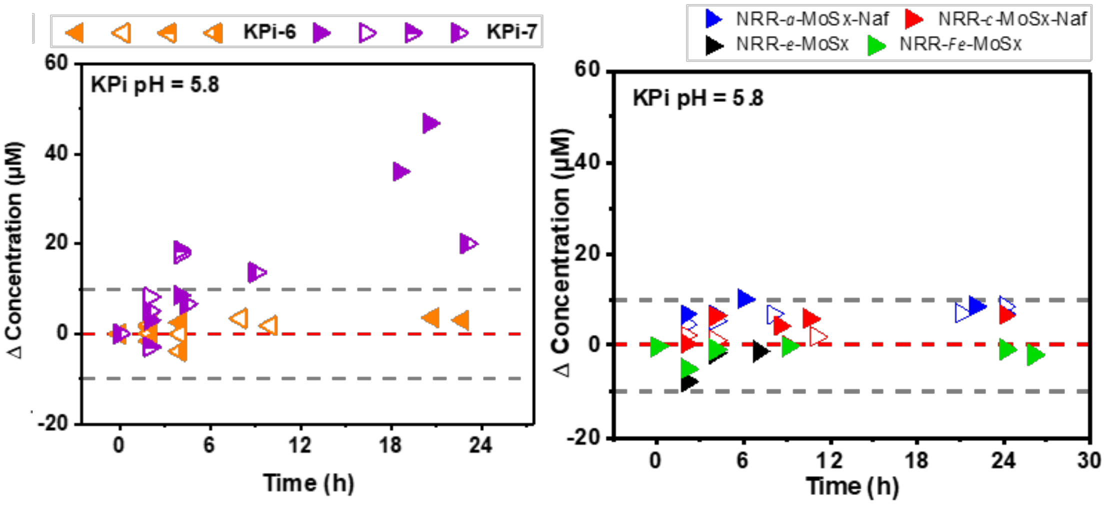

Figure 2: *Évolution de la concentration apparente de NH_3 dans l'électrolyte pendant l'électrolyse à potentiel contrôlé dans un milieu HCl à 0,1 M ou du tampon KPi à 0,1 M saturé en N_2 (pH = 5,8) sur film de a-MoS_x incorporant du Nafion (gauche), ou ; dans du tampon KPi 0,1 M saturé en N_2 (pH = 5,8) (droite) après élimination des NOx sur des films a-MoS_x, c-MoS_x et Fe-MoS_x incorporant du Nafion et déposés sur des électrodes en carbone vitreux. Le e- MoS_x a été préparé directement par électrodéposition. L'électrode de travail a été polarisée à –0,3 V par rapport au RHE.*

La raison de l'énorme différence d'activité d'ENRR apparente entre nos matériaux et ceux décrit dans la littérature et ayant une structure proche, reste encore incertaine mais souligne que le domaine de l'ENRR manque encore de fondations solides.

Comme nous n'avons pas pu confirmer le potentiel des matériaux dérivés de MoS_x pour la réduction directe du diazote, nous avons ensuite étudié leur activité potentielle pour l'activation d'autres substrats de la nitrogénase contenant de l'azote. Par le biais d'une courte étude de criblage chronoampérométrique sur *a*-MoS_x de divers substrats incluant : l'hydrazine (N_2H_4), l'hydroxylamine (NH_2OH), le nitrate (NO_3^-), le nitrite (NO_2^-), et l'azide (N_3^-), nous avons constaté que *a*-MoS_x possède une activité claire pour la réduction électrocatalytique des azotures inorganique (N_3^-) en ammoniac (EN$_3$RR). Ce processus pourrait conduire à des intermédiaires similaires à ceux supportant l'ENRR, et leur étude pourrait nous aider à estimer et développer le potentiel la famille des MoS$_x$ pour la catalyse de réduction du diazote. Comme précédemment, nous avons étendu l'investigation aux autres matériaux de sulfure de molybdène disponibles dans notre groupe, y compris les clusters {Mo_3S_7}, qui partagent la structure des unités formant *a*-MoS$_x$.

Les premiers tests avec ces différents catalyseurs hétérogènes en milieu aqueux suggèrent que les diverses formes de MoS$_x$ portent différents types de sites catalytiques, qui ont à leur tour un impact notable sur la vitesse et la sélectivité de la reaction d'EN$_3$RR. En particulier lors du dopage avec le fer (*Fe*-MoS$_x$). De plus, les clusters de type {Mo_3S_7} présentent des vitesses de production d'ammoniac comparables mais inférieures au sulfures métalliques amorphes, ce qui peut résulter d'une connexion electroniques des unités {Mo_3S_7} moins bonne que dans *a/e*-MoS$_x$. En même temps, les clusters preentent une meilleure sélectivité du fait de leur caractère plus homogène (***Figure 3***).

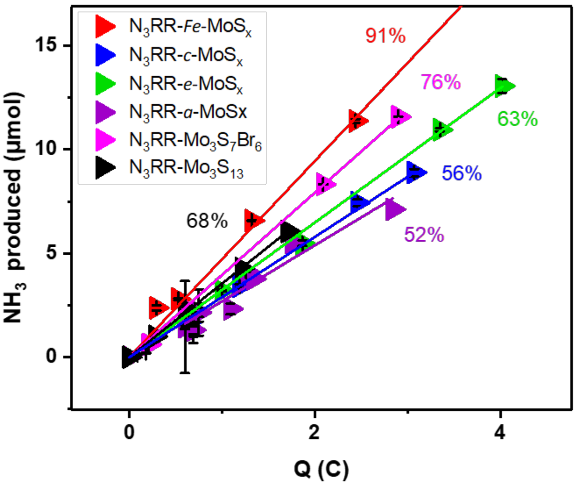

Figure 3*: Evolution de la quantité d'ammoniac produite en fonction de la charge passée (à droite) d'une solution 10 mM d'azide de sodium dans du KPi 0.1 M saturée d'argon, les efficacités faradiques indiquées par les différentes couleurs sont calculées à partir des pentes des droites de fitting.*

Ces systèmes moléculaires offrent donc des modèles uniques pour étudier l'EN$_3$RR catalysée par des matériaux portant des fragments {Mo_3S_7}, dans des conditions homogènes, à l'aide de méthodes analytiques classiques. En utilisant une combinaison de méthodes électrochimiques et spectroscopiques IR, nous avons pu sonder l'évolution du noyau {Mo_3S_7} d'un cluster type, $[Mo_3S_7Br_6](NBu_4)_2$ **Mo-1**, en présence du substrat N_3^- dans des conditions réductrices.

Grâce à ces études, nous avons démontré que le noyau {Mo_3S_7} subit d'abord une réorganisation électrodynamique en {Mo_3S_4} via le clivage réducteur des liaisons μ_2-S-S et la perte de fragments S^{2-}, comme le confirment les CV (***Figure 4***), et l'IR et l'UV-Visible. Cette évolution structurelle induit une grande complexité pour l'analyse de la réactivité des clusters

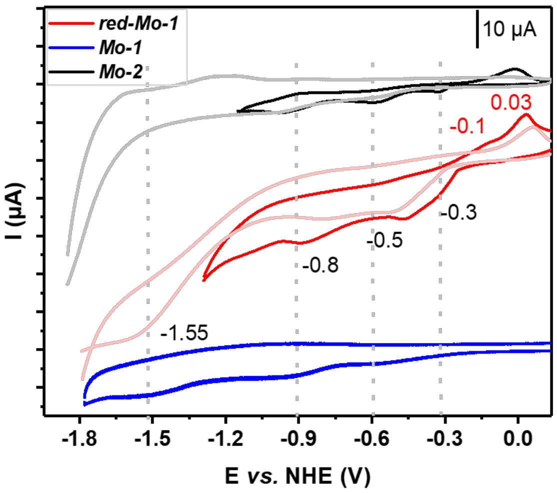

***Figure 4**: Voltampérogrammes cycliques (CV) de solutions 1mM de **Mo-1** (bleu), **Mo-2** (noir) et de **Mo-1** réduit (rouge) dans de la DMF anhydre en presence de 50 mM de KPF_6. Vitesse de balayage 100 mV/s. Le **Mo-1** réduit a été obtenu après 3h d'une électrolyse à potentiel contrôlé d'une solution de 1 mM de **Mo-1** à –0.4 V vs. NHE.*

à base de $\{Mo_3S_7\}$, c'est pourquoi nous avons préparé le **Mo-2** portant le noyau $\{Mo_3S_4\}$ et l'avons utilisé comme système de référence. En utilisant ce modèle, nous avons pu affiner notre compréhension de la réactivité de cette famille de clusters vis-à-vis des azotures. Il est intéressant de noter que dans **Mo-2**, deux modes de coordination du ligand azoture ont été caractérisés par spectroscopie IR. Ces deux modes se distinguent par les fréquences de la bande d'étirement antisymétrique de l'azoture qui apparaissent à ν_1= ~2050 cm^{-1} et ν_2= ~2085 cm^{-1} respectivement. En condition réductrice, le mode ν_1 apparaît plus réactif et conduit rapidement à l'évolution de l'ammoniac en présence de protons (***Figure 5***). La nature de ces deux modes de coordination reste encore inconnue, ce qui pourrait être abordé par des travaux théoriques dans le futur. L'observation d'une diminution significative de l'intensité du mode ν_1 lors de la première réduction de **Mo-2** (à –0.4 V *vs.* NHE), et la nette apparition de bandes d'étirement N-H en présence de protons nous ont permis de proposer que l'initiation du cycle catalytique puisse impliquer la séquence suivante :

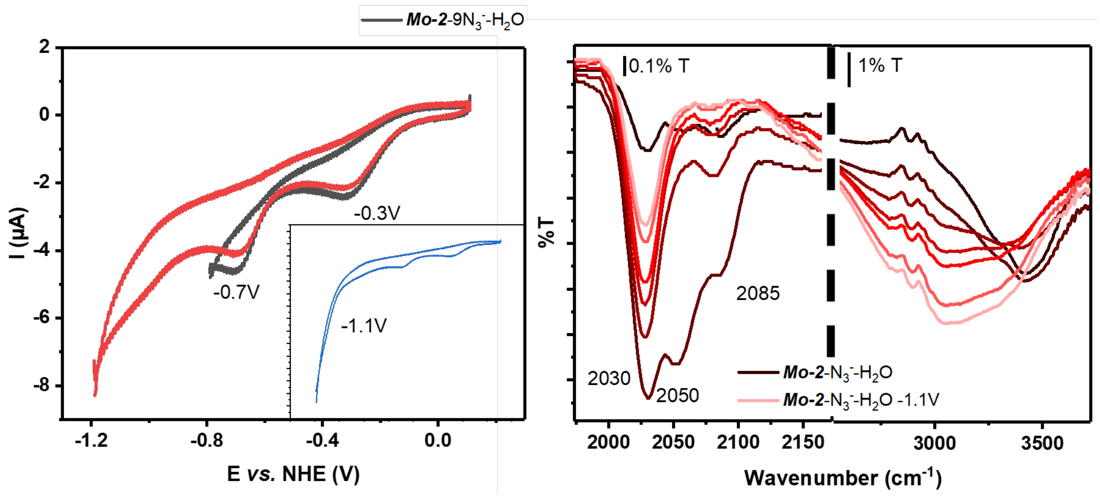

***Figure 5**: Voltampérogrammes cycliques de **Mo-2** avec 9 équiv. de N_3^- ajouté un jour avant dans du DMF anhydre (20% H_2O) avec KPF_6. Vitesse de balayage 100 mV/s (gauche). Spectres FT-IR sur Ge-ATR de l'étirement asymétrique de N_3^- dans **Mo-2** avec 20 équiv. de N_3^- fraîchement ajouté dans DMF (20% H_2O) réduit à –1,1 V par rapport à NHE (droite).*

$$\textbf{Mo(IV)}_3\textbf{-2}\text{-}9N_3 + e^- \rightarrow \textbf{Mo(IV)}_2\textbf{Mo(III)}\textbf{-2}\text{-}9N_3 + 3H^+ \rightarrow \textbf{Mo(IV)}_2\textbf{Mo(V)}\textbf{-2}\text{-}8N_3\text{-}(NH_3) + N_2$$

Cependant, des expériences supplémentaires sont nécessaires pour comprendre les étapes suivantes et décrire un cycle catalytique complet pour l'EN$_3$RR.

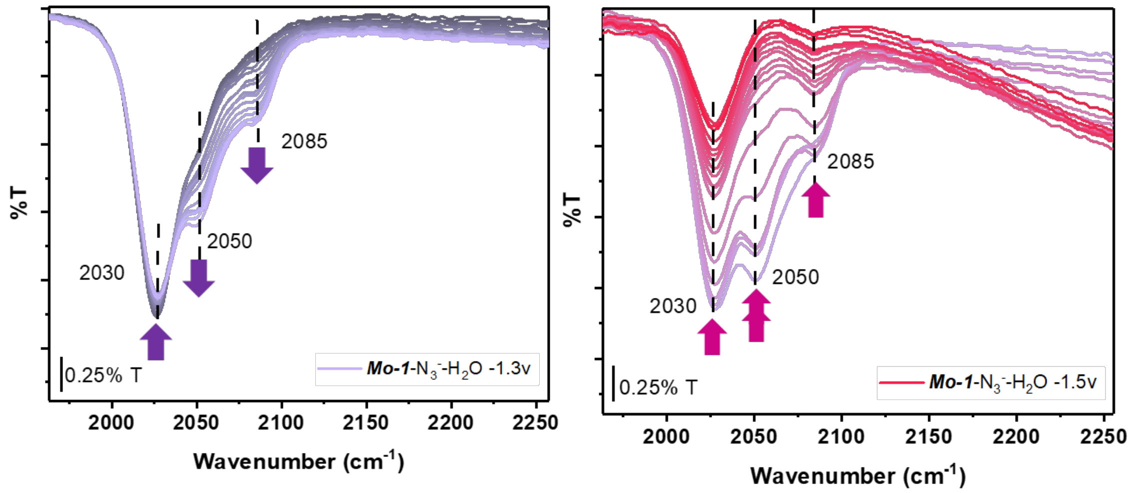

***Figure 6**: Spectres FT-IR sur Ge-ATR de l'étirement asymétrique de N_3^- et dans **Mo-1** avec 20 équiv. de N_3^- fraîchement ajouté dans DMF (20% H_2O) réduit à différents potentiels (gauche). Spectres FT-IR sur Ge-ATR de l'étirement asymétrique de N_3^- dans l'échantillon solide de a-*MoS$_x$ *coordonné à N_3^- ou après avoir utilisé l'électrolyse contrôlée par le potentiel (–0.2 V vs. RHE) d'une solution 10 mM de NaN_3 0.1 M KPi (droite).*

Il est important de noter qu'en suivant l'évolution de la signature IR de l'azoture en présence de **Mo-1** dans des conditions réductrices, nous avons pu clairement identifier la formation d'intermédiaires apparentés, les composants ν_1 (2050 cm^{-1}) et ν_2 (2085 cm^{-1}) apparaissant lors de la réduction de **Mo-1**. Ceci indique que les deux clusters suivent une voie similaire après la conversion initiale du noyau {Mo_3S_7} en {Mo_3S_4} (***Figure 6***). Nous notons que la coordination de l'azoture au noyau {Mo_3S_7} pur ne conduit qu'à l'apparition d'un seul mode de coordination de l'azoture, qui rappelle ν_1 (2050 cm^{-1}).

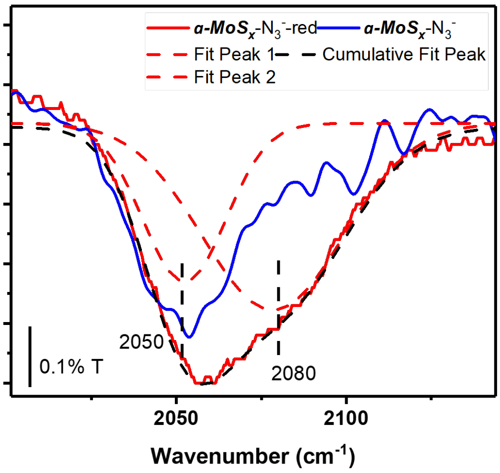

***Figure 7**: Spectres FT-IR sur Ge-ATR de l'étirement asymétrique de N_3^- dans l'échantillon solide de a-MoS$_x$ coordonné à N_3^- ou après avoir utilisé l'électrolyse contrôlée par le potentiel (–0.2 V vs. RHE) d'une solution 10 mM de NaN_3 0.1 M KPi.*

De plus, en suivant l'évolution de la signature IR de N_3^- coordonné à *a*-MoS$_x$, nous avons observé une évolution similaire, où sur *a*-MoS$_x$ vierge un seul mode de coordination est apparent, avec ν_1 = 2050 cm^{-1} alors qu'après application d'une courte électrolyse contrôlée par le potentiel

(–0,2 V vs RHE) en présence d'azide, deux modes de coordination peuvent être distingués avec ν_1 = 2050 cm^{-1} et ν_2 = 2080 cm^{-1} (***Figure 7***). Limités par le temps, de nombreuses questions restent en suspens, telles que la nature exacte des deux modes de coordination de N_3^-; l'évolution des liaisons Mo-S au cours de la réduction; la nature des sites actifs sur Mo et la variation des états d'oxydation de chaque centre au cours du cycle catalytique...

Le cluster $\{Mo_3S_7\}$ apparaît donc comme un modèle intéressant pour étudier en détail la réactivité de *a*-MoS_x. Malheureusement, le cluster **Mo-1** "nu" souffre de son instabilité dans des conditions réductrices, surtout après sa conversion en noyau $\{Mo_3S_4\}$ dans les conditions testées, ce qui complique l'analyse du système. Sachant que le FeMoCo préserve sa structure grâce à l'utilisation d'une matrice protéique complexe, nous avons voulu préparer des ligands de type cavitands pour stabiliser le cluster $\{Mo_3S_7\}$. Le choix d'un macrocycle porphyrinique comme plateforme de taille et de rigidité appropriées est apparu comme particulièrement bien adapté à la construction d'un tel système de ligand. Inspirés par le concept de *picket fence porphyrins* proposé par Collman et al.,[3] nous avons d'abord envisagé la préparation de **H_2-1o-a** où le macrocycle de la porphyrine est fonctionnalisé avec des imidazoles par l'intermédiaire de courtes chaînes d'acétamide greffées sur les positions ortho des phényles. Nous avons également envisagé une variété d'autres ligands apparentés à base d'imidazoles de flexibilité croissante ou des ligands présentant d'autres motifs de liaison. Au total, 5 ligands potentiels ont été proposés et ont fait l'objet d'un criblage *in silico* pour trouver les meilleures cibles synthétiques.

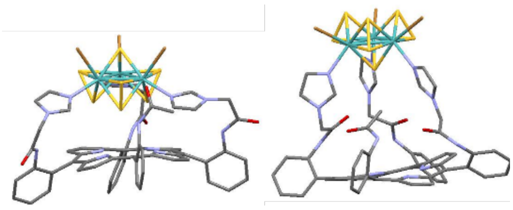

Figure 8: *$\{Mo_3S_7Br_3\}$ orienté vers le haut (gauche)/bas (droite) assemblé à **H_2-1o-a**.*

Grâce au calcul théorique de l'énergie de liaison entre ces modèles de ligands et **Mo-1**, nous avons constaté que 1) les groupes imidazoles semblent être les motifs de liaison les mieux adaptés; 2) un degré croissant de flexibilité du lien entre les motifs de liaison imidazole et le macrocycle de la porphyrine semble bénéfique favoriser la complexation ; 3) la conformation où le ligand μ_3-S du cluster est orienté à l'opposé du macrocycle de la porphyrine (orientation vers le haut) est généralement plus favorable pour la complexation. Ceci nous a conduit à sélectionner les ligands **H_2-1o-a**, **H_2-1m-a**, **H_2-1m-b**, et **H_2-1m-c** comme principales cibles synthétiques pour la conception de ligands pour **Mo-1** (***Figure 9***). Les énergies totales prédites des complexes entre **Mo-1** et ces ligands diminuent comme suit : **H_2-1o-a** > **H_2-1m-a** > **H_2-1m-**

b > **H$_2$-1m-c** indiquant que le ligand le plus flexible (**H$_2$-1m-c**) devrait conduire au complexe le plus stable.

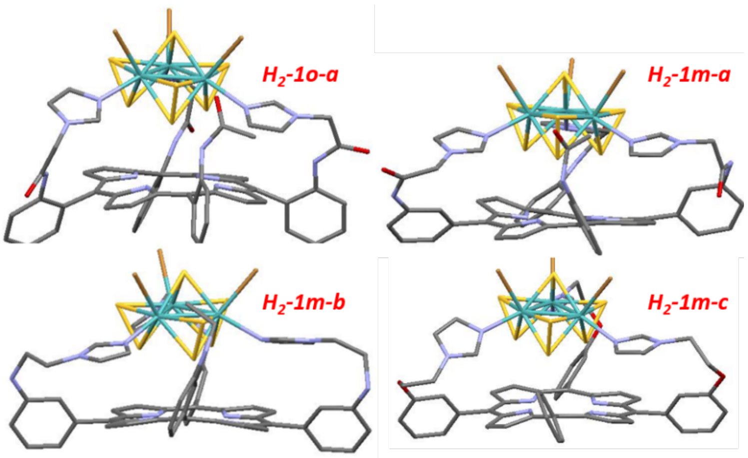

Figure 9: *{$Mo_3S_7Br_3$} orienté vers le haut assemblé à* ***H$_2$-1o-a, H$_2$-1m-a, H$_2$-1m-b, H$_2$-1m-c****.*

Nous avons préparé avec succès **H$_2$-1o-a**, **H$_2$-1m-a**, et **H$_2$-1m-c** par synthèse multi-étapes (***Figure 10***), et avons étudié leur coordination avec **Mo-1**. La coordination effective entre le cluster et chaque ligand a été confirmée par l'extinction de la fluorescence du noyau de porphyrine en solution. Il est intéressant de noter que la forte perturbation des spectres RMN ^{1}H de chaque ligand, en présence du cluster, confirme la formation des assemblages attendus. Il est important de noter que l'élargissement global des spectres RMN ^{1}H des assemblages diminue dans l'ordre **[Mo-1@H$_2$-1o-a]** > **[Mo-1@H$_2$-1m-a]** > **[Mo-1@H$_2$-1m-c]**, ce qui suggère la formation d'espèces plus définies en solution lorsque la flexibilité du ligand augmente. Cette observation est en bon accord avec la formation attendue d'espèces plus stables comme proposé par le criblage *in silico*.

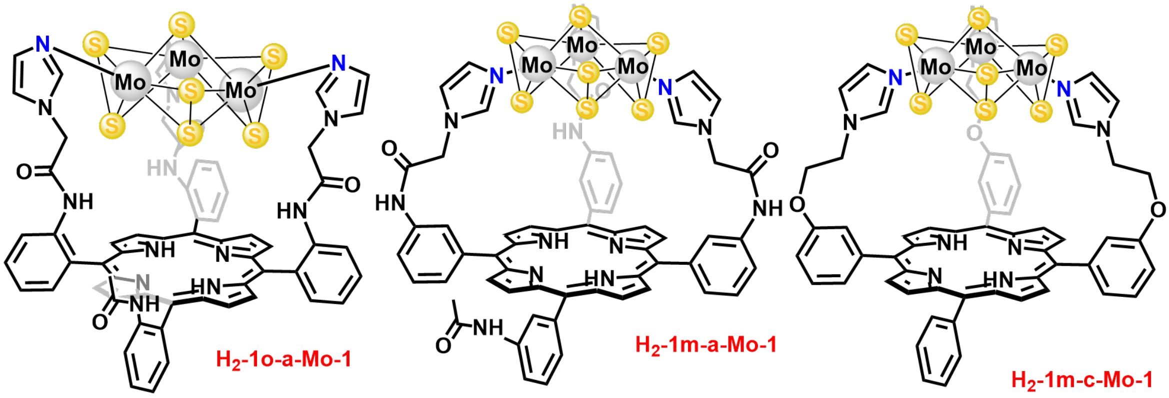

Figure 10: *Assemblage de {$Mo_3S_7Br_3$} à* ***H$_2$-1o-a*** *(gauche),* ***H$_2$-1m-a*** *(milieu) and* ***H$_2$-1m-b*** *(droit)****.***

La recherche d'un électro catalyseur pour la réaction de réduction de l'azote est une tâche exigeante, les problèmes à résoudre comprenant la coordination de l'azote inerte, le transfert multi-électronique vers le substrat, la stabilisation des différents intermédiaires... Jusqu'à présent, aucun catalyseur solide prometteur n'a présenté une activité ENRR satisfaisante. Parallèlement, de plus en plus de catalyseurs moléculaires ENRR performants ont été rapportés récemment. Même si la plupart d'entre eux agissent comme des catalyseurs chimiques avec des rendements médiocres, l'activité de ces molécules nous a permis de mieux comprendre le mécanisme de réduction du diazote. L'étude de l'ENRR en tant que processus alternatif potentiel du HBP, à la fois stimulante et significative, pourrait avoir un impact énorme sur l'agriculture, l'énergie et les problèmes environnementaux auxquels nos sociétés sont confrontées. Pour développer un modèle aussi performant que celui de la nitrogénase, qui a été affinité par la nature au cours de milliers d'années d'évolution, nous devons être un peu plus patients mais toujours ambitieux.

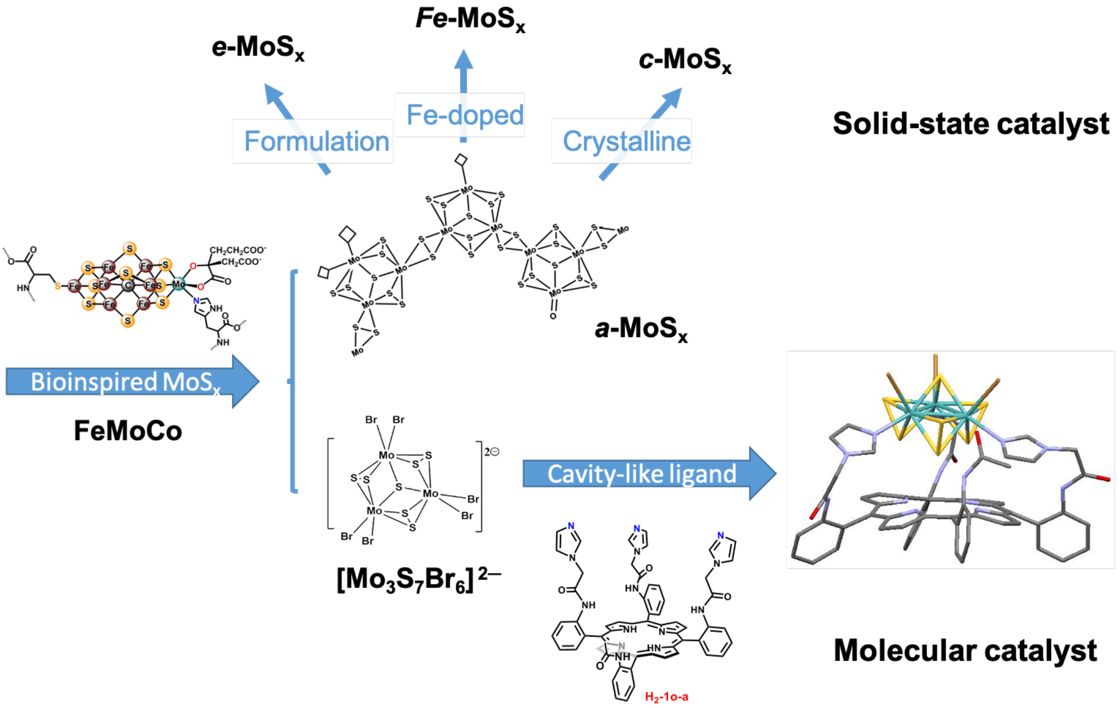

***Figure 11**: Matériaux utilisés dans le travail.*

References

(1) Andersen, S. Z.; Čolić, V.; Yang, S.; Schwalbe, J. A.; Nielander, A. C.; McEnaney, J. M.; Enemark-Rasmussen, K.; Baker, J. G.; Singh, A. R.; Rohr, B. A.; Statt, M. J.; Blair, S. J.; Mezzavilla, S.; Kibsgaard, J.; Vesborg, P. C. K.; Cargnello, M.; Bent, S. F.; Jaramillo, T. F.; Stephens, I. E. L.; Nørskov, J. K.; Chorkendorff, I. A Rigorous Electrochemical Ammonia Synthesis Protocol with Quantitative Isotope Measurements. *Nature* **2019**, *570* (7762), 504–508.

(2) Dabundo, R.; Lehmann, M. F.; Treibergs, L.; Tobias, C. R.; Altabet, M. A.; Moisander, P. H.; Granger, J. The Contamination of Commercial 15N2 Gas Stocks with 15N–Labeled Nitrate and Ammonium and Consequences for Nitrogen Fixation Measurements. *PLOS ONE* **2014**, *9* (10), e110335.

(3) Collman, J. P.; Gagne, R. R.; Reed, C.; Halbert, T. R.; Lang, G.; Robinson, W. T. Picket Fence Porphyrins. Synthetic Models for Oxygen Binding Hemoproteins. *J. Am. Chem. Soc.* **1975**, *97* (6), 1427–1439.

Abstract

The scientific community is actively seeking to develop innovative catalysts for the electrochemical nitrogen reduction reaction (ENRR) to produce ammonia (NH_3), which has and will play a pivotal role in our industrialized societies. Herein we systematically investigated different types of solid-state molybdenum sulfides (MoS_x) as ENRR catalysts, including amorphous molybdenum sulfide (*a*-MoS_x), nanocrystalline MoS_2 (*c*-MoS_x), electrochemically deposited MoS_x (*e*-MoS_x), or Fe doped MoS_x (*Fe*-MoS_x). Using a rigorous protocol for testing the materials in standardized conditions, we establish that none of them showed any catalytic activity towards ENRR, in great contrast with the materials of this family previously discussed in the literature. However, they all exihibited a clear activity towards the electrocatalytic reduction of inorganic azide (N_3^-) to ammonia (EN_3RR). Here we show that the various forms of MoS_x do bear different type of catalytic sites, which in turn have noticeable impact on their EN_3RR rate and selectivity.

Interestingly we demonstrate that the well-defined $\{Mo_3S_7\}$ clusters, sharing the structure of the units forming e/*a*-MoS_x, do exhibited comparable EN_3RR activity to *a*-MoS_x. It offers a unique model to study EN_3RR under homogeneous conditions with the help of classical analytical methods. Through these studies, we demonstrated that the $\{Mo_3S_7\}$ core firstly undergoes an electro-driven reorganization to $\{Mo_3S_4\}$, which provide two coordination modes for the azido ligand, one of which leading to the fast evolution of ammonia in presence of protons. Noteworthy we show that a similar evolution may be at play for *a*-MoS_x during the EN_3RR justifying the use of molecular models to understand catalytic activity of the solid-state MoSx.

In order to stabilize the $\{Mo_3S_7\}$ clusters, we next consider the design of cavity-like tridentate porphyrin ligands (H_2P) using a computational-guided strategy to select a few potential ligands. After the preparation of the latter we demonstrate that this family of ligands is indeed capable of binding the cluster, and as suggested by the computational screening we observe that the complexation is favored as the overall flexibility of the ligand increases. This work lies down the foundations of a systematic investigation of the potential of molecular $\{Mo_3S_7\}$ species towards the activation of nitrogenase substrates.

Résumé

La communauté scientifique cherche activement à développer des catalyseurs innovants pour la réaction électrochimique de réduction de l'azote (ENRR) pour produire de l'ammoniac (NH_3), qui a et aura un rôle central dans nos sociétés industrialisées. Dans cet article, nous avons systématiquement étudié différents types de sulfures de molybdène (MoS_x) à l'état solide en tant que catalyseurs de la réaction de réduction de l'azote, notamment le sulfure de molybdène amorphe (*a*-MoS_x), le MoS_2 nanocristallin (*c*-MoS_x), le MoS_x déposé par voie électrochimique (*e*-MoS_x) ou le MoS_x dopé au Fe (*Fe*-MoS_x). En utilisant un protocole rigoureux pour tester les matériaux dans des conditions standardisées, nous établissons qu'aucun d'entre eux n'a montré d'activité catalytique envers l'ENRR, en grand contraste avec les matériaux de cette famille précédemment discutés dans la littérature. Cependant, ils ont tous porté une activité claire vers la réduction électrocatalytique de l'azide inorganique (N_3^-) en ammoniac (EN_3RR). Nous montrons ici que les différentes formes de MoS_x portent différents types de sites catalytiques, ce qui a un impact notable sur leur taux et leur sélectivité pour l'EN3RR.

De manière intéressante, nous démontrons que les clusters $\{Mo_3S_7\}$ bien définis, partageant la structure des unités formant e/*a*-MoS_x, présentent une activité EN_3RR comparable à celle de *a*-MoS_x. Ils offrent un modèle unique pour étudier l'EN3RR dans des conditions homogènes à l'aide de méthodes analytiques classiques. Grâce à ces études, nous avons démontré que le noyau $\{Mo_3S_7\}$ subit d'abord une réorganisation électrodynamique en $\{Mo_3S_4\}$, qui fournit deux modes de coordination pour le ligand azido, dont l'un conduit à l'évolution rapide de l'ammoniac en présence de protons. Nous montrons qu'une évolution similaire peut être en jeu pour *a*-MoS_x pendant l'EN_3RR, justifiant l'utilisation de modèles moléculaires pour comprendre l'activité catalytique du MoS_x à l'état solide.

Afin de stabiliser les clusters $\{Mo_3S_7\}$ nous considérons ensuite la conception de ligands de porphyrine tridentés en forme de cavité (H_2P) en utilisant une stratégie guidée par le calcul pour sélectionner quelques ligands potentiels. Après la préparation de ces derniers, nous démontrons que cette famille de ligands est effectivement capable de fixer le cluster, et comme suggéré par le criblage computationnel, nous observons que la complexation est favorisée lorsque la flexibilité globale du ligand augmente. Ce travail jette les bases d'une investigation systématique du potentiel des espèces moléculaires $\{Mo_3S_7\}$ vers l'activation des substrats de la nitrogénase.